

TECHNISCHE UNIVERSITÄT MÜNCHEN

TUM School of Engineering and Design

**Analysis of Wind Turbine Wakes Immersed in
Turbulent Boundary Layer Flows Over Rough Surfaces
- An Experimental and Numerical Study**

Victor P. Stein

Vollständiger Abdruck der von der TUM School of Engineering and Design der Technischen Universität München zur Erlangung des akademischen Grades eines

Doktors der Ingenieurwissenschaften (Dr.-Ing.)

genehmigten Dissertation.

Vorsitzender:

apl. Prof. Dr.-Ing. habil. Thomas Indinger

Prüfende der Dissertation:

1. Prof. Dr.-Ing. Hans-Jakob Kaltenbach
2. Prof. Dr.-Ing. Carlo L. Bottasso

Die Dissertation wurde am 17.08.2021 bei der Technischen Universität München eingereicht und durch die TUM School of Engineering and Design am 31.01.2022 angenommen.

Victor P. Stein: Analysis of Wind Turbine Wakes Immersed in Turbulent Boundary Layer
Flows Over Rough Surfaces - An Experimental and Numerical Study ,
Dissertation, Technische Universität München, Germany.

Released 26.04.2022

Copyright ©April 2022, Victor P. Stein

All rights reserved. No part of this publication may be reproduced, modified, re-written,
or distributed in any form or by any means, (electronic, photocopying, recording, or
otherwise) without the prior written permission of the author.

ADDRESS:

Seumestr. 11, 81379 München

E-MAIL:

victor.stein@tum.de

Danksagung

Die vorliegende Dissertation entstand während meiner Zeit als wissenschaftlicher Mitarbeiter im Fachgebiet für Strömungsbeeinflussung und Aeroakustik der Technischen Universität München. An dieser Stelle möchte ich einigen Personen danken, die ganz wesentlich zum Gelingen dieser Arbeit beigetragen haben.

Zuallererst möchte ich mich bei Prof. Hans-Jakob Kaltenbach bedanken. Sie haben mir in vielen Diskussionen immer wieder neue Denkanstöße gegeben, mir aber gleichzeitig auch sehr viel Freiheit bei der Ausgestaltung meiner wissenschaftlichen Arbeit eingeräumt. Darüber hinaus möchte ich Ihnen insbesondere für die Ermöglichung und Unterstützung meiner Gastaufenthalte bei Partnerinstituten danken.

In diesem Zusammenhang möchte ich mich bei Prof. Stefan Hickel bedanken. Du hast mich nicht nur jederzeit in Delft empfangen, sondern mich auch tatkräftig bei der Lösung aller Probleme die ich mit INCA hatte unterstützt - und das waren nicht wenige. Das ist nicht selbstverständlich und dafür danke ich dir.

A special thanks goes to Prof. Fernando Porté-Agel for supporting my research visit at EPFL and letting me use his test facilities. I also want to thank Majid Bastankhah for the fruitful and inspiring discussions we had during this time and other occasions.

Ein großer Dank geht auch an alle Kollegen am Lehrstuhl für die offene und freundschaftliche Atmosphäre, in der man hinter jeder Büro- und Werkstatttür Unterstützung findet, wenn man sie braucht. Bedanken möchte ich mich, insbesondere bei meinem langjährigen Bürokollegen und Leidensgefährten Konstantin. Die vielen On- und Offtopic Diskussionen mit dir haben das manchmal zähe Doktorandendasein leichter gemacht und geholfen so manche Lehrveranstaltung rumzubringen.

Der größte Dank geht an meine Eltern. Ohne eure bedingungslose Unterstützung über die vielen Jahre und den Glauben in mich wäre es nie zu dieser Arbeit gekommen. Eure elterlichen Mühen haben sich gelohnt, aus mir ist doch noch halbwegs was geworden. Insbesondere meinem Vater Stephan bin ich zu Dank verpflichtet für das unermüdliche Korrekturlesen und auffinden jedes falsch und nicht gesetzten Kommas.

Zuletzt möchte ich mich bei meiner Frau Berna bedanken, die viel ertragen musste, damit diese Arbeit einen Abschluss findet. Während meiner Zeit als Doktorand hast du mich immer aufgemuntert, wenn mal wieder ganze Arbeitstage im Windkanal schiefgegangen sind, aber du hattest auch immer Nachsicht mit mir, wenn Arbeit, Konferenzen und Gastaufenthalte überhandgenommen haben. Danke auch das du mir in der Zeit danach in so vielen Situationen den Rücken freigehalten hast damit ich diese Arbeit schreiben konnte. Und zualler-aller-letzt danke auch an meinen Sohn Junus, dass du mir nie böse warst, wenn Papa sich an den Wochenenden zum Schreiben zurückgezogen hat, statt mit dir zu spielen.

Abstract

Analysis of wind turbine wakes immersed in turbulent boundary layer flows over rough surfaces - An experimental and numerical study

Wind turbine wakes interacting with neutrally stratified atmospheric boundary layers over homogeneous flat surfaces of different aerodynamic roughness are systematically assessed by means of an experimental and a numerical study. The experimental study is based on measurements in a boundary layer wind tunnel with a small scale three-bladed horizontal axis wind turbine model (HAWT), which is specifically designed and verified for this project, in order to reasonably cope with relevant scaling effects. The wind tunnel tests consist of triple hot wire measurements of the wake immersed in low turbulence approaching flow and two turbulent boundary layers of significantly different aerodynamic roughness for a variety of tip speed ratios and yaw angles. The numerical study complements the wind tunnel tests by reproducing the experimental set-up in large-eddy simulations, utilizing the Actuator Line Method for modelling the rotor flow and wall models for the generation of turbulent boundary layers over rough surfaces.

With increasing surface roughness, results of both studies exhibit a faster wake recovery and in case of yaw misalignment a reduced wake deflection. It is shown that these effects can be explained by an enhanced momentum transfer from the outer flow into the wake caused by the level of ambient turbulence, which increases with the surface roughness. For moderate surface roughness the often reported linear growth of the wake in downstream direction is confirmed, whereas for high roughness a non-linear wake growth is observed. It is shown that the latter is a result of strong perturbations of the wake caused by interactions with the turbulent boundary layer flow. In a novel approach, non-equilibrium scaling theory for axisymmetric wakes is applied to the wind turbine wake. Through joint assessment regarding self similarity of the velocity deficit and the Reynolds stresses in the wake, a consistent set of power law coefficients for the description of the streamwise evolution of these quantities is derived. Furthermore, it is observed that the anisotropy of the Reynolds stresses in the wake is approximately constant. Based on the findings of this assessment a simple model to predict the diagonal components of the Reynolds stress tensor in the wake is proposed.

Zusammenfassung

Analyse von Windkraftanlagen-Nachläufe in turbulenten Grenzschichtströmungen über rauen Oberflächen - Eine experimentelle und numerische Studie

Windkraftanlagen-Nachläufe, die mit neutral geschichteten atmosphärischen Grenzschichten über homogenen ebenen Oberflächen unterschiedlicher aerodynamischer Rauheit interagieren, werden systematisch in einer experimentellen und einer numerischen Studie analysiert. Die experimentelle Studie basiert auf Messungen in einem Grenzschicht-Windkanal mit einem Modell einer dreiflügeligen Horizontalachsen-Windkraftanlage (HAWT), welche speziell für dieses Projekt entworfen und verifiziert wurde, um relevante Skalierungseffekte angemessen zu berücksichtigen. Die Windkanaltests umfassen 3-Draht Hitzdrahtmessungen der Nachlaufströmung für eine Vielzahl von Schnelllaufzahlen und Gierwinkeln in turbulenzarmer Anströmung und zwei turbulenten Grenzschichten mit deutlich unterschiedlicher aerodynamischer Rauheit. Die numerische Studie ergänzt die Windkanalversuche, indem sie den experimentellen Aufbau in Large-Eddy-Simulationen nachbildet, wobei die Actuator-Line-Methode zur Modellierung der Rotorströmung und Wandmodelle zur Erzeugung von turbulenten Grenzschichten über rauen Oberflächen verwendet werden.

Mit zunehmender Oberflächenrauigkeit zeigen die Ergebnisse beider Studien eine schnellere Nachlauferholung und bei Gierversatz eine reduzierte Nachlaufablenkung. Es wird gezeigt, dass diese Effekte durch einen verstärkten Impulsübertrag von der Außenströmung in die Nachlaufströmung erklärt werden können, der durch das Niveau der Umgebungsturbulenz verursacht wird, die mit der Oberflächenrauheit zunimmt. Für moderate Oberflächenrauigkeit wird das oft berichtete lineare Wachstum des Nachlaufs in Strömungsrichtung bestätigt, während für hohe Rauigkeit ein nichtlineares Wachstum beobachtet wird. Es wird gezeigt, dass letzteres ein Ergebnis starker Störungen des Nachlaufs ist, die durch Wechselwirkungen mit der turbulenten Grenzschichtströmung verursacht werden. In einem neuartigen Ansatz wird die Nicht-Gleichgewichts-Skalierungstheorie für achsensymmetrische Nachläufe auf den Nachlauf einer Windkraftanlage angewendet. Durch kombinierte Betrachtung der Selbstähnlichkeit des Geschwindigkeitsdefizits und der Reynoldsspannungen in der Nachlaufströmung wird ein konsistenter Satz von Potenzgesetzkoeffizienten für die Beschreibung der Entwicklung dieser Größen in Strömungsrichtung abgeleitet. Weiterhin wird beobachtet, dass die Anisotropie der Reynoldsspannungen im Nachlauf annähernd konstant ist. Basierend auf den Ergebnissen dieser Untersuchung wird ein einfaches Modell zur Vorhersage der diagonalen Komponenten des Reynoldsspannungstensors in der Nachlaufströmung vorgeschlagen.

Contents

Contents	ix
List of Figures	xiii
List of Tables	xix
1 Introduction	1
1.1 Motivation	1
1.2 State of Research	5
1.2.1 Wind Turbine Wake Interactions	5
1.2.2 Analytical Wake Models	8
1.2.3 Rotor Flow Modelling	10
1.2.3.1 Wind Tunnel Testing	10
1.2.3.2 Numerical Simulation	11
1.3 Research Objectives & Structure of the Thesis	15
2 Fundamentals	17
2.1 Atmospheric Boundary Layers and Rough Walls	18
2.1.1 Logarithmic Law	18
2.1.2 Power Law	21
2.2 Wind Turbine Aerodynamics	23
2.2.1 Actuator Disc Theory	24
2.2.2 Blade Element Theory	26
2.2.3 Blade Element Momentum Method	27
2.2.4 Optimum Rotor Design for Variable Speed Operation	29
2.3 Wake Aerodynamics	30
2.3.1 Superposition of Wake and Boundary Layer	30
2.3.2 Turbulent Kinetic Energy Budget	34
3 Wind Tunnel Modelling of Atmospheric Boundary Layers	37
3.1 Wind Tunnel & Instrumentation	38
3.2 Tested Boundary Layer Configurations	41
3.3 Evaluation of the Boundary Layer Characteristics	43
3.3.1 Log Law	43
3.3.2 Power Law	43
3.4 Results	45
3.5 Summary	51

4	Model Wind Turbine - Design & Verification	53
4.1	Requirements	54
4.2	Rotor Design	55
4.3	Electrical Components of the Drive Train	59
4.4	Structural Design of the Tower	60
4.5	Determination of Operational Conditions	63
4.6	Rotor Performance	65
4.7	Summary	67
5	Wake Measurements	69
5.1	Experimental Setup	70
5.2	Wake Characteristics	71
5.2.1	Influence of the Tip Speed Ratio	71
5.2.2	Influence of the Ground Roughness on an Un-yawed Wind Turbine	76
5.2.3	Influence of the Ground Roughness on a Yawed Wind Turbine . . .	80
5.3	Spectral Analysis	84
5.3.1	Methodology	84
5.3.2	Tip Speed Ratio Dependency of the Mutual Inductance Instability .	85
5.3.3	Wake Development in the Spectral Domain	87
5.3.4	Self Similarity in the Spectral Domain	94
5.3.5	Wake Meandering	96
5.4	Summary	99
6	Numerical Method	101
6.1	Flow Solver INCA	102
6.2	Generation of Turbulent Boundary Layer Flows	103
6.2.1	Wall Modelling Methodology	103
6.2.1.1	Standard Wall Stress Model	103
6.2.1.2	Virtually Lifted Wall Stress Model	104
6.2.2	Sensitivity Study	107
6.2.2.1	Numerical Setup	107
6.2.2.2	Evaluation Point	108
6.2.2.3	Grid Study	109
6.2.2.4	Roughness Study	112
6.3	Actuator Line Method	116
6.3.1	Numerical Methodology	116
6.3.2	Validation Testcase (NREL-5MW)	118
6.3.2.1	Numerical Setup	118
6.3.2.2	Results	119
6.4	Blade Polar Identification	122
6.4.1	Inverse Blade Element Momentum Method	123
6.4.2	Numerical Setup	123
6.4.3	Results	125
6.5	Summary	128
7	LES of a Model Wind Turbine in Turbulent Boundary Layer Flows	131
7.1	Numerical Setup	132
7.2	Flow Evolution in the Empty Domain	137
7.3	Comparison with Measurements & Grid Study	141

7.4	Influence of the Ground Roughness on an Un-yawed Wind Turbine	145
7.4.1	Wake Characteristics	145
7.4.2	Momentum Budget	149
7.5	Influence of the Ground Roughness on a Yawed Turbine	154
7.5.1	Wake Characteristics	154
7.5.2	Momentum Budget	160
7.6	Summary	164
8	Assessment of Self Similarity & Analytical Wake Modelling	167
8.1	Theory of Self Similarity	168
8.1.1	Wake Width and Velocity Deficit Scaling	168
8.1.2	Streamwise Evolution of Reynolds Stresses	169
8.2	Assessment of Self Similarity in Wind Turbine Wakes	172
8.2.1	Self Similarity in the Wind Tunnel Measurement Results	172
8.2.2	Self Similarity in the Large Eddy Simulation Results	181
8.3	An Analytical Model for Predicting Turbulence Quantities in the Far Wake	189
8.4	Summary	192
9	Summary and Conclusions	195
	Bibliography	199
A	Appendix	209
A.1	Calibration of the Generator	209
A.2	Rotational Matrices	212
A.3	Measurement Positions	212

List of Figures

1.1	Total power generation capacity in the EU	1
1.2	Cumulative onshore and offshore installations in the EU	2
1.3	Wind Atlas Germany	3
2.1	Sand grain roughness k_s	20
2.2	Integration constant $C_r^+(k_s^+)$	20
2.3	Typical values of terrain parameters z_0 and d	21
2.4	Typical values of terrain parameters z_0 and α	22
2.5	The energy extracting stream-tube of a wind turbine	23
2.6	A blade element sweeps out an annular ring	24
2.7	Blade element forces and velocities	27
2.8	Sketch of two superimposed flow fields	31
3.1	Sketch of the boundary layer wind tunnel	38
3.2	Sketch of the boundary layer generation devices	39
3.3	Model wind turbine and traversal system in the wind tunnel	39
3.4	Sketch of the distribution of roughness elements	41
3.5	Boundary Layer quantities for varying roughness density with $h_r \lambda_f = const.$	45
3.6	Normalised Reynolds shear stress $\overline{u'w'}(z)/\overline{u_\infty^2}(z_h)$ in the SBL configuration	46
3.7	Normalised Reynolds stress $\overline{u'u'}(z)/\overline{u_\infty^2}(z_h)$ in the SBL configuration	46
3.8	Normalised axial mean velocity $\overline{u_\infty}(z)/u_\tau$ in the SBL configuration	47
3.9	Normalised Reynolds shear stress $\overline{u'w'}(z)/\overline{u_\infty^2}(z_h)$ in the RBL configuration	48
3.10	Normalised Reynolds stress $\overline{u'u'}(z)/\overline{u_\infty^2}(z_h)$ in the RBL configuration	48
3.11	Normalised axial mean velocity $\overline{u_\infty}(z)/u_\tau$ in the RBL configuration	49
3.12	Normalised roughness lengths z_0/h_r obtained by 2-parameter curve fit	49
3.13	Comparison of SBL and RBL characteristics	50
3.14	Normalised energy spectral density at hub height within the two boundary layers	51
4.1	Reynolds dependency of the maximum lift-to-drag ratio for different types of airfoils	55
4.2	The variation of maximum C_P with design tip speed ratio λ_{dsgn} for various lift-to-drag ratios C_l/C_d	56
4.3	Comparison of experimental and numerical airfoil characteristics of the SD7003 airfoil	57
4.4	Geometry of the SD7003 airfoil	57
4.5	Normalised Chord c/R and Twist Θ distribution as function of the normalised radius μ	58
4.6	3D-Image of the wind turbine blade	58

4.7	Eigenfrequencies of the tower f_n , rotor and blade passing frequencies f_{1P} , f_{3P} as function of the TSR λ	61
4.8	Side and Iso View of Model Wind Turbine	62
4.9	Variation of the averaged chord based Reynolds number \overline{Re}_c as function of free-stream velocity U_∞ and rotational frequency Ω	63
4.10	Variation of the local chord based Reynolds number Re_c with the TSR λ as function of the normalised radius μ	64
4.11	Power C_P and thrust coefficients C_T as function of TSR λ for constant chord based Reynolds number $\overline{Re}_c = 62500$	65
4.12	Power C_P and thrust coefficients C_T as function of yaw angle γ	67
5.1	View of the Model Wind Turbine located in the boundary layer wind tunnel	70
5.2	Profiles of the mean axial velocity component \bar{u} for various TSRs	72
5.3	Profiles of the Reynolds shear stress for various TSRs	72
5.4	Profiles of mean azimuthal velocity component for various TSRs	73
5.5	Profiles of the Reynolds stress in axial direction for various TSRs	74
5.6	Profiles of the Reynolds stress in azimuthal direction for various TSRs	74
5.7	Profiles of the Reynolds stress in radial direction for various TSRs	75
5.8	Wake characteristics of the un-yawed model wind turbine immersed in the SBL configuration for various TSRs	75
5.9	Profiles of the mean axial velocity component \bar{u} for different flow conditions	76
5.10	Profiles of the Reynolds shear stress for different flow conditions	77
5.11	Profiles of the Reynolds stress in axial direction for different flow conditions	78
5.12	Profiles of the Reynolds stress in azimuthal direction for different flow conditions	78
5.13	Wake characteristics of the un-yawed model wind turbine operating at $\lambda = \lambda_{dsgn}$ immersed in different ambient flow conditions	79
5.14	Vertical profiles of the velocity deficit in the wake of the un-yawed model wind turbine operating at $\lambda = \lambda_{dsgn}$ immersed in different flow conditions	80
5.15	Lateral profiles of the axial velocity in the wake of the model wind turbine immersed in different flow conditions	81
5.16	Lateral profiles of the turbulent kinetic energy in the wake of the model wind turbine immersed in different flow conditions	82
5.17	Wake characteristics of the model wind turbine immersed in different ambient flow conditions operating at $\lambda = \lambda_{dsgn}$ under various yaw angles	82
5.18	Lateral profiles of the mean axial velocity and flow skew angle in the wake of the model wind turbine for a yaw angle of $\gamma = 30^\circ$ immersed in different flow conditions	83
5.19	Normalised and pre-multiplied power spectra $f \cdot S_{uu}$ and $f \cdot S_{ww}$ at top tip height for the axial distance $x/R = 2$ and different TSRs	87
5.20	Non-dimensional co-spectra of the shear production term $C_{o_{uw}} \cdot \partial \bar{u} / \partial z \cdot R / \bar{U}_{ref}^3$ at top tip height for the axial distance $x/R = 2$ and different TSRs	87
5.21	Difference of the pre-multiplied power spectra in the wake and the undisturbed boundary layer at the axial position $x/R = 2$ for different TSRs	89
5.22	Normalised and pre-multiplied power spectra in the wake for various downstream positions, heights, flow conditions, and tip speed ratios	90
5.23	Normalised and pre-multiplied co-spectra of the lateral shear stress in the wake at the lateral rotor edges for various downstream locations	92

5.24	Normalised and pre-multiplied co-spectra of the vertical shear stress in the wake at the vertical rotor edges for various downstream locations	93
5.25	Normalised and pre-multiplied co-spectra of the vertical shear production term at the bottom tip for various downstream locations	94
5.26	Normalised and pre-multiplied power spectra of the Reynolds stress in axial direction for different flow conditions and TSRs at various downstream locations	95
5.27	Normalised and pre-multiplied power spectra in the SBL flow condition for various locations	96
5.28	Coherence $Coh_{uv}(f)$ between instantaneous axial u and lateral velocity component v for different flow conditions and TSRs at various downstream distances	98
6.1	Sketch of the Standard and the Virtually Lifted Wall Model	105
6.2	Non-dimensional mean axial velocity u^+ as function of normalised wall distance z/δ computed using m -th grid point adjacent to wall	108
6.3	Normalised shear stress velocity $\bar{u}_\tau/\bar{u}(z_h)$ mean axial velocity $\bar{u}/\bar{u}(z_h)$ as function of m -th grid point adjacent to the wall	109
6.4	Non-dimensional Reynolds stresses as function of normalised wall distance z/δ computed using m -th grid point adjacent to the wall	109
6.5	Non-dimensional mean axial velocity u^+ as function of normalised wall distance z/δ for three different wall-normal grid resolutions	110
6.6	Non-dimensional Reynolds stresses as function of normalised wall distance z/δ for three different wall-normal grid resolutions	111
6.7	Non-dimensional mean axial velocity u^+ as function of normalised wall distance z/δ for different wall-tangential grid resolutions	111
6.8	Non-dimensional Reynolds stresses as function of normalised wall distance z/δ for different wall-tangential grid resolutions	112
6.9	Non-dimensional mean axial velocity u^+ as function of normalised wall distance z/δ for different roughness lengths z_0	113
6.10	Normalised shear stress velocity $\bar{u}_\tau/\bar{u}(z_h)$ and mean axial velocity $\bar{u}/\bar{u}(z_h)$ as function of roughness length δ/z_0	114
6.11	Non-dimensional Reynolds stresses as function of wall distance z/δ for various roughness lengths δ/z_0	115
6.12	Definition of coordinate systems used in the actuator line method	116
6.13	Effect of filtering on normalised vorticity magnitude $\omega R/u_{ref}$ in the wake of the NREL-5MW wind turbine	120
6.14	Spanwise distribution of blade loads	121
6.15	Profiles of the normalised mean axial velocity component \bar{u}/u_{ref} in the mid-horizontal plane for various axial positions	121
6.16	Profiles of the normalised turbulent kinetic energy K/u_{ref}^2 in the mid-horizontal plane for various axial positions	122
6.17	Isosurface of normalised vorticity magnitude	122
6.18	Overview of the simulation domain	124
6.19	Comparison of thrust and power coefficients as function of tip speed ratio for various pitch angles	125
6.20	Comparison of blade polars at selected blade sections	126
7.1	Sketch of the computational domain used in the LES of the model wind turbine.	133

7.2	Isosurfaces of the instantaneous vorticity magnitude in the wake of the model wind turbine	136
7.3	Mean axial velocity $\bar{u}(x, z_h)$ and turbulent kinetic energy $K(x, z_h)$ as function of the axial distance to the rotor	137
7.4	Vertical profiles of the simulated boundary layer configurations at selected locations in the <i>wake region</i> of the empty domain	139
7.5	Normalised energy spectral density of the three different wind components at the rotor center	140
7.6	Comparison of measurements and numerical results for power C_P and thrust coefficient C_T as function of yaw angle γ	141
7.7	Profiles of the normalised mean axial velocity component $\bar{u}/\bar{u}_{bl}(z_h)$ for various axial positions	142
7.8	Profiles of the normalised shear stress for various axial positions	143
7.9	Profiles of the normalised turbulent kinetic energy $K/\bar{u}_{bl}(z_h)^2$ for various axial positions	144
7.10	Wake characteristics of the un-yawed model wind turbine operating at $\lambda = \lambda_{dsgn}$ immersed in sF016 boundary layer configuration	145
7.11	Normalised mean axial velocity $\bar{u}/\bar{u}_{bl}(z_h)$ within the mid-vertical plane of the wake immersed in different boundary layer configurations	146
7.12	Normalised mean axial velocity $\bar{u}/\bar{u}_{bl}(z_h)$ within the mid-horizontal plane of the wake immersed in different boundary layer configurations	146
7.13	Normalised turbulent kinetic energy $K/\bar{u}_{bl}^2(z_h)$ within the mid-vertical plane of the wake immersed in different boundary layer configurations	147
7.14	Normalised turbulent kinetic energy $K/\bar{u}_{bl}^2(z_h)$ within the mid-horizontal plane of the wake immersed in different boundary layer configurations	148
7.15	Wake characteristics of the un-yawed model wind turbine operating at $\lambda = \lambda_{dsgn}$ immersed in different boundary layer configurations	148
7.16	Momentum deficit $\Delta u(1 - \Delta u)$ within the mid-vertical plane of the wake immersed in different boundary layer configurations	149
7.17	Axial change rate of the local momentum deficit of the wake immersed in different boundary layer configurations	150
7.18	Break down of the axial change rate of the momentum deficit of the wake immersed in different boundary layer configurations	151
7.19	Momentum thickness Θ_x^2 and its axial change rate $d\Theta_x^2/dx$ in the wake of the model wind turbine operating at $\lambda = \lambda_{dsgn}$ immersed in different boundary layer configurations	152
7.20	Breakdown of contributions to the axial change rate $d\Theta_x^2/dx$ of the wake immersed various boundary layer configurations	153
7.21	Comparison of computed and modelled wake width σ and centreline velocity deficit Δu_C of the wake immersed in different boundary layers	153
7.22	Normalised mean axial velocity $\bar{u}/\bar{u}_{bl}(z_h)$ within the mid-horizontal plane of the wake immersed in the sF016 boundary layer configuration for various yaw angles	155
7.23	Normalised turbulent kinetic energy $K/\bar{u}_{bl}^2(z_h)$ within the mid-horizontal plane of the wake immersed in the sF016 boundary layer configuration for various yaw angles	155
7.24	Contours of the velocity deficit Δu in yz -planes at different downstream locations and yaw angles γ within the sF016 boundary layer configuration	156

7.25	Contours of the velocity deficit Δu in yz -planes at different downstream locations within the sF014 and sF032 boundary layer configuration for a yaw angle of $\gamma = 30^\circ$	157
7.26	Vertical and lateral wake centre position as function of the axial position for different yaw angles and different boundary layer configurations . . .	157
7.27	Contours of the normalised turbulent kinetic energy $K/\bar{u}_{bl}^2(x_r, z_h)$ in yz -planes at different downstream locations within the sF014 and sF032 boundary layer configuration for $\gamma = 30^\circ$	158
7.28	Velocity deficit Δu within the mid-horizontal plane of the wake for a yaw angle of $\gamma = 30^\circ$ immersed in different boundary layer configurations . .	159
7.29	Wake characteristics of the yawed model wind turbine operating at $\lambda = \lambda_{dsgn}$ immersed in different boundary layer configurations	159
7.30	Lateral momentum Θ_y^2 and its axial change rate $d\Theta_y^2/dx$ within the wake of the model wind turbine operating at $\lambda = \lambda_{dsgn}$ immersed in different boundary layer configurations for various yaw angles	161
7.31	Break down of the axial change rate of the lateral momentum $d\Theta_y^2/dx$ into all contributing terms in the wake immersed in different boundary layer configurations and for various yaw angles	162
7.32	Break down of the axial change rate of the lateral momentum $d\Theta_y^2/dx$ into most dominant terms in the wake immersed in different boundary layer configurations and for various yaw angles	162
7.33	Lateral integral of $\partial \overline{u'v'}/\partial x$ as function of height at the downstream distance of $x/R = 16$ for a yaw angle of $\gamma = 30^\circ$	163
8.1	Vertical profiles of the normalised velocity deficit $\Delta u/\Delta u_M$ versus η_z in the wake of the model wind turbine immersed in the SBL/RBL	173
8.2	Vertical profiles of the added Reynolds shear stress $\Delta \overline{u'w'}$ versus η_z in the wake of the model wind turbine immersed in the SBL/RBL	174
8.3	Wake characteristics of the model wind turbine immersed in the SBL and RBL using different definitions of the normalised velocity deficit	175
8.4	Lateral profiles of the normalised velocity deficit $\Delta u/\Delta u_M$ versus η_y in the wake of the model wind turbine immersed in the SBL and RBL for various yaw angles	175
8.5	Normalised lateral wake width σ_y and normalised centreline velocity deficit Δu_C as function of x/R in linear representation for different scaling laws .	176
8.6	Lateral profiles of the normalised added Reynolds shear stress $\Delta \overline{u'v'}/\Delta \overline{u'v'}_M$ versus η_y in the wake of the model wind turbine immersed in the SBL and RBL for various yaw angles	177
8.7	Vertical and lateral profiles of the normalised added turbulent kinetic energy $\Delta K/\Delta K_M$ versus η_z and η_y in the wake of the model wind turbine immersed in the SBL and RBL for various yaw angles	178
8.8	Vertical and lateral profiles of the normalised diagonal components of the added Reynolds stress tensor $\Delta \overline{u'_i u'_i}/\Delta \overline{u'_i u'_i}_M$ versus η_z and η_y in the wake of the model wind turbine immersed in the SBL	179
8.9	Maximum added Reynolds shear stress $\Delta \overline{u'u'_r}_M$ and maximum added turbulent kinetic energy ΔK_M in the wake of the model wind turbine normalised to different wake growth scaling laws	180
8.10	Structural parameters in the wake of the model wind turbine for $\eta_{y,z} = 1$.	180

8.11	Vertical profiles of the velocity deficit $\Delta u/\Delta u_M$, the added Reynolds shear stress $\overline{\Delta u'w'}/\overline{\Delta u'w'}_M$, and the added turbulent kinetic energy $\Delta K/\Delta K_M$ as function of η_y in the wake for the configurations sF014, sF016, and sF032	182
8.12	Lateral profiles of the velocity deficit $\Delta u/\Delta u_M$ as function of η_y in the wake for the configurations sF014, sF016, and sF032	183
8.13	Lateral profiles of the added Reynolds shear stress $\overline{\Delta u'v'}/\overline{\Delta u'v'}_M$ as function of η_y in the wake for the configurations sF014, sF016, and sF032	184
8.14	Lateral profiles of the added turbulent kinetic energy $\Delta K/\Delta K_M$ as function of η_y in the wake for the configurations sF014, sF016, and sF032	184
8.15	Lateral profiles of the added Reynolds stresses $\overline{\Delta u'_i u'_i}/\overline{\Delta u'_i u'_i}_M$ as function of η_y in the wake for the configurations sF014 and for various yaw angles	185
8.16	Maximum added Reynolds shear stress $\overline{\Delta u' u'_r}_M$ and turbulent kinetic energy ΔK_M in the wake of the model wind turbine normalised to different wake growth scaling laws	187
8.17	Structural parameters $(\overline{\Delta u'_i u'_i}/\Delta K)(\eta = 1)$ in the wake of the model wind turbine for $\eta_{y,z} = 1$	188
8.18	Comparison of model predictions and measurement results for the Reynolds stress components	191
8.19	Comparison of model predictions and LES results for the Reynolds stress components	192
A.1	Sketch of the torque meter rig	210
A.2	Friction losses Q_F for various electric currents I_{LM} of the load machine before the calibration	210
A.3	Standard deviation of the friction losses σ_{Q_F} as function of the motor constant k_M	211
A.4	Friction losses Q_F for various electric currents I_{LM} of the load machine after the calibration	211

List of Tables

3.1	Configuration of roughness elements.	42
3.2	Characteristics of the turbulent boundary layers.	49
5.1	Reference velocity and rotational frequency for selected tip speed ratios with $\overline{Re}_c = 62,500$	70
7.1	Overview on simulated boundary layer configurations and yaw conditions.	135
8.1	Curve fit parameters to the self similarity shape functions of the added Reynolds stresses $\Delta\overline{u'_i u'_i} / \Delta\overline{u'_i u'_i}_M$ in two boundary layer configurations . .	186
8.3	Curve fit parameters for the axial scaling of the added Reynolds shear stress and turbulent kinetic energy	187
A.1	Manufacturer-provided data of the generators and the calibrated motor torque constants.	212
A.2	List of measurement positions in the wind tunnel, axial coordinates	213
A.3	List of measurement positions in the wind tunnel, lateral coordinates . . .	213
A.4	List of measurement positions in the wind tunnel, vertical coordinates . .	214

Introduction

1.1 Motivation

In the increasing worldwide effort to meet the energy demand with renewable energy sources, wind energy has become one of the mayor technologies. With 362 TWh generated in 2018, wind power covered 14% of the European Union’s (EU) electricity demand and is with a total installed capacity of 178.8 GW the second largest form of power generation capacity in the EU [82], see Figure 1.1. Since conventional power sources such as oil, coal and natural gases continue to decommission more capacity than they install, wind power capacity has overtaken that of coal in 2017 and is likely to become the largest energy capacity in 2019.

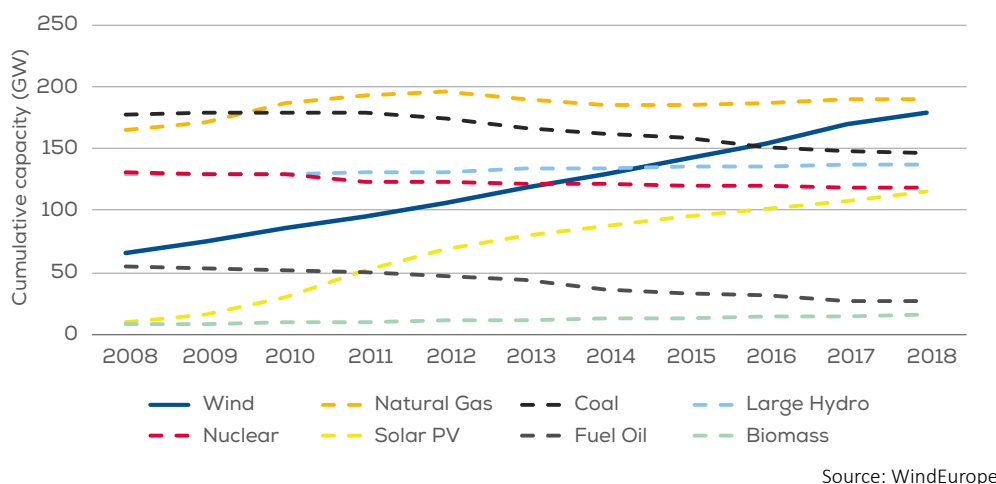
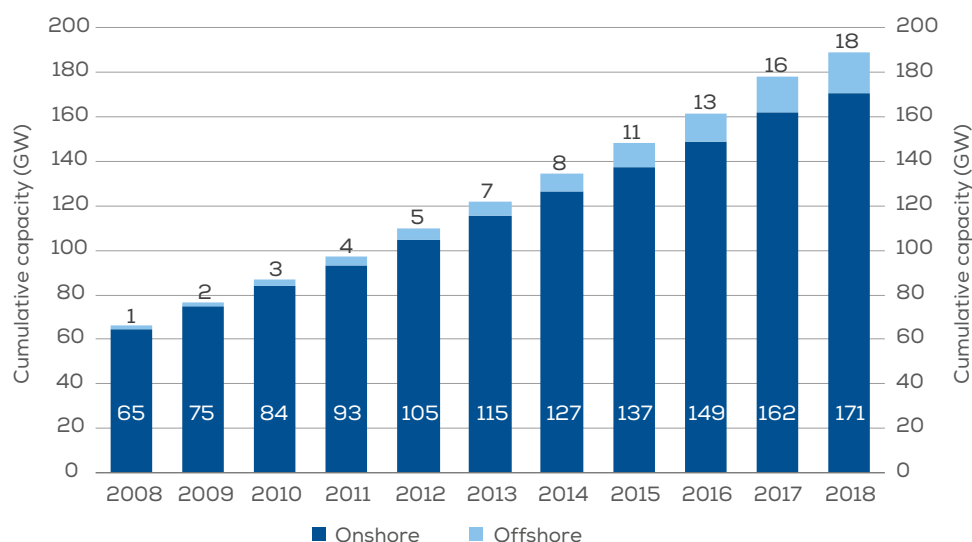


Figure 1.1: Total power generation capacity in the European Union 2008 - 2018 [82]

During the last decade almost each year new offshore windfarms were connected to the electricity network, hitting new records in size and raising their contribution to the cumulative wind energy capacity to nowadays of about 10%, see Figure 1.2. Even though in 2018 already 15% of the annually added wind capacity in the EU was installed offshore, onshore wind turbines are likely to still remain the major contributor of the wind

energy resource in the upcoming decade of the 2020's. This is expected firstly due to increasingly stringent environment protection laws for offshore windfarms (e.g. Germany: Windenergie-auf-See-Gesetz 'WindSeeG' ¹, from 2021 on 700 - 900 MW annually tender volume offshore; in comparison: 2.4 GW added capacity onshore in 2018 [82]) and secondly because of the still significantly higher levelized cost of energy (LCOE) for offshore wind turbines (e.g. Germany 2018: 40-82 EUR/MWh onshore, 75-138 EUR/MWh offshore [83]).



Source: WindEurope

Figure 1.2: Cumulative onshore and offshore installations in the European Union 2008 - 2018 [82]

Considering the above mentioned facts, it becomes clear that onshore wind energy is one of the key technologies in the increasing effort to meet the energy demand with renewable resources. However, available areas in high wind regions with low turbulence atmospheric flow conditions (and access to the energy grid) are a limited resource in populated areas with the corresponding energy demand so that less attractive sites need to be designated for wind turbines. In the following this is briefly outlined on the example of Germany where 31% of the European wind energy capacity is installed.

Till 2030 in Germany 65% of the electric energy consumed shall be covered by renewable energies. As the current share of renewable energies is about 40 % [82], installed renewable energy capacities have to be increased by at least 63%, assuming that the total energy consumption does not increase. Since electric mobility is currently strongly promoted and supported by the government this a rather optimistic assumption. On the basis that in the next 10 years no technological development will give new striking advantages to a particular technology, it can be assumed that within the renewable resources each technology maintains its contribution. With that, the installed onshore wind capacity of 49 GW has to be increased by another 31 GW. A recent investigation [17] shows that in Germany just enough area is available for wind energy usage to meet this goal, however, currently discussed mandatory minimum distances from residential areas (1000m) could cut the area by 20 - 25%. The study also analyses the available area per federal state and shows that federal states in high wind regions with flat land, as Schleswig Holstein and Niedersachsen, see Figure 1.3(a), only contribute 14% to the total available area in Ger-

¹<http://www.gesetze-im-internet.de/windseeg/>

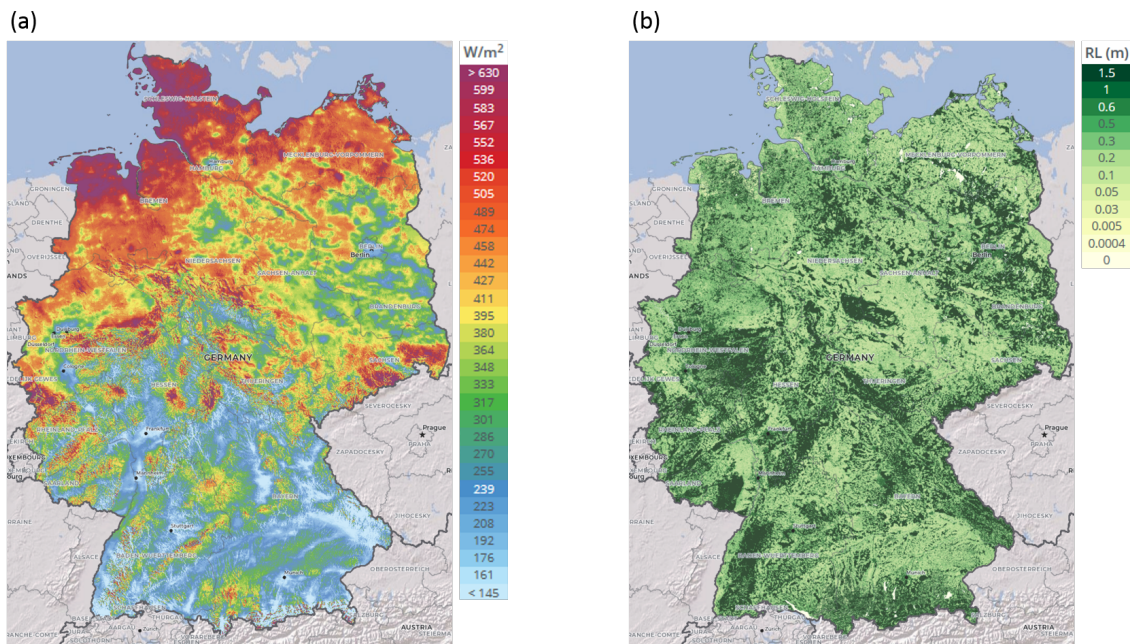


Figure 1.3: Wind Atlas Germany: (a) Mean power density 100m above ground, (b) roughness length; Source: Global Wind Atlas <http://globalwindatlas.info>

many as only 24 - 29% of the designated area in these states is still unused. On the other hand, more than 50% of the total available area is located in low wind regions as Hessen, Rheinland Pfalz and Baden Württemberg. In these federal states hills, forests, and other obstacles cause a higher ambient turbulence, see Figure 1.3(b) (terrain roughness is used here as indicator for ambient turbulence). Due to that the rotor blades, the drive train as well as the tower structure face dynamic loads which can cause fatigue damages and subsequently lead to higher maintenance costs. A low energy production and high maintenance costs can make a site economically unviable. Nevertheless, the technological development in the last decade(s) lead to greater power yields and more operating hours per turbine, making harvesting in previously unattractive locations possible. Consequently, an increasing number of wind turbines are nowadays even installed in forestal areas (in Germany in 2017: 1.850 out of 28.675 turbines) as these are mostly easy to exploit due to a well developed forestal road network and provide sufficient distance from residential areas [155]. In conclusion, current and future wind energy goals will require efficient usage of complex terrain in low wind regions.

This thesis aims at providing an in-depth understanding of the physical processes in the wake development of onshore wind turbines. The findings shall help to improve the design and operation of future onshore wind farms. Therefore, the first aim of this thesis is to provide a detailed investigation of the influence of terrain roughness on the evolution of a wind turbine wake. This includes analysis of the wake recovery and growth, first and second order flow statistics, and the turbulent scales within the wake. The second aim of the thesis is to provide a new simple analytical model for wind farm control applications which describes the evolution of turbulence in the wake, taking into consideration the incoming flow conditions. The work is based on wind tunnel measurements of a small scale generic wind turbine model and is complemented by large-eddy simulations (LES) of the experimental setup. In both, experimental and numerical work, physical and technical limitations exist which make it necessary to model the rotor flow. Emphasis is put

on obtaining a rotor flow and wake structures close to full-scale conditions.

In the following sections, the state of research is documented, the specific research objectives are summarised and an outline of the thesis is given.

1.2 State of Research

1.2.1 Wind Turbine Wake Interactions

Advances in wind turbine aerodynamics, since the pioneering work of Betz [15] and Joukowsky [77] in the 1920s, have led to modern multi megawatt horizontal axis wind turbines (HAWTs) achieving power coefficients close to the theoretical Betz–Joukowsky limit when operating at their intended design conditions. For a detailed review on wind turbine aerodynamics and rotor models for design purposes see [134]. Moreover, if the incoming flow is known a priori, accurate predictions on the performance of such turbines in off-design conditions can nowadays be obtained within short time by applying industrial blade-element-momentum (BEM) codes which are based on the theory of Glauert [53]. However, under real conditions this is a rather challenging task, due to the highly turbulent and non-stationary character of the atmospheric boundary layer (ABL) and its interaction with the wind turbine. Flow physics become even more complex when turbines face situations in which they have to operate in the wake of another wind turbine. Operations in turbulent wake flows are responsible for substantial power losses due to the reduced wind speed and an increased level of turbulence which can cause severe fatigue damages due to additional dynamic loads.

To evaluate the effect on a downwind wind turbine, typically two regions of the wake are distinguished [150]: (i) the region directly downwind of the wind turbine within a distance of a few diameters, called the near wake, and (ii) the subsequent region, called the far wake. The near wake behaviour is dominated by the rotor characteristics and its operational conditions, which includes stalled flow, three-dimensional helical tip and root vortices, and strong local pressure gradients along the rotor blade. See Vermeer *et al.* [150] for a review on near wake behaviour, and more recent Porté-Agel *et al.* [114]. The far wake region is less influenced by details of the wind turbine characteristic but rather by the global thrust and power coefficient, and incoming flow conditions. As it moves downstream, the outer flow penetrates the wake due to turbulent fluctuations. Thereby, the wake grows in lateral and vertical direction and the streamwise velocity increases until the wake completely recovers far downstream.

A strict distinction between near- and far wake region does not exist since the wake fluently transits from one to the other. Nevertheless, since the far wake can be approximated by a self similar Gaussian velocity-deficit distribution, a common definition for the onset of the far wake is the distance at which the wake can first be described by such a distribution. The length of the near wake and the recovery of the far wake are known to be affected by a range of parameters such as the incoming flow characteristics, the mechanical shear generated by the turbine, and the operational states of the turbine. Sørensen *et al.* [133] used data from large-eddy simulations (LES) of a wind turbine in uniform (synthetic) turbulent flow to analyse the length of the near wake as function of the ambient turbulence intensity. They showed that the length of the near wake significantly decreases from $l/R \approx 26$ in low-turbulence conditions ($I_u = 0.2\%$) to $l/R \approx 13.5$ in high-turbulence conditions ($I_u = 9.3\%$), where R denotes the rotor radius.

In atmospheric boundary layers over flat homogeneous terrain, obstacles like trees or buildings cause an increase of the vertical wind shear and the ambient turbulence. Due to the variation of the flow quantities over the height in the incoming flow, wind turbine wakes become asymmetric with a more complex flow physics. Zhang *et al.* [159] modelled the near wake behaviour of a small scale wind turbine in a boundary layer wind

tunnel with neutral stratification. Their spectral analysis showed strong spectral peaks at multiples of the frequency of consecutive rotating blades at the top-tip and side-tip levels, whereas at the bottom-tip height no similar tip vortex signature was present. They attributed this effect to the higher background turbulence level near the ground. Chamorro & Porté-Agel [28] carried out similar wind tunnel measurements but over smooth and rough surfaces. In the far wake region they observed a non-axisymmetric behaviour of the velocity deficit and the turbulence intensity with respect to the incoming flow. However, they concluded that the velocity deficit with respect to the incoming flow can be approximated as axisymmetric, whereas the non-axisymmetry of the turbulence intensity distribution of the wake was found to be stronger over the rough surface. In a numerical study of neutrally-stratified atmospheric boundary layer flows over homogeneous flat surfaces with different aerodynamic roughness lengths Wu & Porté-Agel [157] showed that the different wind shears and turbulence intensity levels of the incoming flow lead to substantial differences in the spatial distribution of the mean velocity deficit, turbulence intensity, and turbulent shear stress in the turbine wakes. With increasing roughness they observed a faster wake recovery, due to higher turbulent entrainment fluxes into the wake, and locations of the maximum turbulence intensity closer to the rotor. In a detailed analysis of the turbulent kinetic energy (TKE) budget in the wake they showed that the TKE is mainly redistributed by both mean-wind advection and turbulent transport in the axial and radial directions, respectively. Bastankhah & Porté-Agel [10] proposed an analytical model to predict the streamwise velocity in the far wake, assuming a Gaussian distribution and considering mass and momentum conservation. The model was tested, among others, against the LES results of Wu & Porté-Agel [157] by fitting the Gaussian curves to the velocity deficit profiles. They found that the wake width grows approximately linear, whereby the growth rate increases with surface roughness. More recently Jin & Chamorro [73] analysed effects of freestream turbulence and the large-scale motion of the background flow on the evolution of a wind turbine wake. It was found that the turbulent integral length scale in the wake grows linearly with distance and more rapidly for higher levels of freestream turbulence.

Changing heat fluxes during the day lead to a varying atmospheric stability (diurnal cycle) with different levels of ambient turbulence and density stratification which can cause buoyancy effects within a wind turbine wake. Hancock & Pascheke [56] carried out wind tunnel measurements in the wake of a model wind turbine immersed in a neutral and a stable atmospheric boundary layer. As for stability they distinguished between 'direct' effects due to changes in the stratification and 'indirect' effects due to changes in the background turbulence. Their results showed that, compared to results obtained within a neutral boundary layer with a higher level of turbulence, within the stable atmospheric boundary layer the wake growth in lateral direction was increased, which they inferred as 'direct' effect of the stratification. Later Hancock & Zhang [57] conducted a similar wind tunnel study within a convective boundary layer and observed a faster wake growth in the vertical and lateral direction, which they inferred as 'indirect' effect of the high turbulence level within the convective boundary layer. In an LES study Abkar & Porté-Agel [1] studied the influence of atmospheric thermal stability on wind-turbine wakes. Their results confirmed the experimental findings mentioned above that the wake growth rate is larger in the convective case than in the neutral and stable one. Thereby, in all cases, the wake grows linear and faster in width than in height. Furthermore, they showed that wake meandering is also stronger under the convective conditions compared to neutral and stable conditions.

Since on-shore sites are typically a limited resource, an efficient site-usage with a dense

spacing of wind turbines is necessary for on-shore windfarms. As already indicated, due to the resulting proximity, turbines can face situations in which they have to operate in the wake of another wind turbine. Strong velocity gradients and a level of turbulence significantly higher than in the surrounding atmospheric boundary layer then induce additional dynamic loads which can cause severe fatigue damages. Therefore, such wake operations have to be avoided. For example, this can be an issue at sites where old wind turbines are decommissioned and replaced by larger modern machines, the so called 're-powering', since the dimensions of the wake scales with the rotor diameter.

Besides the wind farm layout optimisation, control strategies can be used to increase the overall power production and/or alleviate fatigue loads by actively controlling the blade loads, the strength of the wake and its direction. Blade loads are typically controlled by cyclic pitch control. However, in the last years individual pitch control (IPC) has caught attention, as the necessary actuators have become available for commercial turbines. The technique aims to reduce the asymmetric loads due to wind speed variations across the rotor disc and has been shown to be beneficial in numerical studies [18] and wind tunnel measurements [19].

Wake control strategies in general aim either at controlling the strength or the direction of the wake. Then, by applying any kind of wake model the resulting interaction between the wind turbines can be predicted and increasing the efficiency of the wind farm can be stated as an optimisation problem. The strength of the wake can be influenced by 'derating' the wind turbines. This can be achieved by adjusting the blade pitch collectively, what reduces the axial flow induction and therefore also the blade loads. For a detailed overview see [79]. The direction of the wake can be influenced in the horizontal but also vertical direction by yawing or tilting the rotor, or even by an individual pitch control. Fleming *et al.* [46] used large-eddy simulations of a two-turbine fully waked scenario to study the potential of intentional yaw- and tilt-misalignment techniques, as well as combinations with individual pitch control. They showed that for all techniques operating points can be found that couple an improved power capture with a reduced loading. However, since adjusting the rotor tilt angle is not implemented in current wind turbines, most studies in this field focus on redirecting the wake by intentional yaw misalignment. Quite recently Bartl *et al.* [9] presented a wind tunnel study of two yaw-controlled model wind turbines operating in full and partial wake overlap. They analysed the effect of intentional yaw-misalignment on the power production and blade loads for different lateral offset positions and inflow conditions with low ($I_u = 0.23\%$) and high ($I_u = 10.0\%$) turbulence intensity. Their results indicate that intentional yaw misalignment of the upstream turbine is able to increase the combined power production for both partial and full wake overlap, however, on the expense of increased yaw moments. For partial wake overlap they were able to reduce the yaw moments on the downstream turbine by yawing it in the opposite direction, while still observing an increase in the combined power production. Nevertheless, their measurements showed that with increasing inflow turbulence the increase in combined power production due to yaw-misalignment is reduced. Using the same experimental setup Bartl *et al.* [8] analysed the influence of grid-generated inflow turbulence on the wake characteristics of a yawed wind turbine. They observed a very similar wake deflection for low and high turbulence inflow conditions. However, since the rotor-swept area of the turbine model blocks 12.8 % of the wind tunnel's cross-sectional area, the authors point out that an influence of the wind tunnel walls on the wake expansion and deflection cannot be excluded.

Similar to the wake evolution, atmospheric stability effects can alter the trajectory of the

wake significantly. Using large-eddy simulations Vollmer & Steinfeld [151] studied the wake deflection in atmospheric boundary layers with different thermal stability. They found that, for a given yaw angle and decreasing atmospheric stability, the wake deflects less whereas the variance of its trajectory increases.

In conclusion, variations of the atmospheric stability and the terrain roughness do significantly alter the spatial distribution of the mean velocity deficit, the turbulence statistics in the wake region, the wake meandering characteristics downwind of the turbine, and the wake trajectory. Therefore, for an efficient application wind farm controllers capable of wake control strategies rely on wake models which take these effects into account. Since the velocity and direction of the wind continuously changes, they also need to be capable to make these predictions in real time. These requirements can be met by analytical wake models.

1.2.2 Analytical Wake Models

Most of the available analytical wake models make use of the assumption of an approximately self similar mean velocity deficit within the far wake region, which has been confirmed in various numerical and experimental studies, see e.g. [1, 28, 158, 160]. By stating mass and momentum conservation within the wake, the velocity deficit and the wake width become directly linked. These can then initially be determined by the momentum deficit caused by the thrust of the turbine. Together with a further assumption on the underlying axial scaling (i.e., decay of the velocity deficit or the spreading rate), the velocity deficit in the wake can be explicitly stated.

One of the pioneering analytical wake models was developed by Jensen [67] and has later been further developed by Katić & Jensen [78]. Since then it has been extensively used in the literature and commercial software (e.g., WASP, WindPRO, WindSim, Wind-Farmer, and OpenWind). The model is essentially built on the mass conservation of the flow. It assumes a linear wake growth and a constant velocity deficit across the wake. Based on the conservation of mass and streamwise momentum, Larsen [85] developed a model in which the velocity profiles are represented by a self similar polynomial function. The model predicts a wake growth and a decay of the velocity deficit proportional to $x^{1/3}$ and $x^{-2/3}$, respectively. It is important to notice that the derivation of the model is based on the assumption that shear-generated turbulence due to the wake is mainly responsible for the wake recovery and the effect of the incoming flow turbulence is negligible [114].

Jiménez & Crespo [72] derived an analytical wake model capable of predicting the wake deflection in yawed conditions. The model is based on mass and momentum conservation, a constant velocity deficit across the wake, and a linear wake growth. They found that the model prediction were in satisfactory agreement with results of a large-eddy simulation of a single wind turbine immersed in synthetic turbulent flow.

It is important to notice that the above mentioned analytical models assume an axisymmetric flow field. Bastankhah & Porté-Agel [12] relaxed this assumption and modelled the velocity deficit by a two dimensional Gaussian distribution, in which the lateral and vertical wake width are assumed to grow linearly but with different rates. Furthermore, they do not only take into account the conservation of mass and streamwise momentum but also the conservation of the spanwise momentum. Thereby, the model also allows to predict the lateral deflection of the wake in case of a yaw misalignment. Furthermore, based on theoretical considerations, the model predicts the onset of the far wake and the wake deflection, amongst other parameters, as a function of the turbulence intensity,

showing a decrease in the wake deflection with increasing turbulence intensity.

Despite the recent progress in modelling the mean velocity field, analytic wake models, capable of predicting turbulence quantities in the wake, are less developed. A common approach is to model the streamwise turbulence intensity I_u in the wake of the wind turbine by means of an added turbulence intensity I_+ caused by the wind turbine which is added to the turbulence intensity of the ambient flow I_0 . Based on this concept Quarton [115] derived from fitting measurement data all the way from near wake to far wake that $I_+ \propto C_T^{0.7} I_0^{0.68} \xi^{-0.57}$ with $\xi = x/R$ being the non-dimensional distance to the turbine, R the rotor radius and C_T the thrust coefficient of the turbine. Crespo et al. [34] concluded from fitting data obtained by Reynolds-averaged Navier-Stokes simulations that in the far wake region $I_+ \propto (1 - \sqrt{1 - C_T})^{0.83} I_0^{-0.0325} \xi^{-0.32}$. On the other hand, more recently Frandsen [48] proposed a wake model which states for the far wake region $I_+ \propto C_T^{0.5} \xi^{-1.0}$. The quite different exponents in these empirical formulas illustrate the difficulty in obtaining a distinct set of optimal parameters in a curve fit with multiple unknowns. Furthermore, only Frandsen's model considers the radial distribution of the turbulence intensity by assuming a Gaussian shape. Chamorro & Porté-Agel [28] analysed changes in the radial distribution of the turbulence intensity as function of the downstream distance and analysed the influence of the ground roughness. They thereby distinguished the axial scaling of the maximum, minimum and mean value of the added turbulence intensity and observed different exponents. Based on their wind tunnel measurements, they found that $I_+ \propto \xi^{-0.7}$ for a low ground roughness and $I_+ \propto \xi^{-0.46}$ for a case with high roughness. Later Barlas *et al.* [5] performed similar analysis based on wind tunnel measurements but with contradictive results as they found decreasing exponents with increasing ground roughness ($I_+ \propto \xi^{-0.5}$ for smooth case and $I_+ \propto \xi^{-0.6}$ for rough case).

Even for simpler flows, such as the axisymmetric turbulent wakes of bluff bodies immersed in low turbulence uniform background flow, the research is still ongoing. Under the assumption of an equilibrium of production of turbulent kinetic energy at large scales and its dissipation at small scales (Kolmogorov cascade), George [50] showed for high Reynolds number flows the self similarity of the velocity deficit Δu , the radial Reynolds shear stress $\overline{u'v'}$ and the turbulent kinetic energy $K = 1/2 \overline{u_i' u_i'}$. His theory not only predicts an axial scaling of the centreline velocity deficit $\Delta u_C \propto x^{-2/3}$ and the wake width $\sigma \propto x^{1/3}$, but also of the shear stress and the turbulent kinetic energy with $\overline{u_i' u_j'}$, $K \propto \Delta u_C^2$. However, more recently several numerical and experimental studies have observed different scalings in the lee of fractal and regular axisymmetric grids (see [128, 99, 105]). For this reason Nedic [107], Dairay [35], and Vassilicos et al. [149] extended George's theory on the basis of a non-equilibrium assumption of the energy cascade and showed a good agreement with the observed scaling. Their theory, however, does not necessarily limit the underlying scaling law to specific exponents. It rather allows for various but, and most important, consistent sets of exponents for the axial scaling of Δu_C , σ , $\overline{u_i' u_j'}$ and K . The specific values of the exponents are then determined by the level of turbulent dissipation.

The concepts of equilibrium and non-equilibrium wakes are based on the assumption that the velocity deficit in the wake is small compared to the free stream velocity as only under this condition the momentum equation can be linearised and exact self similarity can be obtained [112]. In case of wind turbine wakes, these conditions are given in the far wake region. However, as indicated before, the onset of this region is largely governed by the turbulence intensity of the approaching flow. Therefore, studies concerning the

self similarity of axisymmetric wakes are commonly carried out in uniform approaching flow conditions with low turbulence intensity ($< 0.5\%$). In these conditions, the onset of the far wake and, hence, self similarity of the velocity deficit is typically reported to be found at distances of $x/l > 15$ with l being the characteristic obstacle dimension, see e.g. [35, 26, 74]. In special cases, the onset is even found at distances as far as $x/l > 50$, see [145]. However, in the case of wind turbines immersed in turbulent background flows, the mixing between the wake and the outer flow is enhanced and the wake reaches far wake conditions and hence a self similar state at shorter distances. For example, Abkar et al. [1] showed in an LES study of wind turbines immersed in boundary layers of different atmospheric stability an onset of the far wake as early as $x/D \approx 8R$.

1.2.3 Rotor Flow Modelling

Almost all of the above mentioned studies are either wind tunnel experiments based on scaled model wind turbines or numerical simulations, instead of field experiments with full scale wind turbines. This is owed to the fact that insights into the wake development of full scale wind turbines are difficult to obtain, since (i) wind is an uncontrollable natural resource of which strength and direction can barely be predicted for short time frames or reproduced and (ii) the measurement equipment for field experiments is rather costly. Therefore in wind energy research the majority of studies make use of approaches which can 'easily' be controlled, are reproducible, and are - last but not least - cheaper. Nevertheless, both wind tunnel experiments and numerical simulations have its limitations, either of physical or numerical kind, which typically makes a modelling of the rotor flow necessary.

1.2.3.1 Wind Tunnel Testing

In wind tunnel experiments the size of wind tunnel itself is typically the limiting factor. The largest wind tunnel experiment was performed at NASA's Ames Research Center with the $24.4 \times 36.6 \text{ m}^2$ area wind tunnel and a 10-m-diameter wind turbine designed by the National Renewable Energy Laboratory (NREL). The purpose of this test was to acquire aerodynamic and structural measurement data on a wind turbine in an environment free from pronounced inflow anomalies which gave insights on e.g. 3D stall effects, tip effects and yaw. For more informations see e.g. [58]. A similar experiment was carried out on a wind turbine model with a diameter of 4.5 m, the so called MEXICO turbine, which was placed in the largest European wind tunnel, the LLF facility of the German Dutch Wind Tunnel, DNW with a cross section of $9.5 \times 9.5 \text{ m}^2$. In this project not only pressure and load data were measured but in addition detailed flow field data were taken with the Particle Image Velocimetry (PIV) technique [130]. Even though such 'large' scale experiments gave invaluable insights into wind turbine aerodynamics, representative of full scale machines, they were limited to uniform flow conditions with low turbulence and the wake development could only be measured over short distances.

For this reason many research groups make use of smaller models. Krogstad & Adaramola designed a model wind turbine with a rotor diameter of 0.9 m, which exhibits an energy conversion similar to a full scale turbine [84]. Bartl *et al.* [7] used similar turbines to measure the wake behind an array of two model wind turbines. More recently Bartl *et al.* [9] measured the power output and yaw moments of an array of two yaw-controlled model wind turbines. Nanos *et al.* [106] designed a model wind turbine with a rotor diameter of

0.6 m and torque, pitch and yaw control, making it suitable for complex terrain studies and deep array wind farm control tests. In conclusion wind tunnel experiments based on 'medium' sized model wind turbines are capable to model a realistic rotor flow and give the opportunity to study many aspects of wind energy, such as the wake development in (grid generated) turbulent approaching flow, interactions with upstream turbines, the structural behaviour of the turbine, and control strategies.

Modelling the interaction of wind turbines with atmospheric boundary layers, however, typically requires even smaller models. Boundary layers generated in wind tunnels are often limited to a thickness of about 2 m. Since even modern multi-megawatt wind turbines have a maximum total height of about 1/3 of the boundary layer thickness, model wind turbines for the application in boundary layer wind tunnels need to be sufficiently small. Due to their scale of 1:250 and smaller these 'small' scale wind turbines operate in a Reynolds number regime significantly lower compared to a full scale turbine. Therefore, special care has to be taken in the design to obtain a realistic rotor performance. Bastankhah *et. al* [11] studied the interaction between the wake of a small scale wind turbine model (15 cm rotor diameter) and a turbulent boundary layer for different tip speed ratios (TSRs) and yaw angles. They showed that the near wake region is significantly influenced by the TSR of the turbine and the wake rotation. It is important to notice that small scale model wind turbines, like in the aforementioned study but also in others e.g. [5, 28, 159], are typically operated at TSRs lower than 5 whereas full-scale wind turbines are designed for TSRs around 7. This mismatch can be considered to be a result of limitations regarding achievable Reynolds numbers in wind tunnel modelling. For low chord based Reynolds numbers airfoils exhibit a low efficiency (lift to drag ratio), which in result leads to a lower maximum power coefficient at a lower design TSR compared to full-scale wind turbines [22]. In some situations it is even not feasible to work with small scale models. In these cases surrogate models can be applied. Aubrun *et al.* [3] showed that the velocity deficit in the (far) wake of a rotating model and a porous disc developing in a modelled atmospheric boundary layer were indistinguishable starting at 3 rotor diameters downstream of the rotor, whereby the porous disc was designed to match the velocity deficit in the wake of the rotor at a downstream distance of 0.5 rotor diameters. For higher-order statistics, however, significant differences were observed, especially in the near wake.

1.2.3.2 Numerical Simulation

During the last two decades, using computational fluid dynamics has become increasingly popular in wind energy research, as it gives the opportunity to conduct studies of single turbines as well as of wind farms at full scale. However, due to the high Reynolds numbers of the atmospheric boundary layer and the rotor flow, direct numerical simulations are still prohibitively expensive. Nevertheless, considering that wind turbine wakes are always turbulent and exposed to turbulent boundary layer flow conditions, simulation techniques are mandatory which resolve a large fraction of the turbulent scales. Since a large eddy simulation (LES) resolves all scales of turbulent transport larger than the grid scale while smaller scales are modelled using a subgrid-scale (SGS) model, LES has become an established tool in wind energy research.

However, blade geometry resolving large eddy simulations of wind turbines immersed in turbulent boundary layer flows constitute a multi-scale problem. The flow within the boundary layer forming at the blade consists of vortical structures with lengths multiple

orders smaller than the rotor diameter. The atmospheric boundary layer, however, is characterised by vortical structures which are in the order of the rotor diameter or even larger. Within the wake, eddies which shed from the blade subsequently reorganize to larger ones as they are transported downstream. Hence, the far wake development is rather influenced by the large atmospheric turbulent structures than by the signature of the small turbulent boundary layer emerging at the blade. Therefore it is not mandatory to resolve the latter to study the wake development, though it is necessary to predict the impact of the rotor on the flow field as it determines the velocity deficit.

One common approach which makes use of this observation is the actuator disc method. The general concept of this method is to model the effect of the rotor blades upon the flow field, typically by body forces or by the pressure jump which occurs across the rotor disc. The simplest formulation is the constantly loaded actuator disc, in which the forces representing the rotor are prescribed and distributed on a permeable disc of zero thickness. Based on this approach Jimenez *et al.* [70],[71] performed large eddy simulations of the wind turbine interaction with an atmospheric boundary layer to study the Reynolds stresses and the spectral coherence in the wake.

A more accurate approach is the generalised actuator disc method, in which the forces acting on the disc are determined from the local flow field, informations on the blade geometry and tabulated airfoil data. Additionally the forces can be corrected for three-dimensional effects and tip losses. For each annular ring of the rotor disc the calculated forces are averaged in the circumferential direction and distributed evenly across the annulus. Sørensen *et al.* [131] applied this approach in order to study unsteady phenomena in axisymmetric flow conditions. Wu & Porté-Agel [156] compared large eddy simulations of a model wind turbine immersed in a neutral stratified turbulent boundary layer performed with the constantly loaded and the generalised actuator disc. In both cases the numerical results were found to be in good agreement with measurement results in the far wake region, whereas the generalised actuator disc also yielded improved predictions in the near wake. Mikkelsen [102] used the generalised actuator disc approach for simulating the wake of a rotor operating in yawed conditions and showed that the method is incapable of producing skewed wake geometries. As the forces are introduced as circumferential average, the method is strictly speaking only valid for axisymmetric flow conditions. The method furthermore implies an infinite number of blades and cannot capture the influence of blade tip vortices.

Hence, to overcome these drawbacks, Sørensen & Shen [132] introduced the actuator line method, where the forces are distributed along rotating lines representing the blades of the rotor. Other than in the actuator disc model, the forces are not calculated per annulus but per blade section due to which the local effect of the forces on the flow can be computed. As the actuator line method in principle is fully three dimensional and naturally includes the number of blades, no correction method such as the Prandtl correction is needed [102]. The actuator line method was originally formulated in vorticity-velocity variables and later reformulated by Mikkelsen [102] in primitive variables (i.e. pressure-velocity variables).

Fully resolved LES of high Reynolds number turbulent boundary layers are computationally expensive as the near-wall region contains small vortical structures, e.g. eddies that are important to the flow. The size of these turbulent eddies scales roughly with the distance from the wall, limited by viscous scales. That means that a well resolved LES requires grids nearly as fine as those used in direct numerical simulation (DNS). This restriction applies not only to wall-normal grid spacing but to horizontal grid spac-

ing as well. Baggett et al. [4] estimated that the number of grid points necessary to resolve a channel flow properly with LES scales approximately with the square of the Reynolds number. This near-wall resolution requirement clearly limits the application of LES and makes wall modelling inevitable for high Reynolds number flows such as turbulent boundary layers with considerable surface roughness. The wall model, hence, has to approximate the overall dynamical effects of the unresolved eddies on the basis of the larger outer scales.

A classical modelling approach is to use a coarse near-wall grid and supply wall stresses in cells adjacent to the wall. The wall stress, however, cannot be computed accurately on coarse wall-normal grids that extend to the wall and must therefore be determined from models matched to outer flow conditions. Schumann [125] applied wall stresses based on the known steady-state result and assumed a linear relation between the instantaneous streamwise velocity at the first grid point off the wall and the instantaneous wall shear stress. Grötzbach [54] later extended Schumann's model to avoid having to know the mean shear stress a priori and used the instantaneous fit of the logarithmic law to the spatial mean velocity profile. Mason & Thomson [98], however, argue that use of averaged quantities is hard to support as the surface rather than the flow interior is the only place where turbulence scales are much smaller than the horizontal mesh scale and where a local deterministic parametrization can be justified. For that reason Mason & Callen [97] preferred to use the instantaneous fit of the logarithmic law to the local instantaneous values of the flow field.

As aforementioned, in large eddy simulation the evolution of non-universal larger scales are resolved whereas smaller scales are modelled. This is obtained by approximating the continuous flow solution by grid functions while spatial and temporal scales which cannot be resolved are removed by applying a spatial low-pass filter operation [88]. The removed unresolved scales are then modelled using a (explicit) subgrid-scale (SGS) model.

One of the earliest SGS models is the Smagorinsky eddy-viscosity model [129] which was developed in the 1960's. It is limited in its accuracy, as it requires the a priori input of the Smagorinsky coefficient for modelling the subgrid-scale eddy viscosity, which however is strongly case dependent. Later, in 1991, Germano *et al.* [51] proposed to view the Smagorinsky coefficient as a function of space and time. They developed a dynamic procedure, which is based on assuming the scale invariance of the model coefficient and using information from the smallest resolved scales to optimise the value of the model coefficient at every position and time step without any ad hoc tuning.

In wind energy research still some well established flow solvers make use of the standard Smagorinsky model like e.g. SOWFA [141] or PALM [151]. However, other research groups have developed SGS models specially tailored for the application in wind energy. The flow solver EllipSys3D, developed at the Technical University of Denmark, makes use of a mixed scale model in which a velocity scale is used to compute the eddy-viscosity from a similarity-model like approach [133]. For the simulation of atmospheric boundary layers Porté-Agel *et al.* [113] proposed the so-called scale-dependent dynamic model by relaxing the assumption of the scale invariance of the model coefficient on which the dynamic Smagorinsky model relies. Their simulation results of neutral boundary layers over homogeneous surfaces showed that the dynamically computed coefficients are scale-dependent. Later the model was extended by Bou-Zeid *et al.* [16] and yielded improved predictions of the flow statistics compared with the Standard Smagorinsky model and its dynamic version. More recently, Sarlak *et al.* [121] studied the role of various SGS models in LES simulations, where the wind turbine is modelled

by the Actuator Line Method. They found that the SGS models have only a minor impact on the wake and the predicted power performance.

The above mentioned SGS models make use of the filter concept of Leonard, which is typically employed without taking into account the discretisation scheme. However, the explicitly computed SGS stress is affected by the truncation error of the discretization scheme. In a theoretical study Ghosal [52] analysed this problem and found that the truncation error even of a fourth-order central-difference discretisation can have the same order of magnitude as the modelled SGS stress. In so-called implicit large eddy simulation (ILES) this interference is taken into account by discretising the unmodified Navier Stokes Equations and the numerical regularisation acts as an SGS model. Since in this case the SGS model is implicitly contained within the discretisation scheme, an explicit computation of model terms is unnecessary. Hickel [61] developed a non-linear finite-volume scheme involving a solution adaptive reconstruction (deconvolution) of the numerical solution. Free discretisation parameters were calibrated in such a way that the effective spectral numerical viscosity is identical to the spectral eddy viscosity from turbulence theory for asymptotic cases.

1.3 Research Objectives & Structure of the Thesis

This thesis focuses on providing a detailed investigation and advances in understanding the influence of terrain roughness on the evolution of a wind turbine wake. The specific research questions which shall be answered in this thesis are:

- How does the aerodynamic roughness length upstream of a wind turbine influence the wake evolution? Of particular interest are the influence on characteristics in the near wake as e.g. tip vortices and their break down, the onset of the far wake region, and the re-energising of the wake and evolution of turbulence in distances of a potential downstream turbine.
- How does the aerodynamic roughness length upstream of a wind turbine misaligned to the incoming wind influence the wake trajectory? Intentional yaw misalignment is considered as a beneficial wake control strategy to increase the overall power output of wind farms or alleviate fatigue loads. The effect of the aerodynamic roughness and the atmospheric turbulence on the wake trajectory, however, is insufficiently covered in literature. For the application in on-shore wind farms an in-depth knowledge on such effects can be crucial.
- Does a wind turbine wake immersed in a turbulent boundary layer exhibit some type of self similarity as known from wakes behind generic bluff bodies? Only few studies found in literature covered this issue in more detail. Therefore, to answer this question a theoretical discussion is necessary regarding the conditions under which self similarity can be expected in this specific flow situation. Moreover the influence of the boundary layer state upstream the wind turbine on the degree of self similarity of the mean velocity and its higher moments has to be examined. Furthermore, the axial scaling of the self similar profiles and the universality of these laws needs to be analysed. Finally, having carried out such an investigation, the question arises if this knowledge can be used to predict the wake evolution.

The thesis is organised as follows: Theoretical fundamentals that serve as a base for this research are given in Chapter 2. As a systematic investigation of the aforementioned effects is not feasible in field studies, wind tunnel tests on a small scale model wind turbine are carried out as this provides controllable and reproducible conditions. In the available wind tunnel facilities this approach, however, is limited to neutrally stratified boundary layers over surrogate roughness elements. In Chapter 3 the modelling approach is described and boundary layer configurations for the application in wind turbine wake measurements are selected. To simulate the wake of a large (multi megawatt) wind turbine the experiment shall be based on a physical scale model. Due to the Reynolds number sensitivity of the rotor blades such a model has to be designed specifically for the flow conditions present in the wind tunnel. The corresponding design steps and the performance verification are provided in Chapter 4. The investigation shall include the analysis of the wake recovery and growth, profiles of velocity and turbulent quantities in the wake, spectral analysis, and in case of an intentional yaw misalignment also the trajectory of the wake. Results and execution of corresponding analysis tasks are described in Chapter 5. The specific features and research tasks associated with this experimental investigation unfold as follows:

- Modelling of two turbulent neutrally stratified boundary layers of significantly different roughness length which reach an equilibrium state within the test section of the wind tunnel.

- Design and development of a small scale model wind turbine for operation at low Reynolds numbers which exhibits a realistic energy conversion in terms of power production while meeting the scale of the simulated turbulent boundary layers.
- Systematic analysis of the effect of tip speed ratio and roughness length on the evolution and spectral content of a wind turbine wake immersed in a turbulent boundary layer. Of particular interest are the streamwise evolution of the mean velocity and its higher moments, characteristic parameters as the wake recovery and growth, and the power spectra.
- Assessment of intentional yaw misalignment as wake control strategy in different terrain conditions, by means of the mean wake trajectory.

To complement the experimental study, high-fidelity large-eddy simulations (LES) similar to the wind tunnel experiment shall be conducted. Since geometry resolving LES, even of a small scale wind turbine, is still prohibitively expensive in terms of computational costs, the rotor flow and the roughness producing elements shall be modelled. The applied numerical methods and their verification are described in Chapter 6. The results from the LES, given in Chapter 7, shall then be used to analyse flow quantities not obtainable by the measurements and to verify assumptions made in the course of the experimental investigation. Development details on the framework along with execution of corresponding analysis tasks specifically consist of:

- Development and implementation of a Wall Model for the simulation of fully rough turbulent boundary layers into the in-house Navier-Stokes solver INCA.
- Implementation and verification of the Actuator Line Method (ALM) into INCA.
- Calibration of the ALM with respect to the three-dimensional flow around the model wind turbine rotor.
- Analysis of the LES results of the model wind turbine immersed in turbulent boundary layers of different surface roughness with regard to the evolution and momentum budget of the wake.

As its final aim this thesis provides a new simple analytical model for wind farm control applications which describes the evolution of turbulence quantities in the wake, taking into consideration the incoming flow conditions. In Chapter 8 that model is derived and compared to the experimental and numerical data. The necessary steps in deriving this model consist of:

- Derivation of the concept for added turbulence quantities in the wake
- Assessment of self similarity in the wake of wind turbine
- Derivation of the semi-analytical model and evaluation for description of turbulence evolution in the wake

At the end of each chapter, major findings and conclusions are summarized. Finally, concluding remarks, an outlook, and recommendations for future work are given in 9.

The analyses presented in this work are based on wind tunnel experiments and numerical simulations conducted during the course of the Greentech-03 Wind project by the Eurotech Initiative.

Fundamentals

This chapter gives an introduction to the theoretical background relevant for the present investigations on the interaction of wind turbine wakes with the atmospheric boundary layer. First, two physical laws used to characterise neutrally-stratified atmospheric boundary layer flows over flat homogeneous terrain are given in Section 2.1. In Section 2.2 the classical one-dimensional momentum theory and blade element theory are introduced, which are subsequently used to introduce the blade element method, which can be used to determine the operational state of a wind turbine or even to derive an optimal rotor design.

Wake aerodynamics are addressed in Section 2.3 with special emphasis on the evolution of the far wake. Since self similar flows facilitate the development of analytical models, a concept to approximate the flow field as superposition of a boundary layer flow and an axisymmetric and self similar wake is derived and the limitations of the approach are discussed. Furthermore, the momentum and turbulent kinetic energy budget in the wake are introduced and discussed regarding the most relevant contributing terms.

2.1 Atmospheric Boundary Layers and Rough Walls

In general, the atmospheric boundary layer (ABL) can be divided into three layers in the vertical. The layer closest to the surface is the roughness or viscous sublayer, which is of similar height as the roughness causing object itself and of no relevance for wind energy applications. Above it is the so-called constant-flux or Prandtl layer. It can be up to about 100 m thick and within the wind speed increases strongly with height and forces that are caused by turbulent fluctuations of the air are dominant. The last and upper layer is the Ekman layer, whose thickness can vary between about 100 m at night with low winds and about 3 km at daytime with strong thermal convection. In this layer the Coriolis force is of importance, which causes a turning of the wind direction with height.

The simplest form of the ABL is found over flat, horizontally homogeneous terrain with a uniform distribution of roughness elements (trees, buildings, etc.). The characteristics of the flat-terrain ABL is mainly determined by the diurnal variation of the energy balance of the Earth's surface and the density of roughness elements [40]. During daytime, when solar irradiation heats the ground, thermal convection due to ascending warm air causes an intense vertical mixing and thus little vertical shear. Therefore, this kind of boundary layer is named the convective boundary layer (CBL). At night-time, when the earth surface is cooled by a net loss of radiation, a downward heat flux can lead to a stably stratified ABL (SBL). The SBL is characterised by large vertical gradients and low turbulence intensity. In situations where strong winds and clouds override the effect of solar radiation, and the surface and the air above it are of similar temperature, a neutrally-stratified boundary layer (NBL) can form. Due to the almost constant temperature over height within this boundary layer buoyancy effects are small and vertical wind gradients and turbulent fluctuations are mainly determined by the density of roughness elements on the surface.

When the effect of Coriolis force is neglected, the vertical wind profile in the NBL can be derived from simple physical considerations valid for turbulent boundary layers over rough surfaces. Therefore, the logarithmic law over smooth and rough surfaces is derived in Section 2.1.1. The empirical power law, which is often used instead of the logarithmic law, will be presented in the subsequent Section 2.1.2.

2.1.1 Logarithmic Law

For deriving the logarithmic law of the axial mean velocity $\bar{u}(z)$, the Reynolds Averaged streamwise momentum equation for incompressible flows is considered. It is given by

$$\bar{u} \frac{\partial \bar{u}}{\partial x} + \bar{v} \frac{\partial \bar{u}}{\partial y} + \bar{w} \frac{\partial \bar{u}}{\partial z} = -\frac{1}{\rho} \frac{\partial \bar{p}}{\partial x} - \left[\frac{\partial \overline{u'u'}}{\partial x} + \frac{\partial \overline{u'v'}}{\partial y} + \frac{\partial \overline{u'w'}}{\partial z} \right] + \nu \left[\frac{\partial^2 \bar{u}}{\partial x^2} + \frac{\partial^2 \bar{u}}{\partial y^2} + \frac{\partial^2 \bar{u}}{\partial z^2} \right], \quad (2.1)$$

where ρ is the density and ν the kinematic viscosity. The coordinates x , y , and z denote the axial, lateral, and vertical direction with the corresponding velocity components u , v , and w . The overbar ($\bar{\quad}$) indicates the temporal average and the apostroph ($'$) the fluctuating component of a quantity.

Eq.(2.1) can be simplified by assuming a steady, fully developed, and two dimensional flow, which results in

$$\frac{d\bar{p}}{dx} = \frac{d}{dz} \left(\rho \nu \frac{d\bar{u}}{dz} - \rho \overline{u'w'} \right). \quad (2.2)$$

This shows that the shear stress within a turbulent boundary layer consists of two parts

$$\tau = \tau_\nu + \tau_R, \quad (2.3)$$

the viscous stress $\tau_\nu = \frac{d\bar{u}}{dz}$ and a part which arises from turbulent fluctuations $\tau_R = -\rho\overline{u'w'}$, the so called Reynolds shear stress. Close to the wall, within the viscous sub-layer, the Reynolds stress vanishes, and the viscous stress is dominant. However, within the surface layer the viscous stress is small compared to the Reynolds stress and can be neglected. Therefore, this kind of flow has a two layer structure, for which the equations have to be solved separately.

Within the surface layer the Reynolds stress can be modelled by applying the Prandtl mixing length model. It states that the fluctuating part u' is proportional to the gradient $\frac{d\bar{u}}{dz}$, and that fluid elements fluctuate within the mixing length $l_m = \kappa z$, where $\kappa = 0.41$ is the von Kármán constant. Furthermore, due to considerations regarding the continuity, it can be assumed that $-u' \approx w'$. With that the Reynolds stress can be written as

$$\tau_R = -\rho\overline{u'w'} \approx \rho l_m^2 \left| \frac{d\bar{u}}{dz} \right| \frac{d\bar{u}}{dz} \quad (2.4)$$

To solve this differential equation, it is assumed that within the surface layer the shear stress is approximately constant and, hence, equal to the wall shear stress $\tau_W = \tau(z=0)$. Furthermore, velocities and stresses can be made non-dimensional by the shear stress velocity, which is defined as

$$u_\tau = \sqrt{\frac{\tau_W}{\rho}}. \quad (2.5)$$

With the non-dimensional quantities

$$u^+ = \frac{\bar{u}}{u_\tau}, \quad z^+ = \frac{u_\tau z}{\nu} \quad (2.6)$$

Eq.(2.4) can then be given as

$$\frac{du^+}{dz^+} = \frac{1}{\kappa z^+}. \quad (2.7)$$

Integrating this equation then gives the logarithmic law

$$u^+(z^+) = \frac{1}{\kappa} \ln z^+ + C^+(k_s^+) \quad (2.8)$$

where C^+ is an integration constant which depends on the non-dimensional wall roughness k_s^+ . Various studies have shown that for smooth walls the integration constant is $C^+ = 5.0$.

In reality, however, surfaces have a certain roughness. Since surface textures can be of very different kind, for technical applications a standard roughness is introduced. Thereby, use is made of the idea that the roughness is formed by spheres in tightest packing, as shown in Figure 2.1. A similar texture can be found on sandpaper, therefore it is also often called *sand grain roughness*. In non-dimensional form the standard roughness is expressed as

$$k_s^+ = \frac{u_\tau k_s}{\nu} \quad (2.9)$$

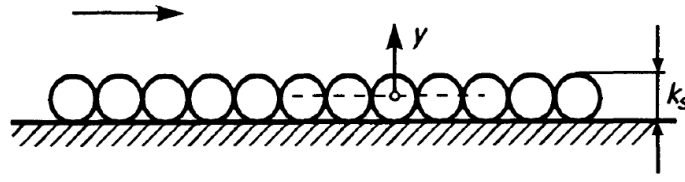


Figure 2.1: Sand grain roughness k_s ; Source [123].

Using the non-dimensional standard roughness, Eq.(2.8) can be reformulated as

$$u^+(z^+) = \frac{1}{\kappa} \ln \left(\frac{z}{k_s} \right) + C_r^+(k_s^+) \quad (2.10)$$

with $C_r^+(k_s^+) = \ln k_s^+ + C^+(k_s^+)$. For large values of k_s^+ the roughness elements become large and penetrate the log law region. For this so called *fully rough regime* the integration constant $C_r^+(k_s^+)$ becomes independent of k_s^+ and reaches a constant value of

$$\lim_{k_s^+ \rightarrow \infty} C_r^+(k_s^+) = \lim_{k_s^+ \rightarrow \infty} \left[C^+(k_s^+) + \frac{1}{\kappa} \ln(k_s^+) \right] = 8.0. \quad (2.11)$$

Figure 2.2 shows C_r^+ as function of k_s^+ . It is interesting to notice that for $k_s^+ > 70$ the integration constant $C_r^+(k_s^+)$ reaches its asymptotic value [123].

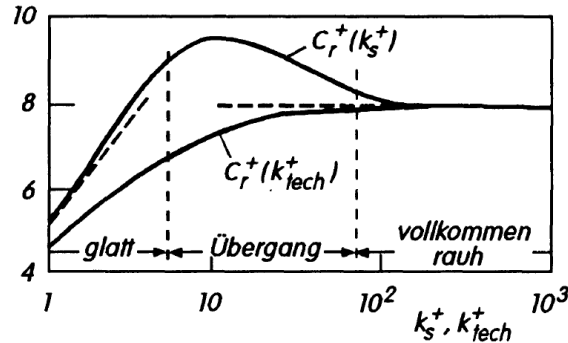


Figure 2.2: Integration constant C_r^+ as function of k_s^+ ; Source [123].

In the field of meteorology, it is common to use the roughness length z_0 instead of the standard roughness k_s to describe the roughness of the terrain. Furthermore, for surfaces which are densely covered with roughness elements, skimming flows can occur in the interspaces between the obstacles, which have a regime quite different from the bulk flow above. As a result the surface appears smooth at the larger scale of the entire surface layer. To take this effect into account, an additional parameter is introduced, the displacement height d . With that the logarithmic law over a rough surface is given as

$$u^+(z) = \frac{\bar{u}(z)}{u_\tau} = \frac{1}{\kappa} \log \left(\frac{z-d}{z_0} \right). \quad (2.12)$$

Typical values of roughness length z_0 and displacement height d are listed in Figure 2.3.

The range of height in which the logarithmic law is valid is not strictly defined and various definitions can be found in literature. A practicable definition for the present work is given by Raupach [116] who specifies the lower and upper limit as $z_{min}/h_r > 2$ and

Terrain Description	z_0 (m)	d (m)
City centres Forests	0.7	15 to 25
Small towns Suburbs of large towns and cities Wooded country (many trees)	0.3	5 to 10
Outskirts of small towns Villages Countryside with many hedges, some trees and some buildings	0.1	0 to 2
Open level country with few trees and hedges and isolated buildings; typical farmland	0.03	0
Fairly level grass plains with isolated trees	0.01	0
Very rough sea in extreme storms (once in 50-yr extreme) Flat areas with short grass and no obstructions Runway area of airports	0.003	0
Rough sea in annual extreme storms Snow covered farmland Flat desert or arid areas Inland lakes in extreme storms	0.001	0

Figure 2.3: Typical values of terrain parameters z_0 and d ; Source [41].

$z_{max}/\delta < 0.3$, where h_r is the average height of the roughness elements and δ the boundary layer thickness.

A conversion between the roughness length z_0 and the standard roughness k_s can be easily derived by equating (2.10) and (2.12), and neglecting the displacement height d . This gives the conversion

$$z_0 = k_s \exp(-\kappa C_r^+(k_s^+)) . \quad (2.13)$$

For the fully rough regime, where the lower limit of the non-dimensional standard roughness is $k_s^+ > 70$, the asymptotic value of $C_r^+ = 8.0$, see Eq.(2.11), can be applied. Inserting the lower limit of the non-dimensional standard roughness itself, the value can be converted to the non-dimensional roughness length $z_0^+ > 2.8$.

2.1.2 Power Law

For practical reasons, e.g. in wind energy applications, an empirical power law is often used to describe the vertical wind profile in the atmospheric boundary layer

$$\bar{u}(z) = \bar{u}_{ref}(z_{ref}) \left(\frac{z}{z_{ref}} \right)^\alpha \quad (2.14)$$

where \bar{u}_{ref} is the mean axial velocity at the reference height z_{ref} , and α is the shear exponent. The exponent α depends on the surface roughness and the thermal stability of the atmospheric boundary layer. In Figure 2.4 typical values of the shear exponent α and roughness length z_0 are listed for terrain categories according to the German National Norm DIN EN 1991.

The power law is usually defined to be valid for heights $z > 50$ m, see e.g. [40]. Based on the assumption that the boundary layer height of an NBL can be approximated to be $\delta \approx 500$ m [33], a lower limit in non-dimensional form can be defined as $z_{min}/\delta > 0.1$.

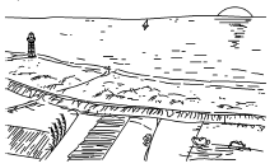
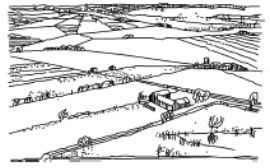
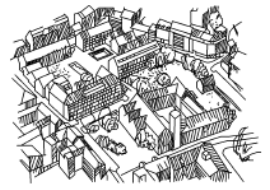
<p>Geländekategorie I</p> <p>Offene See; Seen mit mindestens 5 km freier Fläche in Windrichtung; glattes, flaches Land ohne Hindernisse</p> <p>Rauigkeitslänge $z_0 = 0,01$ m</p> <p>Profilexponent $\alpha = 0,12$</p>	
<p>Geländekategorie II</p> <p>Gelände mit Hecken, einzelnen Gehöften, Häusern oder Bäumen, z. B. landwirtschaftliches Gebiet</p> <p>Rauigkeitslänge $z_0 = 0,05$ m</p> <p>Profilexponent $\alpha = 0,16$</p>	
<p>Geländekategorie III</p> <p>Vorstädte, Industrie- oder Gewerbegebiete; Wälder</p> <p>Rauigkeitslänge $z_0 = 0,30$ m</p> <p>Profilexponent $\alpha = 0,22$</p>	
<p>Geländekategorie IV</p> <p>Stadtgebiete, bei denen mindestens 15 % der Fläche mit Gebäuden bebaut sind, deren mittlere Höhe 15 m überschreitet</p> <p>Rauigkeitslänge $z_0 = 1,05$ m</p> <p>Profilexponent $\alpha = 0,30$</p>	

Figure 2.4: Typical values of terrain parameters z_0 and α for terrain categories according to the German National Norm DIN EN 1991 [38].

2.2 Wind Turbine Aerodynamics

Wind turbines extract kinetic energy from the wind which passes through the rotor disc. Assuming that the affected mass of air remains separate from the surrounding wind, an embracing boundary surface can be imagined which contains the affected mass of air and across which no air is flowing. This surface can be extended in upstream and downstream direction forming a long stream-tube, see Figure 2.5. By removing a part of its kinetic energy the wind crossing the rotor disc is decelerated. As a result, also the air upstream of the turbine is gradually slowed down, such that its velocity is already lower than the free-stream wind speed when it arrives at the rotor disc. Due to the deceleration, the stream-tube expands and its static pressure rises to absorb the decrease in velocity. When the air passes the rotor disc and kinetic energy is extracted, the static pressure drops below the atmospheric pressure level. Downstream of the wind turbine, in the wake, the air then proceeds with reduced speed and static pressure. Far downstream, eventually, the static pressure must return to free-stream conditions. As in this process no work is done on or by the air, the rise in static pressure causes an additional deceleration of the wind and, hence, a further expansion of the stream-tube.

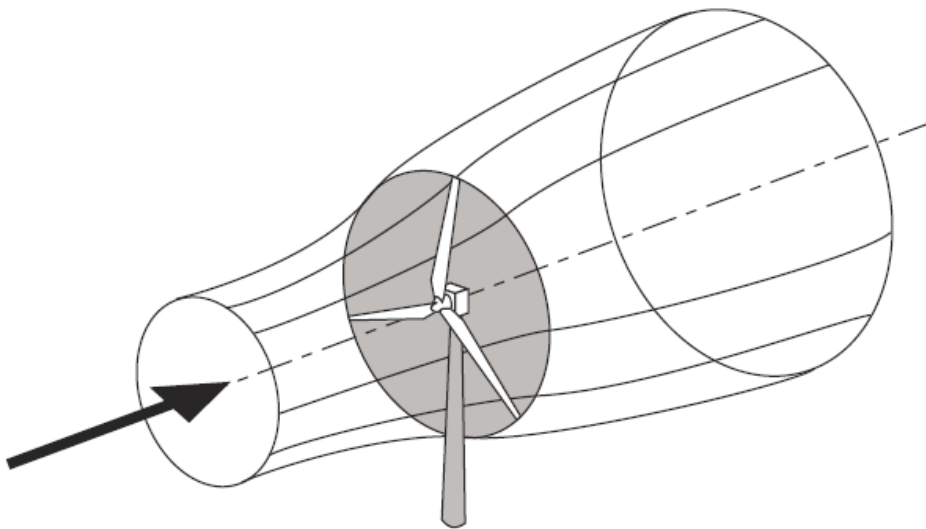


Figure 2.5: The energy extracting stream-tube of a wind turbine; Source [22].

Horizontal axis wind turbines (HAWT) extract kinetic energy from the wind by employing a rotor with a number of blades N_B rotating with an angular velocity Ω about a horizontal axis. The air crossing the rotor plane is doing work on the blades, which, by virtue of their aerodynamic design, develop aerodynamic torque about the rotor axis. As a result kinetic energy is extracted from the wind and is converted into electrical energy by a generator attached to the rotor shaft. By the extraction of kinetic energy, as mentioned above, a pressure difference occurs across the rotor disc due to which the rotor experiences not only torque but also thrust. However, the forces acting on the rotor are not the same for all radial positions and are determined by the specific blade design and the operational state of the wind turbine.

Nevertheless, we can begin an analysis of the aerodynamic behaviour of wind turbines without any specific turbine design just by considering the energy extraction process, which is described in Section 2.2.1 by the concept of the actuator disc theory. Forces,

determined by a specific blade design, which act on the air can then be analysed by the blade element theory given in Section 2.2.3. By combining both, actuator disc theory and blade element theory, an optimum design in terms of power extraction can be derived, as described in Section 2.2.4.

2.2.1 Actuator Disc Theory

The derivation of the actuator disc concept assumes that velocities in axial and azimuthal direction can vary with radial direction, whereas variations in circumferential direction are not taken into account. Therefore, we consider an annular ring of the rotor disc which is of radius r and of radial width δr .

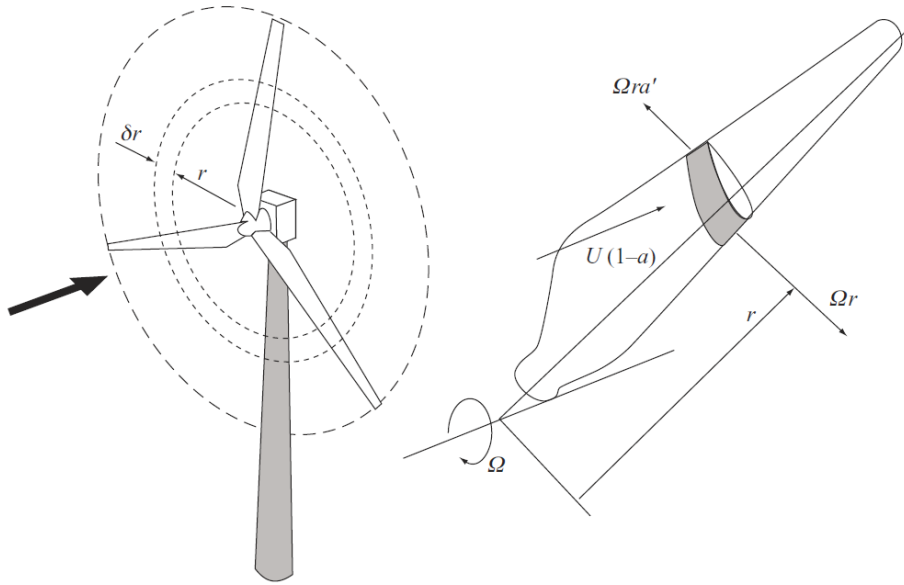


Figure 2.6: A blade element sweeps out an annular ring; Source [22].

In the annular ring the slowdown of the air in the axial direction, due to the extraction of kinetic energy, is described by an induced velocity variation $-aU_\infty$ which is superimposed on the free stream velocity, where a is called the axial flow induction factor. At the disc, therefore, the net stream-wise velocity is

$$U_D = U_\infty(1 - a) \quad (2.15)$$

Hence, the mass flow through the annular ring with the area $\delta A_D = 2\pi r \delta r$ is given by

$$\delta \dot{m} = \rho \delta A_D U_\infty (1 - a) . \quad (2.16)$$

The thrust T exerted on the annular ring equals the rate of change of streamwise momentum, which can be calculated from the overall change of axial velocity from far upwind the turbine U_∞ to far downwind of it in the wake $U_{w,ax}$ times the mass flow, which gives

$$\delta T = \delta \dot{m} \cdot \Delta U_{ax} = \delta \dot{m} \cdot (U_\infty - U_{w,ax}) . \quad (2.17)$$

According to Bernoulli's equation for incompressible flows, the change in momentum and the resultant power extraction also manifest in a drop in total and static pressure from p^+ directly upwind to p^- directly downwind the rotor plane. Hence, the thrust force the wind exerts on the rotor annulus can also be calculated from both the pressure drop across the rotor disk

$$\delta T = \delta A_D \cdot \Delta p = \delta A_D \cdot (p^+ - p^-) . \quad (2.18)$$

Using Eq.(2.16), Eq.(2.18), and additionally applying Bernoulli's equation for incompressible flows from a point far upstream to the rotor disk as well as from the rotor disk to a point far downstream yields the axial wake velocity as function of the axial flow induction

$$U_{w,ax} = U_\infty (1 - 2a) . \quad (2.19)$$

Inserting this relationship and the mass flow rate Eq.(2.16) in Eq.(2.17) the thrust force exerted on the annular ring as function of the axial flow induction can be obtained

$$\delta T = 4\pi r \rho U_\infty^2 (1 - a) a \delta r \quad (2.20)$$

The torque exerted on the annular ring can be derived by a similar approach. The change of angular momentum of the air passing the annular ring causes a tangential force, which multiplied with the radius r of the annulus gives the torque

$$\delta Q = \delta \dot{m} \cdot \Delta U_t \cdot r = \delta \dot{m} \cdot (U_{\infty,t} - U_{w,t}) \cdot r , \quad (2.21)$$

where $U_{\infty,t} = 0$ and $U_{w,t}$ are the tangential velocity far upstream and far downstream of the rotor. Far downstream of the rotor, in the wake, the flow rotates in the opposite direction of the rotor, due to the conservation of angular momentum. Similar to the axial flow induction, the tangential velocity induced by the rotor can be expressed as an induced velocity variation $U_{w,t} = -2\Omega r a'$, where a' is called the tangential flow induction factor. Given that, and applying the mass flow rate Eq.(2.16), the torque exerted on an annular ring can be expressed as

$$\delta Q = 4\pi r^3 \rho U_\infty \Omega (1 - a) a' \delta r . \quad (2.22)$$

The rate of work done by the thrust force $\delta T U_D$ equals the power extracted by the annular ring due to the generation of torque

$$\delta P = \delta T \cdot U_\infty (1 - a) = \delta Q \cdot \Omega . \quad (2.23)$$

Inserting the derived relationships for the thrust Eq.(2.20) and the torque Eq.(2.22) yields

$$U_\infty^2 a(1 - a) = \Omega^2 r^2 a' \quad (2.24)$$

Introducing the tip speed ratio at the edge of the rotor disc $r = R$

$$\lambda = \frac{\Omega R}{U_\infty} , \quad (2.25)$$

and the local speed ratio $\lambda_r = \mu \lambda$, where $\mu = r/R$ is the non-dimensional radius, and inserting these in Eq.(2.24), the radial variation of the tangential flow induction factor a'

can be expressed as function of the axial flow induction factor a and the tip speed ratio λ

$$a' = \frac{a(1-a)}{\lambda_r^2} \quad (2.26)$$

To determine the performance of a wind turbine, commonly the so called thrust coefficient C_T and power coefficient C_P are used as measures. The thrust coefficient is defined as the ratio between the total thrust T exerted on the rotor disc per unit of frontal area and the dynamic pressure

$$C_T = \frac{T}{\frac{1}{2}\rho U_\infty^2 \pi R^2}. \quad (2.27)$$

The power coefficient is defined as the ratio between power extracted by the wind turbine and power of the wind

$$C_P = \frac{P}{\frac{1}{2}\rho U_\infty^3 \pi R^2}, \quad (2.28)$$

where $P = Q\Omega$ is the extracted power, Q the torque at the rotor shaft, and Ω the rotational frequency.

Given that the axial and tangential flow induction factors $a(r)$ and $a'(r)$ are known along the rotor blade, the thrust and power coefficients can simply be obtained by integrating Eq.(2.20) and Eq.(2.22) from root to tip and inserting the results in Eq.(2.27) and Eq.(2.28), which gives

$$C_T = 8 \int_0^1 (1-a)a\mu \, d\mu, \quad C_P = 8 \int_0^1 (1-a)a'\lambda^2\mu^3 \, d\mu. \quad (2.29)$$

It can be shown that the maximum achievable power is obtained for a uniform radial distribution of the axial flow induction factor $a(r) = \frac{1}{3}$ [22], for which the power coefficient results in $C_{P,max} = \frac{16}{27} \approx 0.593$. This limit is known as the Lanchester-Betz limit, named after Frederic Lanchester, a British aeronautical pioneer, and Albert Betz, a German aerodynamicist. Even though wind turbines are designed for the extraction of power, rotor blades typically do not exhibit the optimum uniform radial distribution of the axial flow induction factor for multiple reasons. Among them are to mention the structural loads in the root region of the blade which make it necessary to deviate from the optimum design. However, more important for the discussion here, are tip and root vortices and the number of blades which alter the velocity field at the rotor disc and therefore also the radial distribution of the axial flow induction factor.

A widely used approach to determine the radial distribution of the axial flow induction factor is presented in the next section.

2.2.2 Blade Element Theory

In the derivation of the actuator disc concept, see Section 2.2.1 no specific blade design had to be considered. However, the blade design and the operational state of the wind turbine determine the radial distribution of the axial and tangential flow induction factors $a(r)$ and $a'(r)$. This relation can be provided by the Blade Element Theory.

Therefore, the blade is separated into infinitesimal elements at the radial position r with the width δr , as shown in Figure 2.6. Assuming that the velocity in radial direction and the interaction of neighbouring elements can be neglected, only the forces acting on the

element in axial and tangential direction F_{ax} and F_t , as shown in Figure 2.7(a), need to be determined. These, however, can be computed from the aerodynamic lift and drag forces L and D by using the transformation

$$F_{ax} = L \cos(\phi) + D \sin(\phi), \quad F_t = L \sin(\phi) - D \cos(\phi) \quad (2.30)$$

where ϕ is the relative angle of the incoming wind. Lift and drag forces can then be calculated based on tabulated values of the lift and drag coefficients, C_l and C_d , by using

$$L = C_l \frac{1}{2} \rho U_{rel}^2 c \delta r \quad D = C_d \frac{1}{2} \rho U_{rel}^2 c \delta r \quad (2.31)$$

where U_{rel} is the relative velocity of the incoming wind and c the chord width of the segment. The lift and drag coefficients and also the relative velocity of the incoming wind depend on the local axial and tangential flow induction factors. To derive these relations the velocity triangle shown in Figure 2.7(b) needs to be considered.

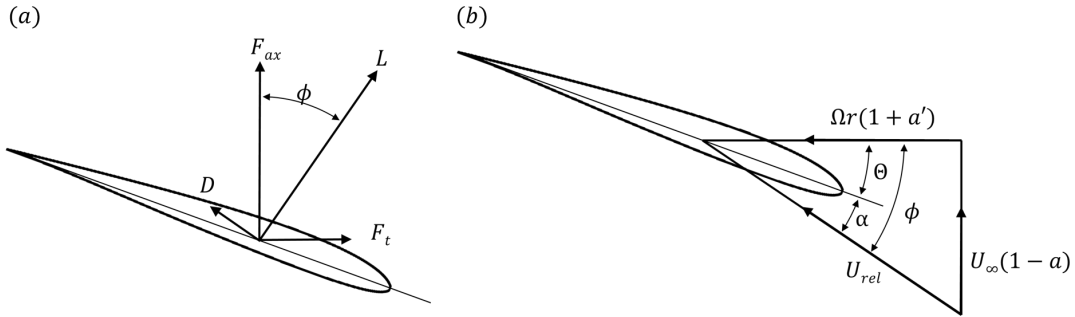


Figure 2.7: Blade element (a) forces and (b) velocities.

The local inflow angle ϕ can be defined by the axial and tangential velocities as

$$\phi = \arctan \left(\frac{(1-a)U_\infty}{(1+a')\Omega r} \right) = \arctan \left(\frac{(1-a)}{(1+a')\lambda_r} \right). \quad (2.32)$$

The lift and drag coefficients C_l and C_d are typically tabulated as function of the angle of attack α . In case of a rotor, this is defined as the difference of the inflow angle ϕ and the local twist angle Θ

$$\alpha = \phi - \Theta. \quad (2.33)$$

Based on the local velocity triangle the relative velocity of the incoming wind can be given as

$$U_{rel}^2 = U_{ax}^2 + U_t^2 = (1-a)^2 U_\infty^2 + (1+a')^2 (\Omega r)^2. \quad (2.34)$$

2.2.3 Blade Element Momentum Method

The problem of determining the flow field around the wind turbine, respectively the axial and tangential flow induction factors, can be solved by combining the actuator disc concept, see Section 2.2.1, and the blade element theory, see Section 2.2.2. Therefore the change of axial and angular momentum Eq.(2.20) and Eq.(2.22), and the local forces acting on the blade segments Eq.(2.30) are equated

$$\delta T = F_{ax}, \quad \delta Q = F_t \cdot r. \quad (2.35)$$

Rearranging the equations gives

$$4(1-a)a = \frac{U_{rel}^2}{U_\infty^2} \sigma_r C_{ax} \quad (2.36)$$

and

$$4\mu\lambda(1-a)a' = \frac{U_{rel}^2}{U_\infty^2} \sigma_r C_t \quad (2.37)$$

where $\sigma_r = \frac{N_B}{2\pi\mu} \frac{c}{R}$ is the solidity, $C_{ax} = C_l \cos(\phi) + C_d \sin(\phi)$, and $C_t = C_l \sin(\phi) - C_d \cos(\phi)$. By applying the trigonometric relations $\sin(\phi) = \frac{U_\infty(1-a)}{U_{rel}}$ and $\cos(\phi) = \frac{\Omega r(1+a')}{U_{rel}}$ Eq.(2.36) and Eq.(2.37) can be written as

$$a = \frac{1}{\frac{4 \sin^2(\phi)}{\sigma_r C_{ax}} + 1} \quad (2.38)$$

and

$$a' = \frac{1}{\frac{4 \sin(\phi) \cos(\phi)}{\sigma_r C_t} - 1}, \quad (2.39)$$

It is important to notice that in the course of the above derivations the existence of aerodynamic losses caused by tip and root vortices have been neglected. These can be accounted for by introducing Prandtl's tip loss factor [22]

$$F = \frac{2}{\pi} \arccos \left(e^{-\frac{N_B}{2} \frac{R-r}{r \sin \phi}} \right), \quad (2.40)$$

with which the axial and tangential flow induction factors result into

$$a = \frac{1}{\frac{4F \sin^2(\phi)}{\sigma_r C_{ax}} + 1} \quad (2.41)$$

and

$$a' = \frac{1}{\frac{4F \sin(\phi) \cos(\phi)}{\sigma_r C_t} - 1}. \quad (2.42)$$

Solving the derived formulas for the flow induction factors a and a' is an iterative process, which is given by the following steps:

1. Initialise a and a' , e.g. $a = a' = 0$
2. Compute the local inflow angle ϕ using Eq.(2.32)
3. Calculate the angle of attack α using Eq.(2.33) and read off $C_l(\alpha)$ and $C_d(\alpha)$ from table.
4. Calculate the flow induction factors a and a' by Eq.(2.41) and Eq.(2.42)
5. If a and a' have changed more than a certain value, go back to step 2. or else continue with next segment

When the flow induction factors for all segments have been calculated, the local velocity field of the incoming wind using Eq.(2.34), the local loads on the segment of the blades using Eq.(2.30), as well as the global power and thrust coefficients using Eq.(2.29) can be computed.

2.2.4 Optimum Rotor Design for Variable Speed Operation

A blade design which results in an optimal power output can be obtained by applying a similar approach as used in the derivation of the blade element momentum method. The only difference is that the optimal flow induction factors a_{opt} and a'_{opt} are now assumed to be known for a given design tip speed ratio λ_{dsgn} and the equations are solved for the radial chord $c(r)$ and twist $\Theta(r)$ distribution. Indeed, from the formulas in Section 2.2.3 it can be shown that the maximum achievable power is obtained for a uniform radial distribution of the axial flow induction factor $a_{opt}(r) = \frac{1}{3}$ [22]. The optimal tangential flow induction factor $a'_{opt}(r)$ can then be obtained from Eq.(2.26)

By neglecting the influence of drag $C_d = 0$ and ignoring blade tip- and root-losses, Eq.(2.37) can be used to derive the chord distribution, which is given by

$$c(r)/R = \frac{2\pi}{N_B C_{l,opt}} \frac{4\lambda_{dsgn} \mu^2 a'_{opt}}{\sqrt{(1 - a_{opt})^2 + (\lambda_{dsgn} \mu (1 + a'_{opt}))^2}}. \quad (2.43)$$

Even though the influence of drag is neglected in the derivation of the chord distribution, it has a significant influence on the rotor performance. Therefore, for the maximum possible power output the desired lift coefficient $C_{l,opt}$ and the corresponding angle of attack α_{opt} should be chosen such that the lift-to-drag ratio is maximum $(C_{l,opt}/C_d)_{max}$. For a given design tip speed ratio λ_{dsgn} the radial distribution of the twist angle $\Theta(r)$ can be determined by applying Eq.(2.32) and Eq.(2.33).

Small scale model wind turbines typically operate in a flow regime in which airfoil aerodynamics, respectively the lift and drag coefficients C_l and C_d , are sensitive to changes in the Reynolds number of the incoming flow. When ignoring blade tip- and root-losses as well as the influence of drag, the radial distribution chord based Reynolds number of a blade designed according to Eq.(2.43) is

$$Re_c = \frac{U_{rel}(r)c(r)}{\nu} = 8\pi \frac{U_\infty R}{\nu} \frac{a_{opt}(1 - a_{opt})}{N_B C_{l,opt} \lambda_{dsgn}}. \quad (2.44)$$

It is interesting to notice that for a uniform radial distribution of the axial flow induction factor a_{opt} the Reynolds number is uniform as well. Moreover, it can be concluded that the chord based Reynolds number Re_c decreases for increasing design tip speed ratio λ_{dsgn} . As will be discussed in more detail in Chapter 4, in the low Reynolds number regime, at which small scale model wind turbines typically operate, lift-to-drag-ratios are significantly lower than for a full scale multi megawatt turbine, and consequently also the maximum achievable power coefficient. Due to this fact and the inverse proportional relation of Re_c and λ_{dsgn} , designing model wind turbines with a realistic energy conversion and which operate at the typical high tip speed ratios of full scale wind turbines is a challenging task.

Because of the significant influence of the Reynolds number on the performance of small scale wind turbines, in this work the radial average of the chord based Reynolds number

$$\overline{Re_c} = \frac{1}{r_2 - r_1} \int_{r_1}^{r_2} Re_c(r) dr \quad (2.45)$$

is used to characterise the operational state of the wind turbine.

2.3 Wake Aerodynamics

The region downwind of the wind turbine is called the wake. In general it can be divided into two regions: (i) the region directly downwind of the turbine, called the near wake, and (ii) the region further downstream, called the far wake.

The near wake is characterised by blade aerodynamics, tip and root vortices, hub and nacelle geometry, and the presence of the tower. As a result the near wake is highly complex, three dimensional, and exhibits a heterogeneous flow distribution. Due to the difference in pressure between the pressure and suction sides of the rotor blade, tip vortices form and are shed from the blade tip and root. They propagate a short distance downstream following helical trajectories before they start to pair and break down eventually. The break down marks the end of the near wake region and is typically within the range of 2-4 rotor diameters downstream of the turbine. The length of the near wake region depends significantly on the operational state of the turbine and the inflow conditions.

The far wake region, in contrast, is less influenced by the wind turbine details. It is mostly determined by global parameters as the wind turbine thrust and the vertical shear and turbulence of the incoming flow. In downstream direction, due to the mixing with the outer flow, the wake recovers by growing in both lateral and vertical direction and the axial velocity increases asymptotically towards the velocity of the surrounding flow. In uniform flow conditions, the profiles of the streamwise velocity in the far wake have an axisymmetric Gaussian distribution. Within boundary layer flows, wake velocity profiles do not exhibit a Gaussian shape, due to the vertical shear of the incoming flow. However, studies have shown that profiles of velocity deficit (i.e. difference between the incoming flow speed and that of the wake) still retain the Gaussian distribution approximately (see e.g. [28]).

One of the key characteristics of flows with Gaussian velocity distributions is their self similar behaviour [112]. This means that for any given downstream distance, profiles of the velocity deficit in the wake, normalised by its maximum value as function of its radial coordinate normalised by the wake width, collapse to a single curve. The assumption of self similarity in the far wake facilitates the development of simple analytical models for predicting the mean velocity and turbulent quantities in the wake. This assumption, however, implies that the flow can be described by an axisymmetric wake which is immersed in a boundary layer flow. Therefore in the following, the theoretical concept for describing the far wake of a wind turbine immersed in a neutrally stratified turbulent boundary layer by a superposition of a wake in uniform (turbulent) flow and a turbulent boundary layer is derived. Thereby, fundamental wake quantities are defined and special emphasis is put on the discussion of the limitations of this approach.

2.3.1 Superposition of Wake and Boundary Layer

As it is the aim to describe the flow as a superposition of a boundary layer flow and a wake, it is helpful to define the spatially dependent quantities in terms of added quanti-

ties

$$\bar{u} = \bar{u}_{bl} - \bar{u}_w \quad (2.46)$$

$$\bar{v} = \bar{v}_{bl} + \bar{v}_w \quad (2.47)$$

$$\bar{w} = \bar{w}_{bl} + \bar{w}_w \quad (2.48)$$

$$\bar{p} = \bar{p}_{bl} + \bar{p}_w \quad (2.49)$$

$$\overline{u'_i u'_j} = \overline{u'_i u'_j}_{bl} + \overline{u'_i u'_j}_w \quad (2.50)$$

where \bar{p} is the time averaged pressure, \bar{u} , \bar{v} and \bar{w} are the velocity components in the axial x , lateral y and wall-normal z direction, p' , u' , v' and w' (in short form u'_i) its fluctuating parts, and $u'_i u'_j$ the components of the Reynolds stress tensor. For the sake of clarity, the superposition of the flow quantities in the wake of a wind turbine is depicted schematically in Figure 2.8. The subscripts bl and w indicate the contributions of the boundary layer and the wake, respectively. An exception is the axial velocity Equation (2.46). It is

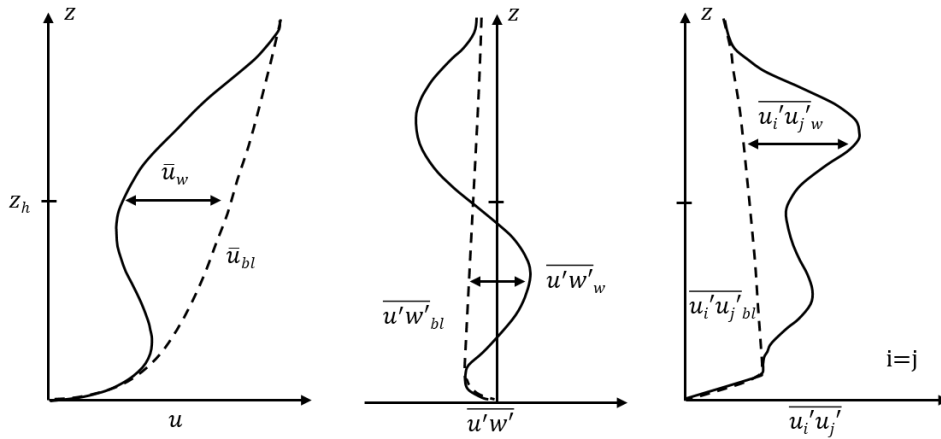


Figure 2.8: Sketch of the two superimposed flow fields.

defined in terms of a deficit variable, as its sign is known a priori. Inserting the Definitions (2.46)–(2.50) in the Reynolds-averaged streamwise momentum equation (2.1) and rearranging it in such a way that just all wake related gradients are on the left hand side, gives

$$\begin{aligned} & (\bar{u}_{bl} - \bar{u}_w) \frac{\partial \bar{u}_w}{\partial x} + (\bar{v}_{bl} + \bar{v}_w) \frac{\partial \bar{u}_w}{\partial y} + (\bar{w}_{bl} + \bar{w}_w) \frac{\partial \bar{u}_w}{\partial z} - \frac{1}{\rho} \frac{\partial \bar{p}_w}{\partial x} \\ & - \left[\frac{\partial \overline{u' u'_w}}{\partial x} + \frac{\partial \overline{v' v'_w}}{\partial y} + \frac{\partial \overline{w' w'_w}}{\partial z} \right] - \nu \left[\frac{\partial^2 \bar{u}_w}{\partial x^2} + \frac{\partial^2 \bar{u}_w}{\partial y^2} + \frac{\partial^2 \bar{u}_w}{\partial z^2} \right] = \\ & (\bar{u}_{bl} - \bar{u}_w) \frac{\partial \bar{u}_{bl}}{\partial x} + (\bar{v}_{bl} + \bar{v}_w) \frac{\partial \bar{u}_{bl}}{\partial y} + (\bar{w}_{bl} + \bar{w}_w) \frac{\partial \bar{u}_{bl}}{\partial z} + \frac{1}{\rho} \frac{\partial \bar{p}_{bl}}{\partial x} \\ & + \left[\frac{\partial \overline{u' u'_{bl}}}{\partial x} + \frac{\partial \overline{v' v'_{bl}}}{\partial y} + \frac{\partial \overline{w' w'_{bl}}}{\partial z} \right] - \nu \left[\frac{\partial^2 \bar{u}_{bl}}{\partial x^2} + \frac{\partial^2 \bar{u}_{bl}}{\partial y^2} + \frac{\partial^2 \bar{u}_{bl}}{\partial z^2} \right], \end{aligned} \quad (2.51)$$

where ρ is the density and ν the kinematic viscosity of the flow. We then apply the classical assumptions used in the derivation of the boundary layer and the axisymmetric wake equation (see [112]). For that, the boundary layer is assumed to be homogeneous in the lateral direction, due to which the lateral velocity $\bar{v}_{bl} = 0$ as well as the lateral gradients of all boundary layer related quantities $\frac{\partial \phi_{bl}}{\partial y} = 0$. Across the wind turbine the static pressure drops due to the extraction of kinetic energy at the rotor and then, in downstream direction, it converges asymptotically towards the atmospheric level. In the far wake the static pressure is assumed to be balanced and therefore the pressure gradient is negligible, $\frac{\partial \bar{p}_w}{\partial x} \approx 0$. As we consider turbulent wakes at high Reynolds number, viscous effects

in the wake are negligible as well, $\nu \frac{\partial^2 \bar{u}}{\partial x^2} \approx 0$. With that Equation (2.51) simplifies to

$$\begin{aligned}
 & \underbrace{(\bar{u}_{bl} - \bar{u}_w) \frac{\partial \bar{u}_w}{\partial x}}_{AWE(I)} + \underbrace{\bar{v}_w \frac{\partial \bar{u}_w}{\partial y}}_{AWE(II)} + \underbrace{\bar{w}_w \frac{\partial \bar{u}_w}{\partial z}}_{AWE(III)} - \underbrace{\left[\frac{\partial \bar{u}'_w}{\partial x} + \frac{\partial \bar{u}'_w}{\partial y} + \frac{\partial \bar{u}'_w}{\partial z} \right]}_{AWE(IV)} \\
 = & \underbrace{\bar{u}_{bl} \frac{\partial \bar{u}_{bl}}{\partial x}}_{BLE(I)} + \underbrace{\bar{w}_{bl} \frac{\partial \bar{u}_{bl}}{\partial z}}_{BLE(II)} + \underbrace{\frac{1}{\rho} \frac{\partial \bar{p}_{bl}}{\partial x}}_{BLE(III)} + \underbrace{\left[\frac{\partial \bar{u}'_{bl}}{\partial x} + \frac{\partial \bar{u}'_{bl}}{\partial z} \right]}_{BLE(IV)} - \underbrace{\nu \left[\frac{\partial^2 \bar{u}_{bl}}{\partial x^2} + \frac{\partial^2 \bar{u}_{bl}}{\partial z^2} \right]}_{BLE(V)} \\
 & \underbrace{- \bar{u}_w \frac{\partial \bar{u}_{bl}}{\partial x}}_{ADD(I)} + \underbrace{\bar{w}_w \frac{\partial \bar{u}_{bl}}{\partial z}}_{ADD(II)} - \underbrace{\bar{w}_{bl} \frac{\partial \bar{u}_w}{\partial z}}_{ADD(III)}. \tag{2.52}
 \end{aligned}$$

Under the assumption that the flow can be described as superposition of a boundary layer and an axisymmetric wake, terms which form the axisymmetric wake equation (AWE) as well as the boundary layer equation (BLE) can be identified. If the superposition of both flows would be an exact description of the problem, the terms of both equations would balance themselves (each equation within itself equals 0).

However, the presence of the additional terms (ADD) can perturb this balance. Nevertheless, the terms ADD(I) and (III) can be considered to have a minor contribution as (i) the axial development of a boundary layer is much slower than of a wake and therefore term ADD(I) can be neglected since $|\partial \bar{u}_{bl} / \partial x| \ll |\partial \bar{u}_w / \partial x|$; (ii) the mean vertical velocity is smaller in the boundary layer than in the wake, $|\bar{w}_{bl}| \ll |\bar{w}_w|$, and hence term ADD(III) must be smaller in magnitude than the term AWE(III) and is for that reason assumed to be negligible as well. The term ADD(II) is, however, of comparable magnitude as AWE(III) and can therefore not be neglected. It especially increases in magnitude with increasing wind shear of the boundary layer.

Furthermore, the additive decomposition of the Reynolds stresses in Equation (2.50) would be physically motivated only in case of different scales dominating in both contributions to the total, invoking the concept of scale-separation. Therefore, the superposition of the velocity fields of both flows can just be an approximation, as long as the ADD terms have no significant contribution to the momentum balance. It has furthermore to be assumed that similar additional terms are present in the transport equations of the Reynolds shear stresses, which affect also the superposition of these. Nevertheless, within the wake, the wake related quantities are typically larger in magnitude and develop faster than the boundary layer related quantities. This justifies the approach of a superposition, except in the very far wake region where the wake quantities become small and vanish in the background turbulence, see e.g., Figure 3.14. To analyse which scales are involved, in Section 5.3 the spectral content in the turbulent boundary layer and in the wake will be assessed.

In the discussion above, within the differential form of the streamwise momentum equation, the axisymmetric wake equation was identified. However, profiles of the velocity deficit $\bar{u}_{bl}(z) - \bar{u}_w$ are not expected to be axisymmetric. According to the actuator disc theory in Section 2.2.1, for the same radial position, the velocity deficit below and above the hub is $a \bar{u}_{bl}(z)$ at the rotor disc, see Eq.(2.15), and $2a \bar{u}_{bl}(z)$ in the wake, see Eq.(2.19), respectively. Since within the boundary layer the axial velocity $\bar{u}_{bl}(z)$ varies with height, the vertical profiles of the velocity deficit cannot be axisymmetric. Moreover, in this situation the local inflow angle ϕ becomes a function of height as well, see Eq.(2.32) and

consequently also the axial induction factor a , see Eq.(2.38). Nevertheless, in the outer blade region, which contributes most to the generation of thrust and torque, the local inflow angle ϕ is small and, hence, the axial induction factor a can be considered to be approximately constant. Given this assumption, vertical profiles of the velocity deficit $\bar{u}_{bl}(z) - \bar{u}$ normalised by the *local* velocity of the boundary layer $\bar{u}_{bl}(z)$ are potentially axisymmetric. Therefore, in this work the normalised velocity deficit is defined as

$$\Delta u(x, y, z) = \frac{\bar{u}_w(x, y, z)}{\bar{u}_{bl}(z)} = \frac{\bar{u}_{bl}(z) - \bar{u}(x, y, z)}{\bar{u}_{bl}(z)}. \quad (2.53)$$

Throughout this work, if not stated differently, the term velocity deficit refers to this definition.

In the following the streamwise momentum deficit flow rate in the wake is derived. To make use of the velocity deficit Eq.(8.14), Eq.(2.52) is normalised by $\bar{u}_{bl}^2(z)$ and written in conservative form. The latter can be obtained by multiplying the continuity equation $\partial \bar{u}_k / \partial x_k = 0$ with \bar{u}_w , adding it to the left hand side of Equation (2.52) and integrating it with respect to y from $-\infty$ to ∞ and with respect to z from 0 to ∞ . Under the assumption that all terms of the boundary layer equation (BLE) balance themselves, they equate to zero. Furthermore, on the left hand side, all terms which are gradients in (lateral) y -direction disappear by the integration as their primitives are 0 at the integration boundaries (e.g., $\int_{-\infty}^{\infty} (\bar{u}_{bl}^{-2} \partial u' v' / \partial y) dy = [\bar{u}_{bl}^{-2} u' v']_{y=-\infty}^{y=\infty} = 0$). Due to the mean wind shear $\partial \bar{u}_{bl} / \partial z$ of the boundary layer, terms containing gradients in (wall-normal) z -direction do not disappear by the integration. Given that, we obtain

$$\begin{aligned} \frac{d}{dx} \Theta_x^2 &= \frac{d}{dx} \int_{-\infty}^{\infty} \int_0^{\infty} \frac{\bar{u}_w (\bar{u}_{bl} - \bar{u}_w)}{\bar{u}_{bl}^2} dz dy = \frac{d}{dx} \int_{-\infty}^{\infty} \int_0^{\infty} \Delta u (1 - \Delta u) dz dy = \\ &= \frac{d}{dx} \int_{-\infty}^{\infty} \int_0^{\infty} \frac{u' u' w}{\bar{u}_{bl}^2} dz dy + \int_{-\infty}^{\infty} \int_0^{\infty} \frac{1}{\bar{u}_{bl}^2} \left[\frac{\partial u' w' w}{\partial z} - \frac{\partial \bar{u}_w \bar{w}_w}{\partial z} + \bar{w}_w \frac{\partial \bar{u}_{bl}}{\partial z} \right] dz dy. \end{aligned} \quad (2.54)$$

The first line of this equation is similar to the change rate of the momentum thickness Θ , only formulated in a two-dimensional manner for Θ^2 . However, it also represents the streamwise momentum deficit flow rate in a normalised form. For wakes within uniform flows, it is typically assumed to be approximately zero (conservation of the streamwise momentum deficit) in the far wake as the axial component of the Reynolds stress tensor $\overline{u' u' w}$ develops slowly in downstream direction. However, within high ambient turbulence the wake develops faster and just as well does the axial component of the Reynolds stress tensor which therefore might not longer be negligible. Furthermore, in the situation of a wake immersed in a boundary layer, the terms within the last integral do not integrate to zero, and with increasing shear they might not be negligible as well. Hence, in these situations it would be possible that either the streamwise momentum deficit is not conserved or the wake becomes asymmetric with respect to its normalised form. Nevertheless, for moderate wind shear the normalised velocity deficit in the far wake can be assumed to be axisymmetric. Given that, it can be approximated by a two dimensional Gaussian distribution

$$\Delta u(x, y, z) = \Delta u_C(x) e^{-0.5 \eta_y^2} e^{-0.5 \eta_z^2} \quad (2.55)$$

with $\eta_y = (y - y_C) / \sigma_y$, $\eta_z = (z - z_h - z_C) / \sigma_z$ being the non-dimensional lateral and vertical coordinates, y_C and z_C being the centreline position at which the velocity deficit Δu_C is found, z_h being the rotor hub height, and σ_y and σ_z being the wake width in the lateral and vertical direction. The lateral wake width σ_y and the wake center position y_C can be derived from the flow field by numerical integration of the velocity deficit and

momentum deficit respectively

$$\sigma_y = \frac{1}{\sqrt{2\pi} \max(\Delta u)} \int_{-\infty}^{\infty} \Delta u \, dy, \quad y_C = \frac{\int_{-\infty}^{\infty} \Delta u^2 y \, dy}{\int_{-\infty}^{\infty} \Delta u^2 \, dy}. \quad (2.56)$$

Their counterparts in vertical direction σ_z and z_C can be calculated analogously.

Assuming that the normalised velocity deficit is small in the far wake and neglecting the presence of the ground, Equation (2.55) can be applied to estimate the momentum thickness, i.e. the normalised streamwise momentum deficit, from Equation (2.54) as

$$\Theta_x^2 = \int_{-\infty}^{\infty} \int_{-\infty}^{\infty} \Delta u (1 - \Delta u) \, dz \, dy = \pi \Delta u_C \sigma_y \sigma_z (2 - \Delta u_C) \approx 2\pi \Delta u_C \sigma_y \sigma_z. \quad (2.57)$$

The analysis of the momentum budget in lateral direction can be carried out in a similar way. For the Reynolds-averaged lateral momentum equation in spanwise direction

$$\bar{u} \frac{\partial \bar{v}}{\partial x} + \bar{v} \frac{\partial \bar{v}}{\partial y} + \bar{w} \frac{\partial \bar{v}}{\partial z} = -\frac{1}{\rho} \frac{\partial \bar{p}}{\partial y} - \left[\frac{\partial \overline{u'v'}}{\partial x} + \frac{\partial \overline{v'v'}}{\partial y} + \frac{\partial \overline{v'w'}}{\partial z} \right] + \nu \left[\frac{\partial^2 \bar{v}}{\partial x^2} + \frac{\partial^2 \bar{v}}{\partial y^2} + \frac{\partial^2 \bar{v}}{\partial z^2} \right] \quad (2.58)$$

viscous effects in the wake at high Reynolds number can be neglected $\nu \frac{\partial^2 \bar{v}}{\partial x_i^2} \approx 0$. Equation (2.58) is then brought in conservative form by adding $\bar{v} \partial \bar{u}_k / \partial x = 0$ to the left hand side. It is then normalised by $\bar{u}_{bl}^2(z)$ and integrated with respect to y from $-\infty$ to ∞ and with respect to z from 0 to ∞ . Similar to the integration of the axial momentum equation, all terms which are gradients in (lateral) y -direction disappear by the integration as their primitives are 0 at the integrations boundaries. Given that, we obtain the change rate of the lateral momentum

$$\frac{d}{dx} \Theta_y^2 = \frac{d}{dx} \int_{-\infty}^{\infty} \int_0^{\infty} \frac{\bar{u} \bar{v}}{\bar{u}_{bl}^2} = - \int_{-\infty}^{\infty} \int_0^{\infty} \frac{1}{\bar{u}_{bl}^2} \left[\frac{\partial \overline{u'v'}}{\partial x} + \frac{\partial \overline{v'w'}}{\partial z} + \frac{\partial \overline{vw}}{\partial z} \right] \, dz \, dy \quad (2.59)$$

For axis and skew symmetric wakes in uniform flows the right hand side equates to zero (conservation of lateral momentum). Within highly sheared boundary layers or yawing the wake can become asymmetric and the terms on the right hand side do not necessarily cancel out.

The main point of the discussion above is that the superposition of an undisturbed boundary layer and an axisymmetric wake is not arbitrary, as this combination allows for reasonable assumptions due to which the momentum thickness Equation (2.57) can be derived in a similar form as for the axisymmetric wake embedded in a uniform flow. However, even though the superposition is theoretically possible, one should keep in mind that this concept can only be valid as long as the perturbation due to the boundary layer is small.

2.3.2 Turbulent Kinetic Energy Budget

Turbulence produced by and around the wind turbine is transported downstream to the far wake region where it interacts with the surrounding boundary layer flow. Analysis of the relevant mechanisms can be given by the transport equation of the turbulent kinetic energy equation (also called TKE budget), which for a neutrally stratified, high Reynolds

number flow (buoyancy effects and viscous diffusion are neglected) can be written as

$$\underbrace{\frac{\partial K}{\partial t}}_{\text{Storage} \approx 0} = \underbrace{-\bar{u}_j \frac{\partial K}{\partial x_j}}_{\text{Advection}} - \underbrace{\frac{1}{\rho} \overline{u'_i p'}}_{\text{Pressure diffusion}} - \underbrace{\overline{u'_i u'_j} \frac{\partial \bar{u}_i}{\partial x_j}}_{\text{Shear production}} - \underbrace{\frac{\partial \overline{u'_j K}}{\partial x_j}}_{\text{Turbulent transport}} - \underbrace{\epsilon}_{\text{Dissipation}}, \quad (2.60)$$

where $K = \frac{1}{2} \overline{u'_i u'_i}$ is the turbulent kinetic energy. Due to the quasi-steady flow conditions the local storage term in Eq.(2.60) is typically assumed to be zero.

In the work of Wu & Porté-Agel [157] it is shown that, pressure diffusion and dissipation only contribute noticeable to the TKE budget in the very proximity of the rotor, and can therefore be neglected in the discussion about mechanisms that distribute turbulence in the wake.

Moreover, they showed that most of the TKE is generated at the edge of the turbine wake where a shear layer separates the wake from the surrounding flow, and which generates strong radial fluxes of momentum. Therefore, the terms $\overline{u' w'} \frac{\partial \bar{u}}{\partial z}$ and $\overline{u' v'} \frac{\partial \bar{u}}{\partial y}$ are the main contributor of shear production at the vertical and lateral rotor edges, respectively. The radial fluxes in the shear layer distribute the produced TKE radially inwards and outwards of the wake, thus contributing to the expansion of the wake. The dominant terms of this mechanism are found to be $\frac{\partial \overline{w' K}}{\partial z}$ and $\frac{\partial \overline{v' K}}{\partial y}$ at the vertical and lateral rotor edges, respectively. Additionally, the TKE generated in the wake is advected by the mean wind. In the wake the axial velocity component is much larger than the vertical or lateral component (even in the near wake), hence, the term $\bar{u} \frac{\partial K}{\partial x}$ dominates the advection of TKE.

Wind Tunnel Modelling of Atmospheric Boundary Layers

In this chapter the generation of atmospheric boundary layers modelled in the wind tunnel for the application in wind turbine wake measurements (Chapter 5) is presented. Therefore, first the modelling principle is introduced and key characteristics of the applied wind tunnel and instrumentation are given (Sec. 3.1). Since two turbulent boundary layers have to be established which meet a specified aerodynamic roughness length systematic testing of various configurations is necessary. Criteria for configuring the wind tunnel accordingly are explained and an overview on the tested configurations is given (Sec. 3.2). Furthermore, relations used to evaluate the resulting boundary layer characteristics are introduced (Sec. 3.3). Subsequently, measured profiles of the mean axial velocity and the Reynolds stresses are presented for different axial locations and are analysed regarding their equilibrium state. Finally, two configurations of significantly different aerodynamic roughness length are selected for the wind turbine wake measurements and are compared regarding their characteristic key parameters, integral length scale and spectral content (Sec. 3.4).

3.1 Wind Tunnel & Instrumentation

Experiments are performed within the closed-loop boundary layer wind tunnel at the chair of aerodynamics at the Technical University of Munich, which has a 2.7 m wide, 1.8 m high and 21 m long test section, see Figure 3.1 for a sketch of the wind tunnel. Flow uniformity at the nozzle outlet is achieved by means of a honeycomb, four sets of screens and a section with a contraction ratio of 2.12:1. At the nozzle the free stream turbulence level is 0.3%. The turbulent boundary layers are simulated using Counihan’s technique [32], where different arrangements of castellated barrier, vertical fins and distributed roughness on the wind tunnel floor result in a family of mean flow profiles. Thereby the castellated barrier produces vortex structures with axis aligned horizontally in the lower region of the boundary layer, whereas the vertical fins precondition the mean velocity profile due to their blockage. This principle is depicted in Figure 3.2. The vortex generators are then followed by a development fetch covered with homogeneously distributed roughness elements. After 6-8 boundary layer heights the boundary layer eventually reaches an equilibrium state at which mean velocity profile $U(z) \sim (z/z_0)^\alpha$ can be characterized by certain values of the shear exponent α and roughness length z_0 . Throughout this work, z denotes the wall-normal, x the axial and y the lateral coordinate. The boundary layer thickness is considered to be approximately equal to the height of the vortex generators $\delta \approx H = 1.5$ m.

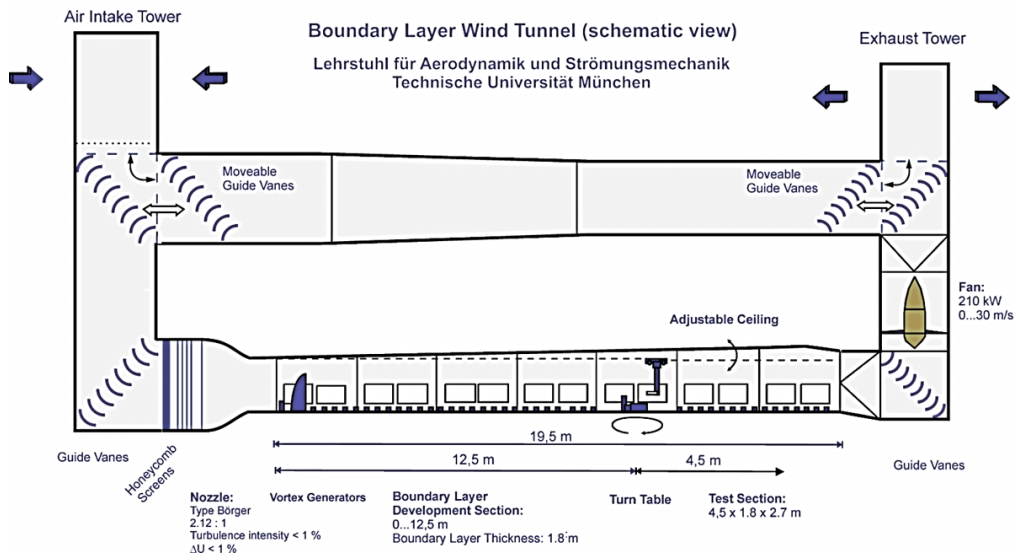


Figure 3.1: Sketch of the boundary layer wind tunnel.

Instantaneous velocities are measured using a triple hot-wire probe which is made of $5 \mu\text{m}$ gold-coated tungsten wires of 3 mm length. The probe is connected to a ten-channel AALAB AN 1003 anemometer system. Each channel consists of a Wheatstone bridge, an amplifier and a low-pass filter with a 1 kHz cut-off frequency. Velocity signals are sampled at 3 kHz using a 12-bit digitizer Data Translation DT2821. Simultaneously the barometric pressure p_{ref} and the temperature within the wind tunnel T_{ref} are recorded as well. With an assumed relative humidity of 50% the current density of the air is then derived from these quantities. The hot-wire probe is calibrated within a calibration tunnel by exposing the probe for $T = 2$ s to a low-turbulence uniform flow at a total of 252

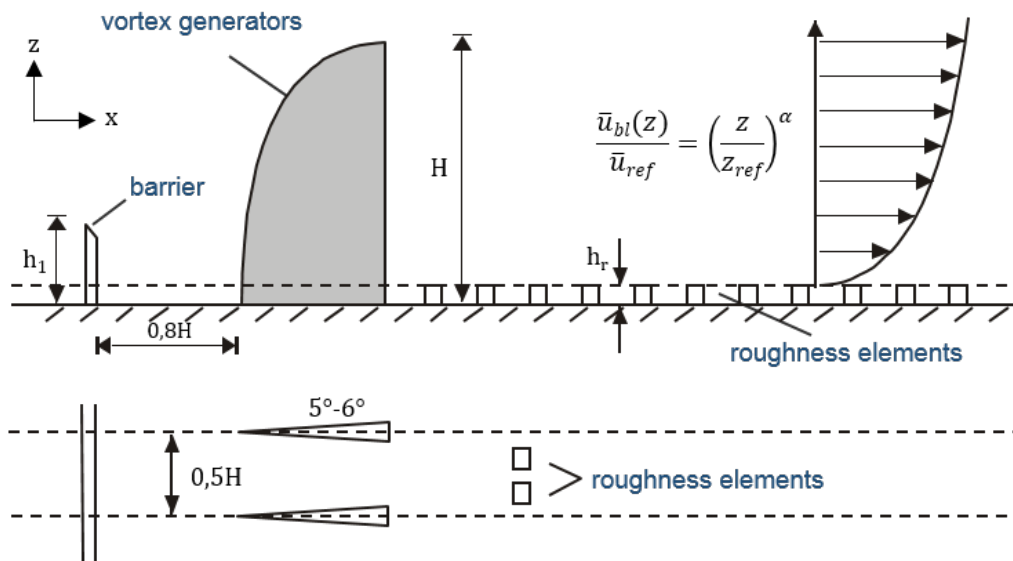


Figure 3.2: Sketch of the boundary layer generation devices.

different orientations, consisting of 7 different yaw angles and 36 angles in circumferential direction. This procedure is repeated for 20 different velocities, ranging from 2.5 - 21 m/s. With this configuration a relative error of the velocity measurement of $\epsilon_u < 3\%$ is obtained, see [21]. The hot-wire probe is then mounted on the 3-axis traversal system of the wind tunnel. To avoid any influence of the measured velocities by blockage effects of the traversal system a 80 cm long boom, made of a carbon fibre tube and brass parts, is used on which end the hot-wire probe is installed, see Figure 3.3. Furthermore, on the bottom of the vertical axis an hydraulic stamp is used to stabilise the traversal system and minimise vibrations during recording.

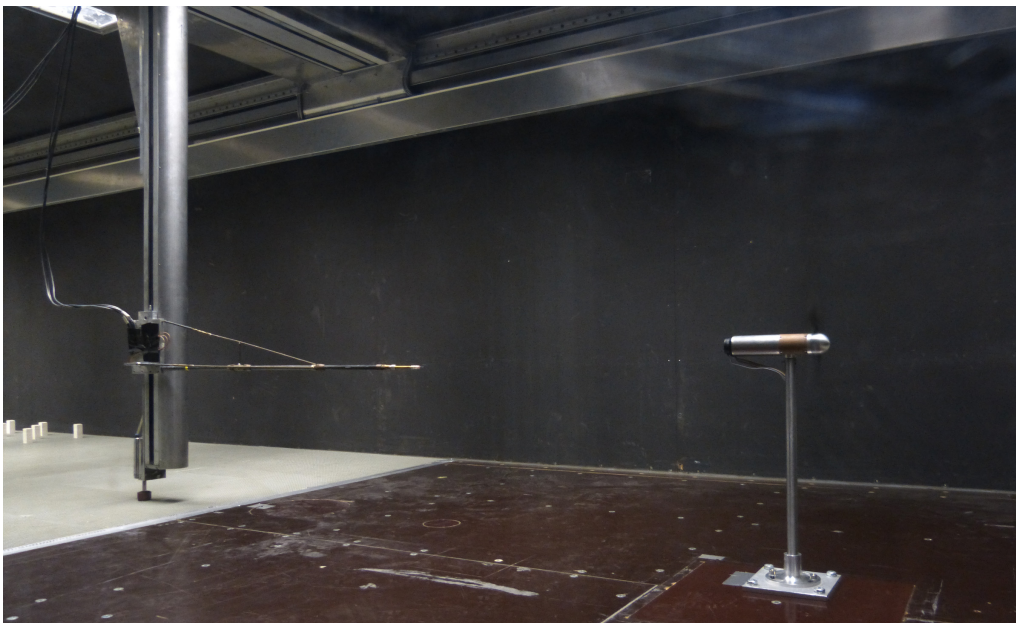


Figure 3.3: Model wind turbine and traversal system located close to the wind tunnel nozzle for measurements in low-turbulence uniform approaching flow (LTU).

To orient the hot-wire probe correctly regarding the wind tunnel coordinate system, first the probe is installed using a positioning device such that a reference point on the probe is directed in the vertical direction. With the probe located in the middle of the wind tunnel cross section close to nozzle where the flow is assumed to be aligned to the axial axis, subsequently the orientation of the boom is adjusted in a try and error procedure such that the mean velocity in the lateral and vertical direction is $< 1\%$ of the axial component. In this work, the reproducibility of the results was tested for by re-measuring certain configurations throughout various measurement campaigns. The results exhibited only minor differences which mainly are attributed to uncertainties in the calibration and alignment procedure. Due to the manual work involved in these procedures an overall error is difficult to estimate. Furthermore, at the end of each measurement campaign the orientation of the probe was tested for by measuring the flow velocity at the same position as during the alignment procedure. Regarding the initial alignment the results of this test typically exhibited small deviations in the lateral and vertical velocities. These are thought to result from thermal expansion and compression of the brass parts due to temperature variations in the wind tunnel.

3.2 Tested Boundary Layer Configurations

As it is the aim of this study to investigate the role of the terrain roughness on the wake development behind a wind turbine, two turbulent boundary layers have to be modelled which differ in their aerodynamic roughness length. The first, in the following named *smooth boundary layer* (SBL), shall represent rural terrain, which in full-scale has a roughness length of about $z_{0,f} \approx 0.1 - 0.2$ m. As the effect of the terrain roughness on the wake development can be subtle, the second boundary layer, in the following named *rough boundary layer* (RBL), is required to have a significantly higher roughness length. Therefore, it shall be designed to have a full-scale roughness length of $z_{0,f} \approx 1 - 2$ m, corresponding to forestal or urban terrain. For an overview on the different terrain categories see section 2.1.

According to Counihan [32] the boundary layer height δ in the wind tunnel is approximately equal to the height of the vortex generators $H = 1.5$ m. With a typical boundary layer height of $\delta_N \approx 500$ m over onshore terrain and this assumption an approximate scale of $S = \delta/\delta_N \approx 1 : \mathcal{O}(350)$ results. Given this scale the targeted roughness lengths of the SBL and RBL are $z_0 \approx 0.3 - 0.6$ m and $z_0 \approx 3 - 6$ mm, respectively. In the discussion of results measurements of the integral turbulent length scale do confirm the assumed scale, see section 3.4.

In Literature a variety of empirical formulas can be found which give a relation between the distribution of the roughness elements and the roughness length. A simple approximation for z_0 can be written as

$$\frac{z_0}{h_r} = C\lambda_f \quad (3.1)$$

where λ_f is the ratio between the frontal area of all roughness elements and the plan area of the wind tunnel floor, and h_r is the height of the roughness elements. As we are just considering uniformly staggered distribution it is possible to define $\lambda_f = A_f/A_t$ as the ratio between the frontal area A_f of one roughness element and the unit plan area of the wind tunnel floor A_t related to this element as it is depicted in Figure 3.4. For values

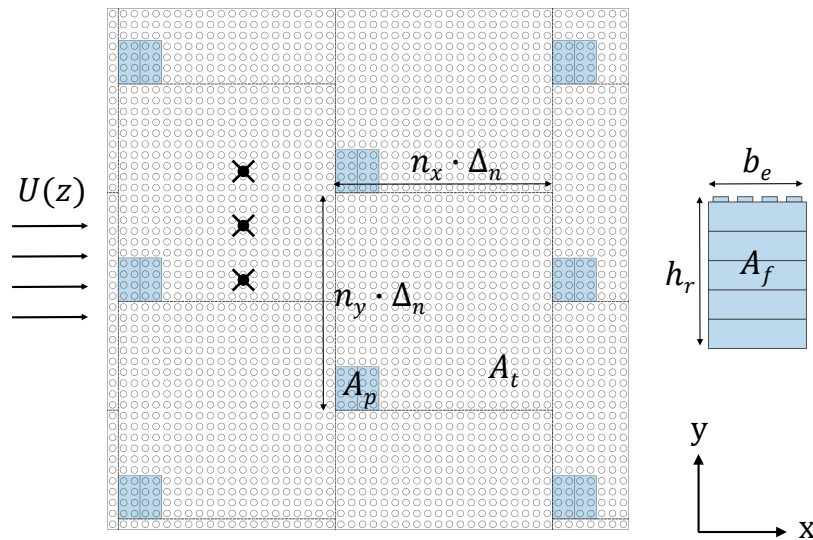


Figure 3.4: Sketch of the distribution of roughness elements. Crosses illustrate the measurement positions along vertical lines above the roughness elements.

$\lambda_f < 0.25$ Lettau [89] reports the constant C in eq. (3.1) to be $C = 0.5$, whereas Fang [43] reports it to be $C = 1.0$. As multiple studies confirm the finding of Lettau and Fang (see e.g. [111], [68], [94]) this relation is used to determine the distribution of the roughness elements.

However, for a specific z_0 eq.(3.1) just requires $h_r \lambda_f$ to be a constant value and hence allows various configurations with different height and density of the roughness elements. Therefore, for the *smooth boundary layer* multiple configurations are tested, which (theoretically) result in the same roughness length z_0 . As starting point the boundary layer configuration established by Kozmar [80] (Scale 1:333, barrier 12, roughness R16) is used as it exhibits the required roughness length. For the rough boundary layer it was found that distributions below a certain height are technically not feasible as the gap between the elements would be insufficient for the traversal system to move in between. On the other hand tall elements could penetrate into the wake region. Therefore, for the rough boundary layer only one distribution of roughness elements is defined with the densest layout possible for the given height of the elements. All distributions are also tested with different barrier heights h_1 with an increment of 20 mm.

All tested configurations are listed in Table 3.1.

Table 3.1: Configuration of roughness elements.

Name	h_r [mm]	n_x	n_y	A_t [mm ²]	A_f [mm ²]	λ_f	λ_p	h_1 [mm]
SBL 1b	9.5	8	8	$3.99 \cdot 10^3$	$3.02 \cdot 10^2$	0.0756	0.2532	145-225
SBL 3b	28.5	25	25	$3.90 \cdot 10^4$	$9.06 \cdot 10^2$	0.0232	0.0259	165-225
SBL 5b	47.5	42	42	$1.10 \cdot 10^5$	$1.51 \cdot 10^3$	0.0137	0.0092	165-225
SBL 7b	66.5	58	58	$2.10 \cdot 10^5$	$2.11 \cdot 10^3$	0.0101	0.0048	165-225
RBL	66.5	18	13	$1.46 \cdot 10^4$	$2.11 \cdot 10^3$	0.1448	0.0692	185-225
Kozmar	47.5	-	-	-	$1.51 \cdot 10^3$	0.0137	0.0092	205

To analyse the axial development of the different configuration hot wire measurements are performed -1800 mm upstream of the turntable center, at the turntable center as well as 1800 mm and 3600 mm downstream of it. This corresponds to the axial positions relative to the model wind turbine (see Chapter 4) $x = -4D, 0D, 4D$ and $8D$, expressed in rotor diameters D . In case of the RBL configuration hot wire measurements are performed at the axial positions $x = 0D, 4D$ and $8D$. In order to minimize the effect of local flow inhomogeneities on the measurement results, hot wire measurements are performed at three lateral positions for each axial location. These three positions are always chosen in such a way that one of them is in front of a roughness element, one behind a roughness element and one in between them, as it is depicted in Figure 3.4.

For each measurement point hot wire signals are sampled at 3 kHz with a record length of 30 s in case of the SBL configurations and 120 s in case of the RBL configurations.

To assure Reynolds number independence of main flow statistics the mean axial velocity at hub height is set to $\bar{u}_\infty(z_h) = 10.8$ m/s. With that the roughness Reynolds number $Re_\tau = u_\tau z_0 / \nu$, where ν is the kinematic viscosity, is $Re_\tau = 19$ and 190 in the smooth and rough boundary layer respectively, which falls well above the lower limit of 1 suggested by Heist & Castro [60], as well as the theoretical limit of 2.8 for the fully rough regime, as derived in Section 2.1.1.

3.3 Evaluation of the Boundary Layer Characteristics

As explained in Section 2.1, the velocity profile within a thermally neutral turbulent boundary layer is typically characterised by two different laws. The lower 25% of the boundary layer can be described by the logarithmic law and the region above by the power law. The determination of their characteristic parameters from hot-wire measurements is discussed in the following.

3.3.1 Log Law

To evaluate the characteristic parameters of a turbulent boundary layer based on the logarithmic law eq.(2.12), introduced in Section 2.1, the roughness length z_0 , the shear stress velocity u_τ and the displacement height d have to be determined. For this purpose different procedures can be found in Literature. Iyengar *et al.* [66] compared parameters determined from balance measured shear velocities, shear velocities computed from X-wire Reynolds stress measurements and indirect procedures where accepted forms of turbulent boundary layer mean velocity profiles are fitted to the measured mean-velocity profiles. They showed, that shear velocities computed by indirect fitting procedures as well as those computed from Reynolds stress measurements can be off by more than 15% from direct balance measurements, leading to large errors in roughness length values. Bottema [20] studied the accuracy of indirect fitting procedures by prescribing and varying one of the parameters u_τ , z_0 and d as well as by using measurement data from different height ranges. He showed that a wide range of u_τ , z_0 and d with nearly optimum curve fits exists. Furthermore, the study shows that z_0 is most sensitive to errors in the prescribed third parameter (d or u_τ) and that the displacement height d is particularly sensitive to inclusion of too low measuring levels. In that case the apparent d can be lower than the ground level.

In order to minimize the sensitivity of the curve fit, the displacement height d is prescribed by the empirical formula derived by MacDonald [94]

$$\frac{d}{h_r} = 1 + A^{-\lambda_p}(\lambda_p - 1) \quad (3.2)$$

with $A = 4.43$ for staggered arrays. Furthermore, the recommendation of Bottema [20] is applied and just measurement data in the range $z_{min} < z < z_{max}$ with $z_{min} = 2h_r$ and $z_{max} = 0.25H$ is used for the the determination of the roughness length z_0 and the shear stress velocity u_τ . For the presented measurements Fleck [44] studied the sensitivity of different fitting methods using the recommendations given above. It was found that the obtained results are just slightly dependent on the particular method. Amongst the tested methods is the build-in least square fitting routine of Matlab, which is used to obtain the results presented bellow.

3.3.2 Power Law

The determination of the characteristic parameters of a turbulent boundary layer based on the power law eq.(2.14), introduced in Section 2.1, is less afflicted with uncertainties, as only the power law exponent α has to be determined. As mentioned in Section 2.1, in Meteorology the power law is typically assumed to be valid down to a height of about 50 m. Hence, with the assumed boundary layer height of $\delta \approx 1.5$ m, only measurement

data with a minimum height of $z_{min} = 150$ mm is used for the power law curve fit. As for some boundary layer configurations an influence of the wind tunnel ceiling is noticeable for measurement points with a height of $z \geq 1350$ mm, these points are excluded from the curve fit. In the following discussion of results, Section 3.4, the assumed scale is confirmed by comparing the turbulent length scale measured in the wind tunnel and a semi-analytical expression found in literature which is derived from field measurements.

3.4 Results

In this section the process to determine the boundary layer configurations used for the measurements in conjunction with the model wind turbine is described. Hot-wire measurements of all preliminary *smooth boundary layer* configurations were carried out by Fleck in the course of his term paper [44]. His work is greatly appreciated by the author.

To reduce the number of parameters which can be varied, as a first step the validity of eq. (3.1) is tested. Therefore, Figure 3.5 shows profiles of the mean axial velocity, the Reynolds shear stress and all normal Reynolds stresses measured within all SBL configurations with the same barrier height of $h_1 = 185$ mm. As can be seen there are just small variations amongst all configurations, which confirms the validity of the empirical formula (3.1).

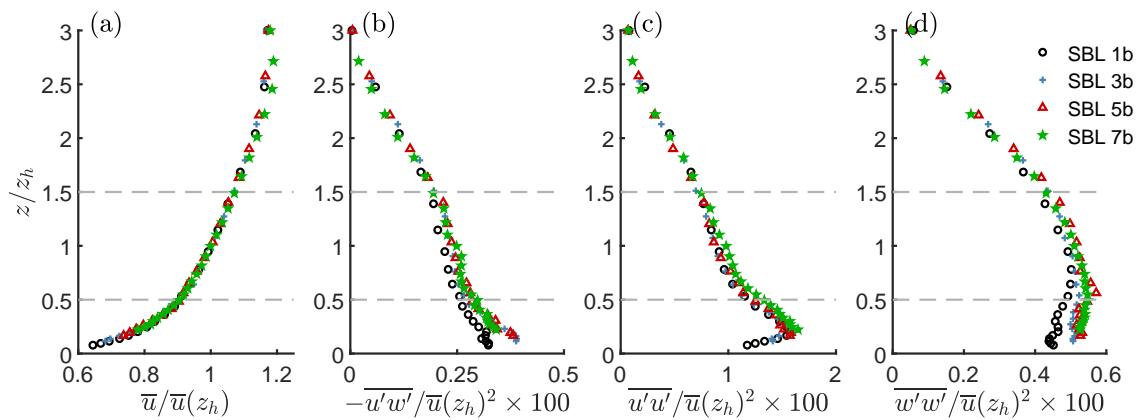


Figure 3.5: Boundary Layer quantities for varying roughness density with $h_r \lambda_f = const.$ and $h_1 = 185$ mm, measured at the turntable center. (a) mean axial velocity, (b) vertical shear stress, normal Reynolds stresses (c) $\overline{u'u'}$, and (d) $\overline{w'w'}$; all normalised by the axial mean velocity at hub height $\overline{u}_\infty(z_h)$

This in turn gives the opportunity to select an appropriate configuration based on other aspects than the flow quantities. Tall roughness elements with a sparse distribution can be disadvantageous, as their local influence can reach the lower region of the wind turbine wake, making the results dependent on the relative position of the wind turbine and the roughness elements. Small elements with a dense distribution on the other side complicate the movement of the traversal system as it needs sufficient space for the vertical support to move in between the arrays of roughness elements, see Figure 3.3. Therefore, it is decided to select the configuration SBL 5b as it is a reasonable compromise between flow homogeneity and sufficient space for the traversal system.

With that, only the height of the castellated barrier can still be varied. Its influence on the mean axial velocity is subtle. However, in a developed boundary layer without pressure gradient the mean axial velocity is mainly determined by the vertical shear stress in axial direction. Indeed, the Reynolds stresses in general are more sensitive as the mean axial velocity to streamwise variations in a developing boundary layer. Therefore, to discuss the influence of the height of the castellated barrier profiles of the vertical shear stress $\overline{u'w'}$ and the normal stress in axial direction $\overline{u'u'}$ are shown for various axial locations and for barrier heights ranging from 165 mm to 225 mm with an increment of 20 mm in Figure 3.6 and Figure 3.7, respectively. Additionally, the measurement data of Kozmar [80]

are shown for comparison. In his work, measurements of the presented boundary layer configuration were carried out only at the center of the turn table which corresponds to the axial position $X = 0D$. The quite similar boundary layer configuration used in the measurements presented here, SBL 5b with a barrier height of $h_1 = 205$ mm, results in a very similar distributions of the vertical shear stress $\overline{u'w'}$ and the normal stress in axial direction $\overline{u'u'}$ at the very same axial location.

It can be clearly seen, that in the region where the wind turbine rotor will be located, i.e. $0.5 \leq z/z_h \leq 1.5$ with increasing barrier height a significant perturbation is visible which regresses in downstream direction. For barrier heights of 165 mm and 185 mm the boundary layer seems to have reached an equilibrium state at the location of the turntable center as the shear stress does only change slightly in downstream direction. This is clearly not the case for barriers taller than that. The same effect can be observed in the development of the normal Reynolds stress $\overline{u'u'}$ in Figure 3.7.

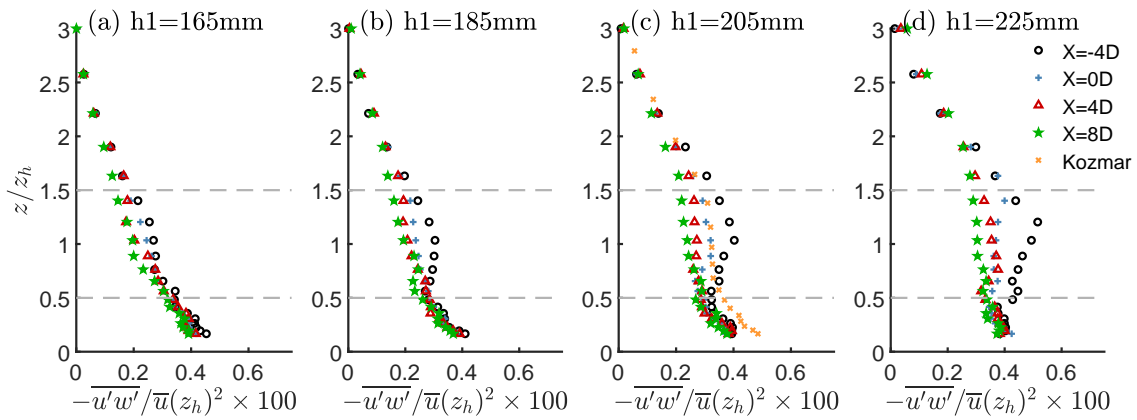


Figure 3.6: Normalised Reynolds shear stress $\overline{u'w'}(z)/\overline{u}_\infty^2(z_h)$ measured at different streamwise locations in the SBL 5b configuration for barrier heights (a) $h_1 = 165$ mm, (b) $h_1 = 185$ mm, (c) $h_1 = 205$ mm, and (d) $h_1 = 225$ mm. Legend denotes the streamwise locations relative to the turntable center.

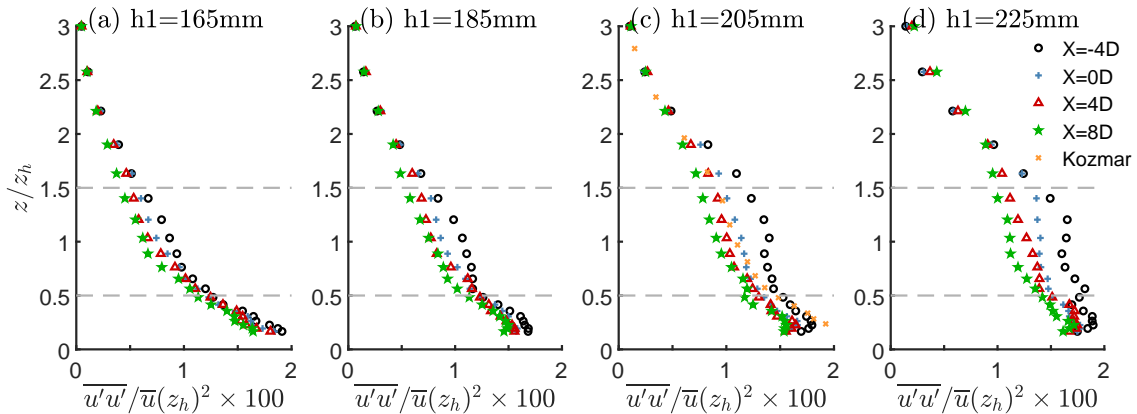


Figure 3.7: Normalised Reynolds stress $\overline{u'u'}(z)/\overline{u}_\infty^2(z_h)$ measured at different streamwise locations in the SBL 5b configuration for barrier heights (a) $h_1 = 165$ mm, (b) $h_1 = 185$ mm, (c) $h_1 = 205$ mm, and (d) $h_1 = 225$ mm. Legend denotes the streamwise locations relative to the turntable center.

A similar trend can also be observed in the semi-logarithmic representation of the non-dimensional velocity \bar{u}/u_τ over the height z/H , see Figure 3.8. As in this representation the virtual intersection of the profile with the x-axis equal the roughness length z_0/H , any deviation between the profiles indicates the development of the roughness length in downstream direction. As it can be seen, with increasing barrier height the offset between

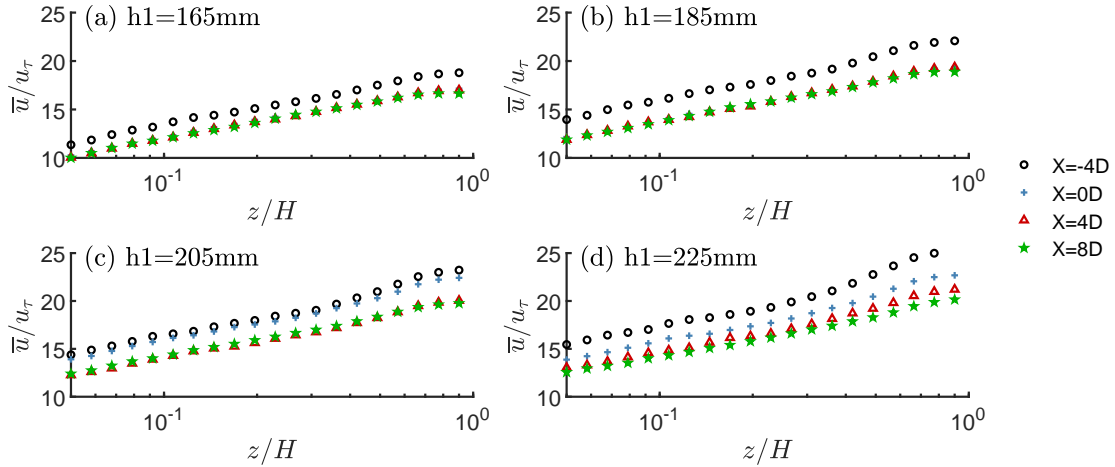


Figure 3.8: Normalised axial mean velocity $\bar{u}_\infty(z)/u_\tau$ in semi-logarithmic representation measured at different streamwise locations in the SBL 5b configuration for barrier heights (a) $h_1 = 165$ mm, (b) $h_1 = 185$ mm, (c) $h_1 = 205$ mm, and (d) $h_1 = 225$ mm. Legend denotes locations relative to the turntable center.

the profile at $x = -4D$ and $x = 8D$ increases, whereas the profiles between $x = 0D$ and $x = 8D$ just differ slightly for barrier heights of $h_1 = 165$ mm and 185 mm. Furthermore, for these barrier heights the profiles do better match the logarithmic law as the profiles, in this representation, do follow a linear distribution up to higher heights than in the cases with taller barriers.

Therefore it can be concluded that both barriers with $h_1 = 165$ mm and 185 mm are an appropriate choice for the generation of boundary layers which shall reach an approximately equilibrium state before the test section. For the measurements with the model wind turbine immersed in the boundary layer it is hence decided to apply the SBL 5b configuration in conjunction with a barrier of height $h_1 = 185$ mm. For the sake of simplicity, this configuration is named the *smooth boundary layer* (SBL) in the following.

Due to the experience with the SBL configuration, the RBL configuration is designed using the same height of the roughness elements and distributing them with the highest possible density which still allows for a collision-free movement of the traversal system. For this configuration then also different barrier heights are tested. As it can be seen in the streamwise development of the vertical shear stress, shown in Figure 3.9, and the axial stress, shown in Figure 3.10, other than the SBL configuration the RBL configuration is less sensible regarding the barrier height. This is mainly due to the higher level of turbulence in case of the RBL configuration, which enhances the momentum transfer in the vertical direction and diminishes the perturbation introduced by the barrier within a shorter distance.

As it was shown above for the SBL configuration, Figure 3.11 shows the semi-logarithmic representation of the non-dimensional velocity \bar{u}/u_τ over the height z/H for all measured axial positions for the RBL configuration using different barrier heights. Other than in the

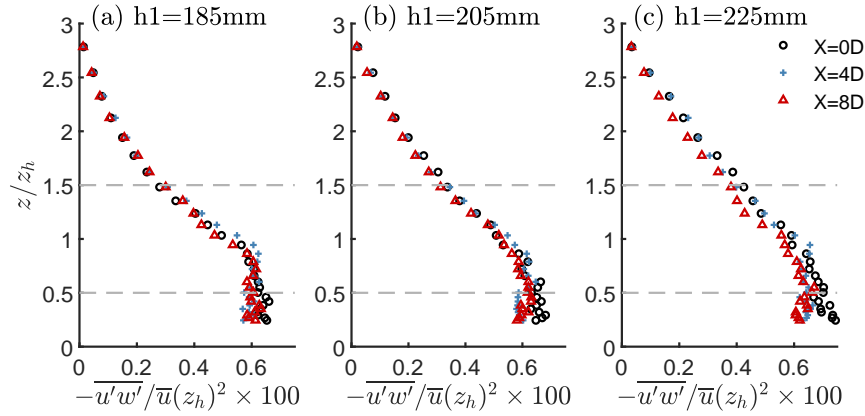


Figure 3.9: Normalised Reynolds shear stress $\overline{u'w'}(z)/\overline{u}_\infty^2(z_h)$ measured at different streamwise locations in the RBL configuration for barrier heights (a) $h_1 = 185$ mm, (b) $h_1 = 205$ mm, and (c) $h_1 = 225$ mm. *Legend* denotes streamwise locations relative to the turntable center.

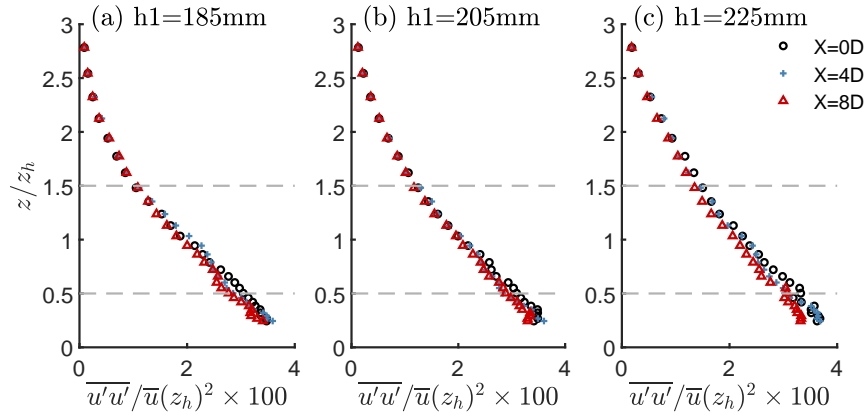


Figure 3.10: Normalised Reynolds stress $\overline{u'u'}(z)/\overline{u}_\infty^2(z_h)$ measured at different streamwise locations in the RBL configuration for barrier heights (a) $h_1 = 185$ mm, (b) $h_1 = 205$ mm, and (c) $h_1 = 225$ mm. *Legend* denotes streamwise locations relative to the turntable center.

SBL cases, independent of the tested barrier, all profiles measured at different axial positions collapse onto a single curve. This again can be argued with the enhanced momentum transfer in the RBL case which causes the boundary layer to reach an equilibrium state within a shorter distance. As there are just insignificant differences between the measurements with different barriers, a barrier height of $h_1 = 205$ mm is chosen for the measurements with the model wind turbine. For the sake of simplicity this configuration is named the *rough boundary layer* (RBL) in the following.

Despite the uncertainties in the determination of the boundary layer parameters u_τ , z_0 and d by a simple curve fitting routine, as it was mentioned before, it is interesting to compare the obtained values with the empirical formula 3.1. Therefore, Figure 3.12(a) shows the determined roughness lengths z_0 for all measured SBL configurations with a barrier height of $h_1 = 185$ mm and the measured RBL configuration with a barrier height of $h_1 = 205$ mm. For the sake of completeness, Figure 3.12(b) shows the displacement heights d calculated by eq.(3.2). Almost all determined roughness length values lie within

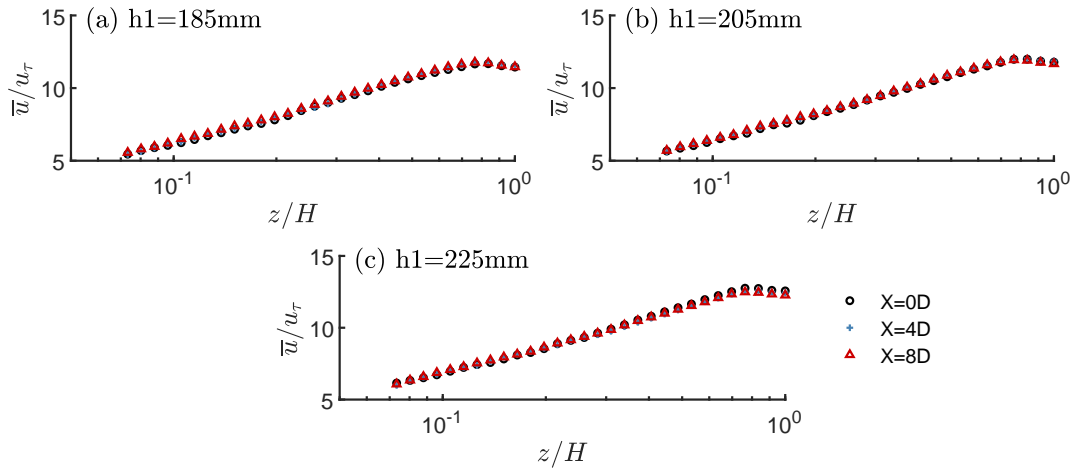


Figure 3.11: Normalised axial mean velocity $\bar{u}_\infty(z)/u_\tau$ in semi-logarithmic representation measured at different streamwise locations in the RBL configuration for barrier heights (a) $h_1 = 185$ mm, (b) $h_1 = 205$ mm, and (c) $h_1 = 225$ mm. Legend denotes streamwise locations relative to the turntable center.

a band which is confined by $C = 0.5$ and $C = 1.0$.

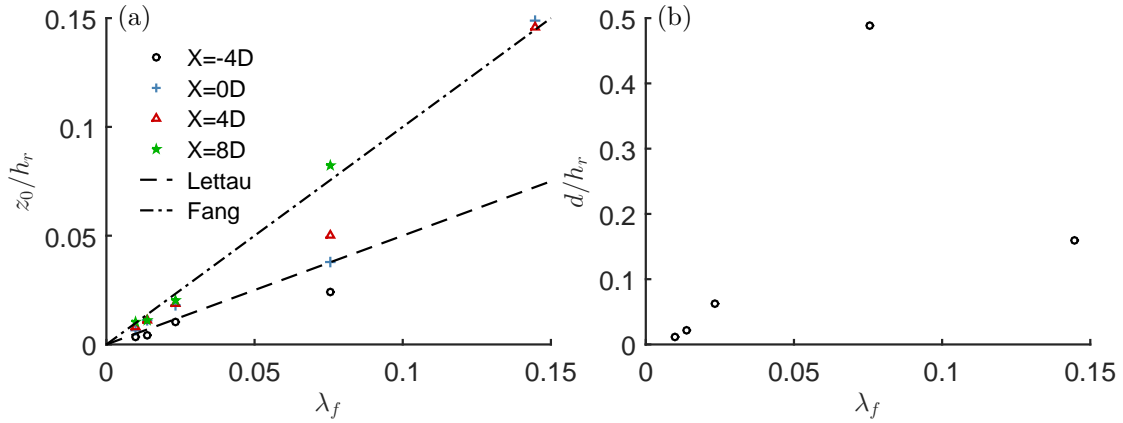


Figure 3.12: (a) Normalised roughness lengths z_0/h_r obtained by 2-parameter curve fit using (b) prescribed displacement height d from eq.(3.2) for SBL 1-7b with $h_1 = 185$ mm and RBL with $h_1 = 205$ mm

All parameters obtained by the curve fit of the logarithmic law and the power law are listed together with other key parameters in table 3.2.

Table 3.2: Characteristics of the turbulent boundary layers.

Name	H [m]	z_0 [mm]	d [mm]	α	$\bar{u}(z_h)$ [m/s]	u_τ [m/s]	$I_u(z_h)$
SBL	1.5	0.51	1.08	0.16	10.8	0.65	8.3%
RBL	1.5	5.06	10.66	0.32	10.8	0.89	13.8%

To finalize the discussion on the generation of atmospheric boundary layers, the established configurations SBL and RBL are compared to each other. Therefore, Figure 3.13

shows the vertical profiles of the (a) mean velocity, (b) turbulence intensity and (c) shear stress measured in the boundary layer using the hub height $z_h = 450$ mm and the mean velocity of the boundary layer $\bar{u}(z_h)$ at this location as reference. Additionally, the longitudinal length scales are compared with Counihan's empirical expression $L_u^x = Cz^\alpha$ [33] in Figure (d). The results show, that despite the significant differences in vertical shear and turbulence intensity, the integral turbulent length scales are almost identical in both boundary layers. Other than predicted by the empirical expression, a slight increase of the length scales with the roughness length can be noticed. Nevertheless, the integral length scales in the wind tunnel follow the correct trend up to half of the hub height z_h . Above this region length scales decrease slightly in size reaching a constant value. This behaviour is thought to be an insufficiency of the applied modelling approach. Moreover, in his study Counihan admits that measurement data used for deriving the above mentioned empirical expression is subject to much scatter [33]. However, the comparison shows clearly that with an assumed scale of $S = 1 : \mathcal{O}(350)$ the integral scales of the boundary layer are well approximated. This is important as the length scales present in the boundary layer do significantly affect the interaction with the wind turbine wake [114].

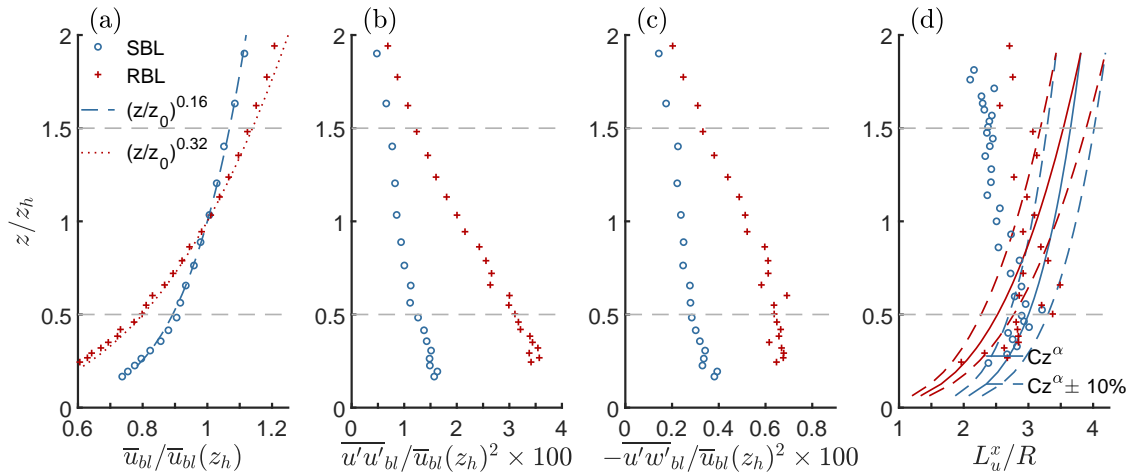


Figure 3.13: Comparison of SBL and RBL characteristics: (a) mean velocity in axial direction \bar{u}_{bl} , (b) axial turbulence intensity $u'u'$, (c) shear stress $u'w'$ within the turbulent boundary layer, all normalised by the mean velocity at hub height $\bar{u}(z_{hub})$ and (d) longitudinal integral length scale L_u^x normalised by the rotor radius R . Horizontal dashed lines indicate the rotor edges. Legend denotes flow conditions.

In Figure 3.14 the energy spectral density, normalised with the friction velocity u_τ , of all three velocity components at hub height within both undisturbed boundary layers are plotted against kz_{hub} , where k is the wave number. Thereby, wave lengths are computed from frequencies based on Taylor's well known hypothesis of frozen turbulence $k = 2\pi f/\bar{u}(z_h)$. Most striking in this comparison is the collapse of the normalised spectra for both boundary layers, which is to be expected as the turbulent length scales, shown in Figure 3.13(d) are nearly identical. As pointed out by Chamorro et al.[30] the point of transition from energy production to the inertial subrange is where $kz \approx 1$. In the case of the presented boundary layers this point is found at slightly smaller values in the range between 0.1 – 1.0, which however is still in good agreement with the theoretical location.

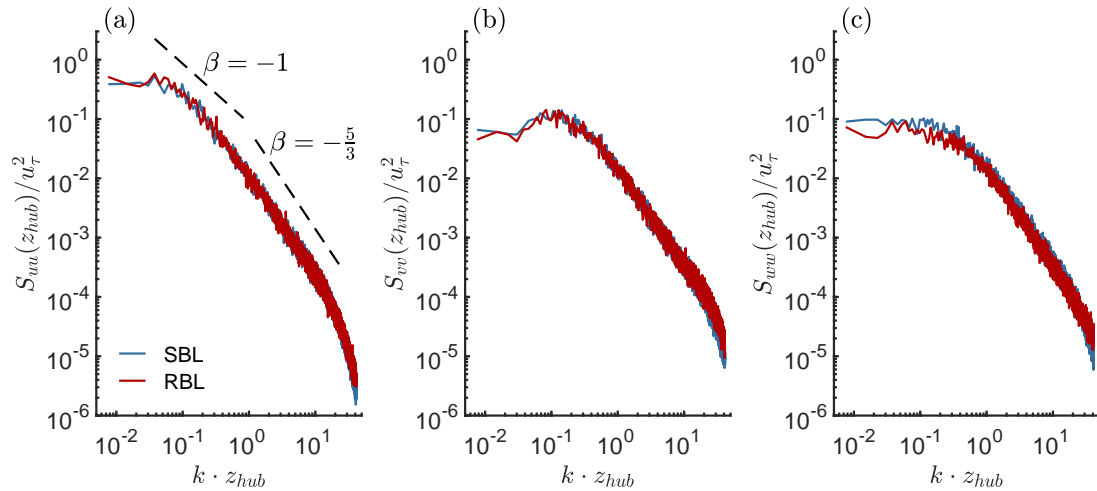


Figure 3.14: Normalised energy spectral density of the three different wind components at hub height within the two boundary layers: (a) u-component, (b) v-component and (c) w-component. Legend denotes flow conditions, dashed lines denote the slope of the Kolmogorov cascade.

3.5 Summary

In the first part of this chapter information on the applied wind tunnel, the modelling principle involved to simulate atmospheric boundary layers, and the procedures to evaluate characteristic values describing the boundary layers were provided. Furthermore, an empirical correlation found in literature which describes the aerodynamic roughness length as a function of the density and height of the roughness elements was introduced. In case of the SBL configuration several layouts were defined which, according to the correlation, are supposed to result in similar roughness lengths. For the RBL, due to technical constraints, only one layout could be defined.

In the second part of this chapter all defined layouts were tested in combination with different heights of the castellated barrier used to precondition the boundary layer. Since for the definition of the SBL configuration one among many had to be chosen the effect of the roughness element layout and barrier height were analysed separately. As a starting point of this study one of the roughness element layouts was defined similar to the boundary layer configuration established by Kozmar [80]. Measurements at the center of the turntable are in good agreement with this configuration. The empirical correlation applied in the definition of the different layouts was confirmed, since for a given barrier height all distributions resulted in nearly identical boundary layers, with regard to the mean flow and turbulence statistics. Thus, an appropriate layout was chosen by mainly technical aspects. Subsequently, the effect of the barrier height on the axial development of the boundary layer was analysed. It was found that for an increasing barrier height the axial distance for the boundary layer to reach an equilibrium state extends. Therefore, a barrier was selected for which the variation of the boundary layer within the test section is sufficiently small. For the definition of the RBL configuration the same sensitivity analysis was carried out. It was shown that due to the significantly higher level of turbulence the vertical momentum transfer is enhanced which diminishes the perturbation introduced by the barrier within shorter distance. Finally, the two selected configurations defining the SBL and RBL cases were compared regarding their characteristic key

parameters, their integral length scale and spectral content. The integral length scales of both boundary layers were compared to empirical trends for full scale atmospheric boundary layers and were shown to reproduce these correctly up to the hub height of the model wind turbine used for the wake measurements presented in Chapter 5. Other than predicted by an empirical formula, the length scales are similar or slightly increased in case of higher roughness. The energy spectral density in both boundary layers was found to be in good agreement with theoretical values reported in literature. Moreover, normalised with the determined shear stress velocity \bar{u}_τ distributions of the energy spectral density nearly collapse to one single curve which is in accordance with the computed similar length scales. The similarity of the length scales within the two boundary layers is here not seen as shortcoming of the modelling technique. It is rather an opportunity, as it reduces the number of effects having influence on the wake evolution. Therefore, differences observed in the wake of the model wind turbine immersed in both turbulent boundary layers, see Section 5, can mainly be attributed to differences in the level of turbulence and vertical shear.

Model Wind Turbine - Design & Verification

In this chapter the design of the model wind turbine developed in this work is presented and discussed. As this wind turbine is designed to mimic the wake of large scale wind turbines the resulting requirements which need to be met by the design are first presented (Sec. 4.1). Subsequently the aerodynamic design of the rotor for operation at low Reynolds numbers (Sec. 4.2), the selection of the electrical components for the drive train (Sec. 4.3), and the structural design of tower with focus on its excitation frequencies (Sec. 4.4) are explained. Finally the rotor performance achieved within different approaching flow conditions as well as in yawed conditions (Sec. 4.6) is presented.

4.1 Requirements

From a strictly aerodynamic point of view it would be favourable to have an experimental setup which fulfils Reynolds similarity. That means that the Reynolds number

$$Re = \frac{U_{ref} \cdot l_{ref}}{\nu} \quad (4.1)$$

with U_{ref} and l_{ref} being a characteristic velocity and length scale and ν the kinematic viscosity, has to be the same in full-scale and in the experiment. In that case all aspects of the flow field would be identical. However, due to the scale of 1: $\mathcal{O}(350)$ given by the dimensions of the wind tunnel, this is neither technical nor physical achievable. As the flow medium and its viscosity is the same in full-scale and in the experiment, it would require a flow velocity somewhere in the supersonic range, where flow physics are completely different to those in the low subsonic range in which wind turbines operate.

As Reynolds similarity is inevitably violated, a simple geometrical scaling of a real wind turbine rotor is not conducive. Flows around slender bodies as airfoils are significantly Reynolds number dependent, leading to a poor rotor performance if airfoil sections of full-scale multi megawatt wind turbines are used for a small scale model wind turbine. However, using airfoils especially designed for the low Reynolds number regime can give a rotor performance comparable to a full-scale wind turbine. This issue will be addressed in more detail in the following section.

With such modifications, the model wind turbine must be seen as a physical scale model rather than a geometrical one. Such a physical scale model must then meet the following characteristic values in order to produce a wake which in its development and interaction with a simulated atmospheric boundary layer meets the behaviour of a full-scale wake as closely as possible:

- The tip speed ratio λ eq.(2.25). The tip speed ratio is important for the formation of blade root and tip vortices which are dominant vortex structures in the wake.
- The thrust coefficient C_T eq.(2.27). It describes the ratio of extracted momentum to momentum contained within the wind and is therefore an important measure for the velocity deficit in the wake.
- The power coefficient C_P eq.(2.28). It is the ratio of extracted power to power contained within the wind. Power is extracted due to the generation of torque at the blades, which induces an angular momentum onto the fluid and hence a rotation of the wake.
- The scale of the atmospheric boundary layer (ABL) which should have a reasonable fit to the scale of the wind turbine model (M) $S_{ABL} \approx S_M$. Eddies within the atmospheric boundary layer have a certain extend and interact with the wind turbine and its wake. Hence for a realistic interaction, these eddies have to be scaled regarding to the scale of the wind turbine model. As a measure the integral turbulent length scales L_u can be used as well as the roughness lengths of the simulated boundary layers $z_{0,M}$

4.2 Rotor Design

As mentioned before, the performance of airfoils and hence also of wind turbine rotors is significantly Reynolds number dependent. The Reynolds number quantifies the relative importance of the inertial effects on the airfoil behavior, compared with the viscous effects. It is the latter effects that essentially control the airfoil performance since they dictate the drag as well as limiting and controlling the maximum lift of the airfoil. Thus, a convenient parameter to measure the effectiveness of an airfoil is its lift-to-drag ratio, C_l/C_d . The maximum achievable value of this quantity $(C_l/C_d)_{max}$ at a specific Reynolds number gives a good indication of the airfoil effectiveness. At lower Reynolds numbers the viscous effects are relatively large, causing high drags and limiting the maximum lift, while at the higher values the lift-to-drag ratio improves, which can be seen in Figure 4.1. There is a critical Reynolds number of about 70,000 at which this performance transition takes place [92].

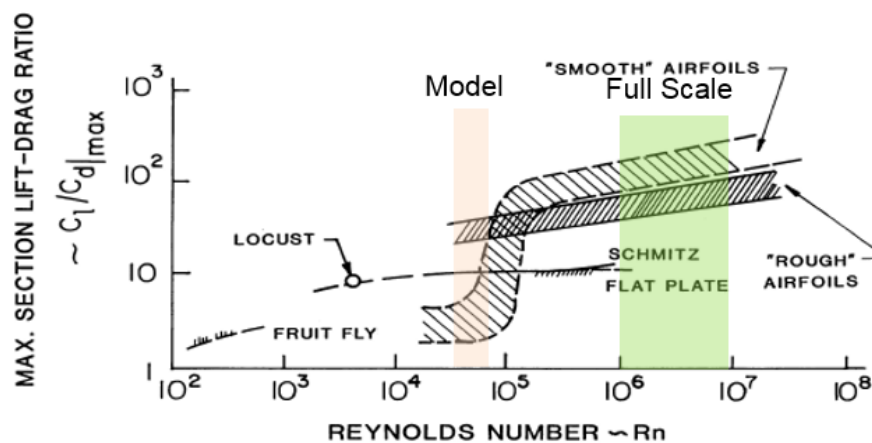


Figure 4.1: Reynolds dependency of the maximum lift-to-drag ratio for different types of airfoils; based on [100]

On the suction side of an airfoil the flow is first accelerated and then again decelerated to approximately free-stream conditions at the trailing edge, experiencing a pressure recovery through an adverse pressure gradient. For airfoils operating at large Reynolds numbers $> 10^6$ the adverse pressure gradient typically occurs after the transition from a laminar to a turbulent boundary layer. These boundary layers can sustain better severe adverse pressure gradients without separation than laminar ones. However, in lower Reynolds-number ranges, the boundary layer at the onset of the pressure rise may still be laminar, and thus unable to withstand any significant adverse pressure gradients. Hence, laminar separation is likely to occur, limiting the produced lift and significantly increasing the drag. However, when a laminar boundary layer separates, the separated layer very rapidly undergoes transition to a turbulent flow. The increased entrainment of this turbulent flow makes it possible for the flow to reattach as a turbulent boundary layer. This forms what is called a laminar separation bubble [92]. It has been pointed out by Carmichael [25] that, as a rough rule, the distance from separation to reattachment can be expressed as a Reynolds number based on bubble length of approximately 50,000. Thus, for airfoils of chord Reynolds number of about this magnitude, the airfoil is physically too short for reattachment to occur. This explains the drastic increase of the lift-to-drag ratio shown in Figure 4.1 at a Reynolds number of about 70,000.

The ratio $(C_l/C_d)_{max}$ directly influences the power extracted from the wind. Using the so called 'optimal design for variable speed operation' of Burton [22] the theoretically maximum achievable power coefficient for a given lift-to-drag ratio and design tip speed ratio can be computed, see Figure 4.2.

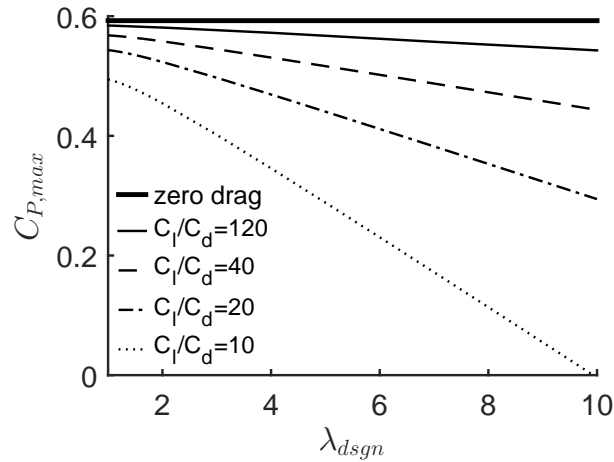


Figure 4.2: The variation of maximum C_P with design tip speed ratio λ_{dsgn} for various lift-to-drag ratios C_l/C_d .

With that it becomes clear, that applying an airfoil designed for the high Reynolds number range, where it can exhibit a $(C_l/C_d) \approx 120$, for a small scale wind turbine rotor would result in a poor energy conversion as the lift-to-drag ratio in low Reynolds number range can drop by a factor of ten. Therefore, one possible measure to improve the power extraction of a scaled model is to use airfoil profiles which are especially designed for operating at low Reynolds numbers.

For that reason, airfoil characteristics of different low Reynold number airfoils have been analysed with regard to their lift-to-drag-ratio at different angle of attacks and varying Reynold numbers. Out of them the airfoil SD7003 was selected as it exhibits a reasonable lift-to-drag ratio over a broad range of angle of attack α as shown in Figure 4.3(a), which in turn results in a good energy conversion for varying tip speed ratios (for a fixed design TSR). As for the rotor design lift and drag polars over a wide range of angle of attacks with a high resolution are necessary, polars are computed with the open source programm Xfoil. It predicts the airfoil characteristics based on a two-equation integral boundary layer formulation, see [39] for more details. A comparison with experimental data published by Selig *et. al* [127] shows a reasonable agreement with the data computed with Xfoil, see Figure 4.3(b). The cross section of the airfoil is shown in Figure 4.4 together with the most important key parameters.

Having selected an appropriate airfoil, in a next step the rotor diameter D and the design tip speed ratio λ_{dsgn} are determined. With focus on the Reynolds number dependency a diameter as large as possible is desirable. Nevertheless, it is limited by the dimensions of the available wind tunnel, especially by the length of the test section, which for this work should cover a sufficient range of the far wake region. Furthermore, the rotor area should not exceed 5% blockage ratio (i.e., the ratio of the blade swept area to the tunnel cross section area), as below this value blocking effects are considered to be negligible. Therefore, the rotor diameter is set to $D = 0.45$ m which corresponds to a blockage ratio of 3.3% and with which the wake development over a length of 9 diameters can be analysed.

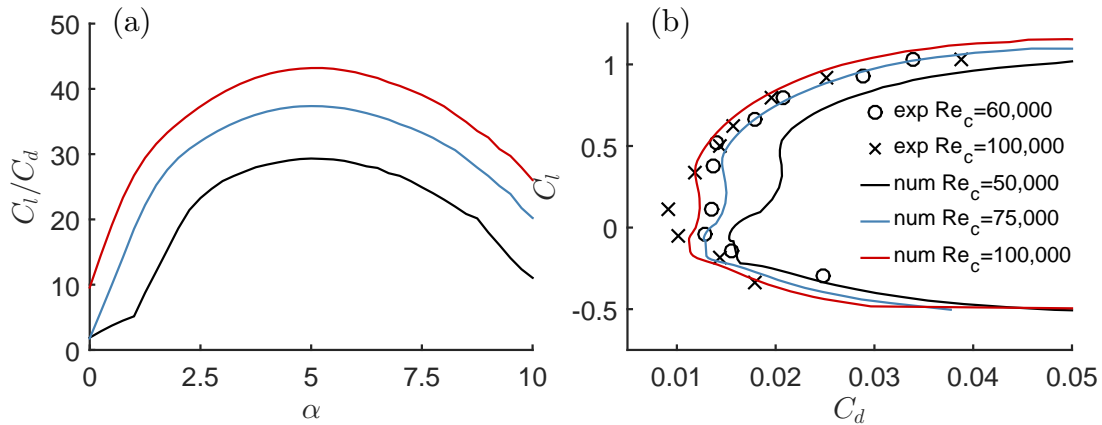


Figure 4.3: Comparison of experimental and numerical airfoil characteristics of the SD7003 airfoil. (a) Lift-to-drag ratio C_l/C_d as function of angle of attack α , (b) Lift C_l and Drag C_d Polars for various chord based Reynolds numbers Re_c . Legend indicates chord based Reynolds number. Source experimental data [127].

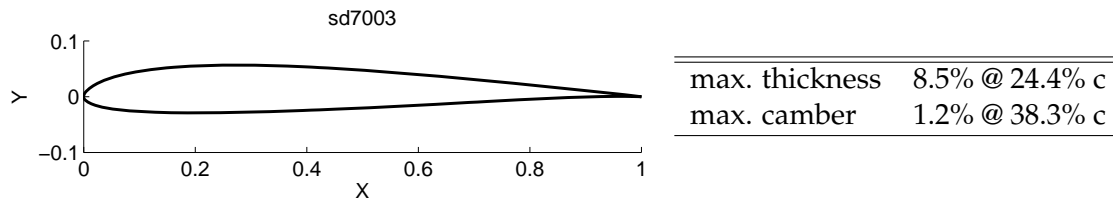


Figure 4.4: Geometry of the SD7003 airfoil; Source [126].

At the considered scale of $1 : \mathcal{O}(350)$ it represents a large multi megawatt wind turbine with a rotor diameter of about 160 m.

As mentioned before the design tip speed ratio should be comparable to those of full-scale modern wind turbines, which is typically in the range of 7 - 9 [22]. However, in the low Reynolds number range where the maximum achievable lift-to-drag ratio is low, the power coefficient significantly decreases for increasing design tip speed ratios as already shown in Figure 4.2. Considering eq.(2.44) it can be seen that for a constant free-stream velocity U_∞ the chord based Reynolds number actually decreases for increasing design tip speed ratio λ_{dsgn} which in turn decreases the maximum lift-to-drag ratio and hence the power coefficient of the wind turbine. With that it becomes clear that for a small scale model wind turbine, achieving a realistic tip speed ratio and a reasonable power coefficient are two opposing requirements. Hence, as a compromise the design tip speed ratio is set to $\lambda_{dsgn} = 6.5$. With that, a chord based Reynolds number of $Re_c = 62500$ is achieved at which the airfoil exhibits a maximum lift-to-drag ratio of $C_l/C_d \approx 33$ at an angle of attack of $\alpha_{opt} = 4^\circ$. To operate at the chosen nominal tip speed ratio and chord based Reynolds number a free-stream velocity of $u_{ref} = 10.8$ m/s and a rotational frequency of $\Omega = 2966$ rpm is necessary.

Based on these parameters and the 'Optimal Design for variable speed operation' explained in Section 2.2.4, the geometry of the the blade can be determined. The chosen approach includes blade tip- and root-losses and gives the chord and twist distribution shown in Figure 4.5.

In order to provide a cylindrical shape at the blade root to connect it with the hub, the

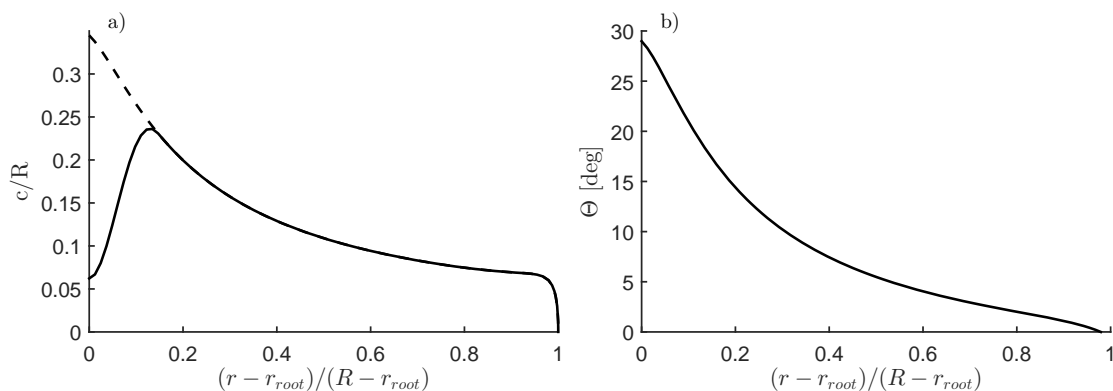


Figure 4.5: a) Normalised Chord c/R and b) Twist Θ distribution as function of the normalised radius $(r - r_{root})/(R - r_{root})$. Dashed line represents Burton's optimum distribution and solid line is the modified distribution.

chord distribution is modified for radial positions $r < 0.2R$. It is assumed, that this modification does not alter the rotor performance significantly since the root region has just a minor contribution to the power generation. Furthermore, the blade root is designed in such a way that different pitch angles can be applied manually. A 3D-Image of the blade is shown in Figure 4.6. As material for the blades a carbon fibre reinforced polymer was

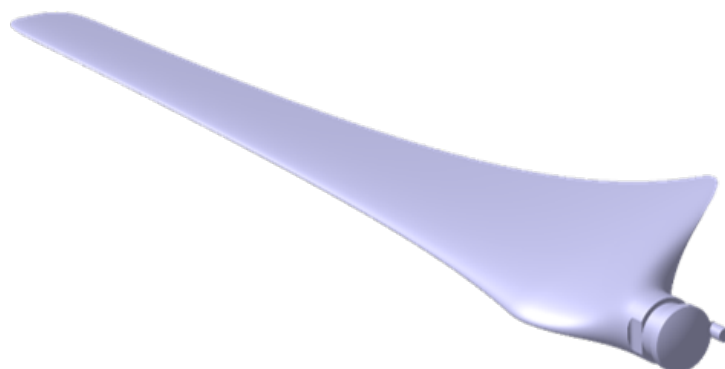


Figure 4.6: 3D-Image of the wind turbine blade

selected which can be laminated by hand into a negative mould of the blade. The whole process, from manufacturing the moulds to laminating the blades was done in cooperation with the student group AkaModell at TUM whose work is highly appreciated by the author. Due to the manual labour involved in the manufacturing process the blades had to be balanced. This was achieved by drilling holes into the blade root and inserting weights such that vibrations were minimized. Due to surface imperfections as well as inaccuracies in the design the optimum pitch angle, by means of power output, had to be determined in preliminary tests and was found to be $\Theta_p = 2^\circ$. Once the optimum pitch angle was found, the rotor blades were kept fixed to the hub for all measurement campaigns.

4.3 Electrical Components of the Drive Train

Wind turbine control systems are designed to seek the highest efficiency of operation that maximizes the power generation and to ensure safe operation under all wind conditions. As the wind turbine behaviour under different conditions just plays a minor role in this work, it is decided to apply a more simple speed control, with which the turbine can be operated at a given tip speed ratio. However, the system is required to be able to record the rotational frequency as well as the generated torque of the rotor during the measurements. As every drive train is designed just for a specific range of loading, it also has to be ensured that any excessive overload does not damage the drive train or any other part of the electronic system. Furthermore, the power generated by the wind turbine has to be 'removed' from the electronic system, as feeding it into the electrical grid is not feasible.

An accurate way to measure the produced torque is the application of a torque meter. However, a careful enquiry revealed that no appropriate torque meter could be found which (i) meets the size of the rotor hub and (ii) is able to measure torque in the range in which the rotor operates. Hence, it is decided to estimate the produced torque from the electric current of the generator. To improve the accuracy of this approach the measurement setup was calibrated by using the torque meter rig developed by Bastankhah & Porté-Agel [13]. A detailed explanation of the calibration procedure is given in the appendix A.1.

As generator the brushless electronic commutation motor *EC-max 40* in combination with the controller *ESCON 50/5* from Maxon Motor is selected. The advantage of brushless electronic commutation motors compared to mechanical commutation motors is that higher rotational frequencies and longer lifetimes can be achieved. The motor has the same diameter as the rotor hub of 40 mm and is designed to produce a torque of $Q = 203 \text{ mNm}$ at a nominal rotational frequency of $\Omega = 3770 \text{ rpm}$, which is close to the desired operational condition specified in the rotor design, see Section 4.2. Furthermore, when operating as generator, the motor can operate at a maximum rotational frequency of $\Omega = 4870 \text{ rpm}$ and hence enables a wide range of operational conditions of the model wind turbine. According to personal information of Maxon Motor technicians, the motor can even be overloaded by about 80% of its nominal value as the motor is sufficiently cooled by the approaching flow.

The *ESCON 50/5* controller is a 4-quadrant servo control, which allows for operating the motor as generator in a speed controlled mode. It measures the rotational frequency by means of an incremental encoder as well as the motor current and can be connected to the analogue digital converter (ADC) of the wind tunnel measurement system. As the electric power generated by the wind turbine cannot be fed into the electrical grid, it is thermally dissipated by connecting the generator to resistors of suitable dimension. The resistors are mounted on a heat sink to avoid overheating.

More details on the design of the drive train and selection of electronic components can be found in [119].

4.4 Structural Design of the Tower

As the model wind turbine shall have a generic geometry, tower and nacelle are required to meet the dimension ratios of a modern full-scale wind turbine. For the nacelle it is found, that its typical diameter is about 5% of the rotor diameter [22]. The diameter of the tower is found to vary from large values at the ground, where all of the forces acting on the structure have to be absorbed, to smaller diameters below the nacelle. For large multi megawatt wind turbines the diameter of the tower varies within $d \approx 4 - 8$ m, see [55]. Another important characteristic parameter is the ratio of hub height to rotor diameter z_h/D . As the tower is one of the most expensive parts of a wind turbine this parameter is mainly determined by a cost-benefit-ratio. Therefore off-shore wind turbines have typically a ratio $z_h/D < 1$, whereas on-shore wind turbines can reach a ratio $z_h/D \approx 1.2 - 1.8$ [49]. Furthermore it is important to consider the eigenfrequency of the tower which should not coincide with (i) the frequency of the vortices which shed from the tower and (ii) the rotor frequency or multiples of it to avoid any excitation of the structure. Therefore, also the distance between rotor plane and tower should be large enough as blade-tower interactions can be a source of excitation.

To meet the requirement of a generic geometry, it is decided to design nacelle and tower with a cylindrical shape. As the generator has a diameter of 40mm it determines the overall size of the nacelle, which is 8.8 % of the rotor diameter. The rotor hub is mounted on a shaft which is supported by some additional bearings. These are necessary as the bearings within the generator cannot sustain the axial forces acting on the rotor. The shaft is connected with the generator via a clutch which compensates for small misalignments. Bearings and a possible misalignment of the shaft introduce additional losses due to friction, which are accounted for in the calibration procedure of the generator mentioned above in Section 4.3.

The hub height of the mode scale tower can be adjusted, such that the ratio of hub height to rotor diameter can be varied from $0.85 < z_h/D < 1.15$. Therefore, eigenfrequency change of the tower with hub height has to be considered. To simplify the calculations and the design a steel tube with a constant diameter is selected. Given that, the first eigenfrequency of the tower can be approximated as [96]

$$f_n = \frac{1}{2\pi} \sqrt{\frac{3EI}{(0.23m_{tow} + m_{nac})L^3}} \quad (4.2)$$

where E is the Young's modulus of the selected material (steel $E = 210\text{GPa}$), I the second area moment of the towers cross section and m_{tow} and m_{nac} the mass of the tower and nacelle respectively. To avoid an excitation of the structure, the eigenfrequency of the tower should not coincide with the rotor frequency f_{1P} and the blade passing frequency f_{3P} as well as the vortex shedding frequency f_v , as these are the most energetic frequencies. The vortex shedding frequency can be approximated as

$$f_v = \frac{SrU_\infty}{d_a} \quad (4.3)$$

where Sr is the well known Strouhal number which for a Reynolds number based on the tower diameter d_a of $Re_{tow} \approx 2 \cdot 10^4$ can be set to $Sr = 0.2$ [6].

For wind turbines three design strategies are typically applied: (i) *soft-soft*, the tower is designed such that its eigenfrequency is below the rotor frequency $f_n < f_{1P}$; (ii)

soft, the eigenfrequency is between the rotor frequency and the blade passing frequency $f_{1P} < f_n < f_{3P}$; (iii) *stiff*, the eigenfrequency is above the blade passing frequency $f_{3P} < f_n$ [55]. For the model wind turbine the *stiff* strategy is not of interest as it would require a diameter d_a larger than the diameter of the nacelle, leading to an unrealistic large wake behind the tower. For the *soft* strategy the eigenfrequency of the tower would coincide with the vortex shedding frequency. The excitation due to it could be reduced by winding wires around the tower. However, applying this strategy would also limit the range of possible tip speed ratios. Hence, the tower is designed according to the *soft-soft* strategy with an inner and outer diameter of the steel tube of $d_i = 16$ mm and $d_a = 20$ mm respectively. The resulting eigenfrequencies of the tower for the mentioned ratios $0.85 < z_h/D < 1.15$ and the vortex shedding frequencies are shown in Figure 4.7 together with the rotor f_{1P} and blade passing f_{3P} frequency for tip speed ratios $5 < \lambda < 12$.

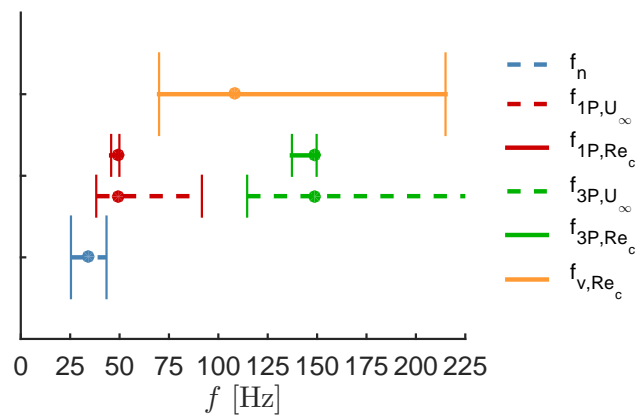


Figure 4.7: Eigenfrequencies of the tower f_n , rotor and blade passing frequencies f_{1P} , f_{3P} as function of the TSR λ for constant free-stream velocity U_∞ and chord based Reynolds number Re_c . Dots mark the design conditions

In the design, two different procedures to set the tip speed ratios are considered. The simplest way is by changing the rotational frequency. This however changes the chord based Reynolds number and hence influences the rotor performance, as explained in detail in Section 4.2. Therefore, a procedure is considered in which the chord based Reynolds number is kept constant. Details of the procedure are explained in Section 4.5. For both procedures the resulting rotor and blade passing frequencies are shown in Figure 4.7 and are distinguished by the subscripts U_∞ and Re_c , which indicates that either the free-stream velocity is kept constant or the chord based Reynolds number. In the case of a constant free-stream velocity an overlap of the tower frequency f_n and the rotor frequency f_{1P,U_∞} can occur for low tip speed ratios and low ratios of z_h/D and should therefore be avoided. As for the constant Reynolds number procedure the free-stream velocity varies between $U_\infty = 7 - 21$ m/s, the occurring vortex shedding frequencies cover wide band from $f_{v,Re_c} = 75 - 215$ Hz. Nevertheless, in every case there is a sufficiently large distance to the eigenfrequency of the tower.

To reduce the blade-tower interaction it is recommended to provide a distance $> 1 \cdot d_a$ between the rotor plane and the tower. For full scale wind turbines this is rather achieved by tilting the rotor then by locating it further upstream as it would introduce an additional bending moment into the structure due to high weight of the rotor. In the case of the model wind turbine this is not an issue and it is designed with a gap of $2.5 \cdot d_a$.

The generated thrust is measured by means of a strain gauge installed between nacelle and tower. Thus, the measurement includes axial component of forces on the blades, spinner and nacelle.

More details on the design of the tower and calculation of eigenfrequencies can be found in [119]. Photos of the wind turbine model are shown in Figure 4.8.

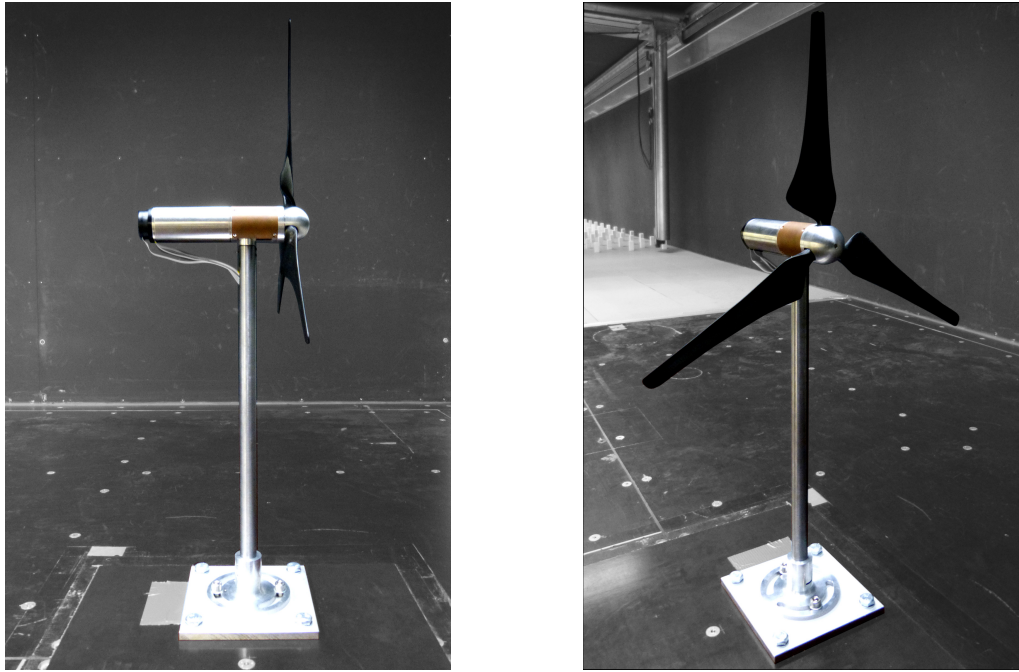


Figure 4.8: Side and Iso View of Model Wind Turbine located close to wind tunnel nozzle for measurements in low turbulence uniform approach flow conditions (LTU).

4.5 Determination of Operational Conditions

As mentioned in Section 4.2 the rotor performance of small model wind turbines is known to be quite sensitive to changes in the Reynolds number as the turbine operates at relatively low values of it. Hence, comparing results intentionally obtained at different tip speed ratios have to be considered carefully if the Reynolds number is not the same. The variation in the average chord based Reynolds number \overline{Re}_c , defined by eq.(2.45) in Section 2.2.4, for various combinations of the free-stream velocity at hub height and rotational frequency of the rotor are shown in Figure 4.9. The bounds for averaging are chosen to be $\mu_1 = 0.5$ and $\mu_2 = 0.95$, reasoning on this choice is given below. Isolines of constant average chord based Reynolds number are shown as dashed coloured contour lines and constant tip speed ratios as black dotted lines. Exemplarily, a green and a blue line indicate the change in the average chord based Reynolds number for tip speed variations with a constant free-stream velocity and a constant rotational frequency, respectively. As by changing the rotational frequency ($U_\infty = const.$) the average chord based Reynolds number changes proportional to it, significant Reynolds number dependencies have to be expected and the proceeding is therefore not recommended. By changing the free-stream velocity ($\Omega = const.$) changes in the average Reynolds number are reduced, nevertheless for small tip speed ratios dependencies can still occur.

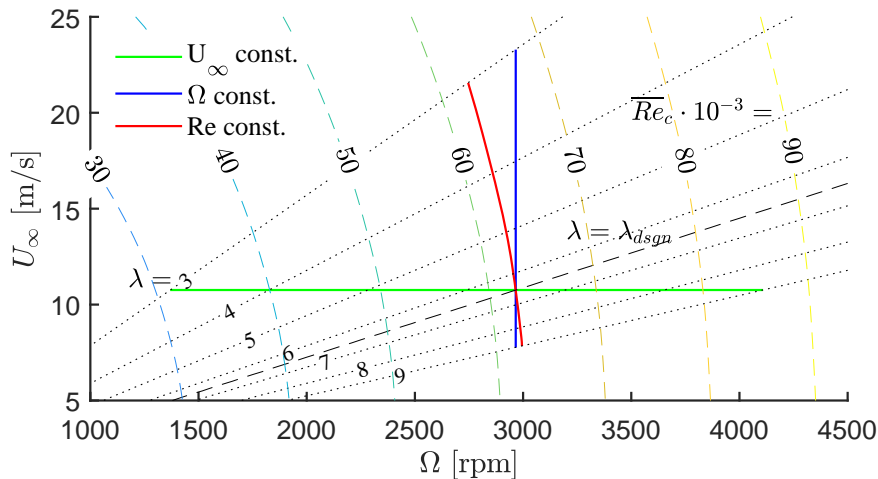


Figure 4.9: Variation of the averaged chord based Reynolds number \overline{Re}_c as function of free-stream velocity U_∞ and rotational frequency Ω . Dashed coloured lines and dotted black lines indicate the corresponding averaged Reynolds number \overline{Re}_c and tip speed ratio λ , respectively. Legend denotes further isolines.

In order to exclude these effects as much as possible all measurements presented in the following Section 4.6 and Chapter 5 were performed for combinations of the rotational frequency Ω and the free-stream velocity U_∞ for which the average chord based Reynolds number is constant $\overline{Re}_c = 62,500$. This setting is depicted by a red line in Figure 4.9. In case of measurements within a turbulent boundary layer the free-stream velocity U_∞ is replaced by the velocity at hub height $\bar{u}_{bl}(z_h)$. It should be noted that in these cases the local chord based Reynolds number along the blade varies over a revolution due to the sheared velocity profile of the boundary layer. Hence, in these cases the mean chord based Reynolds number should rather be interpreted not only by a spatial average but as a time averaged value as well.

As mentioned in Section 4.2 for design conditions the local Reynolds number $Re_c(\mu = r/R)$ is almost constant along the blade, apart from the regions close to the root and tip where losses from strong helical vortices are induced. However, for off-design conditions the local Reynolds number can vary more significantly along the blade span as the axial and azimuthal induction factor $a(\mu)$ and $a'(\mu)$ deviate from their optimal values. To obtain the induction factors in these situations, simulations of the rotor have been performed with the blade element momentum solver FAST v7 [75] for various tip speed ratios. The interested reader is referred to [120] for more details on the simulation. By applying eq.(2.44) the local chord based Reynolds number can then be computed. The resulting distributions are shown in Figure 4.10 for (a) the $U_\infty = const.$, (b) the $\Omega = const.$ and (c) the $\bar{Re}_c = const.$ procedures. It can easily be seen, that for tip speed ratios close to the design condition $\lambda_{dsgn} = 6.5$ the assumption of a constant local Reynolds number is reasonable. Only for tip speed ratios smaller than the design conditions a significant increase at the inboard section of the blade is noticeable. For that reason and due to the tip-losses the average chord based Reynolds number \bar{Re}_c is calculated within the bounds of 50 - 95 % blade radius ($\mu_1 = 0.5$, $\mu_2 = 0.95$). Herein the local Reynolds number just varies within $\pm 4\%$ around the average value.

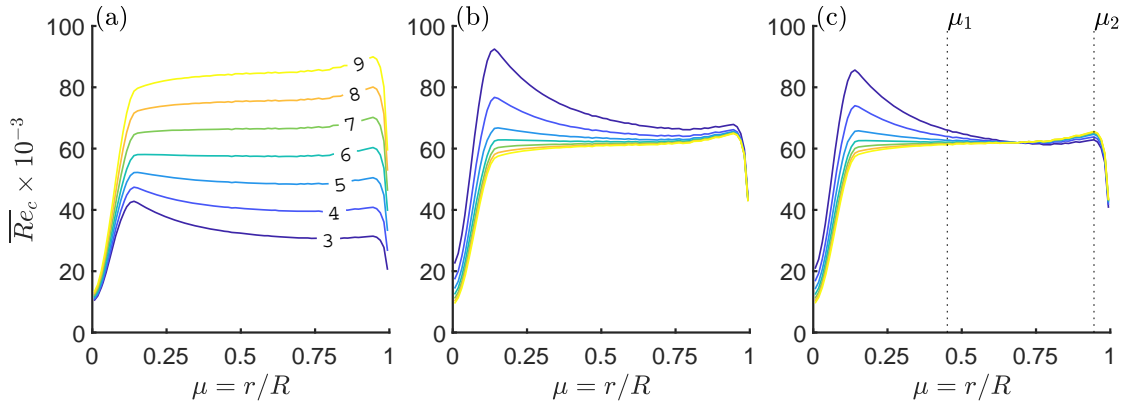


Figure 4.10: Variation of the local chord based Reynolds number Re_c with the TSR λ as function of the normalised radius $\mu = r/R$ for (a) the $U_\infty = const.$, (b) the $\Omega = const.$ and (c) the $\bar{Re}_c = const.$ procedures, all with $\bar{Re}_c(\lambda_{dsgn}) = 62,500$. In (c) $\mu_1 = 0.5$ and $\mu_2 = 0.95$ are used as bounds for the calculation of \bar{Re}_c .

For a given average chord based Reynolds number and tip speed ratio, and with the knowledge on the axial and azimuthal induction factors a and a' , eq.(2.45) and eq.(2.25) can then be solved for the free-stream velocity U_∞ and the rotational frequency Ω .

4.6 Rotor Performance

Measurements of the rotor performance within both turbulent boundary layers *SBL* and *RBL* as well as within a low turbulence uniform approaching flow condition (*LTU*) are presented. The latter is achieved by removing the vertical fins and locating the model wind turbine close to the wind tunnel nozzle. For all flow conditions the rotor performance has been measured for tip speed ratios ranging from $\lambda = 3.75$ to 11.5 with an increment of $\Delta\lambda = 0.25$. For the design tip speed ratio of $\lambda_{dsgn} = 6.5$ the rotor performance also has been measured for yaw angles from $\gamma = 0^\circ$ to 45° with an increment of $\Delta\gamma = 2.5^\circ$. For all tip speed ratios and yaw angles the instantaneous values of thrust T , torque Q , rotational frequency Ω , the reference velocity at the Prandtl tube U_{ref} , the barometric pressure and the temperature within the wind tunnel T_{ref} is sampled with a rate of 3 kHz. Within the turbulent boundary layers for each configuration these signals are recorded for a length of 90 s and within *LTU* flow condition over a length of 30 s. To avoid Reynolds number dependent effects, all measurements were performed at an average chord based Reynolds number of $\overline{Re}_c \approx 62500$.

Figure 4.11 shows the measured (a) power C_P and (b) thrust coefficients C_T as function of the tip speed ratio. Most salient in the comparison of the performance curves is that the power coefficient increases in the turbulent boundary layers for TRSs $\lambda > 6$ compared to the low-turbulence uniform approaching flow condition, whereas the thrust coefficient does not exhibit any significant change. Within the complex flow of a rotor immersed in a turbulent boundary layer, there are a couple of reasons which are likely to affect the performance. Besides other effects, changes in the turbulence intensity and integral length scales of the approaching flow have been reported to have a more pronounced effect on the shear layer separation, reattachment, transition, and formation of separation bubbles at airfoils operation at low chord based Reynolds numbers than at higher Reynolds numbers (see e.g. [152], [153]). More detailed measurements regarding the airfoil aerodynamics are needed to identify the responsible phenomena. However, Wang et al. [152] showed that an increasing turbulence intensity can have a similar effect as an increasing Reynolds number. Following this argument and comparing tabulated airfoil data of the SD7003 airfoil from Selig [126] reveals an airfoil characteristic which for increasing Reynolds number exhibits a decrease in the drag coefficient C_d but a rather constant lift coefficient C_l . According to Blade Element Momentum (BEM) Theory, see Section 2.2.3,

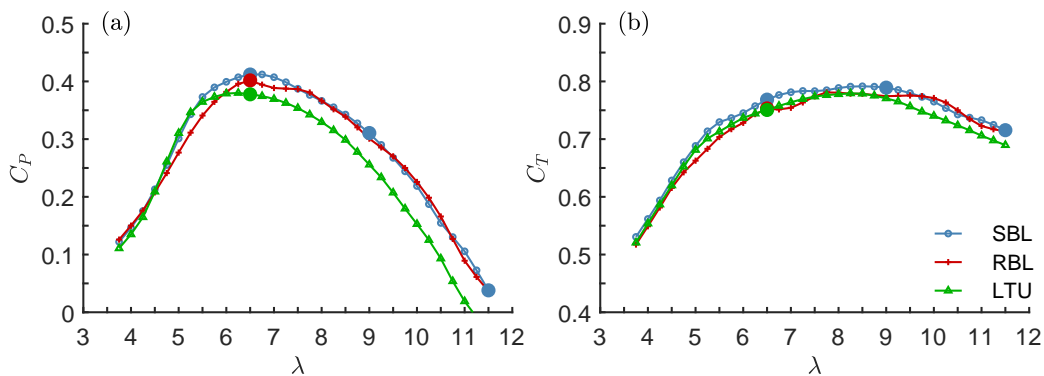


Figure 4.11: a) Power C_P and b) thrust coefficients C_T as function of TSR λ for constant chord based Reynolds number $\overline{Re}_c = 62500$. Legend gives flow conditions. For coloured points hot wire measurements were performed.

the contribution of lift and drag to thrust δT and torque δQ produced by a blade element of the length δr can be described as given in eq.(2.35). Since $\sin(\phi)$ is relatively small for TSRs $\lambda \gg 1$ (except close to the root), a smaller drag coefficient results rather in a more pronounced increase of torque than in a decrease of thrust, which explains the observed trend. A similar effect of the turbulence intensity on the power coefficient using grid generated isotropic turbulence is shown by Al-Abadi et al. [2].

As mentioned in the beginning of this chapter, the intention in this model wind turbine design is to obtain a physical scale model of a multi megawatt wind turbine. Since it is difficult to find data on the rotor performance of commercial wind turbines, the achievement of this goal is evaluated by comparing the performance with that of the NREL-5MW reference wind turbine with a rotor diameter of $D = 126$ m [75]. In the testcase presented in Section 6.3.2 for this wind turbine, thrust and power coefficients of $C_T = 0.78$ and $C_P = 0.48$ were obtained for its design tip speed ratio of $\lambda_{dsgn} = 7.55$. The thrust coefficients of $C_T = 0.75 - 0.77$ measured for the model wind turbine operating at its design tip speed ratio of $\lambda_{dsgn} = 6.5$ is therefore in very good agreement with the full scale reference. The maximum power coefficient $C_P = 0.38 - 0.41$, however, is 14% - 20% percent lower. Considering that the Reynolds number at which the model wind turbine is operated is more than two orders of magnitude lower than that of the reference turbine (NREL-5MW $Re_c \sim 7 \cdot 10^6$), this results is more than acceptable. For comparison, Ode-mark & Fransson [110] obtained for a small scale wind turbine, which made use of the same airfoil as used in this work but with a rotor diameter of $D = 0.23$ m, a maximum power coefficient of $C_P = 0.32$ for a TSR of $\lambda = 5.0$ ($Re_c \sim 2 \cdot 10^4$). More recently, Bastankhah & Porté-Agel [13] achieved a power coefficient of $C_P = 0.38$ for a TSR of $\lambda = 3.8$ for a model wind turbine which uses cambered plates as airfoils and a rotor diameter of $D = 0.15$ m ($Re_c \sim 4 \cdot 10^4$). Therefore, the higher maximum power coefficient achieved for the presented model wind turbine is mainly considered to be a result of the larger rotor diameter $D = 0.45$ m and higher Reynolds number of $Re_c \approx 62500$.

Power and thrust coefficient C_P, C_T as function of yaw angle γ for a TSR of $\lambda = 6.5$ are shown in Figure 4.12(a) and (c), respectively. As for different TSRs, the effect of turbulence intensity is most significant in the comparison of the different flow conditions. Indeed, when normalised to their respective maximum value (un-yawed condition) the curves become self similar, as shown in Figure 4.12(b) and (d). For the sake of comparison, $\cos^n(\gamma)$ graphs are also shown in both Figures. Thereby the exponent n was determined by a least square fit to match the normalised curves, which results in an exponent close to 2.5 for the power coefficient and 1.5 for the thrust coefficient. The corresponding curves are indicated by *dashed lines*. For comparison, curves with an exponent $n \pm 0.5$ are also shown as *dotted lines* additionally. In the literature the value of the exponent n for the power curve as well as for the thrust curve is in dispute. Burton [22] pointed out that distinct momentum theories (Axial, Glauert, Vortex Cylinder) result in different exponents for both coefficients. Krogstad et al. [84] reported for the power curve an exponent close to 3 for a three bladed model wind turbine. Recently, based on wind tunnel measurements Bastankhah et al. [13] showed that the value is strongly dependent on the chosen tip speed ratio. In the range of the design tip speed ratio they however reported an exponent of 2.5 – 3, whereas for the thrust coefficient they found an exponent close to 1.5. These findings are consistent with the results presented here.

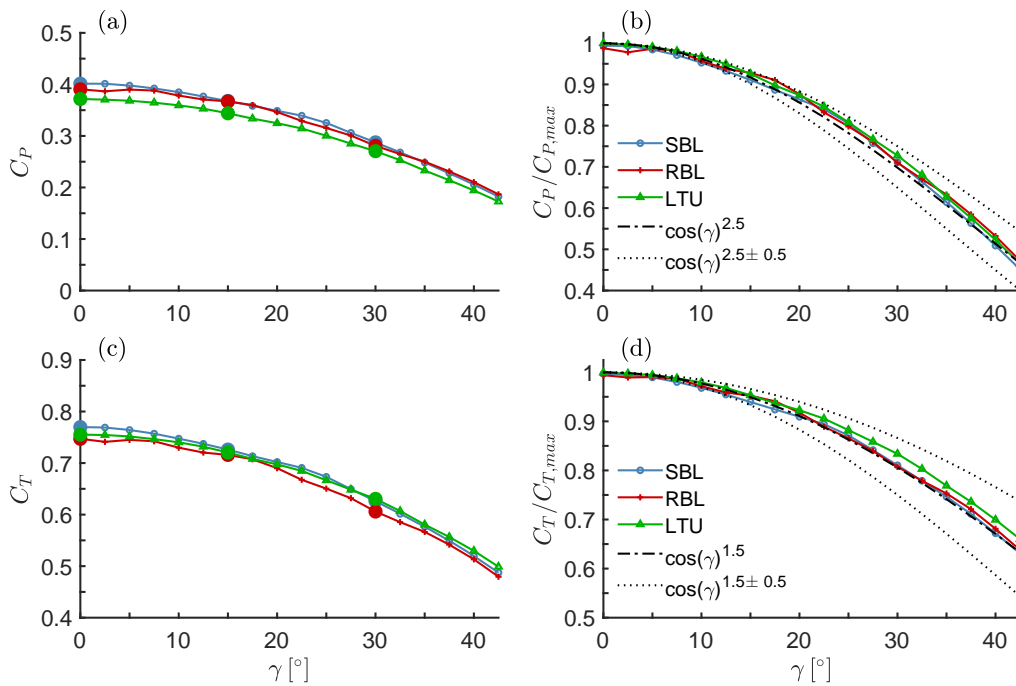


Figure 4.12: Measured and normalised (a),(b) power coefficients C_P and (c),(d) thrust coefficients C_T as function of yaw angle γ . Legend gives flow conditions. For coloured points hot wire measurements were performed.

4.7 Summary

The chapter provided the design of the model wind turbine developed in this work. Particular emphasis was placed on explaining the physical and technical reasons that forbid a simple geometrical scaling from a large wind turbine and require for applying airfoils made specifically for the low Reynolds number range of operation. The resulting blade design, operational parameters, drive train characteristics, and the structural design of the tower were given. In the latter, as the hub height of the tower can be adjusted, special care was taken in the design to avoid any excitation by the rotor.

As a result of the consequent design of the turbine for operation in a low Reynolds number regime a realistic rotor performance over a wide range of tip speed ratios could be shown for different flow conditions, ranging from low turbulence uniform approaching flow to highly sheared turbulent boundary layers. A comparison with a full scale multi megawatt wind turbine with a comparable design tip speed ratio showed that the model wind turbine exhibits very similar thrust coefficients while the maximum power coefficient is about 15% lower. When compared to other small scale wind turbines for wind tunnel applications the maximum power coefficient achieved for the model wind turbine presented here is similar or even superior.

It was found that presence of turbulence improves the rotor performance in terms of power production which can be explained by a reduction of airfoil drag. Yaw-angle dependencies of the power C_P and thrust coefficient C_T are shown to be insensitive to changes in shear and turbulence intensity. It was found that C_P and C_T decrease with increasing yaw angle, following a $\cos(\gamma)^n$ -distribution. For the design tip speed ratio the exponents n are similar to values reported in the literature.

Wake Measurements

Hot wire measurements in the wake of the model wind turbine immersed in two turbulent boundary layers of significantly different vertical shear and turbulence intensity (aerodynamic roughness) were carried out and are presented in this chapter. Thereby, also the flow field with the turbine operating in off-design conditions was recorded, including various tip speed ratios and yaw angles. First, details on the experimental setup are given (Sec. 5.1). The following result analysis unfolds in two parts. Firstly, wake characteristics are described as function of tip speed ratio, ground roughness, and ground roughness in combination with yaw angle (Sec. 5.2). This includes profiles of mean velocity, Reynolds stresses, and derived quantities as the velocity deficit recovery, the wake growth, and the trajectory of the wake centre. Secondly, spectral analysis of the recorded time series of the velocity fields in the wake is performed (Sec. 5.3). Here special emphasis is put on analysing the instability of helical blade tip vortices in the near wake region, the wake development in the far wake, and the presence of wake meandering.

This chapter is partly based on previous publications of the subject at international conferences, see Stein & Kaltenbach [135, 136].

5.1 Experimental Setup

Hot wire measurements within the wake have been performed with the turbine immersed in the LTU, SBL and RBL flow conditions. More details on the flow conditions can be found in 3. For the design TSR of $\lambda_{dsgn} = 6.5$ the measurements were performed for yaw angles of $\gamma = 0^\circ, 15^\circ$ and 30° . Additionally, within the SBL flow condition measurements were also performed with the turbine operating at $\lambda = 9.0$ and $\lambda = 11.5$. For these tip speed ratios, table 5.1 lists the corresponding reference velocity at the Prandtl tube located at hub height U_{ref} and the rotational frequency of the rotor f_{1P} .

Table 5.1: Reference velocity and rotational frequency for selected tip speed ratios with $\overline{Re}_c = 62,500$.

λ	$U_{ref}(\text{m/s})$	$f_{1P}(\text{rpm})$
6.5	10.80	2969
9.0	7.85	2998
11.5	6.08	3008

The wind turbine model is located on the center of a turntable approximately 12.5 m downstream of the fins where the boundary layer thickness is assumed to be $\delta \approx 1.5$ m. Figure 5.1 shows photos of this experimental setup for the boundary layer configurations SBL and RBL . The turntable is followed by a 4.5 m long test section in which the velocity field has been recorded at downstream distances from the model wind turbine $x/R = 2, 4, 6, 10, 14, 18$ within the lateral range of $-2.8 < y/R < 2.8$ and vertical range of $0.45 < z/R < 3.65$. Thereby the lateral direction is resolved by $N_y = 53$ and the vertical direction by $N_z = 35$ non-equidistant distributed measurement points. The coordinates of all positions at which hot-wire measurements were conducted can be found in the appendix A.3. For each measurement point the hot wire signals are sampled at 3 kHz with a record length of $T_{ave} = 120$ s. Simultaneously, thrust T and torque Q produced by the rotor, the current rotational frequency f_{1P} , the reference velocity at the Prandtl tube U_{ref} , as well as the barometric pressure p_{ref} and the temperature within the wind tunnel T_{ref} are measured.

(a) MWT in Smooth Boundary Layer



(b) MWT in Rough Boundary Layer

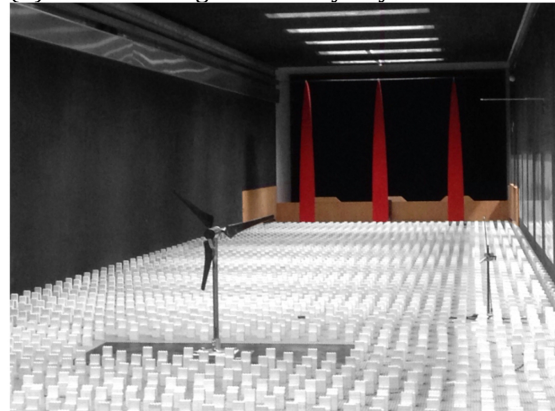


Figure 5.1: View of the Model Wind Turbine located within (a) the smooth boundary layer and (b) the rough boundary layer configuration of the wind tunnel.

5.2 Wake Characteristics

In this section time averaged results from hot wire measurements within the wake of the model wind turbine operating under various conditions are presented. Thereby the analysis focuses on the development of profiles of the mean axial velocity and the Reynolds stresses. To support the discussion and highlight specific features of the wake development, characteristic values as the recovery of the velocity deficit, the wake width and the wake trajectory are taken into account. The influence of different tip speed ratios on the wake of the model wind turbine immersed in the smooth boundary layer is discussed in Section 5.2.1. The wake development for different flow conditions is analysed for the model wind turbine in un-yawed conditions in Section 5.2.2 and for yawed conditions in Section 5.2.3.

5.2.1 Influence of the Tip Speed Ratio

To analyse the influence of the tip speed ratio on the wake development three distinct tip speed ratios have been chosen, namely $\lambda = \lambda_{dsgm} = 6.5, 9.0$ and 11.5 . As shown in the previous chapter, at a tip speed ratio of $\lambda = 9.0$ the wind turbine exhibits almost the same thrust coefficient as it does at design conditions, see Figure 4.11(a) in Section 4.6. For the tip speed ratio of $\lambda = 11.5$ the thrust coefficient is just 10 % lower, the turbine however does almost not extract any energy of the flow since the power coefficient is close to zero as shown in Figure 4.11(b).

First of all, results for the SBL configuration are discussed. Figure 5.2 shows the spatial distribution of the normalised averaged axial velocity component \bar{u} for the three chosen tip speed ratios. For downstream distances of $x/R \leq 6$ the dependency of the axial velocity on the tip speed ratio can clearly be observed. As previously outlined, in all cases the wind turbine exhibits an almost constant thrust coefficient C_T . Therefore deviations between different tip speed ratios must be explained by considerations regarding the rotor aerodynamics. With increasing TSR the angle of attack at the inward section of the blades is decreased, resulting in a lower contribution to the thrust. At the outward section the increasing velocity of the relative wind results in an increasing contribution to the thrust towards the tip. From the Figure this effect can clearly be seen in the vicinity of the rotor ($x/R = 2$), where an increase of \bar{u} with the TSR is observed in the inner region and a decrease in the outer region of the rotor. Due to the momentum exchange caused by the ambient turbulence this effect vanishes in the outer region for a downstream distance of $x/R = 6$. For distances of $x/R \geq 10$ the different profiles become indistinguishable.

Figure 5.3 shows the spatial distribution of the Reynolds shear stress with respect to the radial direction $\overline{u'w'}$ in the mid-vertical and $\overline{u'v'}$ in the mid-horizontal plane, normalised by the velocity at hub height $\bar{u}_{bl}(z_h)$. In the tip regions close to the rotor ($x/R = 2$) shear stresses are increased for high tip speed ratios. This confirms the increasing contribution to the thrust towards the tip at high tip speed ratio.

The velocity distribution in the far wake is mainly associated with the radial distribution of the Reynolds shear stress $\overline{u'w'}$ and $\overline{u'v'}$. Therefore subtle differences in the velocity distribution appear more pronounced in the distribution of the Reynolds shear stresses. As can be observed at a downstream distance of $x/R = 6$, which approximately constitutes the onset of the far wake in this flow condition, for the TSR of $\lambda = 11.5$ the maximum Reynolds shear stresses are decreased compared to lower TSRs. Further downstream, with decaying Reynolds shear stresses the different profiles converge. Even though this

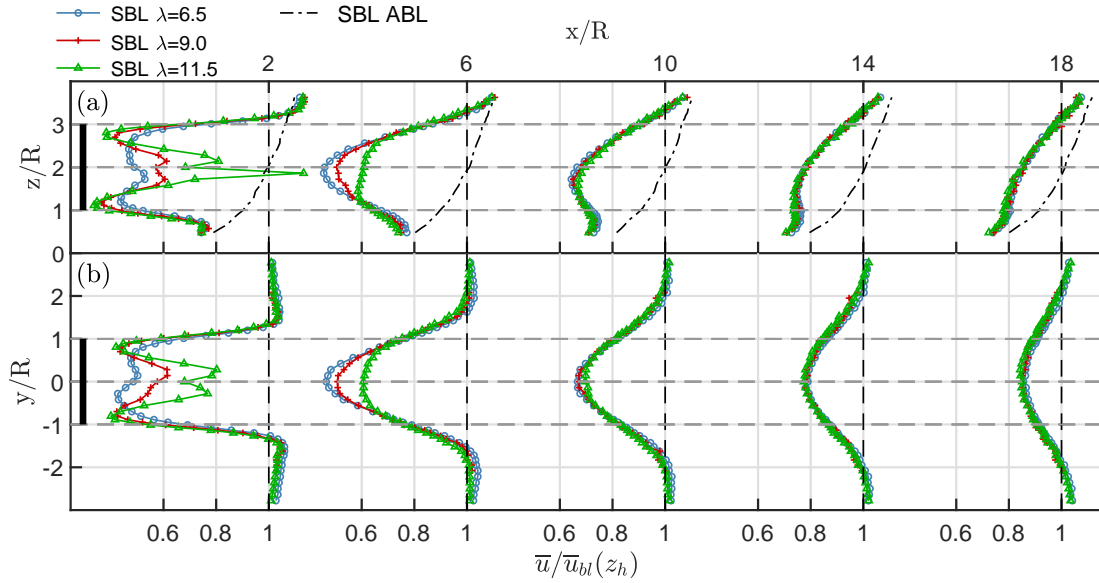


Figure 5.2: Profiles of the mean axial velocity component \bar{u} in the a) mid-vertical and b) mid-horizontal plane for tip speed ratios $\lambda = 6.5, 9.0, 11.5$ at axial positions $x/R = 2, 6, 10, 14, 18$ for SBL. Legend denotes the tip speed ratio for each profile.

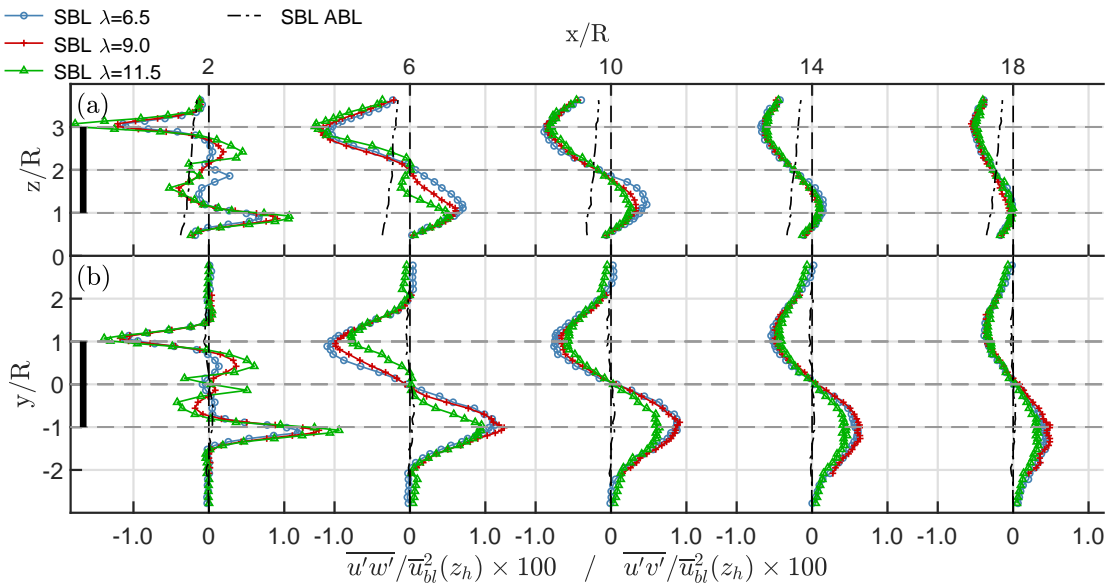


Figure 5.3: Profiles of the Reynolds shear stress (a) $\overline{u'w'}$ in the mid-vertical and (b) $\overline{u'v'}$ in the mid-horizontal plane for tip speed ratios $\lambda = 6.5, 9.0, 11.5$ at axial positions $x/R = 2, 6, 10, 14, 18$ for SBL. Legend denotes the tip speed ratio for each profile.

confirms the observation made above about a convergence of the velocity deficit in the wake, it also shows that for different TSRs subtle differences still exist in the wake for distances of $x/R \geq 10$.

Figure 5.4 shows the spatial distribution of the normalised mean azimuthal velocity component \bar{v} and \bar{w} in the vertical and horizontal plane respectively. As already seen for the axial velocity component, deviations in between different TSRs can clearly be identified, especially in the vicinity of the rotor. In contrast to the almost constant thrust coefficient

C_T , the power coefficient C_P drops from its maximum value to small values with increasing TSR, see Figure 4.11(a). Since the rotation of the wake is directly connected with the power coefficient C_P , the decrease of azimuthal velocity is to be expected.

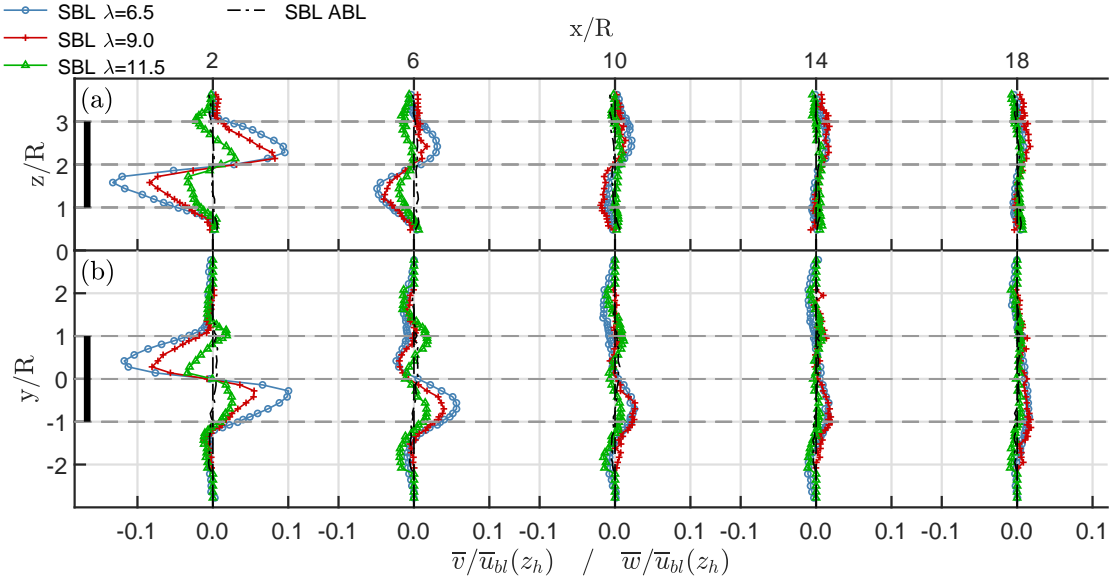


Figure 5.4: Profiles of mean azimuthal velocity component (a) \bar{v} in the mid-vertical and (b) \bar{w} in the mid-horizontal plane for tip speed ratios $\lambda = 6.5, 9.0, 11.5$ at axial positions $x/R = 2, 6, 10, 14, 18$ for SBL. Legend denotes the tip speed ratio for each profile.

For all three Reynolds stresses $\overline{u'u'}$, $\overline{v'v'}$ and $\overline{w'w'}$ a tip speed ratio dependency can be identified, especially in the near wake but also in the far wake region as shown in Figure 5.5 and 5.6. With increasing TSR λ the tip region exhibits an increased contribution to the thrust which, in the vicinity of the rotor ($x/R = 2$), results in sharp peaks in the axial mean velocity, see Figure 5.2, and Reynolds stress in the axial direction, see Figure 5.5. In the far wake region ($x/R \geq 14$) sharp peaks in the Reynolds stresses become smoother due to the turbulent momentum exchange and differences in between the measured cases start to vanish. However, even at this distance a TSR dependency is clearly noticeable, especially for the components of the Reynolds stress in azimuthal, see Figure 5.6, and radial direction, see Figure 5.7. For these components the deviation is up to 20%.

This effect can be explained by the mutual inductance instability, due to which vortices pair and break down causing a sudden increase in the net entrainment of the mean-flow kinetic energy and, thus, generating a more efficient mixing by the action of random flow motion. Lignarolo *et al.* [90] revealed that this instability intensifies for high tip speed ratios as the helical pitch of the vortices decreases. As a result the break down of the tip vortices occurs closer to the rotor. The presence of this effect in the current measurements is analysed and discussed in more detail in Section 5.3.2.

Indeed, the results presented here are in accordance with this explanation, as for a TSR of $\lambda = 11.5$ (i) the wake recovers faster within a distance of $x/R \leq 6$, see Figure 5.2, (ii) at the same axial distance the Reynolds stresses in radial direction close to the tip regions are increased, see Figure 5.7 and (iii) Reynolds stresses in all directions are decreased further downstream.

Another interesting feature of the measured wakes is the effect of the tip speed ratio on the Reynolds stresses for the rotor mid-section in the vicinity of the rotor for $x/R \leq 2$.

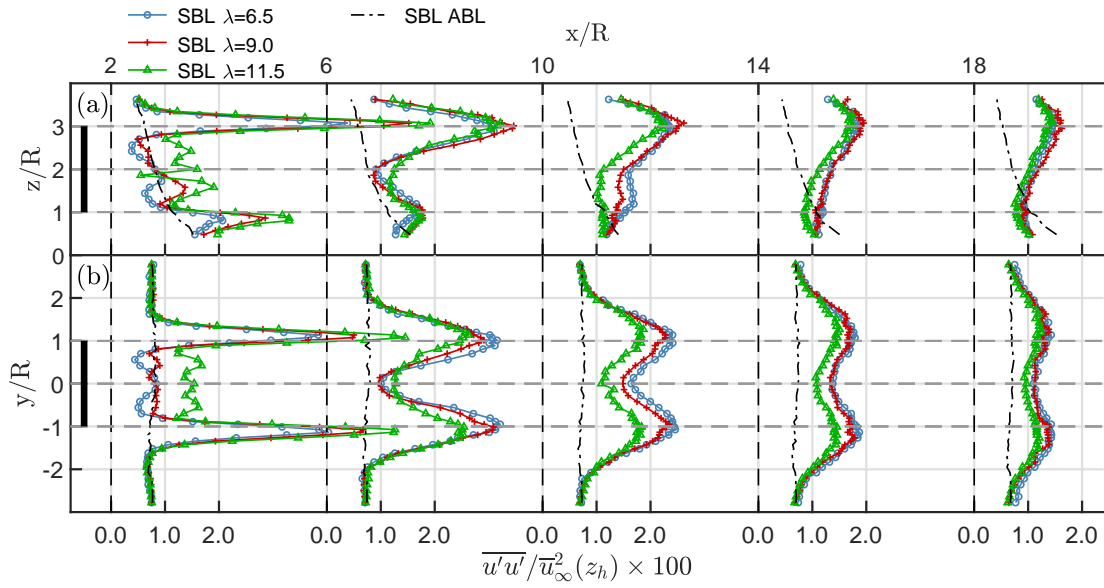


Figure 5.5: Profiles of Reynolds stress in axial direction $\overline{u'u'}$ in the a) mid-vertical and b) mid-horizontal plane for tip speed ratios $\lambda = 6.5, 9.0, 11.5$ at axial positions $x/R = 2, 6, 10, 14, 18$ for SBL. Legend denotes the tip speed ratio for each profile.

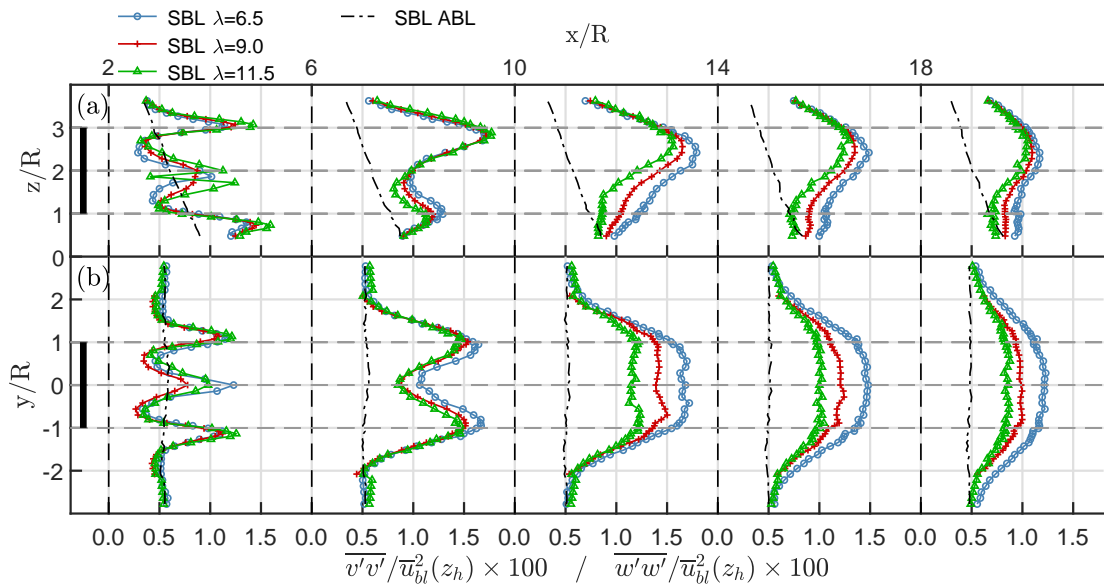


Figure 5.6: Profiles of Reynolds stress in azimuthal direction (a) $\overline{v'v'}$ in the mid-vertical and (b) $\overline{w'w'}$ in the mid-horizontal plane for tip speed ratios $\lambda = 6.5, 9.0, 11.5$ at axial positions $x/R = 2, 6, 10, 14, 18$ for SBL. Legend denotes the tip speed ratio for each profile.

As can be seen in Figure 5.5 for the design tip speed ratio of $\lambda = 6.5$ the Reynolds stress in axial direction $\overline{u'u'}$ drops locally below the level of the ambient flow and rises with increasing tip speed ratio. For the Reynolds stresses in the azimuthal direction, see Figure 5.6, and in the radial direction, see Figure 5.7, a local suppression of the stresses below the ambient level is also observable. It however does not exhibit a significant dependency on the tip speed ratio. Nevertheless, as will be shown in the following section, the suppression of Reynolds stresses in all directions is strongly dependent on the level of ambient

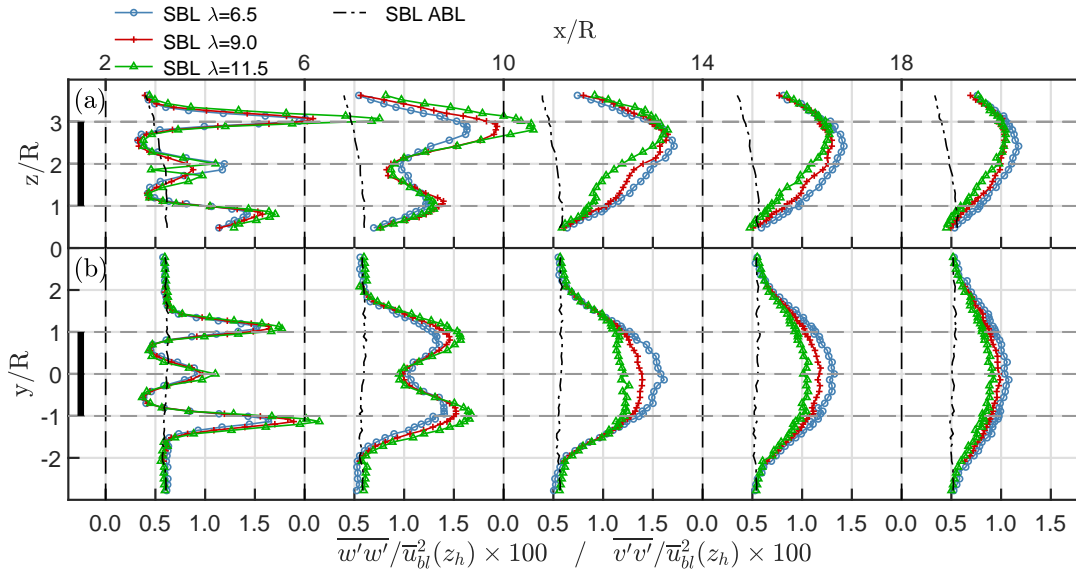


Figure 5.7: Profiles of Reynolds stress in radial direction (a) $\overline{w'w'}$ in the mid-vertical and (b) $\overline{v'v'}$ in the mid-horizontal plane for tip speed ratios $\lambda = 6.5, 9.0, 11.5$ at axial positions $x/R = 2, 6, 10, 14, 18$ for SBL. Legend denotes the tip speed ratio for each profile.

turbulence. This effect is shown in Section 5.2.2 and the origin of the suppression is discussed in more detail in the spectral analysis of Section 5.3.

In Figure 5.8 different quantities characterising the wake development in axial direction are shown. In (a) the centreline velocity deficit is depicted which is defined to be the maximum velocity deficit in the wake $\Delta u_C = \max(\Delta u)$. The lateral and vertical wake width σ_y and σ_z are shown in (b) and (c), respectively and (d) shows the vertical wake center position z_C . All quantities are calculated as defined in Eq.(2.56). It is important to notice that the definition of the lateral and vertical wake widths σ_y and σ_z is based on the assumption that the velocity deficit in the wake can be represented by a Gaussian distribution, which is just the case within the far wake. As it is expected from the mean axial velocity shown in Figure 5.2, the centreline velocity deficit and wake width differ significantly in the near wake but converge to similar values in the downstream direction. The above mentioned instability of the blade tip vortices leads to an enhanced momentum transfer from the outer flow into the wake and hence to a significant wake recovery. This explains the faster initial recovery of the centreline velocity deficit at higher tip speed ratios in Figure 5.8 (a) as well as the increased wake growth in (b) and (c).

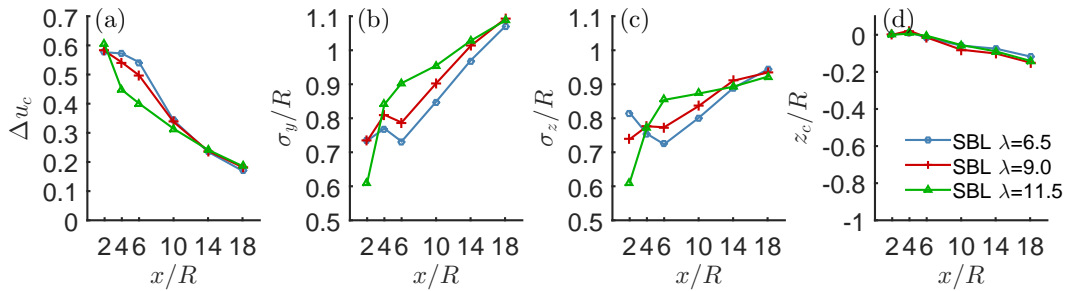


Figure 5.8: Wake characteristics of the un-yawed model wind turbine immersed in the SBL configuration, operating at tip speed ratios $\lambda = 6.5, 9.0, 11.5$: (a) centreline velocity deficit, (b) lateral and (c) vertical wake half width, (d) vertical centreline position.

5.2.2 Influence of the Ground Roughness on an Un-yawed Wind Turbine

Now we focus on the effect of ground roughness on the wake evolution. Figure 5.9 shows the spatial distribution of the normalised averaged axial velocity component $\bar{u}/\bar{u}_{bl}(z_h)$ for three different situations: a smooth and rough boundary layer and a case with low turbulence uniform approaching flow. In this and all following figures of this kind (a) denotes the mid-vertical and (b) the mid-horizontal plane. Most salient in the comparison is the fast wake recovery in case of the measurements within the two turbulent boundary layers (SBL, RBL) compared to the low turbulence uniform (LTU) flow condition. Due to the significant background turbulence within the two turbulent boundary layers, the momentum exchange between the wake and the outer flow is enhanced which results in a faster wake recovery. Since the level of background turbulence is higher in the RBL compared to the SBL, the wake develops even faster.

It is noticeable that in case of the LTU condition, the wake is unsymmetric regarding the rotor axis within the mid-horizontal plane. Below the lower tip of the rotor the flow field does not reach the free-stream velocity over the whole measured range. Most likely for this behaviour is the presence of the tower, which causes an additional wake. Due to the low background turbulence the turbulent momentum exchange with the outer flow is reduced and the wake of the tower persists over a long axial range.

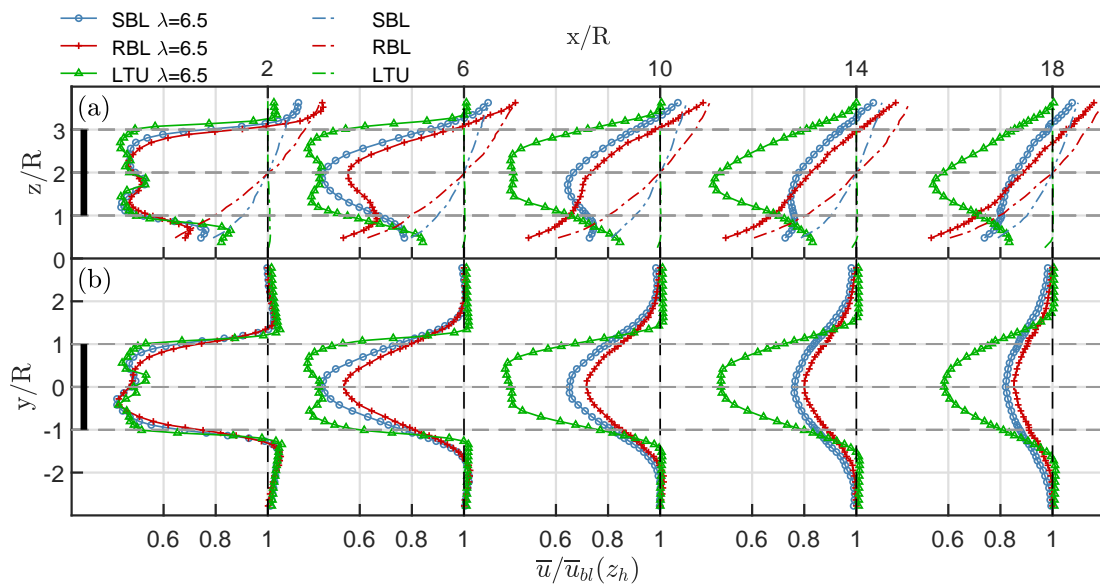


Figure 5.9: Profiles of mean axial velocity component \bar{u} in the (a) mid-vertical and (b) mid-horizontal plane at axial positions $x/R = 2, 6, 10, 14, 18$ for cases SBL, RBL and LTU. Legend denotes flow condition for each profile.

The wake recovery is associated with the rate of change of momentum and hence mainly with the radial distribution of the Reynolds shear stress $\overline{u'w'}$ and $\overline{u'v'}$ but also with the axial development of the Reynolds stress in axial direction $\overline{u'u'}$. Therefore, the spatial distribution of the Reynolds shear stress with respect to the radial direction $\overline{u'w'}$ in the mid-vertical and $\overline{u'v'}$ in the mid-horizontal plane, normalised by the velocity at hub height $\bar{u}_{bl}(z_h)$, is shown in Figure 5.10. Figure 5.11 depicts the spatial distribution of the normalised Reynolds stress in axial direction $\overline{u'u'}/\bar{u}_{bl}^2(z_h)$.

In the near wake ($x/R = 2 - 6$) around the tip region sharp peaks in the shear and normal

stress distribution can be observed, which in downstream distance become smoother and decrease in magnitude. This leads to the fast recovery in this region seen in Figure 5.9. Close to the rotor axis, however, the shear stress exhibits a smoother distribution. In the proximity of the turbine ($x/R = 2$) a plateau is observable, which in case of the LTU flow condition persists downstream to a distance of $x/R = 14$. A similar behaviour can be seen in the distribution of the Reynolds stress in axial direction in Figure 5.11 where for the LTU flow condition the normal stress first starts to rise at a downstream distance of $x/R = 14$. For the measurements within the turbulent boundary layers this rise can be observed at shorter distance. In case of the SBL at a distance of $x/R = 10$ and for the RBL already at a distance of $x/R = 6$.

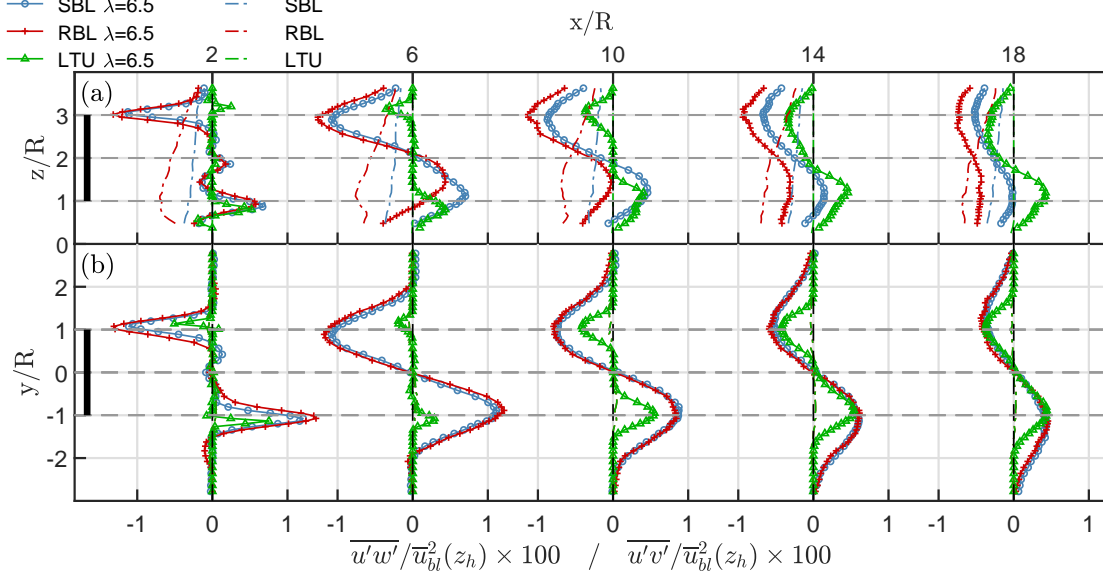


Figure 5.10: Profiles of the Reynolds shear stress (a) $\overline{u'w'}$ in the mid-vertical and (b) $\overline{u'v'}$ in the mid-horizontal plane at axial positions $x/R = 2, 6, 10, 14, 18$ for cases SBL, RBL and LTU. Legend denotes flow condition for each profile.

As mentioned in Section 5.2.1 a local suppression of the Reynolds stresses is observable in the vicinity of the model wind turbine immersed in the smooth boundary layer. Indeed, this suppression is even more significant in case of the model wind turbine operating within the RBL. Here, in the vicinity of the rotor an even stronger suppression of the Reynolds stress in axial direction, see Figure 5.11, as well as in the azimuthal direction, see Figure 5.12, and radial direction (not shown here) is clearly visible. In case of the Reynolds stress in axial direction this suppression persists along the whole measured axial range for the region below the hub $z < z_h$. The origin of the suppression is discussed in more detail in the spectral analysis of Section 5.3.

Figure 5.13 shows (a) the centreline velocity deficit $\Delta u_C = \max(\Delta u)$, (b) and (c) the lateral and vertical wake widths σ_y and σ_z , as well as (d) the vertical wake center position z_C in the vertical plane, determined by the momentum deficit center given in eq.(2.56).

To quantify the onset of the far wake, the velocity deficit $\Delta u_{C,0}$ defined in the analytical wake model of Bastankhah & Porté-Agel [12] can be used as a measure to distinguish between the near and far wake region. Therefore, the predicted value of $\Delta u_{C,0}$ is shown in Figure 5.13(a) as horizontal dashed line for each case. The location where it intersects with the measured centreline velocity deficit Δu_C then denotes the onset of the far wake,

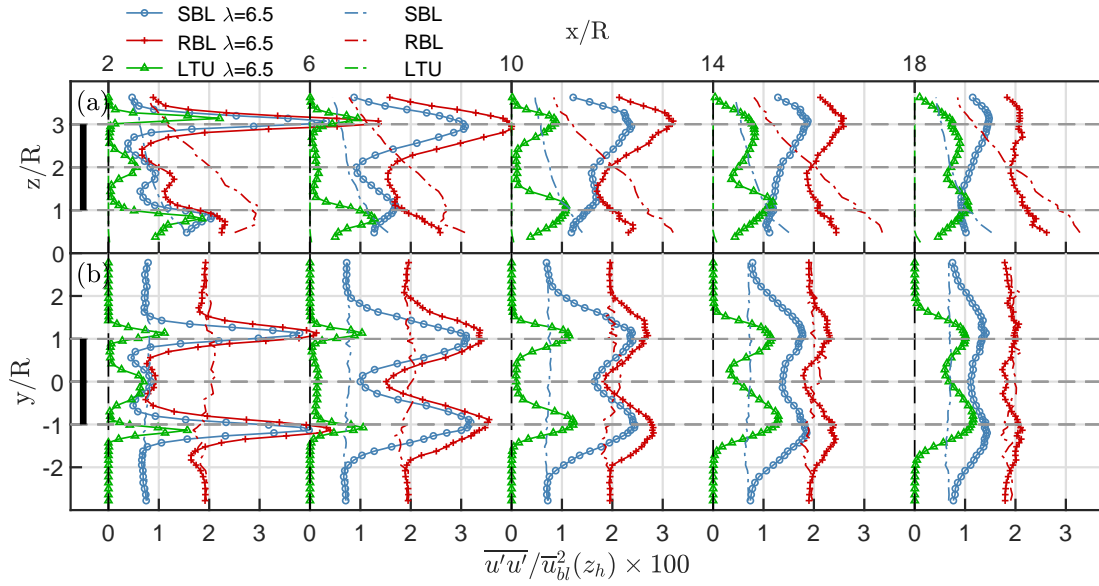


Figure 5.11: Profiles of Reynolds stress in axial direction $\overline{u'u'}$ in the (a) mid-vertical and (b) mid-horizontal plane at axial positions $x/R = 2, 6, 10, 14, 18$ for cases SBL, RBL and LTU. *Legend* denotes flow condition for each profile.

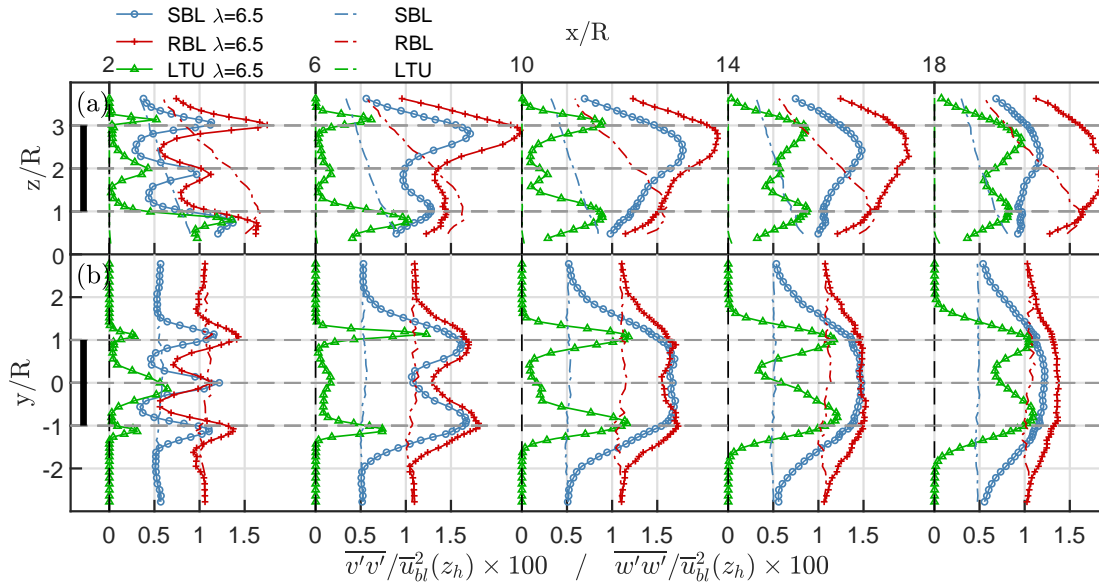


Figure 5.12: Profiles of Reynolds stress in azimuthal direction (a) $\overline{v'v'}$ in the mid-vertical and (b) $\overline{w'w'}$ in the mid-horizontal plane at axial positions $x/R = 2, 6, 10, 14, 18$ for cases SBL, RBL and LTU. *Legend* denotes flow condition for each profile.

which is indicated by a vertical dashed line for each case. A comparison with the distribution of the velocity deficit shown in Figure 5.9 confirms the consistency of prediction and measurements. With that it becomes clear that in case of the LTU flow condition the wake reaches far wake conditions just at the very end of the measured axial range.

It also explains the very distinct development of the lateral and vertical wake width compared to the development of the wakes within the turbulent boundary layers, see Figure 5.13(b) and (c). In these cases far wake conditions are already reached in the region of

$x/R \approx 4 - 6$. Downstream of that, for the smooth boundary layer, both vertical and

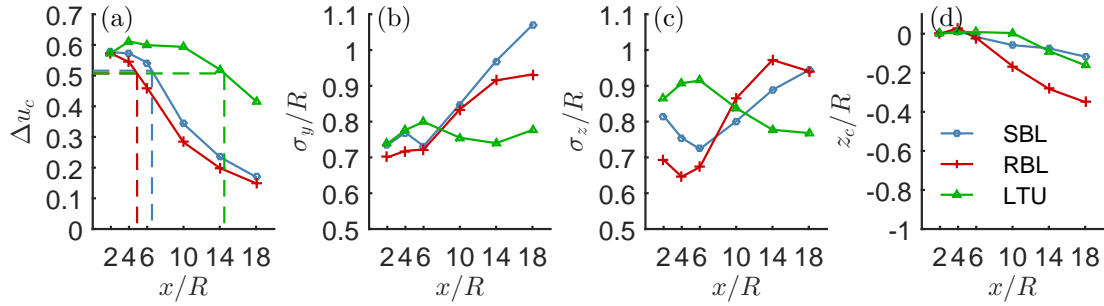


Figure 5.13: Wake characteristics of the un-yawed model wind turbine operating at $\lambda = \lambda_{dsgn}$ immersed in different ambient flow conditions: (a) centreline velocity deficit, (b) lateral and (c) vertical wake half width, (d) vertical centreline position. The legend indicates the flow condition.

lateral wake width exhibit the well known linear wake growth. For the rough boundary layer the vertical wake width grows faster than in the smooth case, which is in agreement with the LES study of Wu & Porté-Agel [157] and the experimental investigation of Jin & Chamorro [73] et al.. However, the lateral wake width is smaller than in the smooth case and both, lateral and vertical growth rates, decrease for downstream distances $x/R > 10$. There is also a noticeable displacement of the vertical centreline position, represented by the momentum deficit eq.(2.56), towards the ground, which is significantly increased in case of the rough boundary layer, see Figure 5.13(d).

This displacement as well as the deviations from the linear wake growth in case of the rough boundary layer can be argued with a change of the streamwise momentum deficit in the wake of a wind turbine which is immersed in a highly sheared boundary layer as it is discussed in Section 2.3.1. As the vertical mean shear is highest close to the ground, according to eq.(2.54) the momentum deficit increases in this region. Consequently this results in a displacement of the momentum deficit center.

This explanation is depicted in more detail in Figure 5.14 where the velocity deficit of the wake in (a) the LTU flow condition, (b) the SBL and (c) the RBL is shown for all measured axial positions. The red dots therein indicate the vertical position of the momentum deficit center. Over the whole measured range in case of the SBL the velocity deficit maintains almost symmetric. In case of the RBL, however, a significant increase of the velocity deficit close to the ground can be seen which then results in an increase of the streamwise momentum deficit and a significant descent of the momentum deficit center. With that, in contrast to the wake immersed in the SBL, the assumption of a conservation of the streamwise momentum deficit ($\Theta \propto \Delta u_C \sqrt{\sigma_y \sigma_z}$) can not be valid for the wake within the RBL. Hence, it is plausible that the wake width in this case develops different to the often observed linear wake growth.

In case of the wake within the LTU flow condition, the velocity deficit is also unsymmetric regarding the rotor axis, see Figure 5.14(a), since below the bottom rotor tip the flow does not reach the free stream velocity. This however, is unlikely to be related to a gradual loss of streamwise momentum as the boundary layer developing at the ground only becomes visible in the measurement at the furthest downstream locations, see Figure 5.9(a). Additionally the velocity deficit does not increase with downstream distance as it is the case in the RBL flow condition. As outlined above, it is most likely that it is the wake of the tower which causes this velocity deficit. With downstream distance the

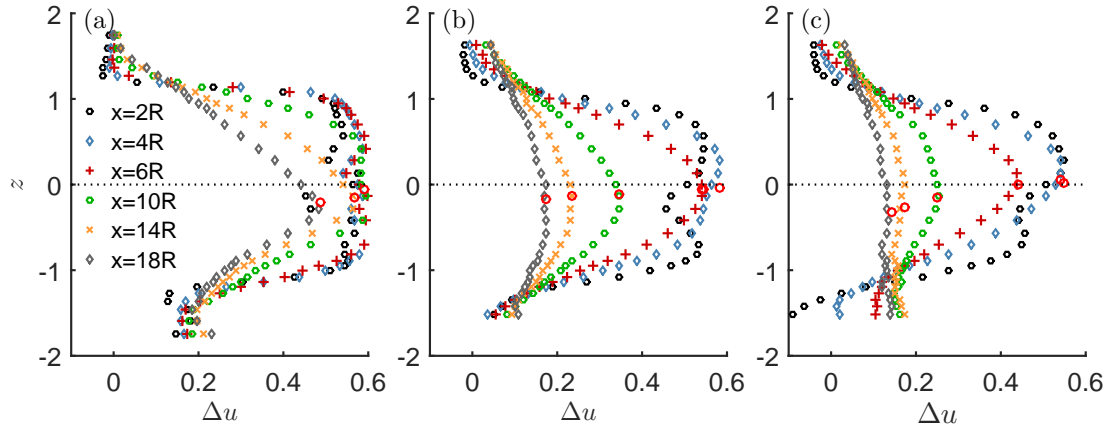


Figure 5.14: Vertical profiles of the velocity deficit in the wake of the un-yawed model wind turbine operating at $\lambda = \lambda_{dsgn}$ immersed in the (a) LTU, (b) SBL and (c) RBL flow condition. The *legend* indicates downstream position and *red dots* indicate the vertical wake centreline position.

wind turbine wake recovers whereas the velocity deficit below the bottom rotor tip persists causing a visible descent of the maximum velocity deficit, see Figure 5.14(a), and of the momentum deficit center, see Figure 5.13(d).

5.2.3 Influence of the Ground Roughness on a Yawed Wind Turbine

As already discussed in Section 5.2.2, a higher level of turbulence in the ambient flow enhances the momentum exchange between the wake and the outer flow which results in a faster wake recovery. In the same manner the wake also loses its potential to penetrate the lateral undisturbed flow in case of a yaw misalignment and is hence less deflected as it can be seen in Figure 5.15(b) and (c). Despite the large yaw angle and the deflection connected with it, the profiles maintain their Gaussian like distribution. However, with increasing yaw angle both the velocity deficit and the wake width, decrease in magnitude.

Similar to the development of the axial velocity, the profiles of the Reynolds stresses, represented by the turbulent kinetic energy in Figure 5.16, are decreased in magnitude in yawed conditions and follow the same trajectory as the velocity deficit while maintaining a shape similar to the un-yawed condition. Only in the case of RBL the shape is distorted for a yaw angle of $\gamma = 30^\circ$. The similarity of the profiles of the velocity deficit and the Reynolds stresses in the far wake is discussed in detail in Chapter 8.

Figure 5.17 shows (a) the centreline velocity deficit $\Delta u_C = \max(\Delta u)$, (b) the lateral wake width σ_y and (c) the lateral wake center position y_C , determined by the momentum deficit center given in eq.(2.56). As previously mentioned, in yawed conditions the maximum velocity deficit and the wake width decrease in yawed conditions, which for all flow conditions becomes most salient for a yaw angle of $\gamma = 30^\circ$. By yawing the turbine, the frontal area (e.g. the area normal to the incoming flow) becomes elliptic with a lateral semi-minor axis which is smaller than the radius of the circular rotor frontal area in un-yawed conditions. Therefore, the forces acting normal to the rotor disc reduce, which results consequently in a reduced thrust coefficient, shown in Figure 4.12, and hence in a reduced velocity deficit. As the lateral axis of the rotor frontal area becomes smaller with increasing yaw angle, the initial lateral wake width shown in (b) decreases as well.

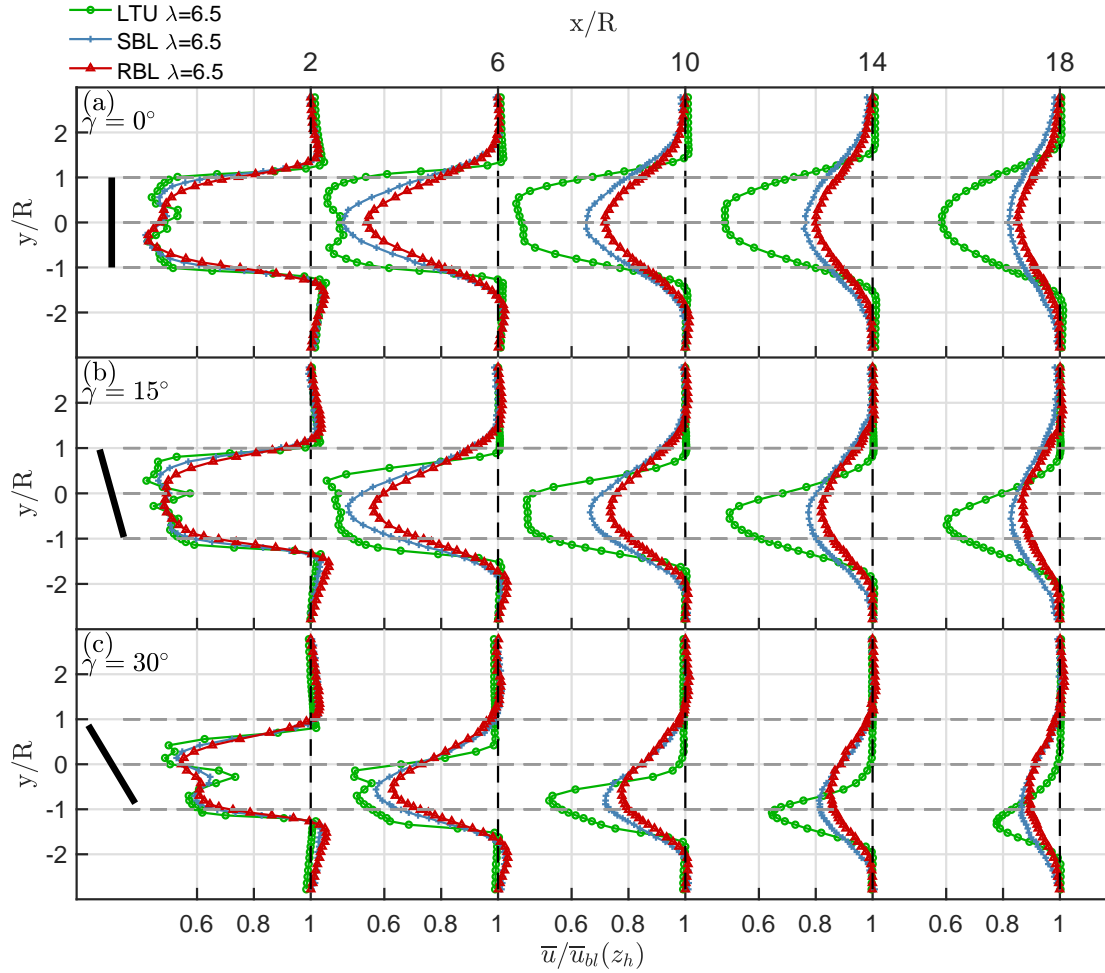


Figure 5.15: Lateral profiles of the normalised streamwise velocity $\bar{u}/\bar{u}_{bl}(z_h)$ in the wake of the model wind turbine immersed within the SBL (blue line) and RBL (red line) and LTU flow condition (green line) operating at (a) $\gamma = 0^\circ$, (b) $\gamma = 15^\circ$ and (c) $\gamma = 30^\circ$.

However, for all flow conditions the spreading rate in downstream direction seems to be uninfluenced by the yawing. These findings are in accordance with the results of Bastankhah & Porté-Agel [12]. The effect of the flow condition on the spreading rate is discussed above in Section 5.2.2. As outlined above, with increasing turbulence level of the ambient flow, the wake loses its potential to penetrate the lateral undisturbed flow and is hence less deflected in yawed conditions. This is clearly observable in the far wake region shown in Figure 5.17(c). In the near wake region, however, the initial wake deflection seems to be unaffected by the flow condition.

Another important measure to characterise the deflection of the wake is the skew angle, which here is defined to be the ratio of the local lateral and axial velocity $\theta = \bar{v}/\bar{u}$ (using the small-angle approximation $\tan(x) \approx x$). It can also be interpreted to indicate the alteration of the wake as it is the lateral tangent to the velocity vector of the flow.

Bastankhah *et al.* [12] provided a mathematical proof that in the far wake of a yawed wind turbine the skew angle θ has an asymmetric distribution with respect to the wake centre and that the lateral gradient of the mean axial velocity $\partial\bar{u}/\partial y$ has an extremum if the skew angle has an extremum ($\partial\theta/\partial y = 0$). Moreover, they showed that lateral profiles of the skew angle also exhibit a Gaussian like shape with a half width similar to the half

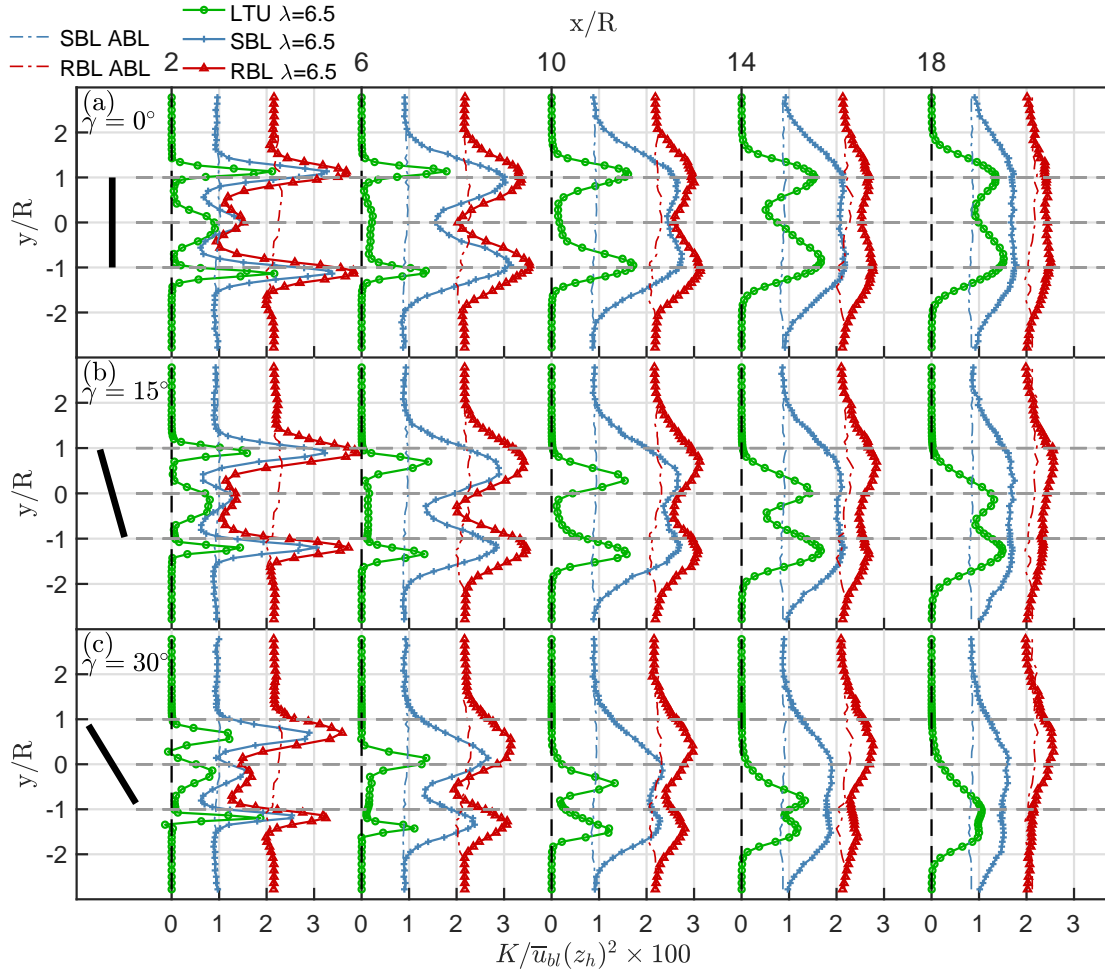


Figure 5.16: Lateral profiles of the normalised turbulent kinetic energy $K/\bar{u}_{bl}(z_h)^2$ in the wake of the model wind turbine immersed within the SBL (blue line) and RBL (red line) and LTU flow condition (green line) operating at (a) $\gamma = 0^\circ$, (b) $\gamma = 15^\circ$ and (c) $\gamma = 30^\circ$.

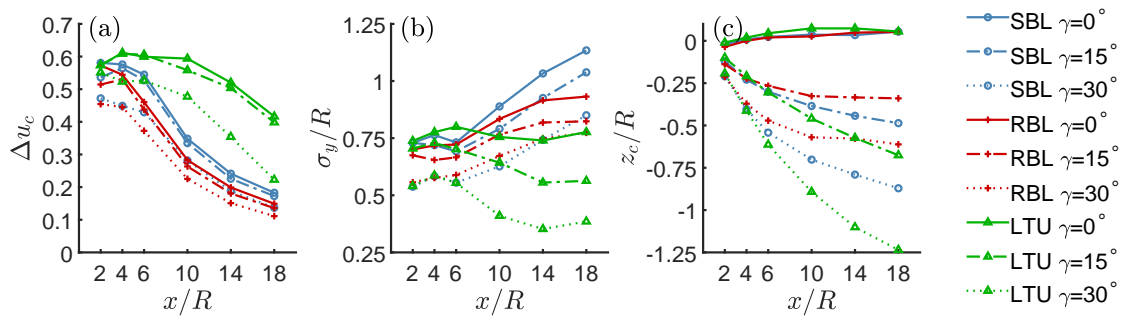


Figure 5.17: Wake characteristics of the model wind turbine immersed in different ambient flow conditions operating at $\lambda = \lambda_{dsgn}$ under various yaw angles: (a) centreline velocity deficit, (b) lateral wake half width and (d) lateral centreline position. The legend indicates the flow condition and yaw angle.

width of the mean axial velocity σ_y . That, however, implies that the lateral gradient of the skew angle $\partial\theta/\partial y$ must have an extremum at the location where the mean axial velocity has an extremum ($\partial\bar{u}/\partial y = 0$) and hence at the wake center.

Therefore, Figure 5.18 compares lateral profiles of the mean axial velocity and the skew angle in the wake of the model wind turbine at a yaw angle of $\gamma = 30^\circ$ for all flow conditions. To facilitate the comparison, the corresponding values of the mean axial velocity

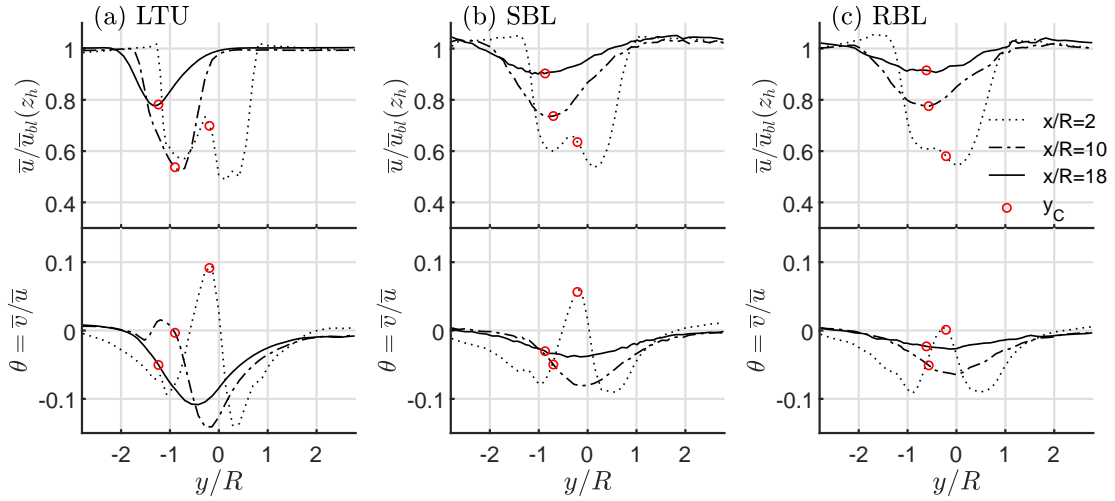


Figure 5.18: Lateral profiles of normalised mean axial velocity $\bar{u}/\bar{u}_{bl}(z_h)$ and flow skew angle $\theta = \bar{v}/\bar{u}$ in the wake of the model wind turbine immersed within (a) LTU flow condition, (b) the SBL and (c) the RBL flow condition operating at a yaw angle of $\gamma = 30^\circ$. The legend indicates the axial position.

and the skew angle at the wake center position are marked by red dots. It shows that within the far wake region (see Figure 5.13; SBL/RBL: $x/R \geq 6$; LTU: $x/R \geq 14$) the measurements support the statement given above. In the near wake region ($x/R = 2$), however, for all flow conditions it can be clearly seen that the skew angle exhibits an extremum at the wake center position and its lateral distribution is not asymmetric regarding this location. Other than expected from the initial wake deflection, see Figure 5.17(c), which is similar for all flow conditions, the magnitude of the skew angle decreases with increasing turbulence level of the ambient flow. This observation is somehow surprising as the lateral distribution of the mean axial velocity at that downstream location is quite similar for all flow conditions. From these results it can be concluded that within the near wake region the skew angle is not an appropriate measure for the wake deflection.

5.3 Spectral Analysis

The complex dynamics of turbulent wakes can be further investigated by means of spectral analysis. By decomposing a series of measurements into frequency components, the contribution of eddies of different scales to the evolution of the wake can be analysed in detail. Therefore, in this section spectral analysis of selected time series from hot wire measurements in the wake of the model wind turbine operating under various conditions are presented. For this purpose in Section 5.3.1, a brief description of the spectral postprocessing methods applied in the course of the following analysis is given. Other than the analysis of the wake characteristics which is organised by turbine state and flow condition, the spectral analysis is organised regarding specific effects in the wake. Therefore, the analysis focuses in Section 5.3.2 on the instability of the helical blade tip vortices, in Section 5.3.3 on the evolution of the spectral content in the wake, in Section 5.3.4 on considerations regarding the existence of self similarity in the wake, and in Section 5.3.5 on the meandering of the wake.

5.3.1 Methodology

The Fourier transform of a time series $x(t)$ of a stationary random process recorded over the time interval $0 < t < T$ is defined as

$$\hat{x}(f) = \frac{1}{T} \int_0^T x(t) e^{-i2\pi ft} dt \quad (5.1)$$

where f is the frequency. To analyse the contribution of different frequency components to the variance of the time series, the power spectrum $S_{xx}(f)$ of the signal can be computed. It is defined as

$$S_{xx}(f) = \hat{x}(f) \cdot \hat{x}(f)^* \quad (5.2)$$

with $\hat{x}(f)^*$ being the complex conjugated of $\hat{x}(f)$. For turbulence, it is typically anticipated that the original signal is not physically like waves, but it is useful to break the signal into components of different frequencies that are associated with different eddy sizes [139]. For the following spectral analysis it is important to notice that integrating the power spectrum over all frequencies equals the variance of the time series $\sigma_x^2 = \int S_{xx}(f) df$. Therefore, the integral of the power spectrum of a velocity component equals the corresponding Reynolds stress, e.g. $\overline{u'u'} = \int S_{uu}(f) df$.

Similar to the power spectrum, the cross spectrum of the time series $x(t)$ and $y(t)$ is defined as

$$S_{xy}(f) = \hat{x}(f) \cdot \hat{y}(f)^* = Co_{xy} + iQ_{xy} \quad (5.3)$$

Other than the power spectrum, the cross spectrum is a complex number, where the real part is defined as the cospectrum $Co_{xy}(f) = Re(S_{xy}(f))$ and the imaginary part is defined as the quadrature spectrum $Q_{xy}(f) = Im(S_{xy}(f))$. Analogously to the integral of the power spectrum, integrating the cospectrum over all frequencies equals the covariance of the time series $\sigma_{xy}^2 = \int Co_{xy}(f) df$. Therefore, the integral of the cospectrum of two velocity components equals the corresponding Reynolds shear stress, e.g. $\overline{u'v'} = \int Co_{uv} df$ and $\overline{u'w'} = \int Co_{uw} df$.

Given the definitions above, the coherence spectrum can be defined as

$$C_{xy} = \frac{S_{xy}S_{xy}^*}{S_{xx}S_{yy}} = \frac{Co_{xy}^2 + Q_{xy}^2}{S_{xx}S_{yy}}. \quad (5.4)$$

The coherence spectrum is a real number in the range of 0 to 1. Large values at any frequency f implies that $x(t)$ is strongly correlated to $y(t)$ at that frequency, regardless of phase differences between $x(t)$ and $y(t)$. Therefore, within a turbulent flow for a given frequency this can indicate if an organised flow motion is present, such as wake meandering.

In this work, power and cross spectra are estimated using Welch's averaged, modified periodogram method of spectral estimation [154]. The signals are recorded over 120 s and sampled with a time-resolution of 3 kHz. The spectra are estimated using Hanning window segments with equal window length of $2^{14} = 16384$ samples and 50% overlap between subsequent segments.

5.3.2 Tip Speed Ratio Dependency of the Mutual Inductance Instability

In various studies, mutual inductance instability has been shown to be the main cause of wake destabilization, which results in pairing of tip vortices and ultimately their breakdown. Sarmast *et al.* [122] showed that the most unstable modes of the instability are characterized by an out-of-phase displacement of successive helix turns which lead to local vortex pairing. Based on stereoscopic particle induced velocimetry (PIV) Lignarolo *et al.* [91] analysed the mixing properties in the wake by applying phase locked averaging of the velocity fields. They revealed that in the very proximity of the rotor the tip vortices inhibit mixing of the wake during its expansion. Whereas further downstream, due to the mutual inductance instability, tip vortices pair and break down, causing a sudden increase of the net entrainment of the mean-flow kinetic energy and, thus, generating a more efficient mixing by the action of random flow motion. By analysing the turbulent kinetic energy (TKE) budget obtained from large eddy simulations, Wu *et al.* [157] showed that the mixing process in the near wake consists of the advection of incoming flow turbulence into the wake as well as the redistribution of shear-produced TKE in radial direction, both inwards and outwards. In an earlier work Lignarolo *et al.* [90] observed that higher tip speed ratios intensify the mutual inductance instability which causes the tip vortices to break down closer to the rotor. Since in Section 5.2.1 it was observed that with increasing tip speed ratio the wake produced by the model wind turbine grows and recovers faster, in this section spectral analysis is applied to discuss the effect of the mutual inductance instability on the near wake behaviour.

Therefore Figure 5.19 shows the pre-multiplied power spectra (a) $f \cdot S_{uu}$ and (b) $f \cdot S_{ww}$ in the vicinity of the rotor $x/R = 2$ at the height of the top tip $z/R = 3$ for the SBL flow condition. Just for the sake of visibility, only results for tip speed ratios of $\lambda = 6.5$ and 11.5 are shown. For comparison the power spectra of the flow measured in the undisturbed boundary layer and presented in Chapter 3, are given. As the free-stream velocity and the rotational frequency of the rotor is different for both tip speed ratios, the frequency axis is normalised by the rotational frequency of the rotor f_{1P} and the power spectra are normalised by the mean velocity at hub height within the undisturbed boundary layer $\bar{u}_{bl}(z_h)$. Pre-multiplied spectra are chosen here and in the following analysis as they give weight to the less energetic small scales in the flow and thereby help to visualise peaks at the rotor frequency f_{1P} and the blade passing frequency f_{3P} . For time series recorded

in the proximity of the turbine close to the rotor edge, singular peaks were present at the rotor frequency f_{1P} . These are considered to stem from vibrations induced by a pitch misalignment of one of the blades and are therefore removed from the spectra presented in the following.

For both TSRs significant differences can be identified in the composition of the power spectra. For the design tip speed ratio of $\lambda_{dsgn} = 6.5$, significant peaks can be observed at the turbine and blade passing frequencies, f_{1P} and f_{3P} , especially in the spectral content of the vertical velocity component $f \cdot S_{ww}$, see Figure 5.19 (b). Furthermore, in the power spectrum of the axial velocity component $f \cdot S_{uu}$ a low-frequency peak is observable near $0.1f_{1P}$. The low-frequency content of the power spectra at design TSR is, however, significantly smaller than at the high TSR of $\lambda = 11.5$. For the latter no peaks are present at the turbine and blade passing frequencies but the power spectrum of the axial velocity component $f \cdot S_{uu}$ is significantly increased for $f/f_{1P} \approx 0.1$ and the power spectrum of the vertical velocity component $f \cdot S_{ww}$ is increased for $0.1 \leq f/f_{1P} \leq 1$.

These changes in the low- and high-frequency content of the power spectra for both TSRs can be argued with the effect of the mutual inductance instability. The vanishing of peaks at the blade passing frequency for the high TSR can be explained by the advanced process of vortex pairing and their break down, due to which single blade tip vortices might no longer be detectable in the wake. In case of the design tip speed ratio $\lambda = 6.5$ the situation is different. The presence of a clear peak at the blade passing frequency f_{3P} in the $f \cdot S_{ww}$ power spectrum indicates the presence of single blade tip vortices. However, the origin of the peaks at the turbine frequency f_{1P} and its double $2f_{1P}$ is not completely clear. A similar constellation can be observed in the data of Chamorro *et al.* [30], whereas Hancock *et al.* [56] also observed a peak at the turbine frequency f_{1P} and suggest that it occurred due to deficiencies at one of the blades. From the work of Lignarolo *et al.* [91], however, it can be concluded that it is due to the process of vortex pairing. They argue that for a three-bladed horizontal-axis wind turbine tip vortices form groups of three, even though their study has been conducted for a two-bladed wind turbine.

As mentioned in the beginning of this section, the break down of the tip vortices causes a sudden increase of the net entrainment of TKE into the wake, partially due to the vertical transport of turbulence produced in the shear layer between the wake and the free-stream flow, and partially due to the advection of turbulence of the incoming flow. Following this argument, the significant increase in the power spectra $f \cdot S_{uu}$ at $f/f_{1P} \approx 0.1$ for both TSRs and the increase in $f \cdot S_{ww}$ in the range of $0.1 \leq f/f_{1P} \leq 1$ for $\lambda = 11.5$ indicate the break down of the tip vortices and the entrainment of TKE, just at different stages of this process for the two different TSRs.

The large-scale turbulence of the incoming flow is then amplified within the shear layer between the wake and the outer flow. This can be deduced from the co-spectra of the shear production term $C_{o_{uw}} \cdot \partial \bar{u} / \partial z$, shown in Figure 5.20 in non-dimensional form, which, as discussed in Section 2.3.2, in the top tip region is the dominant turbulence production term. Here the negative peak in the frequency range $0.1 \leq f/f_{1P} \leq 0.3$ for the TSR $\lambda = 11.5$ indicates a significant production of turbulence. The positive peaks at f_{1P} and f_{3P} for the TSRs $\lambda = 11.5$ and $\lambda = 6.5$, respectively, are thought to be a result of the tip vortex pairing and their break down.

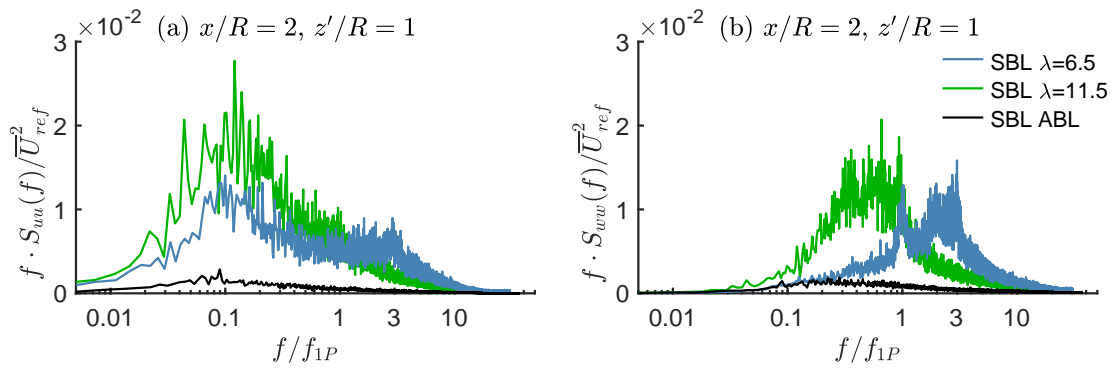


Figure 5.19: Normalised and pre-multiplied power spectra $f \cdot S_{uu}$ and (b) $f \cdot S_{wv}$ for the axial distance $x/R = 2$ and vertical height $z'/R = (z - z_h)/R = 1$ for $\lambda = 6.5$ and $\lambda = 11.5$. The legend denotes the tip speed ratio and flow condition.

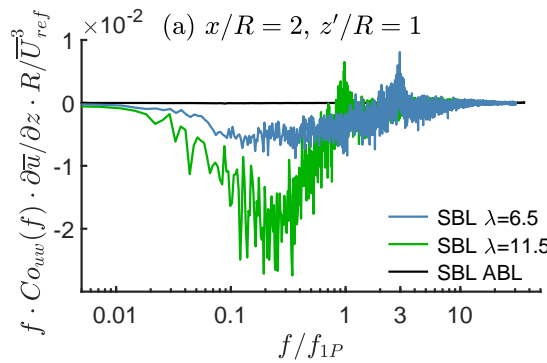


Figure 5.20: Non-dimensional co-spectra of the shear production term $C_{o_{uw}} \cdot \partial \bar{u} / \partial z \cdot R / \bar{U}_{ref}^3$ for the axial distance $x/R = 2$ and vertical height $z'/R = (z - z_h)/R = 1$ for $\lambda = 6.5$ and $\lambda = 11.5$. The legend denotes the tip speed ratio and flow condition.

5.3.3 Wake Development in the Spectral Domain

An interesting view on the spectral content of the flow within a wind turbine wake was given by Chamorro *et al.* [31]. They found that the turbine introduced strong turbulent energy in the high frequency range but also damped large scales of the incoming turbulent boundary layer flow. The latter was observed especially below hub height where it locally suppressed the Reynolds stress in the axial direction below the ambient level. They suggested that the turbine acts as an 'active filter', introducing small-scale structures which happen to disrupt the large-scale structures. More recently, Hancock *et al.* ([56],[57]) also observed such a local suppression for measurements within an unstable (suppression of Reynolds stresses in axial and radial direction) and a neutral boundary layer (just suppression in axial direction). Measurements within a stable boundary layer did not exhibit this effect. The authors suggested this phenomena might be a consequence of the turbine blocking streamwise fluctuations similar to the effect of a porous screen, as used in wind tunnel settling chambers. Even though Hancock *et al.* analysed the effect of thermal stability on the wake development, in their studies the level of suppression raised with increasing background turbulence (stable $I_u(z_h) \approx 5\%$, neutral $I_u(z_h) \approx 6.5\%$, unstable $I_u(z_h) \approx 9\%$), similar as it is observed in the present work. Indeed, as discussed in Section 5.2.2 the level of ambient turbulence significantly affects

the suppression. For the design tip speed ratio of $\lambda = 6.5$ the suppression in the wake immersed in the SBL flow is just noticeable in the vicinity of the rotor whereas in the RBL flow the suppression can even be observed within the far wake region. Therefore, to connect the mentioned studies with the present work, in the following first the spectral content of the flow in the near wake for different flow conditions is analysed in detail and subsequently the evolution of the far wake.

To analyse the spectral content in the near wake within both boundary layer configurations, Figure 5.21 shows the difference in the spectral content between the wake and the undisturbed boundary layer for the normalised and pre-multiplied power spectra (named power difference spectra in the following) of each velocity component (a)-(c) $f \cdot S_{uu}^\Delta / \overline{u_{bl}^2}(z_h)$, (d)-(f) $f \cdot S_{vv}^\Delta / \overline{u_{bl}^2}(z_h)$, and (g)-(i) $f \cdot S_{ww}^\Delta / \overline{u_{bl}^2}(z_h)$ at the axial position $x/R = 2$ within the SBL and RBL for $\lambda = 6.5$. Additionally, results are shown obtained within the SBL for $\lambda = 11.5$.

From Figure 5.21(a), in case of the SBL condition for a TSR of $\lambda = 6.5$, it can clearly be observed that the suppression of the Reynolds stress $\overline{u'u'}$ for $z/R < 2.7$ in the vicinity of the rotor stems from a reduction of the power difference spectra $f \cdot S_{uu}^\Delta / \overline{u_{bl}^2}(z_h)$ in the frequency range of $f/f_{1P} < 0.1$, which contributes most to the magnitude of $\overline{u'u'}$. In case of the RBL condition for the same TSR of $\lambda = 6.5$, see Figure 5.21(c), the reduction of the power difference spectra $f \cdot S_{uu}^\Delta / \overline{u_{bl}^2}(z_h)$ in the low frequency range is even more dominant. In the power difference spectra of the velocity components in lateral and vertical direction, $f \cdot S_{vv}^\Delta / \overline{u_{bl}^2}(z_h)$ and $f \cdot S_{ww}^\Delta / \overline{u_{bl}^2}(z_h)$, similar suppressions can be observed, yet less intense and at higher frequencies. This is due to the fact that vertical and lateral motions in the turbulent boundary layers do not exhibit strong large-scale organisation, as it occurs for the streamwise component [81].

In case of the wake in the SBL for a TSR of $\lambda = 11.5$ the power difference spectra of all velocity components differ significantly from the respective spectra for a TSR of $\lambda = 6.5$. For the power difference spectra $f \cdot S_{uu}^\Delta / \overline{u_{bl}^2}(z_h)$, see Figure 5.21(b), the low frequency content of $f/f_{1P} < 0.1$ is less suppressed. Furthermore, in the inner region of the rotor $1.5 < z/R < 2.5$ frequencies $f/f_{1P} \geq 0.1$ are increased, which results in a magnitude of the Reynolds stress $\overline{u'u'}$ above the ambient level. In the vicinity of the rotor, the Reynolds stresses in the lateral and vertical direction, $\overline{v'v'}$ and $\overline{w'w'}$, were shown to be rather independent of the chosen TSR, see Section 5.2.1. This is in accordance with the power difference spectra $f \cdot S_{vv}^\Delta / \overline{u_{bl}^2}(z_h)$ and $f \cdot S_{ww}^\Delta / \overline{u_{bl}^2}(z_h)$ presented here, compare Figure 5.21 (d),(g) with (e),(h). These exhibit TSR dependent differences only in the blade tip and root region, which are considered to stem from the break down of the blade tip vortices and the entrainment of large scale turbulence of the incoming flow into the wake as discussed in section 5.3.2.

As mentioned before Chamorro *et al.* [31] found that the turbine introduced strong turbulent energy in the high frequency range but also damped large scales of the incoming turbulent boundary layer flow and suggested that the turbine acts as an 'active filter', introducing small-scale structures which happen to disrupt the large-scale structures. The observed damping of frequencies below $f/f_{1P} < 0.1$ and amplification of frequencies above $f/f_{1P} > 0.1$ in the power spectra of the axial velocity component in the vicinity of the rotor shown in Figure 5.21(a) and (c) is in very good agreement with these findings. Unfortunately Chamorro *et al.* have not mentioned if any suppression of the Reynolds stresses below the ambient level is present in the measurement results nor do they mention the level of turbulence in the approaching boundary layer flow. Moreover, they also proposed that a turbine can be parametrised from a spectral perspective. The results

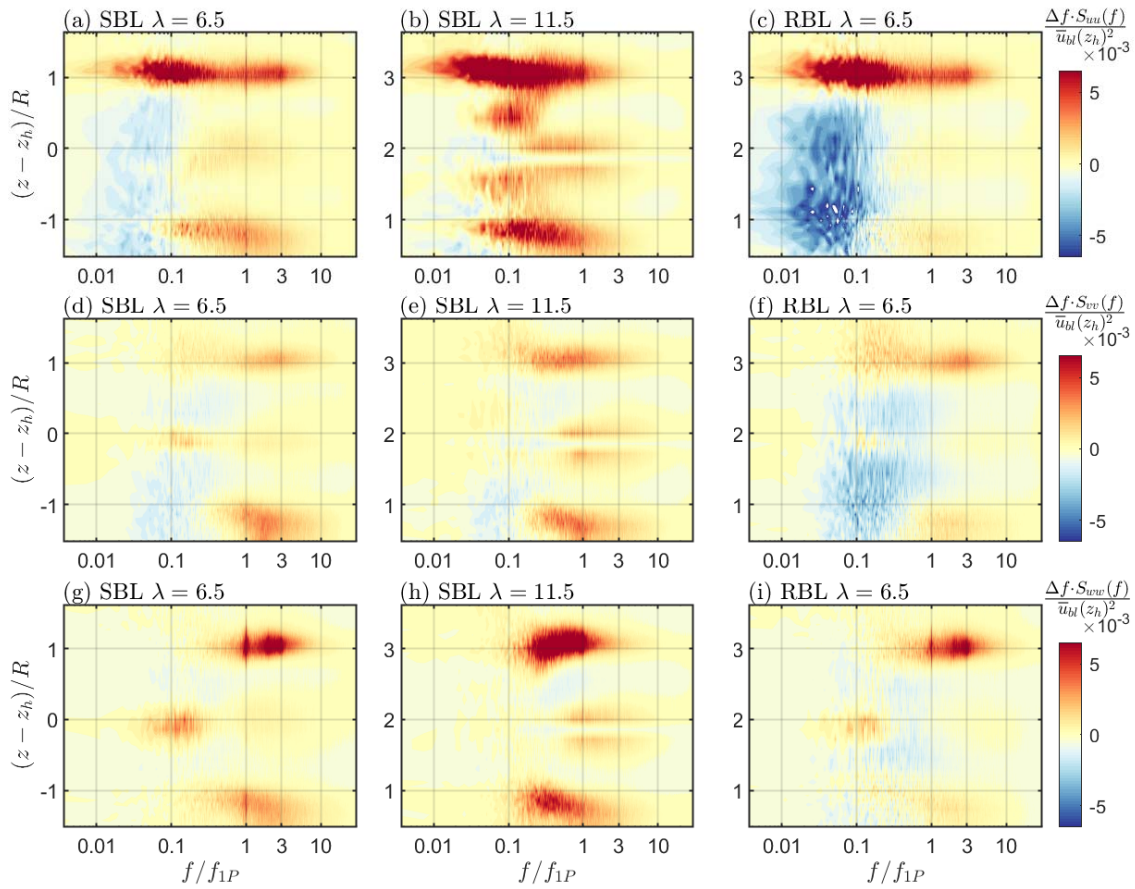


Figure 5.21: Difference of the pre-multiplied power spectra in the wake and the undisturbed boundary layer (a)-(c) $f \cdot S_{uu}^{\Delta} / \bar{u}_{bl}^2(z_h)$, (d)-(f) $f \cdot S_{vv}^{\Delta} / \bar{u}_{bl}^2(z_h)$, and (g)-(i) $f \cdot S_{ww}^{\Delta} / \bar{u}_{bl}^2(z_h)$ at the axial position $x/R = 2$; (a)/(d)/(g) SBL $\lambda = 6.5$, (b)/(e)/(h) SBL $\lambda = 11.5$, (c)/(f)/(i) RBL $\lambda = 6.5$.

shown here indicate that such a parametrisation would depend on the chosen tip speed ratio.

In the context of perceiving the wind turbine as an active filter, the analysis of the axial wake development in the spectral domain provides some interesting results. Therefore, Figure 5.22 shows the axial development of the normalised and pre-multiplied spectra $f \cdot S_{uu} / \bar{u}_{bl}^2(z_h)$ for various axial distances of the wake in the SBL, RBL, and LTU flow configuration, in (a)-(d) at hub height $z = z_h$ and (e)-(h) at 75% blade span in vertical direction $z = z_h + 0.75R$. For comparison power spectra of the recorded undisturbed boundary layer flow are shown additionally.

In the vicinity of the rotor at hub height, see Figure 5.22(a), the already mentioned local suppression of the power spectra below the ambient level is clearly visible for the wakes within the SBL and RBL flow for a TSR of $\lambda = 6.5$. Despite the significantly different magnitudes of the power spectra in the flow of the two undisturbed boundary layers, the power spectra within the wakes are rather similar. Even the power spectra for the LTU flow condition is similar in the high frequency range whereas it is more damped below the turbine frequency f_{1P} . Indeed, the difference in the power spectra of the wakes for different TSRs of $\lambda = 6.5$ and $\lambda = 11.5$ within the same boundary layer flow is much

bigger than the differences in the wakes for different flow conditions but with the same TSR.

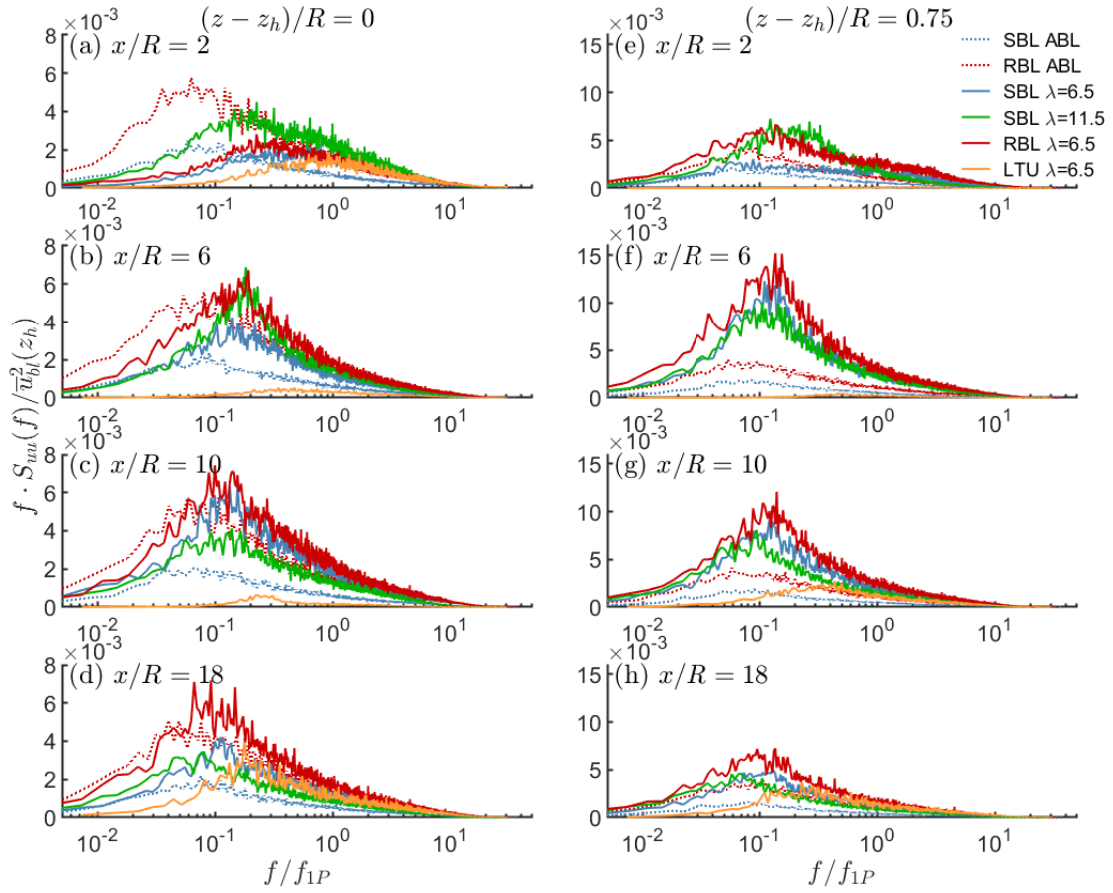


Figure 5.22: Normalised and pre-multiplied power spectra $f \cdot S_{uu} / \bar{u}_{bl}^2(z_h)$ in the wake and the undisturbed boundary layer at various downstream positions for vertical heights (a)-(d) $z' = (z - z_h)/R = 0$ and (e)-(h) $z'/R = (z - z_h)/R = 0.75$. The legend denotes the flow condition and tip speed ratio.

At the outward blade position in vertical direction, see Figure 5.22(e), the situation is clearly different. Here the wakes within different flow conditions but with the same TSR of $\lambda = 6.5$ also exhibit significant differences in the power spectra. These quite different observations in the inner and outer region of the wake can be explained by the influence of the ambient turbulence. In the near wake region, the shear layer between wake and outer flow is affected by turbulent momentum exchange which contributes to the breakdown of the helical tip vortices and initiates the recovery of the wake, whereas the inner region of the near wake is rather insensitive to the characteristics of the incoming flow. This can also be observed in the nearly identical mean axial velocities \bar{u} and similar Reynolds stress $\overline{u'u'}$ within both boundary layers at hub height, which, however, differ clearly in the outer regions of the wake (this even holds for LTU flow condition), see Figure 5.9 and 5.11 for axial distance of $x/R = 2$. From these results it can be hypothesised that in the very proximity ($x/R \ll 1$) of the rotor the power spectra become almost independent of the turbulence level of the incoming flow. This would support the view of describing the wind turbine as an 'active filter' which modulates the incoming turbulent structures almost independently of the incoming flow condition. Therefore, the wind turbine does actually not 'add' turbulence, it rather modulates the turbulent scales

according to its operational state.

As discussed in Section 5.3.2, the mutual inductance instability leads to the breakdown of the helical blade tip vortices and ultimately to a net entrainment and amplification of the incoming large-scale turbulence in the boundary layer. Similar to the intensification of the mutual inductance instability at large TSRs, the high level of ambient turbulence in the RBL flow leads to a break down of the helical blade tip vortices in short distance to the rotor. This can be observed in Figure 5.22(a),(b) and (e),(f) where scales in the range of $f/f_{1P} \approx 0.1$ are more rapidly amplified in the RBL flow than in the SBL. Further downstream the turbulent mixing with the boundary layer introduces less turbulent flow to the wake, due to which the power spectrum of the wake approaches that of the boundary layer asymptotically. The most significant difference of the wake development in the different boundary layers from the spectral point of view is that in the RBL the described process runs off in shorter axial distance due to the higher level of background turbulence. This statement also holds for the wake development at high tip speed ratio.

However, regarding the suppression of Reynolds stresses below the ambient level, a significant difference can be observed between the wake development in the SBL and RBL condition. Since in the inner region of the near wake the power spectra are rather similar compared to the power spectra of the flow in the different undisturbed boundary layers, after the initial amplification of large-scales at $x/R = 6$, these scales have to be further amplified in case of the RBL flow to converge towards the spectral content of the undisturbed boundary layer, whereas in case of the SBL flow they have to decay, see Figure 5.22(b),(c) and (d). This constitutes a substantial difference in the wake development. In case of the wake in the SBL flow to recover to boundary layer conditions, turbulence has to be dissipated or transported out of the wake as part of the mixing process, whereas for the wake in the RBL more turbulence needs to be generated or transported into the wake.

To understand this process in more detail, the TKE budget in the wake as discussed in Section 2.3.2 needs to be considered. Therefore, it should be recalled that at the lateral and vertical rotor edges the main contributor of shear production are $\overline{u'v'} \frac{\partial \bar{u}}{\partial y}$ and $\overline{u'w'} \frac{\partial \bar{u}}{\partial w}$, turbulent transport is dominated by $\frac{\partial \overline{v'K}}{\partial y}$ and $\frac{\partial \overline{w'K}}{\partial z}$, and advection is dominated by $\bar{u} \frac{\partial K}{\partial x}$. Hence, it can be concluded that turbulence produced at the rotor edges is mainly distributed inwards and outwards of the wake by turbulent transport. From the flow quantities recorded by means of triple hot-wire measurements, the complete TKE budget can not be analysed. However, analysis of the shear production term at the rotor edges are possible and can give some valuable insights.

In the following co-spectra of the Reynolds shear stresses $\overline{u'v'}$ and $\overline{u'w'}$ at the rotor edges in the mid-horizontal plane and the mid-vertical plane are analysed. Therefore, Figure 5.23 (a)-(d) show the pre-multiplied co-spectra $f \cdot Co_{uv}(y/R = -1, z_h)$ and (e)-(h) the pre-multiplied co-spectra $f \cdot Co_{uv}(y/R = +1, z_h)$ in the wake for various downstream positions. In the near wake the spectra are first amplified and subsequently decay with downstream direction, whereby the spectral distribution of the lateral shear stress is similar within both boundary layer configurations. In the far wake, for distances $x/R \geq 6$ it can clearly be observed that the spectra at $y/R = -1$ and $y/R = +1$ are skew symmetric and peak at $f/f_{1P} \approx 0.1$. Within the wake the lateral gradient of the axial velocity component at $y/R = -1$ and $y/R = +1$ is skew symmetric as well and opposite in sign to the lateral shear stress, hence $\partial \bar{u}(y/R = -1, z_h)/\partial y < 0$ and $\partial \bar{u}(y/R = +1, z_h)/\partial y > 0$, compare with Figure 5.9(b). Therefore, the shear production term $\overline{u'v'} \partial \bar{u}/\partial y$ is negative at these positions for all downstream locations and turbulence is produced at all scales.

It should be noticed that in the mid-horizontal plane for the flow to recover to boundary layer condition, the lateral shear stress $\overline{u'v'}$ and, therefore, the shear production term $\overline{u'v'} \partial \overline{u} / \partial y$ has to become zero.

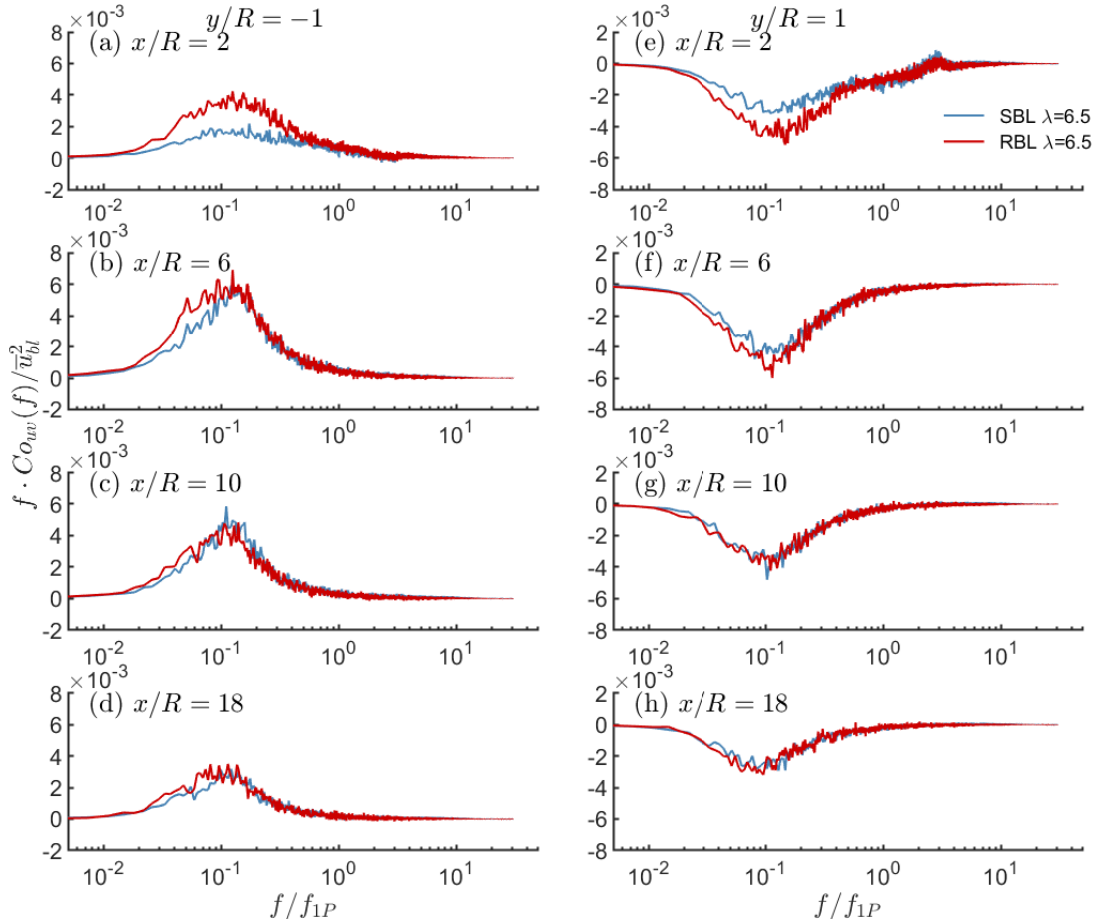


Figure 5.23: Normalised and pre-multiplied co-spectra of the lateral shear stress $f \cdot Co_{uv}(f) / \overline{u}_{bl}(z_h)^2$ at the rotor edges at hub height z_h for various downstream locations (a)-(d) at $y/R = -1$ and (e)-(h) at $y/R = 1$. The legend denotes the flow condition.

In the mid-vertical plane the situation is different since in the undisturbed boundary layer the Reynolds shear stress $\overline{u'w'}$ is negative for all heights. Figure 5.24 (a)-(d) show the pre-multiplied co-spectra $f \cdot Co_{uw}(y = 0, z'/R = -1)$ and (e)-(h) the pre-multiplied co-spectra $f \cdot Co_{uw}(y = 0, z'/R = +1)$ in the wake and the undisturbed boundary layers for various downstream positions. At the top tip for distances $x/R \geq 6$ the co-spectra of the vertical shear stress is negative for all scales and decays in downstream direction towards the spectral distribution of the undisturbed boundary layers with a peak at $f/f_{1P} \approx 0.1 - 0.2$. Similar to the situation at the rotor edges in the mid-horizontal plane, the vertical gradient of the axial velocity component at the top tip is opposite in sign to the vertical shear stress $\partial \overline{u}(y = 0, z'/R = +1) / \partial z > 0$, compare with Figure 5.9(a), and hence the shear production term $\overline{u'w'} \partial \overline{u} / \partial z$ is also negative for all downstream locations.

At the bottom tip, however, the co-spectra of the vertical shear stress is positive for all scales at the onset of the far wake $x/R = 6$, yet it has to decay to negative values in order to reach boundary layer conditions, see Figure 5.24 (a)-(d). At this height within the SBL, both the co-spectra of the vertical shear stress Co_{uw} and the vertical gradient of the

axial velocity component $\partial\bar{u}/\partial z$ become approximately zero at a downstream distance of $x/R = 18$. Therefore, for this configuration the shear production term $\overline{u'w'} \partial\bar{u}/\partial z$ remains negative over the complete measured distance. As mentioned above, since for the wake immersed in the SBL no suppression of the Reynolds stresses below the ambient level is present in the far wake region, the turbulence in the wake has to decay as the wake recovers. Therefore, the turbulence produced has to be transported out of the wake (or has to be dissipated). Within the RBL, however, $\partial\bar{u}/\partial z$ and $C_{o_{uw}}$ already become approximately zero at distances of $x/R = 6$ and $x/R = 10$, respectively, which results in a low turbulence production within this distance. This can be observed in Figure 5.25 where the pre-multiplied co-spectra of the vertical shear production term $f \cdot C_{o_{uw}}(f) \partial\bar{u}/\partial z$ at bottom tip height is shown in normalised form for various downstream locations. With this observations it becomes clear that the suppression of Reynolds stresses caused by the wind turbine cannot be overcome by production of turbulence over large downstream distances. Instead, the turbulence level within the wake can only rise by transport of turbulence of the surrounding flow into the wake, which is naturally limited to the ambient level.

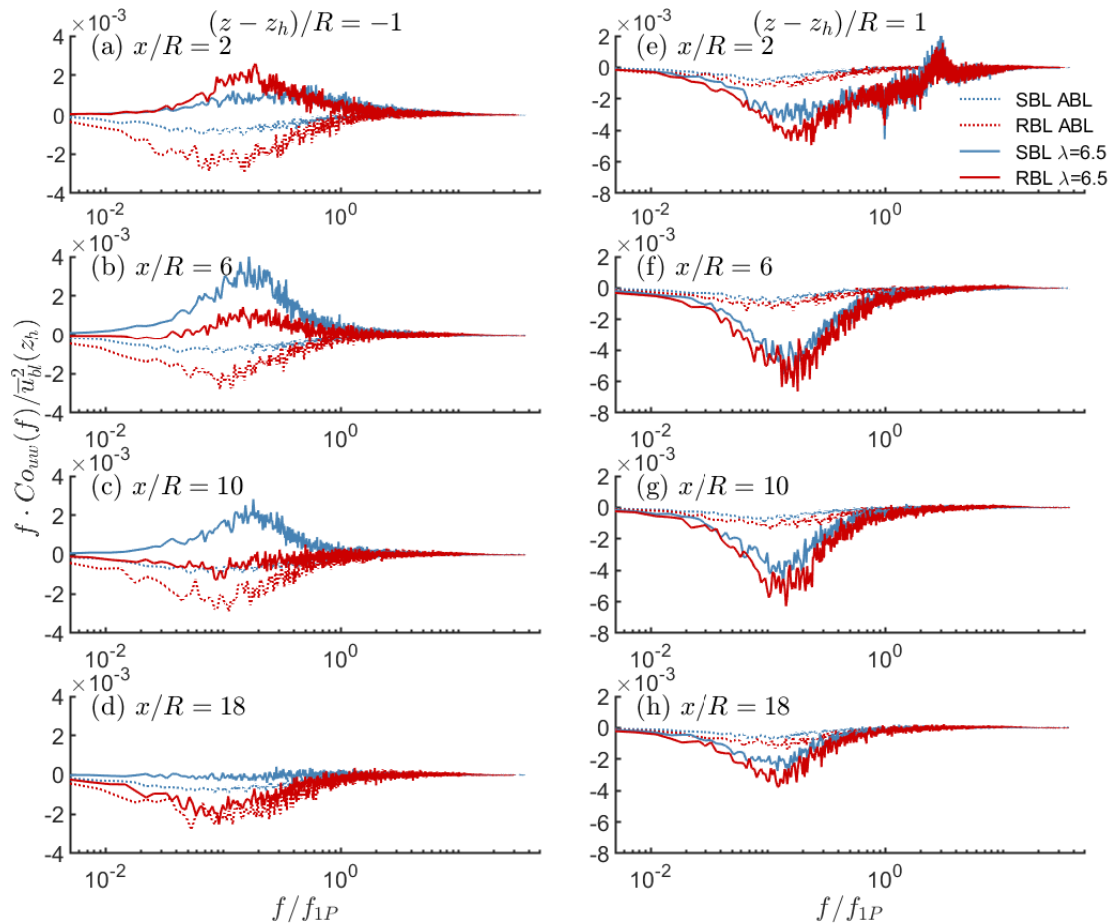


Figure 5.24: Normalised and pre-multiplied co-spectra of the vertical shear stress $f \cdot C_{o_{uw}}(f) / \bar{u}_{bl}(z_h)^2$ at the rotor edges in the mid-vertical plane for various downstream locations (a)-(d) $z' = (z - z_h)/R = -1$ and (e)-(h) $z'/R = (z - z_h)/R = 1$. The legend denotes the flow condition.

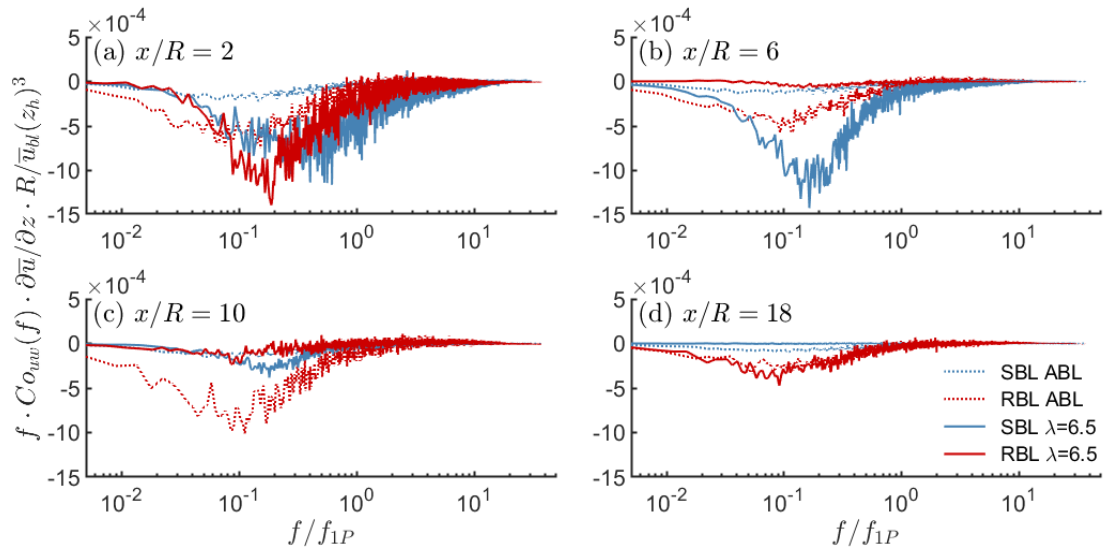


Figure 5.25: Normalised and pre-multiplied co-spectra of the vertical shear production term $f \cdot C_{ouw}(f) \cdot \partial \bar{u} / \partial z \cdot R / \bar{u}_{bl}(z_h)^3$ at the bottom tip $(z - z_h) / R = -1$ for various downstream locations in the wake and the undisturbed boundary layer (a)-(d). The *legend* denotes the flow condition.

5.3.4 Self Similarity in the Spectral Domain

Another interesting observation on the development of the wake can be made when the power spectra presented in Figure 5.22 are normalised to the local axial Reynolds stress $\overline{u'u'}$ instead of to the square of the mean axial velocity of the undisturbed boundary layer at hub height $\bar{u}_{bl}^2(z_h)$, as shown in Figure 5.26 for various axial distances of the wake and the undisturbed boundary layers (a)-(d) at hub height $z = z_h$ and (e)-(h) at 75% blade span in vertical direction $z = z_h + 0.75R$. Since the integral of the power spectrum yields the Reynolds stress itself $\overline{u'u'} = \int_f S_{uu}(f) df$ [139], this representation provides information on the relative contribution of the different turbulent scales to the magnitude of the Reynolds stress and makes signals comparable, even though the level of turbulence is different.

Therefore, first of all the resulting similarity of the power spectra of the two boundary layers in this representation should be noticed. This has already been shown in a different representation for the power spectra of all three velocity components in Figure 3.14 found in Section 3.4. As mentioned there, this is attributed to the technique applied to generate the turbulent boundary layers. Similar to these power spectra, the distribution of the power spectra within the wakes immersed in the two boundary layers become similar for a given location in the far wake $x/R \geq 6$ and subsequently converge towards the power spectra distribution of the undisturbed boundary layer. Nevertheless, it is important to notice, that in the pre-multiplied spectra more weight is given to higher frequencies, yet the scales in the low frequency range are the stress carrying motions. Therefore, differences in the low frequency range are of more importance. The evolution of the power spectra distribution in the wake is mostly characterised by the entrainment of large-scales contained in the boundary layer flow which causes the decrease of the dominant frequencies in the range of $0.1 < f/f_{1P} < 1.0$ in favour of lower ones. Just in the proximity of the rotor, notable differences in the power spectra distribution can be observed, especially for different TSRs, see Figure 5.26(a),(e). These differences are

assumed to be related to the instability of the helical tip vortices.

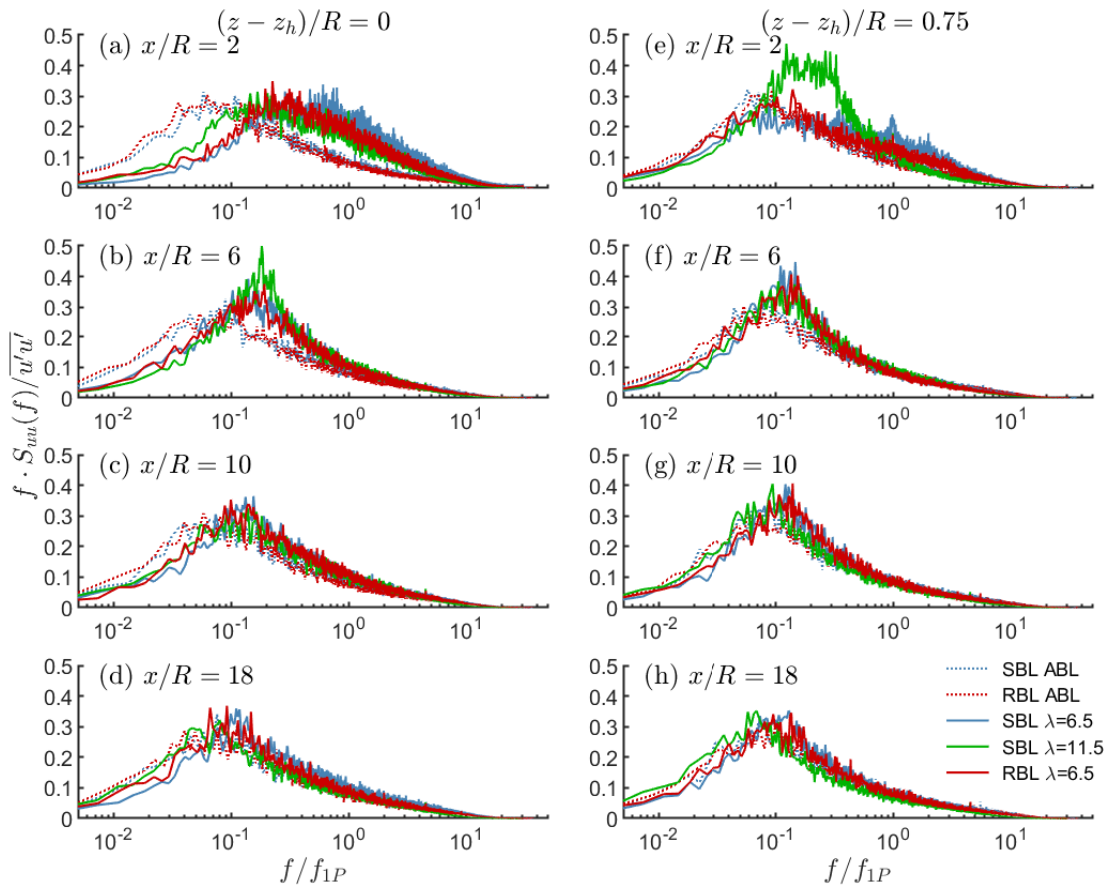


Figure 5.26: Normalised and pre-multiplied power spectra $f \cdot S_{uu} / \overline{u'u'}$ of the wake and the undisturbed boundary layer at various downstream positions for vertical heights (a)-(d) $z'/R = (z - z_h)/R = 0$ and (e)-(h) $z'/R = (z - z_h)/R = 0.75$. The legend denotes the flow condition.

The observation of similar spectral content in the far wake region is an important finding as it is a necessary prerequisite for the existence of self similarity in the wake. To analyse this more in detail, Figure 5.27 shows the normalised power spectra distributions for various locations in the axial, lateral, and vertical direction in (a),(c),(e) the undisturbed SBL and in (b),(d),(f) the far wake for a TSR of $\lambda = 6.5$ at the very same location. The normalised spectral distributions in the axial and lateral direction of (a),(c) the undisturbed boundary layer and (b),(d) in the wake are nearly identical. This is especially the case in the low frequency range, which as mentioned before, contributes most to the Reynolds stress $\overline{u'u'}$. Nevertheless, in the vertical direction the spectral distributions in (e) the undisturbed boundary layer and (f) in the wake deviate notably in the low frequency range. This is assumed to result from the quite different levels of turbulence and changes of the integral turbulent length scale over height present in the undisturbed boundary layer, see Figure 3.13 in Section 3.4. Therefore, in the vertical direction it might not be possible to find self similarity in the wake.

From these observations several conclusions can be drawn. In the far wake the spectral distributions of flow quantities become independent from the particular operational state of the wind turbine. Indeed, as will be shown in the next section, the low-frequency peak at $f/f_{1P} \approx 0.1$ corresponds to a Strouhal number of $St \approx 0.2$. Strouhal numbers in

this range are commonly found in the wakes of bluff bodies, such as spheres or porous discs, which also often exhibit self similarity. Therefore, it is justified to apply modelling approaches originally developed for bluff bodies to describe the development of a wind turbine wake. This is not limited to the description of the velocity deficit, for which various models can be found in literature, it also allows to model the evolution of turbulence in the wake, as it will be discussed in detail in Chapter 8.

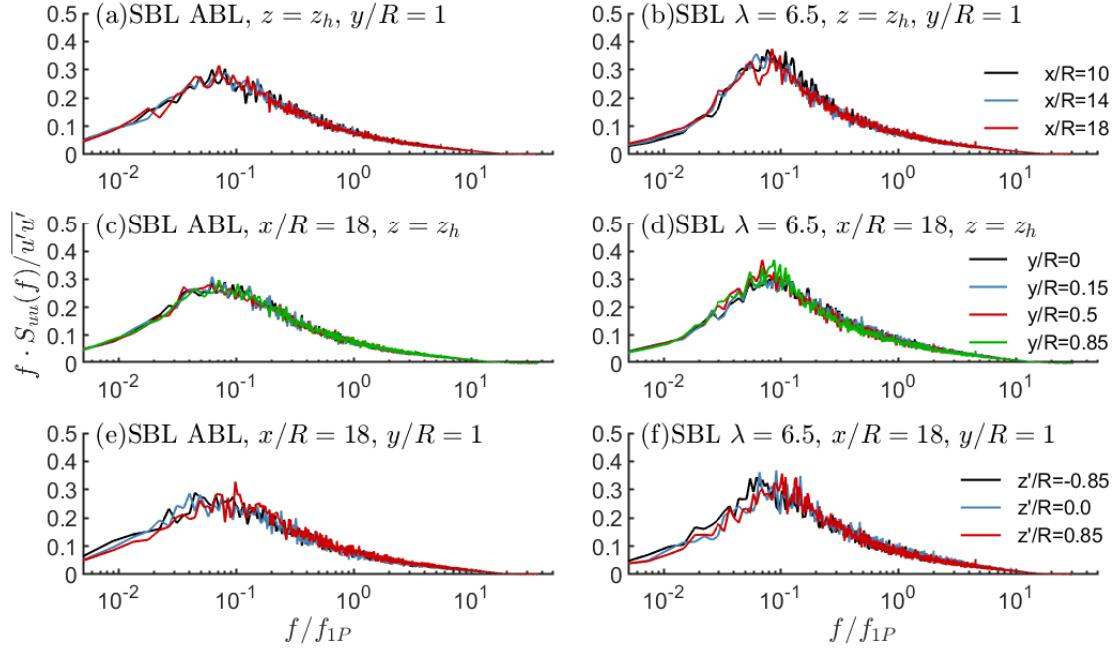


Figure 5.27: Normalised and pre-multiplied power spectra $f \cdot S_{uu}/\sqrt{u'u'}$ in the undisturbed SBL flow and the wake for $\lambda = 6.5$ at various locations in the (a)/(b) axial, (c)/(d) lateral, and (e)/(f) vertical direction. The legend denotes the position.

5.3.5 Wake Meandering

The amplification of the power spectra in the low-frequencies range $f/f_{1P} \approx 0.1$ observed within the far wake region, see Figure 5.26, is often attributed to wake meandering. Wake meandering describes the random unsteady oscillation of the whole wake in the lateral and vertical direction, which leads to strong turbulent fluctuations and can hence induce fatigue loads on another downstream wind turbine. In wind tunnel measurements, with and without freestream turbulence, Medici and Alfredsson [101] reported the existence of the meandering effect, observable as a low-frequency component in spectra. Larsen *et al.* [86] postulated that the entire wake is advected passively by turbulent eddies larger than twice the rotor diameter. Indeed, recently España *et al.* [42] found that in the wake of a porous disk wake displacements from the mean streamwise axis only occur when turbulence length scales larger than the wake width exist in the incoming flow. They concluded that the instantaneous wake width remains nearly constant downstream of the wind turbine and that the growth of the mean wake width is dominated by the meandering process. Even more recently Bastankhah & Porté-Agel [14] showed that the wake meandering amplitude does not depend on turbine operating conditions, e.g. tip speed ratio or yaw angle. However, beside other studies, Barlas *et al.* [5] showed that the wake meandering amplitude is sensitive to the incoming

flow conditions. They studied the influence of ground roughness on the wake evolution by comparing wind turbine wakes immersed in two turbulent boundary layers of similar characteristics (shear exponent $\alpha = 0.16$ and 0.3 with a turbulence intensity at hub height of $I_u \approx 7.5\%$ and 14% , respectively) as presented in this work. Within the wake immersed in the boundary layer flow over smooth ground roughness, they reported a low-frequency peak in the power spectra S_{uu} , whereas over high ground roughness such a peak was not observed in the wake. This observation is quite distinct to the results presented here, where a low-frequency peak is clearly visible within the far wake region for both boundary layer configurations, see Figure 5.26. In light of the aforementioned role of the turbulent length scales of the incoming flow, it is important to notice that in the work of Barlas *et al.* the turbulent length scales of the boundary layer flow over high ground roughness were significantly smaller than over smooth roughness, whereas in the boundary layer configurations used in this work the turbulent length scales are similar, see 3.13 in Section 3.4.

However, strictly speaking, the power spectrum does not give any information if a phase-correlated organised flow motion, like wake meandering, is present or if peaks in the spectrum are rather caused by stochastic fluctuations. Hence, the observed low-frequency peak in the wake should rather be seen as an indicator. A more accurate measure is the spectral coherence, as defined in eq. (5.4) in Section 5.3.1. Muller *et al.* [103] used spectral coherence to analyse the correlation between the incoming boundary-layer flow and the instantaneous wake centre position. They showed that it correlates well for wavelengths larger three times the rotor diameter ($St < 0.3$), whereas it does not correlate at all for wavelengths smaller than twice the rotor diameter ($St > 0.5$). Furthermore, they observed that the coherence decreased with downstream distance. From these results they concluded that the wake is a rather passive scalar/tracer advected by the surrounding large scale turbulent structures.

Even though the coherence of the axial and lateral velocity component measured at one point in the wake $Co_{uv}(f)$ does not give information on the advection of the wake as a passive scalar, it still can be used to measure the correlation between the velocity components and hence allows for analysing the presence of wake meandering. Therefore Figure 5.28 shows the coherence of the lateral Reynolds shear stress at hub height $Co_{uv}(f)$ as function of the Strouhal number $St = f \cdot D/\bar{u}_{bl}(z_h)$ at the lateral position $y/R = 1$ for selected downstream distances and various flow conditions. The low-frequency peak in the range of $f/f_{1P} \approx 0.1$ observed above in the power spectra, see Figure 5.26, can be converted into a Strouhal number of $St \approx 0.2$. This value can be obtained by using eq.(2.25) together with $\Omega = 2\pi f$ and inserting it in the definition of the Strouhal number, which gives $St = \lambda/\pi \cdot f/f_{1P}$. In the near wake the coherence peaks at about $St \approx 0.1$ and decreases asymptotically for the wakes at $\lambda = 6.5$ within both boundary layer conditions, see Figure 5.28(a). Within the SBL for a Strouhal number of $St \approx 2.07$ a clear peak is visible which correlates with the rotor frequency f_{1P} . As already observed in the power spectra S_{uu} for the near wake immersed in the RBL, this peak is not observable due to the faster break down of the helical tip vortices. As already mentioned above, a similar effect occurs at high tip speed ratios as well, see Section 5.3.2. Due to the lower dissipative character of the SBL flow condition (and the distinct load distribution at high TSR), the break down of the helical tip vortices for the TSR of $\lambda = 11.5$ leads to an increase of coherence for $St > 0.5$ which correlates with frequencies $f/f_{1P} > 0.1$ for which an amplification in the power spectrum is observed, see Figure 5.26(e). At the onset of the far wake region which is about $x/R = 6$, see Figure 5.28(b), the coherence reaches its maximum values and forms a plateau for $0.1 < St < 0.3$. For larger Strouhal numbers

the coherence decreases steeper as in the near wake, becoming negligible for $Str > 1$. Further downstream, at $x/R = 10$, shown in Figure 5.28(c), the coherence decreases slightly while the plateau for $0.1 < Str < 0.3$ is still noticeable. Within the RBL flow conditions the coherence becomes smaller than in the SBL which is attributed to the high dissipative character of boundary layer flows over large ground roughness. The observed plateau is in very good agreement with the results of Muller *et al.* [103] and therefore the presence of wake meandering in the measurements presented here can be concluded. It is also important to notice that in the far wake the distributions of coherence for $\lambda = 6.5$ and $\lambda = 11.5$ become similar, which supports that the Strouhal number of the wake meander does not depend on the tip speed ratio.

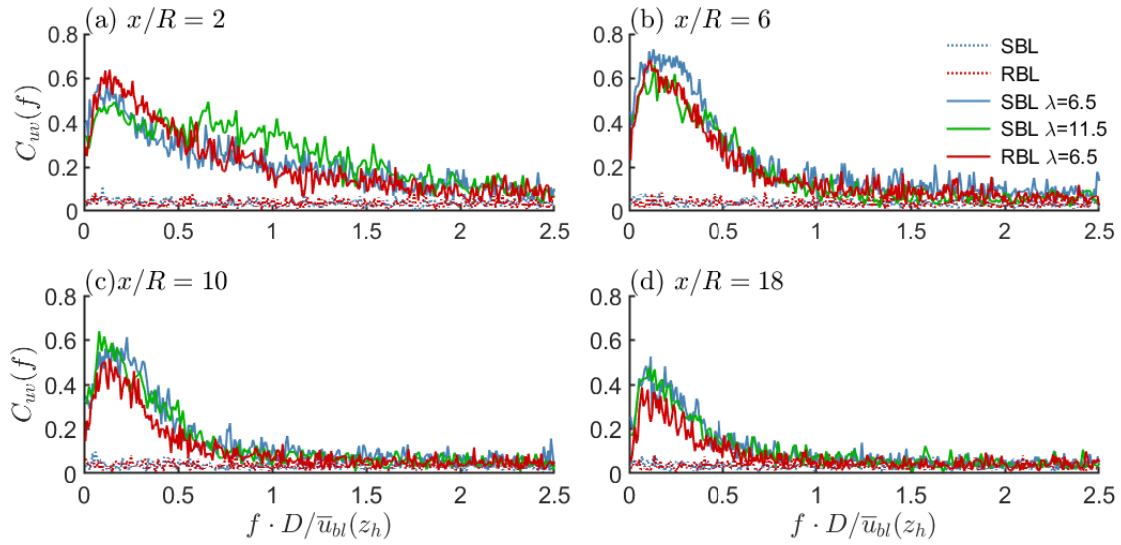


Figure 5.28: Coherence $Co_{uv}(f)$ between instantaneous axial u and lateral velocity component v within SBL flow conditions at $\lambda = 6.5, \lambda = 11.5$ and RBL flow condition at $\lambda = 6.5$ for various downstream distances at $z'/R = (z - z_h)/R = 0, y/R = 1$. The legend denotes the flow and the operational condition. The legend denotes the flow condition.

5.4 Summary

In the foregoing chapter results of hot wire measurements in the wake of a model wind turbine immersed in low-turbulence uniform approaching flow conditions and two turbulent boundary layers of significantly different ground roughness were presented. Besides measurements in the wake of the wind turbine aligned to the incoming flow while operating at design tip speed ratio $\lambda_{dsgn} = 6.5$, the flow field was also recorded for tip speed ratios of $\lambda = 9.0$ and 11.5 , and yaw angles of $\gamma = 15^\circ$ and 30° . Triple-wire anemometry was used to characterize the mean velocity field as well as the Reynolds stress tensor in the wake for downwind distance of $x/R = 2 - 18$. The presented measurements can be considered to be Reynolds number independent.

It was shown that the near wake is strongly influenced by the tip speed ratio, local thrust distribution and wake rotation. With downstream distance, differences in the axial mean velocity rapidly vanish and become indistinguishable for distances $x/R \geq 10$, whereas significant differences in the Reynolds stresses can even be noticed at a distance of $x/R = 18$. Thereby, it is observed that Reynolds stresses decrease with increasing tip speed ratio. This behaviour is in accordance with the mutual inductance instability described in literature, which for high tip speed ratios cause the helical blade tip vortices to break down closer to the rotor and cause an initially faster recovery of the wake. Spectral analysis confirms the early break down of the blade tip vortices at high tip speed ratio. These findings indicate that for accurate near and far wake predictions based on physical scale models, rotors with design tip speed ratios close to those found in full-scale are to be preferred.

Comparison of the wake evolution in three different flow conditions revealed a slow wake recovery within a low turbulence uniform approaching flow (LTU), due to which far wake conditions were not reached within the test section of the wind tunnel $x/R \leq 18$. Wind turbine wakes immersed in two turbulent boundary layers of different surface roughness recovered significantly faster with increasing surface roughness, since background turbulence enhances the momentum exchange between the wake and the outer flow. The wake development of the far wake immersed in the smooth boundary layer flow (SBL) exhibited a linear wake growth as frequently reported in literature. Within the rough boundary layer flow (RBL) the wake was shown to grow faster in the vertical direction than in the SBL but slower in the lateral direction. Thereby the wake growth in both directions was found to be first nearly linear but then decreases in downstream direction. This behaviour is argued to stem from a change of the streamwise momentum deficit, since in the region below the bottom tip an increase of the velocity deficit in downstream direction was observed. Due to that the Gaussian character of the velocity deficit distribution becomes distorted.

For yawed conditions, it was shown that an increase in the turbulence intensity decreases the lateral wake deflection, whereas the wake growth is independent of the yaw angle. Considering yaw misalignment as a control strategy to improve the power production in on-shore windfarms, might hence be less beneficial with increasing terrain roughness. Similar to the deflection of the momentum deficit center, the flow skew angle is influenced by the level of the ambient turbulence intensity as well. However, in the near wake the deflection of the momentum deficit center is similar for all flow conditions whereas the flow skew angle is reduced with increasing ambient turbulence. This result suggests that the flow skew angle is not an appropriate measure for the near wake deflection as assumed in current analytical wake models used to predict the wake deflection.

Spectral analysis of the recorded flow field in the near wake region revealed that the wind turbine destroys the large scale vortex organisations found in the turbulent boundary layers while generating turbulence at a much smaller scale. Therefore, it is concluded that the concept of added turbulence is not applicable in the near wake region. Still in the near wake region, the normalised power spectra $S_{uu}/\overline{u'u'}$ and the axial Reynolds stress $\overline{u'u'}$ show up to be quite similar within both boundary layers. From that it is concluded that the turbine rather modulates the turbulent scales according to its operational state.

Below hub height, with the wind turbine aligned to the incoming flow and operating at the design tip speed ratio $\lambda_{dsgn} = 6.5$, a suppression of the Reynolds stresses below the level of the undisturbed boundary layer flows was observed. For high surface roughness this suppression becomes more dominant and persists even into the far wake region. From spectral analysis it is concluded that this suppression is a result of the damping of large turbulent scales by the turbine. Furthermore it is found that at the onset of the far wake within the smooth boundary layer, large scales are amplified compared to the undisturbed boundary layer flow, whereas for the rough boundary layer large scales are still below the ambient level. Spectral analysis of the dominant shear production term in the region of the bottom tip shows that for high surface roughness turbulence production is reduced, due to which the suppression of Reynolds stresses can persist over long downstream distances.

Even though the distribution of Reynolds stresses differs significantly in the far wake region within the two considered boundary layer flows, the normalised power spectra $S_{uu}/\overline{u'u'}$ in the wakes are similar and converge asymptotically towards the spectra of the undisturbed boundary layer. Since the latter is nearly self similar, differences in the normalised power spectra within the wakes are considered to result from the different levels of ambient turbulences, which, as previously stated, alters the rate at which the wake recovers. Indeed, analysis of the normalised power spectra $S_{uu}/\overline{u'u'}$ evaluated at hub height for various lateral and axial positions within the wake immersed in the SBL flow revealed a self similar distribution of the power spectrum. This is considered to be a necessary prerequisite for the existence of self similarity for the lateral distribution of the mean axial velocity and the components of the Reynolds stress tensor. Due to the decreasing level of ambient turbulence with height and changing turbulent length scales, the normalised power spectra are not self similar in this direction and therefore vertical profiles of flow quantities cannot be expected to be self similar either.

Furthermore, a low-frequency peak present in the power spectra of the axial Reynolds stress S_{uu} in the far wake within both boundary layer configurations and both considered tip speed ratios is shown to coincide with a Strouhal number of $St \approx 0.2$. In literature, this value is frequently reported to indicate the presence of wake meandering. Analysis of the spectral coherence in the wake shows an organised flow motion for Strouhal numbers $0.1 < St < 0.3$ which confirms this finding. Thereby the distribution of the spectral coherence in the far wake is found to be independent of the chosen tip speed ratio and is only slightly decreased within the RBL flow condition.

Numerical Method

The current work is the first time the in-house flow solver INCA ¹ is used for a wind energy application. For this purpose various implementations and adaptations were carried out and needed to be tested and validated. Therefore, in this chapter the applied flow solver and its numerical methodology are introduced in Section 6.1. For the simulation of turbulent boundary layer flows over rough surfaces an established wall-model was implemented and adapted for large surface roughness. In Section 6.2 the wall model and its adaptations are given and results of a sensitivity study are discussed. Since wall resolving large eddy simulations of wind turbines are still prohibitively expensive, in this work the rotor flow is modelled by applying the actuator line method, which is explained and validated in Section 6.3. The accuracy of the method relies primarily on the quality of the used airfoil data. Therefore, in Section 6.4 an inverse lifting line approach is used to determine lift and drag characteristics including three-dimensional and rotational effects from results of a steady state Reynolds Averaged Navier-Stokes simulation of the rotor geometry.

¹INCA Computational Fluid Dynamics, URL <https://www.inca-cfd.com>

6.1 Flow Solver INCA

All simulations presented in this chapter and in Chapter 7 have been carried out using the in-house Navier–Stokes flow solver INCA. It is parallelized (MPI and OpenMP), allowing simulations with several thousand processors, and provides a large number of solvers for linear problems, time integration schemes, and discretisation methods. Even it is the first wind energy application computed with INCA, it was chosen for this work as support for all necessary implementations could always be given by colleagues and it is extensively applied and tested for the available supercomputing architecture.

The governing equations for incompressible, viscous flow are solved on a staggered Cartesian grid, and a pressure projection method is used. For time integration an explicit third-order Runge-Kutta scheme is applied. Thereby, the Poisson equation for the pressure is solved in every Runge–Kutta sub step. Diffusive terms and the pressure Poisson equation are discretised by second-order central differences. Instead of using an explicit subgrid scale (SGS) turbulence model, an implicit LES approach is applied, which discretises the convective terms of the governing equations by the simplified adaptive local deconvolution method (ALDM) [62].

Subgrid scale effects are modelled explicitly if the underlying conservation law is first modified by adding model terms and subsequently discretised. On the other hand, implicit LES denotes approaches in which the unmodified conservation law is discretised and the numerical regularisation acts as an SGS model. Since in the latter case the SGS model is implicitly contained within the discretisation scheme, an explicit computation of model terms becomes unnecessary. ALDM is based on a nonlinear finite-volume scheme involving a solution adaptive reconstruction (deconvolution) of the numerical solution. Thereby, ALDM adopts the idea of the weighted-essentially-non-oscillatory (WENO) scheme where interpolation polynomials are selected and combined nonlinearly. The essential difference between ALDM and WENO is that all interpolants are superposed to allow for lower-order contributions to the truncation error for implicit SGS modeling. The superposition introduces free discretization parameters which have been calibrated by means of an evolutionary optimization algorithm in such a way that the effective spectral numerical viscosity is identical to the spectral eddy viscosity from turbulence theory for asymptotic cases. The truncation error of ALDM, when formally determined by Taylor series expansion, is less than second order in terms of the mesh width [61].

It is important to notice that due to the implicit nature of ALDM contributions of the SGS model can not be stated explicitly. Therefore a break down of computed Reynolds stresses in resolved and modelled parts is not possible.

In INCA Cartesian grids are organized in blocks, of which each is assigned to a single core for the computation of the governing equations. On the verge of each block three additional layers of cells are defined for the communication with the neighbouring blocks. For the applied supercomputing architecture *SuperMUC Phase 2* of the Leibnitz Rechenzentrum a number of 2^{16} cells per block is recommended.

In various applications INCA and ALDM have been validated for incompressible flows, among them isotropic and stratified homogeneous turbulence [61, 117], turbulent wall bounded flows [63], passive scalar mixing [64], and aeronautical engineering [161].

6.2 Generation of Turbulent Boundary Layer Flows

In this section two wall-models implemented in the flow solver for simulating turbulent boundary layer flows over rough surfaces are introduced and results of a sensitivity analysis are presented and discussed. For this work a classical wall shear stress model was adapted for the evaluation on arbitrary grid points and a second wall model for the simulation of large surface roughness was derived, see Section 6.2.1. In a sensitivity study given in Section 6.2.2, the influence on the boundary layer flow of the chosen grid point for evaluating the wall model, the grid resolution, and the roughness length is analysed.

6.2.1 Wall Modelling Methodology

Classical wall stress models have in common that prescribed wall shear stress is determined on the basis of the streamwise velocity at the first grid point off the wall, see e.g. [54, 97, 125]. Larsson & Kawai [87], Cabot & Moin [23], Nicoud *et al.* [108] and others, however, argue that wall-modelled LES at high Reynolds number are unavoidably affected by numerical and subgrid modelling errors as simulations are commonly under-resolved close to the wall. The argument is that the wall-stress can only be computed accurately by a wall model if the stress carrying motions of length scale $L_i = C_i z$ are well resolved, where C_i is a constant for each direction. That is only the case if

$$L_i = C_i z \geq \alpha \Delta x_i \quad (6.1)$$

where the value of α (i.e. the number of grid points per wave length) depends on the particular numerical method. Using the first grid point to evaluate the wall-stress implies $C_i \Delta z \geq \alpha \Delta z$ and hence $C_i \geq \alpha$. Larsson & Kawai argue that this is highly unlikely as the Nyquist criterion gives $\alpha \geq 2$ and the kinematic damping by the wall makes $C_2 \leq 2$ a reasonable upper bound. Therefore, they suggest to estimate the wall-stress from any other grid point z_m which lies within the logarithmic region of the boundary layer. With that the criterion 6.1 yields

$$\frac{z_m}{\Delta x_i} \geq \frac{\alpha}{C_i} \quad (6.2)$$

which simply states that either the grid spacing Δx_i has to be refined or the point for evaluating the wall model z_m has to be increased till numerical and subgrid modelling errors are sufficiently small.

6.2.1.1 Standard Wall Stress Model

For this reason the wall-stress model of Mason & Callen [97] is used here but adapted for the evaluation of the wall-stress on arbitrary grid points. The general functioning of the wall model is sketched in Figure 6.1(a). The local instantaneous wall-stress vector can be computed as

$$\boldsymbol{\tau}_w(x, y, t) = \begin{pmatrix} \tau_{w,xz} \\ \tau_{w,yz} \end{pmatrix} = \frac{\tau_w}{U_t(x, y, z_m, t)} \begin{pmatrix} u(x, y, z_m, t) \\ v(x, y, z_m, t) \end{pmatrix} \quad (6.3)$$

with the magnitude of the velocity tangential to the surface $U_t(z_m) = \sqrt{u(z_m)^2 + v(z_m)^2}$. For the sake of a better readability here and in the following equations the spatial coordi-

nates x , y and the time t are left out. The magnitude of the wall stress is given by

$$\tau_w = \rho \left(\frac{U_t(z_m)}{u^+(z_m)} \right)^2 = \rho \left(\frac{\kappa}{\ln(z_m/z_0)} \right)^2 U_t^2(z_m). \quad (6.4)$$

This classical parametrization of the boundary condition neglects effects of pressure gradients, unsteadiness, streamline curvature, etc., which occur in the instantaneous LES fields. Mason & Callen already noticed that the time-mean flow departs from the law of the wall. They argue, however, that this behaviour is inevitable as scales of motion other than those involved in the local wall equilibrium are present. For the analysis of the non-dimensionalised flow field it is hence important to consider this behaviour. The main difference is, that in the derivation of the law of the wall the three-dimensionality of the instantaneous values is not considered. Consequently, the time-mean of the wall stress magnitude $\bar{\tau}_w$ is not equal to the time-mean of the wall-stress component in the axial direction $\bar{\tau}_{w,xz}$, though the time-mean of the lateral component is zero $\bar{\tau}_{w,yz} = 0$. Therefore, the time-mean of the shear stress velocity in the simulation is defined to be

$$\bar{u}_\tau = \sqrt{\frac{\bar{\tau}_{w,xz}}{\rho}} \quad (6.5)$$

whereas the time-mean of the wall shear stress in axial direction can be computed to

$$\frac{\bar{\tau}_{w,xz}}{\rho} = \frac{\overline{(u(z_m)^2 + v(z_m)^2)^{1/2} \cdot u(z_m)}}{u^{+2}(z_m)} \quad (6.6)$$

Reynolds stresses can then be non-dimensionalised by

$$\overline{u'_i u'_j}^+ = \frac{\overline{u'_i u'_j}}{\bar{u}_\tau^2} \quad (6.7)$$

6.2.1.2 Virtually Lifted Wall Stress Model

As will be shown in the discussion of results, Section 6.2.2.4, for large roughness lengths in the order of the wall normal grid size $z_0 = \mathcal{O}(\Delta z_1)$ the current implementation of the standard wall-stress model in the flow solver INCA results in negative mean axial velocities in the wall nearest grid cells. In the scope of this thesis, the underlying reason could not be clarified and no similar problem is reported in literature. Furthermore, due to time limitations, it was not possible to reproduce the setup in a different solver, so that it still remains unclear if this behaviour is solver specific. However, preliminary tests showed that it is not a problem related to implicit LES, since simulations carried out in INCA using the dynamic Smagorinsky model resulted also in negative values of the axial velocity for the wall nearest grid cells.

The main problem with this behaviour is that the computations presented in Chapter 7 with high surface roughness tend to be unstable if negative values occur over larger fractions of the inlet or outlet. In this case the only possibility to obtain positive mean axial velocities in the wall nearest grid cells is to reduce the wall-normal resolution of the grid. For the application in wind turbine wake simulations that, however, is not a convenient approach as the resolution of the wake requires small grid cells, also in the proximity of the wall. In the mentioned boundary layer configuration *sF032* the roughness length is $3/5$ of the height of the first grid cell. Only in this case the wall model, which is derived

in the following, is applied. Other boundary layer configurations considered in the numerical study presented in Chapter 7 have roughness lengths significantly smaller, and are therefore computed with the standard wall model presented above.

In the following a wall model is derived in which the domain is virtually lifted above ground and the no-slip wall condition at the lower domain boundary is replaced with divergence-free velocity disturbances. Such perturbed velocity boundary conditions were tested for smooth walls by Flores & Jiménez [47] who interpreted these as roughness effect. Based on these observations, Saito *et. al* [118] developed a virtually lifted wall model for sub-grid roughness. Thereby it is assumed that the lower boundary of the computational domain is lifted into the overlap region where total shear stress can be assumed to be constant and the logarithmic law can be applied to calculate a non-zero axial mean velocity disturbance. Indeed, the model assumes the validity of the logarithmic law in the region between the actual wall and the lifted boundary. Here, this is used as point of criticism as it either requires to lift the boundary well above ground into the log-layer region, which might be impractical for wind turbine simulations, or enforces log-law assumptions in the sublayer region.

Therefore, the wall model derived in this work makes use of a lifted boundary to obtain a resolution independent (with regard to the surface roughness) wall-model but follows the approach of Flores & Jiménez and applies divergence-free velocity disturbances at the boundary. Nevertheless, the model still requires assumptions which are based on the validity of the logarithmic law, but only at the boundary surface. As divergence-free velocity disturbances are imposed at the boundary, it is assumed that the boundary itself is lifted by the roughness length z_0 , where the logarithmic law predicts a zero-mean axial velocity. The general functioning of the wall model is sketched in Figure 6.1(b).

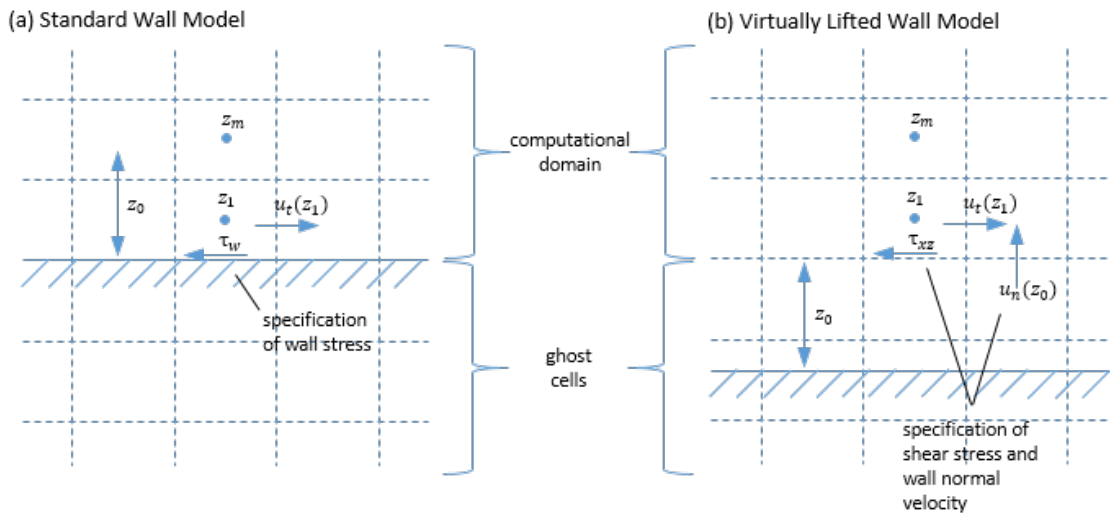


Figure 6.1: Sketch of (a) the Standard Wall Model and (b) the Virtually Lifted Wall Model

Flores & Jiménez prescribed single Fourier modes characterized by the amplitudes and the streamwise and spanwise wavelengths. Here instead, it is made use of the computed velocity field. With the argument used above, that stress carrying motions are commonly under-resolved close to the wall, the fluctuating part of the velocity tangential to the boundary at an arbitrary grid point can be utilised. If the profile of the Reynolds stresses would be known, the fluctuating part then could be scaled accordingly. As this is typically not known a priori, it is simply assumed that the fluctuating part of the tangential

velocity at the boundary is in phase with the tangential velocity at the chosen grid point and has the same magnitude and is therefore

$$\mathbf{u}'_t(z_0) = \mathbf{u}'_t(z_m). \quad (6.8)$$

To obtain the fluctuating part $\mathbf{u}'_t(z_m)$ it would require the time mean $\bar{\mathbf{u}}_t(z_m)$ which is also not known a priori. However, Taylors' hypothesis of frozen turbulence can be applied which allows to approximate the time mean $[\cdot]$ by the spatial mean in the wall parallel xy -plane $\langle [\cdot] \rangle_{xy}$. With that the zero-mean velocity disturbance tangential to the boundary can be computed as

$$\mathbf{u}'_t(z_0) = (\mathbf{u}_t(z_m) - \langle \mathbf{u}_t(z_m) \rangle_{xy}). \quad (6.9)$$

As a next step the wall-normal velocity disturbance at the boundary has to be derived. A simple approach is to assume a mean profile between the actual wall and the boundary of the computational domain $\mathbf{u}'_t(z) = f^+(z_0, z) \cdot \mathbf{u}'_t(z_0)$, with the non-dimensional profile f^+ , and to integrate then the continuity equation $\partial u_i / \partial x_i = 0$ from the wall (non-slip) to the boundary in order to obtain the wall-normal velocity

$$u_n(z_0) = - \int_0^{z_0} f^+(z_0, z) dz \cdot \frac{\partial u_{t,i}(z_0)}{\partial x_i}. \quad (6.10)$$

The difficulty of this approach is to find an appropriate profile f^+ . For a boundary lifted well into the logarithmic region, an approximation on the basis of the logarithmic law can be appropriate, as done by Saito *et. al* [118] where the considered roughness elements are subgrid. In the case considered here the boundary is, physically speaking, located in between the roughness elements, and an a priori defined universal profile f^+ would rather be based on hand waving arguments. As the main purpose of the derived wall model is to avoid negative axial mean velocities in the first grid cells, instead a non-dimensional parameter K_{PI} is introduced, which is dynamically adjusted by a proportional-integral controller, to replace the integral in eq.(6.10), giving

$$u_n(z_0) = -z_0 \cdot K_{PI}(t) \cdot \frac{\partial u_{t,i}(z_0)}{\partial x_i}. \quad (6.11)$$

Thereby, the parameter $K_{PI}(t)$ is defined such that the spatial mean axial velocity of the first grid cells $\langle u(z_1) \rangle_{xy}$ results in a positive value. Since the upper bound for this value is the velocity predicted by the logarithmic law $u_{target}^+(z_1) = u_{log}^+(z_1)$, the target velocity is defined as function of the logarithmic law, given by

$$u_{target}^+(z_1) = C \cdot u_{log}^+(z_1). \quad (6.12)$$

As the first grid point is considered to lay below the logarithmic region, the velocity is expected to be smaller than predicted by the logarithmic law. In preliminary tests $C = 0.5$ was found to give reasonable results. Therefore, the dynamically adjusted parameter $K_{PI}(t)$ is defined as

$$K_{PI}(t) = K_S + K_P \Delta u^+ + K_I \frac{1}{t_{ref}} \int_0^t \Delta u^+ dt \quad (6.13)$$

with

$$\Delta u^+ = \frac{u_{target}^+(z_1) - \langle u(z_1) \rangle_{xy}}{u_{target}^+(z_1)}. \quad (6.14)$$

where $t_{ref} = \delta/u_{ref}$ with the bulk velocity u_{ref} . The constants $K_S = 1$, $K_P = 0.1$, and $K_I = 0.1$ were adjusted by try-and-error and are chosen such that the controller reacts rather to large scale motions than to the effect of smaller eddies. For the *sF032* boundary layer configuration presented in Chapter 7 the mean value of the controller parameter is $\bar{K}_{PI} = 1.63$ with a standard deviation of $\sigma_{K_{PI}} = 0.057$.

For the computation of the shear stress it is set equal to the wall-stress since the boundary is just lifted below the logarithmic region where the total shear stress can be assumed to be constant. However, preliminary test showed that simulations using eq.(6.4) in combination with the velocity perturbation eq.(6.9) tend to be unstable. It is hypothesised here that the instability occurs since wall-stress and velocity disturbance are in phase. Therefore, instead the total shear stress at the lifted boundary is defined as

$$\tau_{xz} = \tau_w = \rho \left(\frac{\langle u(z_m) \rangle_{xy}}{u^+(z_m)} \right)^2 = \rho \left(\frac{\kappa}{\ln(z_m/z_0)} \right)^2 \langle u(z_m) \rangle_{xy}^2, \quad \tau_{yz} = 0. \quad (6.15)$$

By this the wall stress is always pointing in axial direction and no local fluctuations are present. It should be noted that therefore also the time mean of the wall shear stress does not incorporate local velocity fluctuations.

6.2.2 Sensitivity Study

6.2.2.1 Numerical Setup

For the following sensitivity studies a domain of height $L_z = \delta = 2250$ mm, width $L_y = 4\delta$ and length $L_x = 6\delta$ is chosen. In view of the subsequent wind turbine simulation, the channel height $\delta = 10 \cdot R$ is defined as an integral multiple of the rotor radius R in order to simplify the selection of an appropriate grid resolution. This way it enables to describe the wall-normal grid resolution $\Delta z = \delta/(10 \cdot N)$ in terms of grid points per rotor radius N . Furthermore, in the subsequent wind turbine simulation cubic cells are recommended for resolving the wake. Therefore, choosing the same constant wall-normal resolution in the upstream region, used to generate the boundary layer flow, facilitates the mesh refinement towards the wake region. Even though this region will extend to a height of half the boundary layer, the wall-normal grid resolution in this study is set constant only up to a height of $z < 0.1\delta$. In the region above, the wall-normal resolution is gradually coarsened by the linear distribution $\Delta z_i = 1.04\Delta z_{i-1}$. This is considered as an acceptable trade-of between computational costs and accuracy, as the largest gradients in the boundary layer flow occur below this height. In the following studies, if not defined otherwise, the wall-normal resolution is defined by $N = 18$ and the axial and lateral aspect ratios are $\Delta x/\Delta z = 8$ and $\Delta y/\Delta z = 4$, respectively.

The lateral and axial boundary conditions are set to be periodic. For the top boundary a free-slip condition is prescribed and for the bottom boundary condition the wall models described in Section 6.2.1 are chosen. The fluid mass flow in the computational domain is controlled by body forces, which are prescribed such that at the reference height $z_{ref} = z_h$ a specified spatial mean velocity $u_{ref} = \langle u(z_h) \rangle_{xy}$ is obtained.

In the beginning of each simulation the flow field is initialised by setting the axial velocity to $u(z) = u_{ref}(z/z_{ref})^{0.15} + u_{rand}$, where u_{rand} is some random fluctuation. The simulation is then run for 100 flow-through times $T_{ft} = L_x/u_{ref}$ to let decay any transitional effect and is then run for another 200 flow-through times in which the flow field is

recorded.

6.2.2.2 Evaluation Point

As a first test of the implemented wall model, the grid point to evaluate the wall stress is varied from $m = 1$ to $m = 6$. This analysis is performed using a grid resolution of $N = 18$ and a roughness length of $\delta/z_0 = 4500$ (e.g. for $z < 0.1\delta$ $\Delta z/z_0 = 25$).

Figure 6.2 shows the non-dimensional mean velocity profile $u^+(z)$ in semi-logarithmic representation for all computed cases, where *coloured dots* indicate the grid point m used for evaluating the wall-stress. Additionally, the logarithmic distribution $u_{log}^+ = 1/\kappa \ln(z/z_0)$ is shown as *black dashed line*. It can clearly be seen that using the first grid point $m = 1$ results in a significant overprediction of u^+ . The non-dimensional velocity distribution, however, rapidly converges toward the logarithmic law u_{log}^+ as the grid point m is increased, making the distributions for $m \geq 3$ almost indistinguishable by eye.

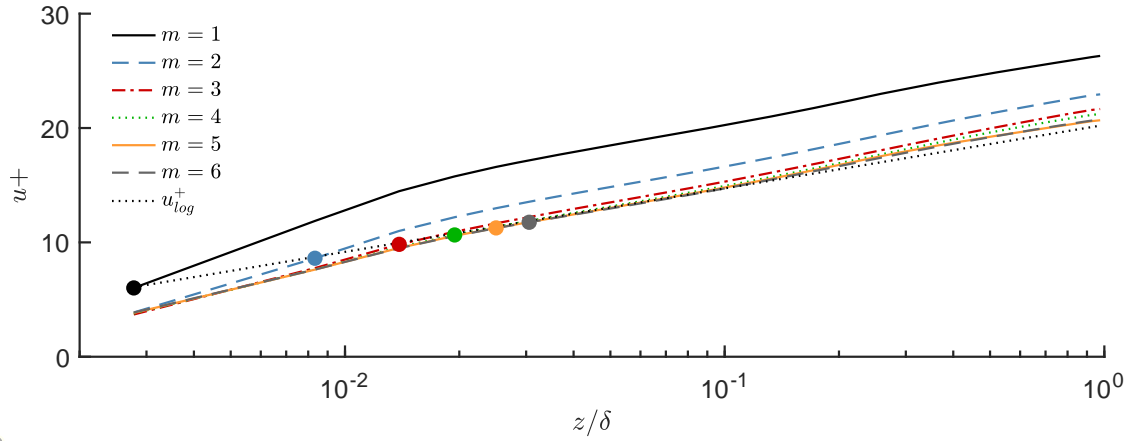


Figure 6.2: Non-dimensional mean axial velocity u^+ as function of normalised wall distance z/δ computed using m -th grid point adjacent to wall. Grid point is also indicated by *coloured dots*. The *legend* denotes the grid point and the *black dashed straight line* denotes the logarithmic law for rough walls 2.12 with $\delta/z_0 = 4500$.

The significant overprediction of u^+ for $m \leq 2$ is directly connected with an underprediction of the mean wall stress $\bar{\tau}_{w,xz}$ and hence of the mean shear stress velocity \bar{u}_τ . As shown in figure 6.3(a) the predicted mean shear stress velocity \bar{u}_τ is significantly lower for $m = 1$ compared to cases with larger values of m , where \bar{u}_τ converges towards a constant value. The underprediction of the mean wall stress $\bar{\tau}_{w,xz}$ also results in a reduced vertical gradient of the axial velocity as it can be observed in figure 6.3(b). Here the velocity distribution is shown as function of wall distance in double-logarithmic representation and is normalised to the velocity at a reference height, which for practical reasons is chosen to be the hub height z_h of the model wind turbine. In this representation the power law distribution $\bar{u}/\bar{u}(z_h) = (z/z_h)^\alpha$ appears linearised, whereas the shear exponent α is equal to the gradient of the line. It can clearly be observed that for $m = 1$ the vertical gradient of the axial velocity is reduced, which increases and converges with increasing m . In the context of an approximation by the power law, the argument also holds for the shear exponent α .

The non-dimensional Reynolds stress $\overline{u'u'^+}$, shown in figure 6.4(a), exhibits a similar behaviour as the normalised velocity distribution u^+ . For $z > 0.01\delta$ the profiles converge

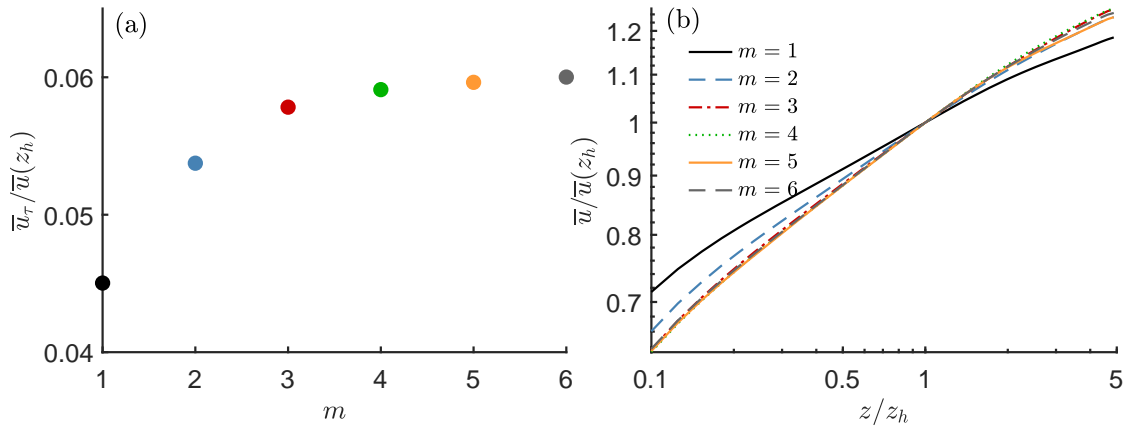


Figure 6.3: (a) Normalised shear stress velocity $\overline{u}_\tau / \overline{u}(z_h)$ as function of m -th grid point adjacent to the wall used for evaluation and (b) normalised mean axial velocity $\overline{u} / \overline{u}(z_h)$ as function of wall distance.

with increasing m and become indistinguishable for $m \geq 3$. The normalised stresses $\overline{v'v'^+}$, $\overline{w'w'^+}$ and $\overline{u'w'^+}$, shown in figure 6.4(b),(c) and (d), however are even less sensitive and are indistinguishable for $z > 0.03\delta$ disregarding the choice of m . In the more inner region $z < 0.01\delta$ the variation of m has a more significant effect. All stresses increase with increasing m , whereas they also seem to converge for $m \geq 5$. Hence, considering the criterion Eq.(6.2) it can be concluded that for the given grid resolution the stress carrying motions are well resolved for $z \geq z_5$.

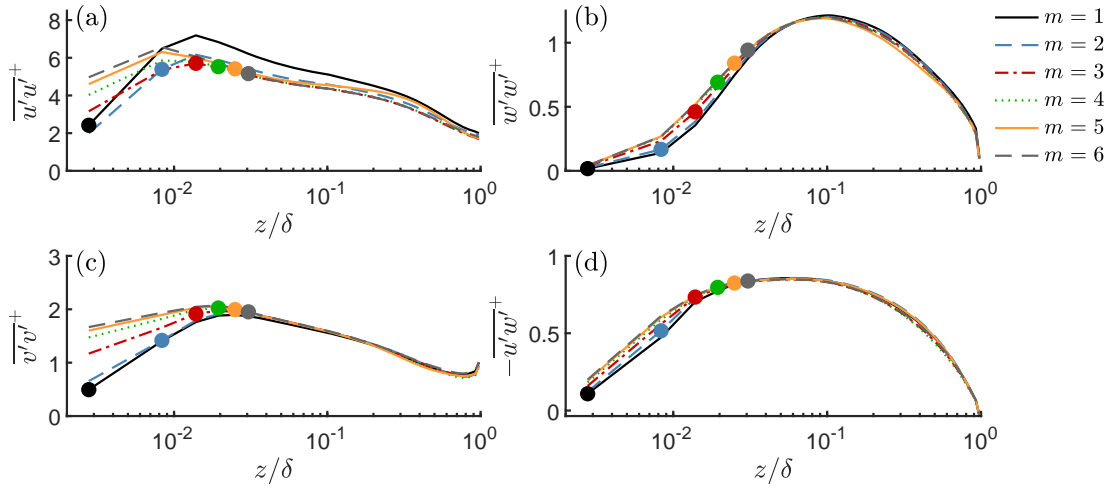


Figure 6.4: Non-dimensional Reynolds stresses (a) $\overline{u'u'^+}$, (b) $\overline{w'w'^+}$, (c) $\overline{v'v'^+}$, and (d) $\overline{u'w'^+}$ as function of normalised wall distance z/δ computed using m -th grid point adjacent to the wall used for evaluation.

6.2.2.3 Grid Study

To determine an appropriate grid resolution for the simulation of the model wind turbine immersed in turbulent boundary layers, the grid sensitivity of the boundary layer flow with regard to the wall-normal and wall-tangential resolution is analysed in this section.

For three different wall-normal grid resolutions of $N = 9, 18$ and 27 the Figure 6.5 shows the non-dimensional mean velocity profile $u^+(z)$ in semi-logarithmic representation. As it is known that cell aspect ratios can affect the numerical results, the ratio of edge length in axial direction to normal direction $\Delta xz = \Delta x/\Delta z = 8$ and the ratio of the edge length in lateral direction to axial direction $\Delta yx = \Delta y/\Delta x = 0.5$ is kept constant. The roughness length is set to $\delta/z_0 = 4500$ and the wall-normal grid point to evaluate the wall-stress prescribed during the simulation is selected such that $z_m/\delta \approx 0.03\delta$ ($m = 3, 6, 8$). As can easily be observed, in the logarithmic region $0.03 \leq z/\delta \leq 0.3$ all profiles are indistinguishable by eye. Only minor differences exist below and above this region.

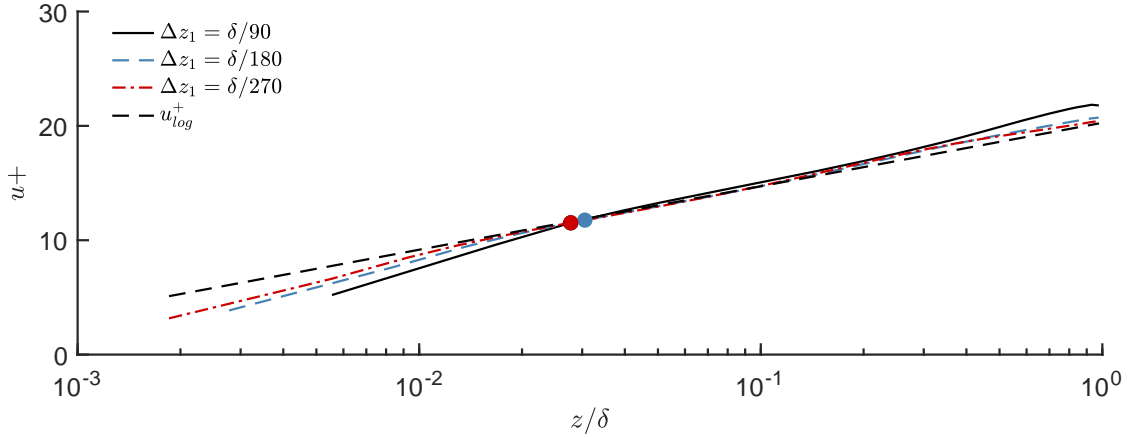


Figure 6.5: Non-dimensional mean axial velocity u^+ as function of normalised wall distance z/δ for three different wall-normal grid resolutions. The *legend* denotes the grid resolution and the *black dashed line* denotes the the logarithmic law for rough walls 2.12 with $\delta/z_0 = 4500$.

For the Reynolds stresses a more significant grid sensitivity can be identified, see Figure 6.6. In the lowest region $z/\delta < 0.03$ smaller cell sizes have a significant effect on the resolved stress carrying motions. However, in the region above Reynolds stresses seem to converge for grid resolutions $\Delta z_1 \leq \delta/180$.

As will be explained in Section 7.1, to simulate the wake of the model wind turbine immersed in a turbulent boundary layer, two main regions in the computational domain are defined. A so called *recycling region* to generate the boundary layer flow and a so called *wake region* in which the wind turbine is located. Since the computational costs to resolve the flow in the *recycling region* with the same resolution of cubic cells as used for the *wake region* are prohibitively high, the undisturbed boundary layer flow has to be computed using grids with coarser resolution. Therefore, the sensitivity of the flow with respect to different aspect ratios of the grid cells is analysed. In this study the wall-normal resolution of $\Delta z_1 = \delta/180$ is kept constant while two different ratios of edge length in axial direction to normal direction, $\Delta xz = \Delta x/\Delta z = 8$ and 4 , as well as two different ratios of the edge length in lateral direction to axial direction, $\Delta yx = \Delta y/\Delta x = 1$ and 0.5 are applied. Hence, in total four different grid configurations are considered.

Figure 6.7 shows the non-dimensional mean velocity profile $u^+(z)$ in semi-logarithmic representation for these four grid configurations. For all configurations a roughness length of $\delta/z_0 = 4500$ is chosen, while the $m = 6$ -th grid point adjacent to the wall is used to evaluate the applied standard wall model. On the first sight the most significant differences can be observed in the proximity of the wall $z/\delta < 0.03$ where with increas-

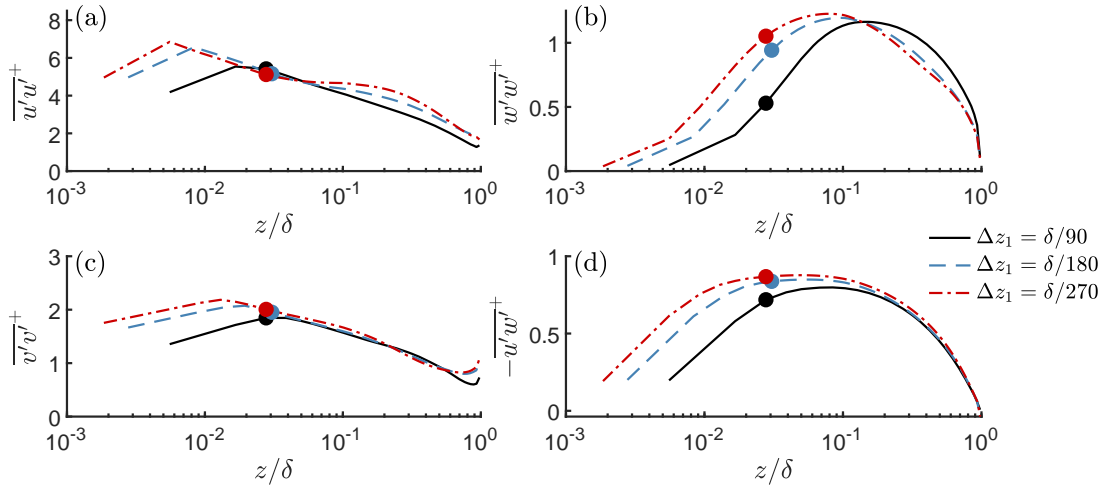


Figure 6.6: Non-dimensional Reynolds stresses (a) $\overline{u'u'^+}$, (b) $\overline{w'w'^+}$, (c) $\overline{v'v'^+}$, and (d) $\overline{u'w'^+}$ as function of normalised wall distance z/δ for three different wall-normal grid resolutions. The *legend* denotes the grid resolution.

ing grid resolution the profiles converge toward the logarithmic law, as more of the stress carrying motions are resolved. However, more important to notice is that in the region $0.03 < z/\delta < 0.3$ configurations with a ratio $\Delta yx = 1$ exhibit a slightly steeper gradient than the configurations with a ratio $\Delta yx = 0.5$, whereas the gradient is independent of the ratio Δxz . This is especially remarkable, since the configuration $\Delta xz = 8$, $\Delta yx = 0.5$ and $\Delta xz = 4$, $\Delta yx = 1$ have the same edge length Δy but different Δx , thus the configuration with a coarser Δx resolution results in a better approximation of the logarithmic law.

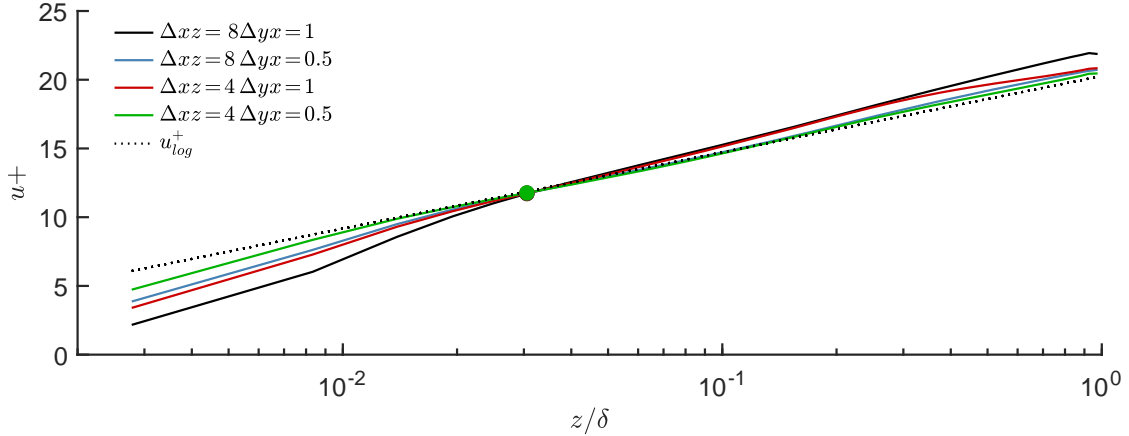


Figure 6.7: Non-dimensional mean axial velocity u^+ as function of normalised wall distance z/δ for different wall-tangential grid resolutions. The *legend* denotes the grid resolution, with $\Delta xz = \Delta x/\Delta z_1$ and $\Delta yx = \Delta y/\Delta x$, and the *black dashed line* denotes the the logarithmic law for rough walls 2.12 with $\delta/z_0 = 4500$.

A similar behaviour can be observed in the distribution of the non-dimensional Reynolds stress $\overline{u'u'^+}$ shown in Figure 6.8(a) where for $z/\delta > 0.03$ configurations with the same ratio Δyx result in similar values, whereas for the non-dimensional Reynolds stress $\overline{w'w'^+}$ the ratio Δxz seems to control the distribution in the outer part of the boundary layer

$z/\delta > 0.1$. Only in the region close to the wall $z/\delta < 0.03$ a clear trend for increasing grid resolution can be seen, although no convergence for the considered configurations can be observed.

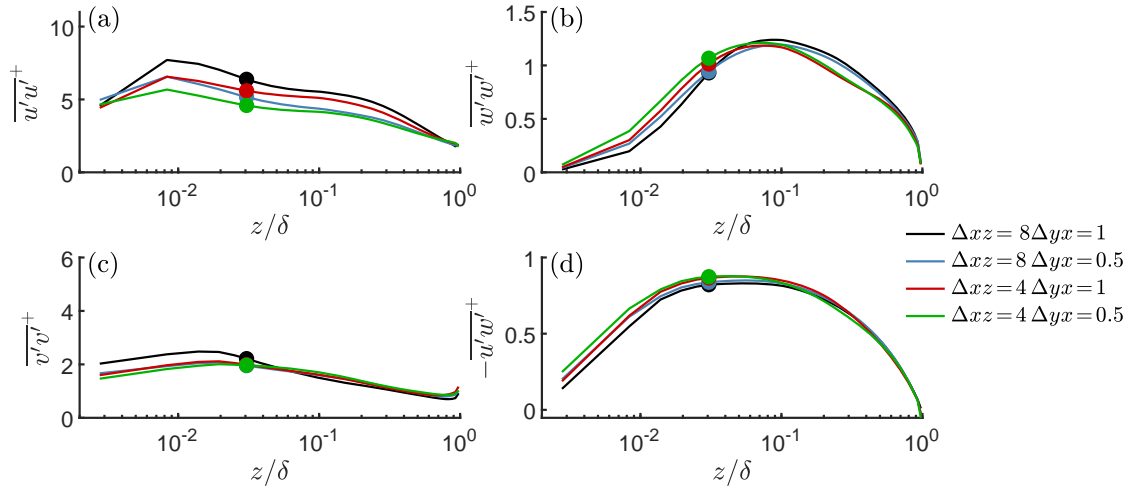


Figure 6.8: Non-dimensional Reynolds stresses (a) $\overline{u'u'^+}$, (b) $\overline{w'w'^+}$, (c) $\overline{v'v'^+}$, and (d) $\overline{u'w'^+}$ as function of normalised wall distance z/δ for different wall-tangential grid resolutions. The legend denotes the grid resolution, with $\Delta x z = \Delta x/\Delta z_1$ and $\Delta y x = \Delta y/\Delta x$.

At this point, unfortunately, it can not be clarified if smaller aspect ratios done to cubic cells do result in grid convergence due to the limited resources available for this preliminary study. Nevertheless, the results already show that a grid refinement from cells with a certain aspect ratio to cubic cells does inevitably cause a transition of the boundary layer as more turbulent scales are resolved. Since only a low sensitivity with regard to the wall-normal resolution is observed for resolutions $\Delta z_1 \leq \delta/180$, it can be expected that this statement also holds for grid resolutions higher than the considered $\Delta z_1 = \delta/180$.

6.2.2.4 Roughness Study

As already mentioned in the derivation of the Virtually Lifted Wall Stress Model, see Section 6.2.1.2, for large roughness lengths in the order of the grid size $z_0 = \mathcal{O}(\Delta z_1)$ the standard wall-stress model results in negative mean axial velocities in the wall nearest grid cells. Hence, for this study a grid configuration with a wall-normal resolution of the first cell of $\Delta z_1 \leq \delta/180$ ($\Delta x z = 8$, $\Delta y x = 0.5$) was chosen to simulate boundary layers with roughness lengths of $\delta/z_0 = 4500, 450, 180$, and 90 . To emphasize the importance of the ratio of grid resolution to roughness length, in the following all roughness lengths are expressed by this ratio and result into $\Delta z_1/z_0 = 25, 2.5, 1.0$, and 0.5 .

In Figure 6.9 the resulting non-dimensionalised mean velocity profiles in semi-logarithmic representation for various roughness lengths ranging from $\Delta z_1/z_0 = 25$ to 0.5 are shown, each computed with the Standard Wall-Stress Model (SW) and the Virtually Lifted Wall-Stress Model (LW). In case of the standard model negative values in the first grid cells occur for $\Delta z_1/z_0 \leq 2.5$. For these cells, as intended, the lifted wall model results in positive values close to the prescribed value $u_{target}^+(z_1)$. It is important to notice that both wall models result in similar axial velocity distributions for small roughness lengths, e.g. $\Delta z_1/z_0 = 25$, but depart with increasing values, whereas profiles u^+ predicted by the standard model result in values below the corresponding logarithmic law.

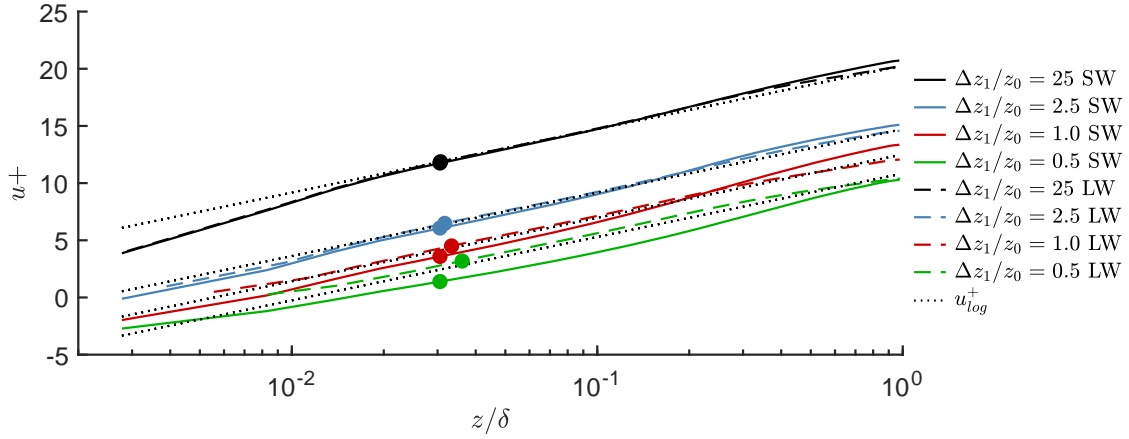


Figure 6.9: Non-dimensional mean axial velocity u^+ as function of normalised wall distance z/δ for different roughness lengths z_0 , computed with the standard wall model (SW) and the lifted wall model (LW). The *legend* denotes ratio of wall-normal cell size to roughness length $\Delta z_1/z_0$ and the applied wall model, *dotted lines* denote the logarithmic law for rough walls 2.12, and *coloured dots* indicate grid point used for evaluation of the wall shear stress.

This behaviour stems from the different definitions used in both models to compute the instantaneous wall shear. The standard wall model uses the local instantaneous velocity field and takes into consideration the three-dimensionality of the flow, see Eq.(6.3). Therefore, for this model the time mean of the shear stress velocity \bar{u}_τ results in

$$\bar{u}_\tau = \sqrt{\frac{\tau_{w,xz}}{\rho}} = \frac{\sqrt{\bar{U}_t(z_m)\bar{u}(z_m) + \overline{U_t' u'(z_m)}}}{u^+(z_m)} \quad (6.16)$$

whereas the lifted wall model only uses the spatial average of the axial velocity components, see Eq.(6.15), for which the time mean of the shear stress velocity results in

$$\bar{u}_\tau = \sqrt{\frac{\tau_{w,xz}}{\rho}} = \frac{\sqrt{\langle u(z_m) \rangle_{xy}^2}}{u^+(z_m)} \approx \frac{\bar{u}(z_m)}{u^+(z_m)} \quad (6.17)$$

Therewith, as the standard model incorporates the velocity fluctuations tangential to the wall the predicted time mean of the shear stress velocity \bar{u}_τ results in larger values as predicted by the lifted model. This becomes especially prominent for large roughness values, as shown in Figure 6.10(a). As mentioned before, Mason & Callen [97] already noticed the departure of the time mean flow from the logarithmic law of the wall and it does not necessarily constitute a deficiency of the model, as the logarithmic law of the wall neglects the three-dimensionality of the flow. It should rather be interpreted as a modified roughness length which results since a parameter based on two-dimensional assumptions is used in a three-dimensional model. With this in mind, differences in between the models regarding the predicted velocity distribution in double-logarithmic representation, as shown in Figure 6.10(b), can be attributed to this effect. As the roughness length increases the vertical gradient of the mean axial velocity does as well, or in other words the shear exponent α of the power law. Due to the 'modification' of the roughness length in case of the standard model, these distributions result in larger vertical gradients (higher shear) than in case of the lifted model.

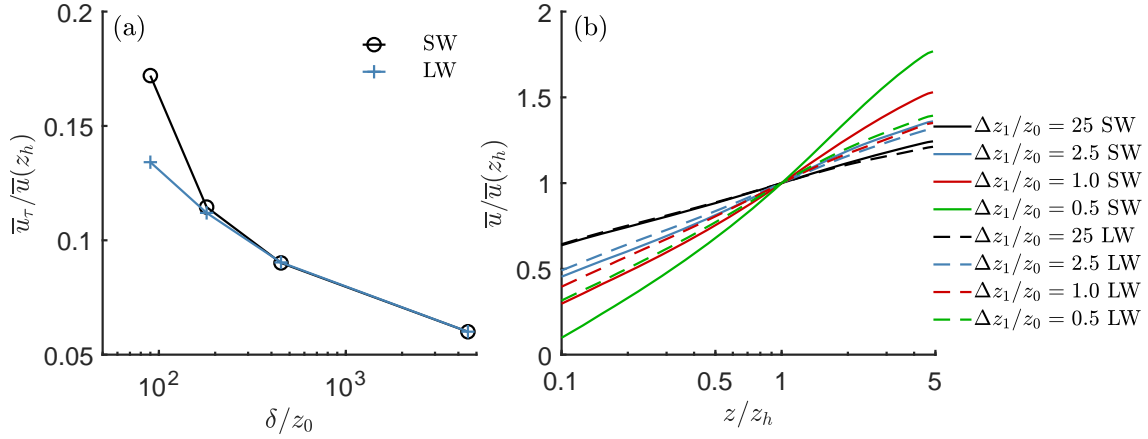


Figure 6.10: (a) Normalised shear stress velocity $\bar{u}_\tau / \bar{u}(z_h)$ as function of roughness length δ / z_0 and (b) normalised mean axial velocity $\bar{u} / \bar{u}(z_h)$ as function of wall distance, computed with the standard wall model (SW) and the lifted wall model (LW). The legend denotes ratio of wall-normal cell size to roughness length $\Delta z_1 / z_0$ and applied wall model

Figure 6.11 shows the computed non-dimensional Reynolds stresses as function of wall distance in semi-logarithmic representation. Thereby the most noticeable feature of the distributions predicted with the lifted wall model are the excessive stresses in the region adjacent to the wall $z / \delta < 0.03$ which also increase with roughness. From the results it can not be clarified if these excessive stresses have an influence on the outer layer of the flow. However, as the results within a wall model exhibit similar trends with varying roughness, it is supposed that the effect is rather small and that in the outer layers differences between the models can rather be attributed to the different definitions used to compute the wall shear stress. Nevertheless, it is important to discuss the influence of roughness on the non-dimensional Reynolds stresses. For smooth walls self similarity over the complete height of the boundary layer is expected and for transitional roughness only in the outer layers, which is known as Townsend's hypothesis [142]. However, for fully rough boundary layer flows roughness elements become large and penetrate well into the log law region thus affecting a significant portion of it and causing a breakdown of similarity in the outer-layers [27]. Jiménez [69] suggested that this breakdown can be observed for roughness elements with a sand grain roughness $k / \delta > 1 / 40$, which as roughness length can be expressed as $\delta / z_0 < 1000$ (for transformation see Section 2.1.1). Hence, as can be seen in Figure 6.10(a), except for the lowest roughness length considered here, all computed boundary layers fall well below this value. Therefore, they can be considered as fully rough and are not expected to exhibit self similarity of the Reynolds stresses.

For a qualitative verification of the predicted Reynolds stresses, Figure 6.11 (a) and (b) show measurement data reproduced from [69] for the non-dimensional Reynolds stresses $\overline{u'u'^+}$ and $\overline{w'w'^+}$ over a smooth surface (sbl) with $\delta^+ = u_\tau \delta / \nu = 7.300$ and a rough surface (woven mesh, wm) with $k_s^+ = u_\tau k_s / \nu = 345$, whereby the latter is equivalent to a roughness length of $\delta / z_0 \approx 6.200$. From this comparison it can be concluded that for large surface roughness, in the outer region of the boundary layer $z / \delta > 0.03$ the Reynolds stresses $\overline{u'u'}$ predicted by the virtually lifted wall model are in better agreement with the measurement results than those predicted by the standard model. However, both models do not correctly capture the distribution of the Reynolds stresses $\overline{w'w'}$. Since, as discussed

above, this component of the Reynolds stress tensor shows only little sensitivity to variations of the roughness length, the wall-normal grid resolution, the cell aspect ratio, and the grid point for evaluating the wall stress, this mismatch is considered to stem from the subgrid scale model ALDM, which is calibrated to meet the eddy viscosity of isotropic turbulence, see [61].

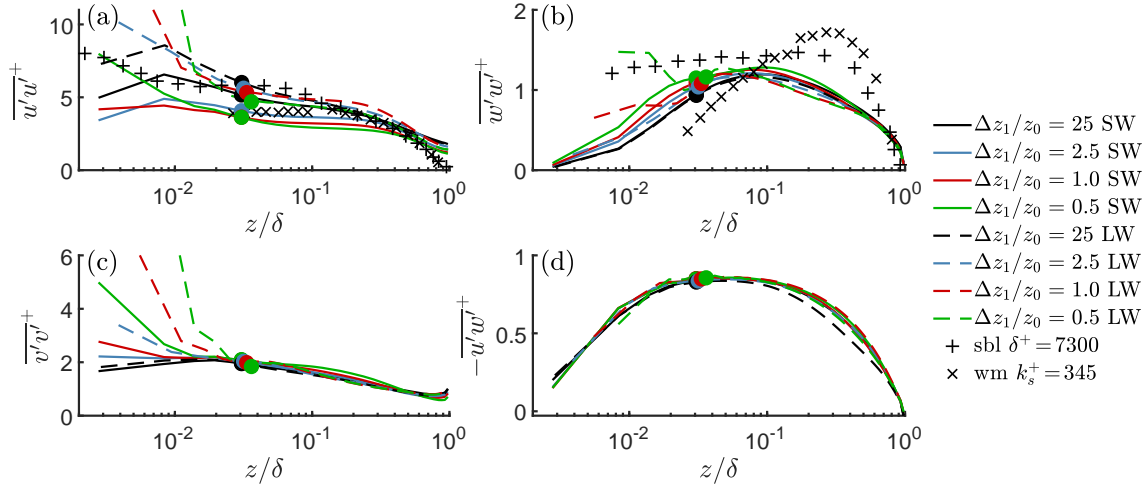


Figure 6.11: Non-dimensional Reynolds stresses (a) $\overline{u'u'^+}$, (b) $\overline{w'w'^+}$, (c) $\overline{v'v'^+}$, and (d) $-\overline{u'w'^+}$ as function of wall distance z/δ obtained with the standard wall model (SW), the lifted wall model (LW), and from measurements. The legend denotes ratio of wall-normal cell size to roughness length $\Delta z_1/z_0$ and applied wall model. Coloured dots indicate grid points used for evaluation of the wall shear stress. Experimental results over smooth surface (sbl) and woven mesh (wm) are reproduced from [69].

6.3 Actuator Line Method

To simulate the rotor flow of the model wind turbine the Actuator Line Method (ALM) is implemented in the applied flow solver. The methodology is given in Section 6.3.1. For validation purposes results of a test case are presented in Section 6.3.2 and are compared with numerical data found in literature.

6.3.1 Numerical Methodology

In the following the Actuator Line Method (ALM) and its implementation in INCA are described. Since INCA makes use of the Navier-Stokes Equations formulated in primitive variables (i.e. pressure-velocity variables), the method reformulated by Mikkelsen [102] was chosen for the implementation.

It is convenient to determine the blade forces in the rotating aerodynamic frame of each blade segment in which the coordinate system is aligned with the velocity of the relative wind. However, as the Navier-Stokes equations are solved in an inertial stationary frame the forces have to be transformed into this frame. To determine the velocity of the relative wind in the aerodynamic frame the procedure has to be performed vice versa as the flow field is given in the stationary frame. For that reasons the following coordinate systems are introduced, additionally to the inertial system (no subscript) of the flow solver: (i) the stationary frame I which is aligned with the inertial system but with its origin in the rotor center; (ii) with the same origin, the stationary frame II of which the z- and x-axis are aligned with the rotational axis of the rotor and the initial axis of the 1st blade; (iii) the rotating frame r , which rotates around the rotor axis with the angular velocity Ω ; (iv) the rotating and blade fixed frames b_i with $i = 1, \dots, N_b$ where N_b is the total number of blades which are shifted in phase regarding the rotor frame by the angle of $\Psi_{0,i} = 2\pi(i - 1)/N_b$; (v) the aerodynamic frames a_{ij} which are defined for each blade i and segment j and which not only rotate with the blade but also with the direction of the local relative wind, having its y- and z-axis pointing parallel and normal to the the direction of the relative wind. The definition of all mentioned coordinate systems is depicted in figure 6.12. The coordinate transformations are given by rotational matrices ${}_bR_a$ where the subscripts indicate the transformation from frame a to frame b . All used matrices can be found in the appendix A.2.

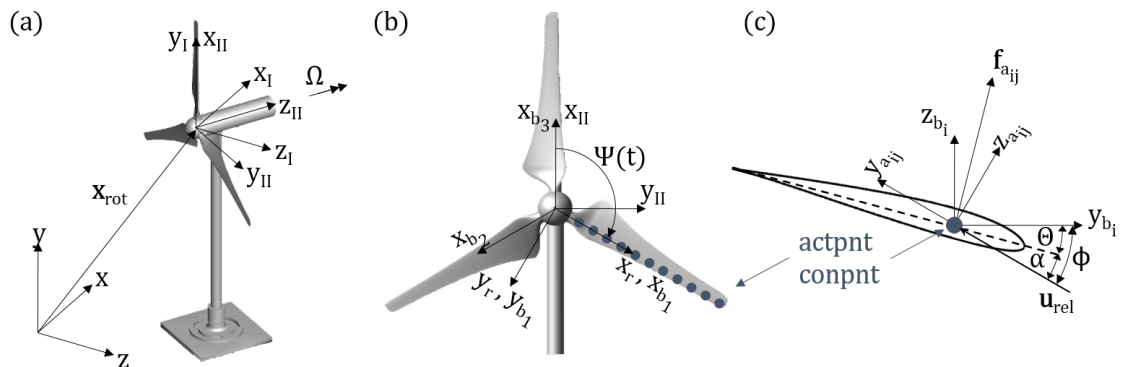


Figure 6.12: Definition of coordinate systems used in the actuator line method

The actuator points are defined to lie on the chord line with 25% chord length distance

to the leading edge. The positions of all actuator points on the 1st blade $\mathbf{x}_{b_1,act}$ have to be provided as tabulated data by the user, which also allows to provide swept blades. Furthermore it is necessary to provide the local chord length $c(r)$ and the local twist angle $\Theta(r)$ as function of the radius r . The positions of all actuator points within the rotor frame $\mathbf{x}_{r,act}$ are then computed upon initialisation. For each actuator point (actpnt) an additional control point (conpnt) is introduced. The purpose of these points is to determine the vector of the relative wind. In principle actuator and control point can be located separately at a user defined position within the cross section of the blade segment. In this work, however, the common approach is used to set the control point on the same location as its corresponding actuator point.

At each time instance t the current position of an actuator/control point is calculated by

$$\mathbf{x}_{act/con} = \mathbf{x}_{rot} + {}_I\mathbf{R}_r(\Psi(t))\mathbf{x}_{r,act} \quad (6.18)$$

The local flow velocity at the control point \mathbf{u}_{con} is then determined by means of a distance weighted interpolation from the neighbouring grid points and is then transformed into the blade fixed frame where it represents the velocity of the relative wind

$$\mathbf{u}_{b,rel} = \mathbf{u}_{b,con} = \frac{d}{dt} \{ {}_b\mathbf{R}_I(\Psi(t)) \} (\mathbf{x}_{con} - \mathbf{x}_{rot}) + {}_b\mathbf{R}_I(\Psi(t))\mathbf{u}_{con}. \quad (6.19)$$

The angle of the relative wind ϕ can then be determined from the components v_b, w_b of the vector $\mathbf{u}_{b,rel}$ which lie within the cross sectional plane of the blade segment

$$\phi = \tan^{-1} \left(\frac{-w_b}{v_b} \right). \quad (6.20)$$

The magnitude of the relative wind normal to the blade $|\mathbf{u}_{rel,\perp}|$ is computed as

$$|\mathbf{u}_{b,rel\perp}| = \sqrt{u_b^2 + v_b^2}. \quad (6.21)$$

The tabulated lift and drag coefficients $C_L(\alpha)$ and $C_D(\alpha)$ are provided as function of the angle of attack (AoA) α , which for each segment can be calculated by the angle of the relative wind ϕ and the local twist angle Θ by applying Eq.(2.33). Given that, the force per segment can be calculated in the aerodynamic frame as

$$\mathbf{f}_{a_{ij}} = \frac{1}{2}\rho|\mathbf{u}_{b,rel\perp}|^2 c(r) \Delta s_j \begin{pmatrix} 0 \\ C_D(\alpha) \\ C_L(\alpha) \end{pmatrix} \quad (6.22)$$

where Δs_j is the width of the segment in spanwise direction. It is then transformed to the inertial frame by

$$\mathbf{f} = {}_I\mathbf{R}_r(\Psi(t)) {}_r\mathbf{R}_b {}_b\mathbf{R}_a \mathbf{f}_{a_{ij}} \quad (6.23)$$

To avoid singular behaviour, the loading is then distributed as body force smoothly on several grid points in order. This is achieved by distributing them along and away from the actuator lines in a three-dimensional Gaussian manner by taking the convolution of the computed local force \mathbf{f} and a regularisation kernel η_ϵ

$$\mathbf{f}_\epsilon = \mathbf{f} * \eta_\epsilon, \quad \eta_\epsilon = \frac{1}{\pi^{3/2}\epsilon^3} \exp \left[- \left(\frac{d}{\epsilon} \right)^2 \right] \quad (6.24)$$

where ϵ is a regularisation parameter that serves to adjust the concentration of the regularised force, and d is the distance between the actuator point and the considered grid point for which the body force is calculated. The choice on the value of the regularisation parameter and the number of actuator points per blade can have a significant influence on the flow solution. Choosing a small value for ϵ or too few actuator points can introduce numerical instabilities. On the other hand, if the value of ϵ is chosen too big, flow features as the tip vortices are not resolved correctly and introducing too much actuator points can slow down the computation. Mikkelsen [102] and Tossas [141] investigated this matter in detail and recommend a value of $\epsilon > 2\Delta x$ for cubic cells with an edge size of Δx . Furthermore, Tossas recommends a density of actuator points of $\Delta b < \Delta x$ where Δb is the distance between two actuator points. However, the appearance of numerical instabilities and their strength depend strongly on the choice of the specific flow solver.

Preliminary tests with INCA (not shown here) suggest an optimum parameter of $\epsilon = 3\Delta x$. Nevertheless, within laminar and uniform approaching flow conditions numerical wiggles are observed which are persistent even for large values of ϵ or high densities of actuator points Δb . In these cases the whole simulation can become unstable. Therefore, in numerical simulations with these flow conditions presented in this work, a high order low pass filter is applied at each time step which is particularly made to remove numerical oscillations. The characteristic of the instability and the filtering procedure is explained in more detail in Section 6.3.2. It should be emphasised that in simulations where the actuator line method is applied in combination with turbulent boundary layer flows no numerical instabilities were observed. Therefore, in these cases the filtering procedure was not applied.

6.3.2 Validation Testcase (NREL-5MW)

To validate the implementation of the Actuator Line Method, the 5MW reference wind turbine designed by the National Renewable Energy Laboratory [76] with a rotor radius of $R = 63$ m and a hub height of $z_h = 90$ m is simulated in uniform laminar background flow operating at design conditions and is compared to results obtained with the Navier-Stokes flow solver EllipSys3D [144].

6.3.2.1 Numerical Setup

The computational domain in total has an extent of $L_x = 40R$ in the axial, $L_y = 32R$ in the lateral, and $L_z = 16R$ in the vertical direction. In this domain, centric in x- and y-direction but adjacent to the lower z-surface, a region of cubic cells is located with the dimensions $l_x \times l_y \times l_z = 20R \times 4.25R \times 2.3R$. The edge length of each cell in this region is $\Delta x = \Delta y = \Delta z = R/N$, where $N = 30$ are the grid points per rotor radius. Away from the cubic cell region and towards the domain boundaries the grid is linearly coarsened by 5% per cell in the axial direction and 8% per cell in the lateral and vertical direction.

The upstream boundary is set to be a classical inflow with the reference velocity $u_{ref} = 8$ m/s prescribed and zero pressure gradient. Therefore, the downstream boundary is defined as a Neumann condition for the flow velocity $\partial u_i / \partial x_i = 0$ and a Dirichlet condition for the local static pressure p which is dynamically adjusted such that the total pressure p_t remains constant. The lateral and vertical boundaries are defined as free-slip wall conditions. The regularisation parameter of the actuator line method is set to $\epsilon = 3\Delta x$ and each rotor blade is described by 34 equidistant distributed actuator points. The airfoil

data used in the simulation is provided by Jonkman *et. al* [76].

Since the design tip speed ratio is chosen to be $\lambda_{dsgn} = 7.55$, with the given wind speed of u_{ref} this results in a angular velocity of $\Omega = 0.964$ rad/s. The simulation advances in time such that the rotor rotates by 2° per time step Δt resulting in a CFL number $c = 0.138$. A total of 100 rotor revolutions is simulated of which the last 50 revolutions are used to obtain the flow field statistics.

6.3.2.2 Results

As insinuated in Section 6.3.1, in the realisation of this testcase numerical wiggles were observed even for large values of the regularisation parameter ϵ and high densities of actuator points Δb . These wiggles seem to be similar to those reported for results obtained for small values of $\epsilon < 3\Delta x$ and with other flow solver, as e.g. in [141] see Figure 12 for comparison. These wiggles are small in the current test case and can only be observed on contours where the colourmap is scaled to small values of the considered quantity, see Figure 6.13(a) and (b) of the normalised vorticity magnitude ω shown for different ranges of contour levels. Nevertheless, these oscillations are first transported upstream towards the inlet boundary with a velocity of about $2u_{ref}$ where they are reflected and transported downstream to the outlet boundary where the process repeats. With each reflection the oscillations are amplified until the flow field is eventually corrupted.

Even though the origin of this numerical oscillation could not be clarified, they can be damped by applying a high order Taylor filter. These kind of filters is designed to selectively damp short waves while having a minimal effect on long waves. The filter uses a symmetric one-dimensional stencil of $2N + 1$ grid points. Therefore, it can be applied in each direction, however, it was found that in this case applying it solely in the x-direction is sufficient. The filtering procedure of the velocity vector \mathbf{u} at grid point (i, j, k) at the time instance n can, hence, be written as

$$\bar{\mathbf{u}}_{i,j,k}^n = \mathbf{u}_{i,j,k}^n + a_f \sum_{l=-N}^N w_l \mathbf{u}_{i+l,j,k}^n \quad (6.25)$$

where a_f is the relative filtering amplitude, $\bar{[\cdot]}$ denotes the filtered quantity, and w_l are the filter coefficients which can be found in [147]. The used definition describes the filter as a change with respect to the original value. The advantage of it is that it allows to adjust the contribution of the filter by setting the filtering amplitude a_f . Indeed, in the testcase presented below for the applied 7-point filter stencil ($N = 3$) a value of $a_f = 0.01$ was found to already damp the numerical oscillations such that they do not amplify in the course of the simulation. The resulting normalised vorticity magnitude ω is shown in Figure 6.13(c) and (d).

As already mentioned in Section 6.3.1, it is important to notice that in the LES study of the model wind turbine immersed in turbulent boundary layer flows, presented in Chapter 7, no numerical instabilities could be observed. Therefore, in these cases the filtering procedure was not applied.

The validation of the current implementation of the ALM is carried out in two steps. First the ALM is applied to calculate the blade loads as described in Section 6.3.1 and compared to results considered as reference. In a second step the rotor loads computed in a simulation based on the fully resolved rotor geometry are prescribed in the ALM. Thus,

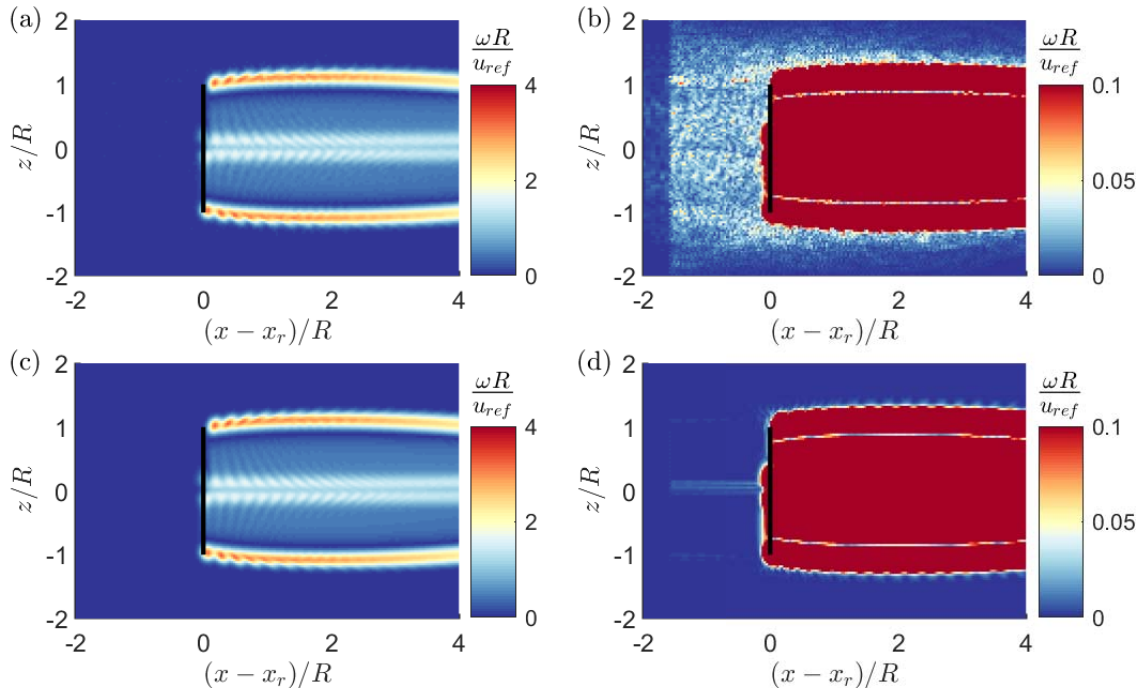


Figure 6.13: Normalised vorticity magnitude $\omega R/u_{ref}$ in the wake of the NREL-5MW wind turbine after 10 revolutions shown for two different ranges of contour levels, (a)/(b) unfiltered and (c)/(d) filtered vorticity field using a 7-point Taylor filter.

differences in the resulting velocity fields do not arise from differences in the predicted rotor forces.

Figure 6.14 shows the computed time mean of the normalised rotor loads, (a) in the direction normal to the rotor disc and (b) in azimuthal direction. As a reference results computed with the flow solver EllipSys3D using the ALM (EllipSys3D ALM) are shown as well. Blade forces obtained by a detached-eddy simulation (EllipSys3D DES) and prescribed in the subsequent step are also given. Both datasets were published and provided by Troldborg *et. al* [144]. The blade loading predicted by the implementation used in this work (INCA ALM) is in almost perfect agreement with the reference data (EllipSys3D ALM). Only in the blade tip region slight deviations can be observed. It is also worth noticing that the blade loading normal to the rotor disc predicted by the ALM is in good agreement with the geometry resolving detached eddy simulation.

With prescribed blade loading the velocity distributions predicted by all three simulations in the vicinity of the rotor perfectly match, see Figure 6.15 at $x/R = 2$. Only near the rotor axis, the ALM reference data deviates significantly from the predictions of the DES and the current ALM implementation. Nevertheless, besides this region both ALM simulations result in nearly equal velocity distributions in the considered axial range. The significantly faster recovery of the wake predicted by the DES originates from vortices shedding of the rotor blade and cause the wake to become unstable at approximately $x/R = 4$ [144]. Subsequently it reaches a fully turbulent state and the resulting velocity fluctuations enhance the lateral momentum transfer which causes the wake to recover faster. As these vortices are not resolved in case of the ALM simulations the wake maintains stable for longer downstream distances and does not recover significantly.

As can be seen in Figure 6.16, in case of the DES the transition of the wake to turbulent

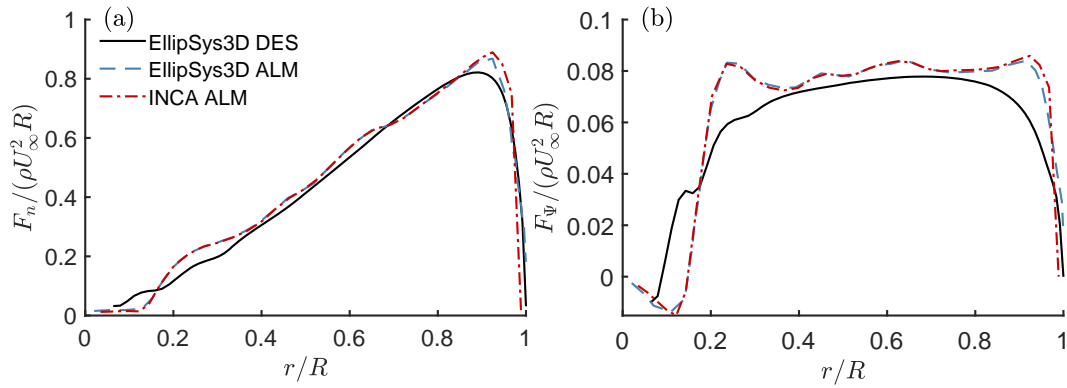


Figure 6.14: Spanwise distribution of (a) normal and (b) azimuthal blade loads. Legend denotes applied flow solver and method.

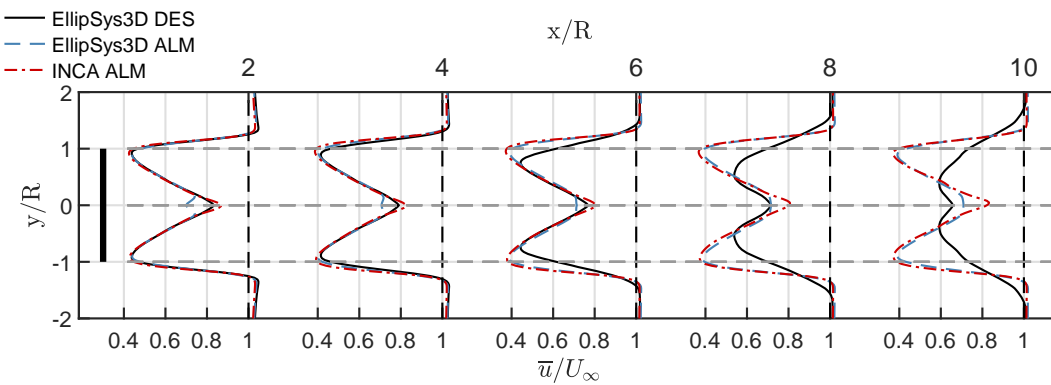


Figure 6.15: Profiles of the normalised mean axial velocity component \bar{u}/u_{ref} in the mid-horizontal plane at axial positions $x/R = 2, 4, 6, 8, 10$. Legend denotes applied flow solver and method.

state can be characterised by a significant rise of the turbulent kinetic energy (TKE) K in the range $4 < x/R < 6$ after which it maintains an almost constant level. For both ALM simulations the TKE is negligible for distances $x/R < 10$. Further downstream a rise of the TKE can be observed, marking the onset of the transition to a turbulent state. The involved breakdown of tip vortices can well be observed by the instantaneous isosurface of the vorticity magnitude as shown in Figure 6.17.

In the absence of turbulence in the approaching flow, the onset of transitions is very sensitive to small disturbances which can be caused by various factors, including numerical oscillations as mentioned above. As shown by Troldborg *et. al* [144] within turbulent flows the interaction of the wake with the approaching turbulent structures completely dominates the process of wake transition, resulting in similar flow fields computed by DES and ALM and making the effect of numerical disturbances become insignificant. Hence, even though the results in this section are in good agreement with reference data, an in-depth validation of the applied numerical methods of ALM and implicit LES modelling should be carried out within a turbulent environment. This is presented in Section 7 where LES results of the model wind turbine immersed in turbulent boundary layer flow is analysed in detail including a comparison with wind tunnel measurements.

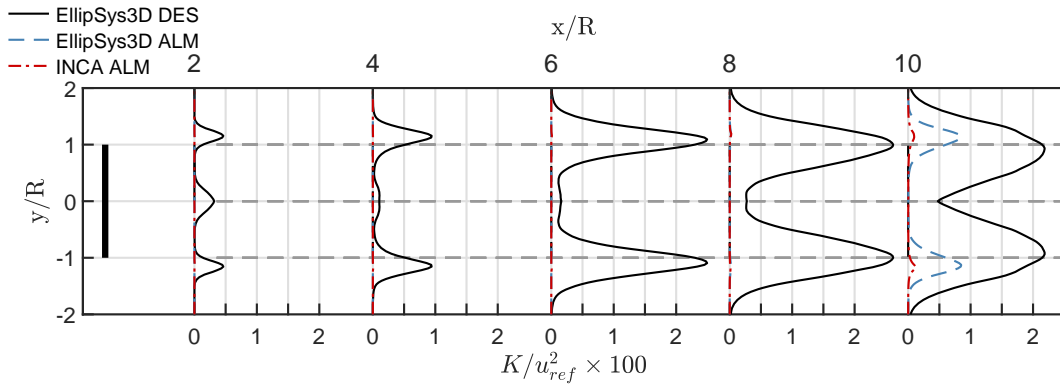


Figure 6.16: Profiles of the normalised turbulent kinetic energy K/u_{ref}^2 in the mid-horizontal plane at axial positions $x/R = 2, 4, 6, 8, 10$. Legend denotes applied flow solver and method.

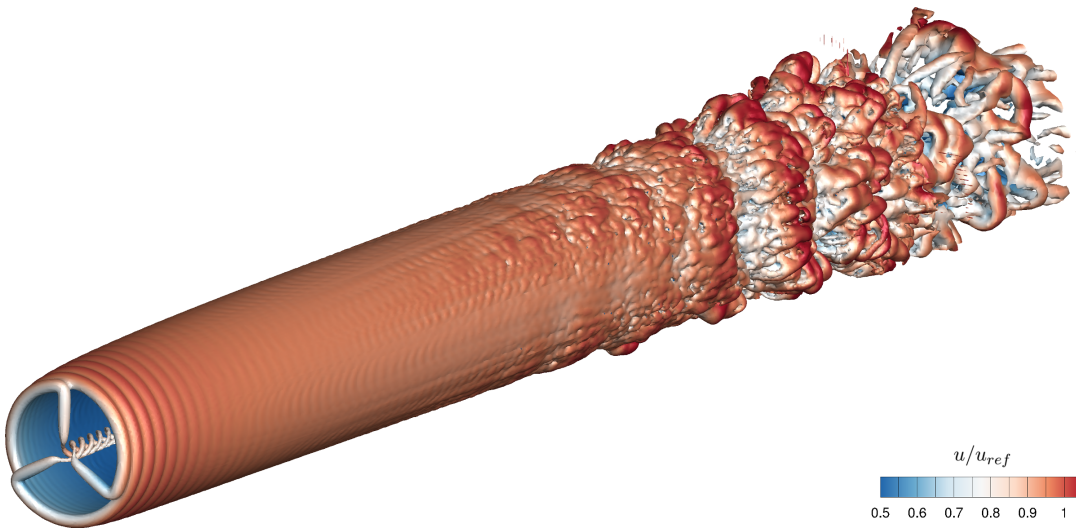


Figure 6.17: Isosurface of normalised vorticity magnitude $\omega R/u_{ref} = 1.57$. Colour indicates normalised axial velocity u/u_{ref}

6.4 Blade Polar Identification

As mentioned in Section 6.3 the body forces introduced by the actuator line method and acting on the fluid are mainly dependent on the tabulated airfoil data. Since the body forces determine the flow field in the wake of the wind turbine, the quality of the tabulated airfoil is crucial for an accurate modelling. In the design process of the model wind turbine, described in Section 4.2, airfoil data obtained by solving two-dimensional boundary layer equations was used. These computations do not take into account any rotational or three-dimensional effects, nor the finite length of the blades at which tips strong vortices form and interact with the flow field around the blade. The latter, however, is taken into account in the calculation of the blade chord and twist.

During the measurements presented in Chapter 5, it was observed that the measured rotor performance significantly deviated from its predicted values. Even though uncertainties in the measurement results were reduced by repetition and applying a calibration routine for the motor, see Section 4.3, significant differences remained. Therefore, on the

basis of a lifting line model and the measured power and thrust coefficients of the rotor, the lift and drag characteristics were calibrated by applying the optimisation approach developed by Cacciola *et al* [24]. In the calibrated characteristics drag was corrected in particular, yielding substantial improvements in the accuracy of the prediction by the lifting line model regarding the produced power. However, the thrust predictions were not significantly improved. Therefore, it was assumed that providing only integral parameters as input parameters is not sufficient to state a well-posed optimisation problem. The study was carried out by Bastian Salbert as part of his term paper [120].

To overcome the lack of input parameters necessary to calibrate the lifting line model, a purely simulative approach [124] was tested. Since in numerical flow simulations all flow quantities and body forces are observable at every point in space, the problem of determining lift and drag characteristics simplifies significantly and can be solved by an inverse lifting line calculation. The study was carried out by Katharina Mütze as part of her term paper [104]. Here only the most important details of it shall be described. Therefore, the inverse lifting line method is explained in the following Section 6.4.1. In Section 6.4.2 the numerical setup is described and in Section 6.4.3 the results are presented.

6.4.1 Inverse Blade Element Momentum Method

In this approach the Blade Element Momentum (BEM) calculation as described in Section 2.2.3 is, as the name says, inverted. That means, that the axial and induction factors a and a' are determined iteratively from the blade forces and are then used to calculate the angle of attack as well as the lift and drag characteristics.

Including Prandtl's tip loss correction and Glauert's correction for large induction factors, the inverse BEM method can be implemented as described in [124] using the following steps for each segment:

1. Initialise a and a' , e.g. $a = a' = 0$
2. Compute the local inflow angle ϕ by Eq.(2.32)
3. Calculate the angle of attack α using Eq.(2.33)
4. Calculate the induction factors a and a' by Eq.(2.41) and (2.42)
5. If a and a' have changed more than a certain value, go back to step 2., else
6. Compute the local inflow velocity U_{rel} by Eq.(2.34)
7. Calculate the lift and drag coefficients C_l and C_d using Eq.(2.30) and Eq.(2.31), where F_{ax} and F_t are the sum of all point forces in the RANS solution in the axial or tangential direction, respectively.

6.4.2 Numerical Setup

To obtain lift and drag coefficients over a broad range of angles of attack with sufficient resolution, blade forces for different tip speed ratios and blade pitch angles have to be computed. For this purpose the fully compressible viscous steady state RANS solver CFX by ANSYS Inc. is applied. Despite the 'moderate' fidelity of this flow solver, due the high number of necessary simulations, the computational costs are significant. Therefore, to reduce these costs only a 120° segment of the wind turbine is simulated and the presence of the tower is neglected. To take into account the rotational forces acting on the fluid, the segment is simulated as rotating frame of reference with periodic boundary

conditions at the circumferential boundaries. Due to numerical instabilities the rotating domain is additionally surrounded by a non rotating outer domain and all fluxes at its interfaces are interpolated in a conservative manner (general grid interface). In order to be able to set different blade pitch angles without having to re-mesh the computational domain, the region around the blade is modelled in a separate domain with a cylindrically shaped general grid interface. To obtain accurate blade forces the computational domain is discretised by a block-structured grid which is designed to have a resolution of approximately 15 grid cells within the wall boundary layer of the blade and an average size of the first wall adjacent grid cell of $y_{ave}^+ = 0.88$. With this the computational domain consists in total of 10 million computational cells. For the numerical discretisation of the advective terms the so called 'high resolution' discretisation is applied, which dynamically blends between a 1st and 2nd order discretisation in regions with slow convergence of the residuals. Turbulence is modelled by using the two-equation $k - \omega$ shear stress transport (SST) model. An overview of the computational domain, as well as all interfaces and boundary conditions is given in figure 6.18.

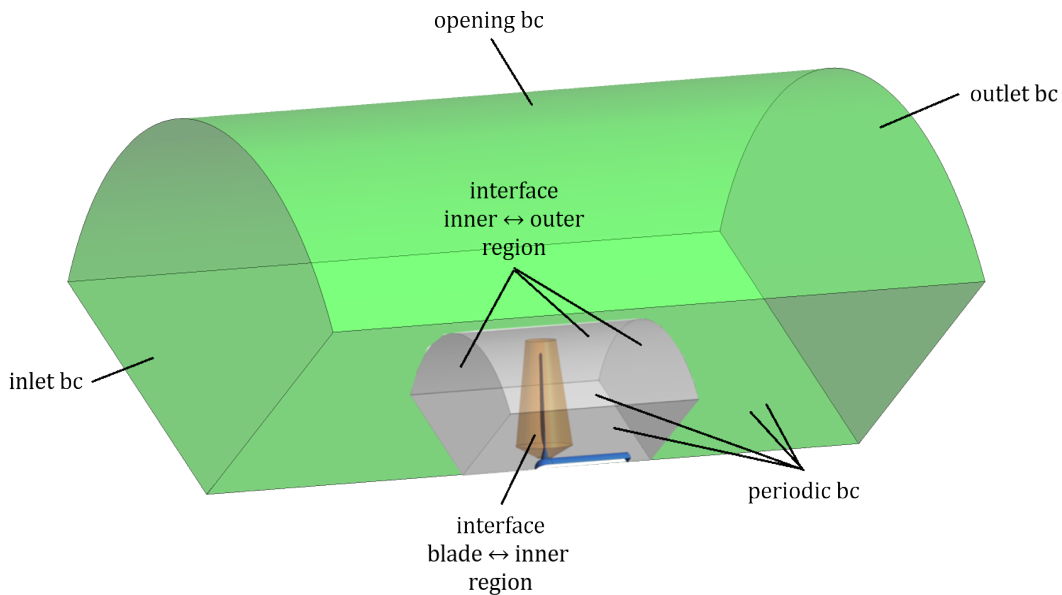


Figure 6.18: Overview of the simulation domain, the boundary conditions (bc) and interfaces.

As explained in Section 4.5 Reynolds number effects can occur if operational conditions are chosen without care. Therefore, in order to exclude any Reynolds number dependency of the blade forces, the rotational frequency of the rotating domains and the freestream velocity at the inlet are set as described in Section 4.5 for an average chord based Reynolds number of $\overline{Re}_c = 62,500$.

To obtain the required resolution of blade forces as function of the angle of attack, numerical simulations have been carried out for blade pitch angles $\Theta_p = -2^\circ$ to 6° with an increment of $\Delta\Theta_p = 1^\circ$. For each pitch angle the tip speed ratio is varied from $\lambda = 2$ to 12 with an increment of $\Delta\lambda = 0.5$.

6.4.3 Results

To verify the accuracy of the simulation results, figure 6.19 shows the power and thrust coefficient as function of the tip speed ratio for pitch angles of $\Theta_p = 0^\circ, 1^\circ, 2^\circ$ obtained from the simulation (RANS) and compares them with the results of the wind tunnel measurements (EXP), the results from the lifting line calibration (CAL) and the values predicted initially in the design process (DSGN). As mentioned before, in the rotor design only one airfoil polar was used which is derived from two-dimensional boundary layer equations without taking into account any rotational and three-dimensional effects nor the finite length of the blade. Most salient in the comparison of the thrust coefficients in figure 6.19(a)-(c) is the good agreement of the simulation and measurement data in comparison to the values predicted in the design process, whereas the comparison of the obtained power coefficients shown in figure 6.19(d)-(f) shows no significant improvement by the RANS simulation. On the other hand, the power coefficients obtained using the airfoil characteristics from the lifting line calibration is in very good agreement with the measurements whereas the calibration only results in a minor improvement of the thrust coefficients.

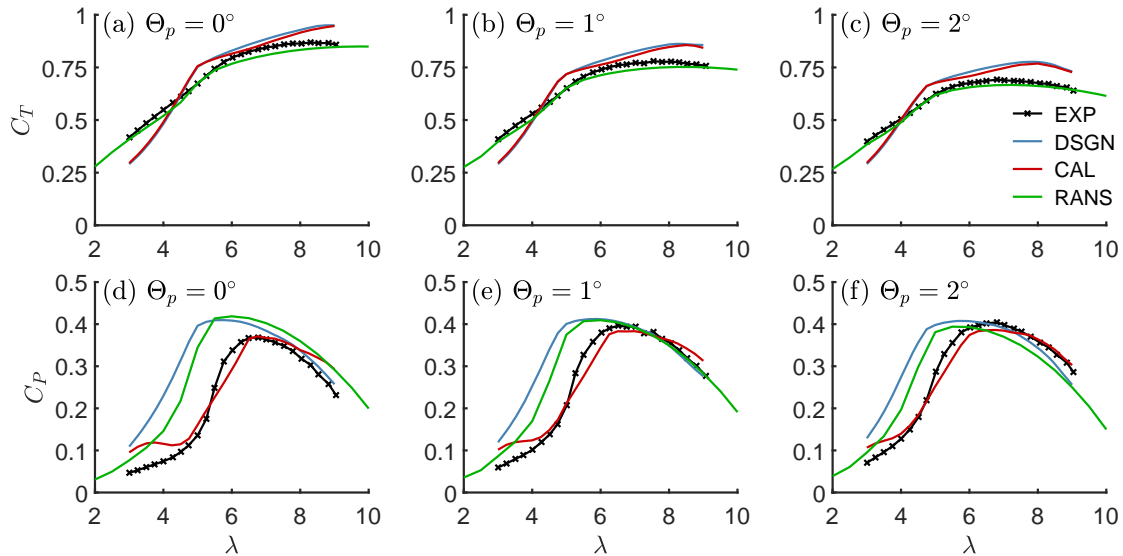


Figure 6.19: Comparison of (a)-(c) thrust C_T and (d)-(f) power coefficients C_P as function of tip speed ratio λ obtained from measurement (EXP), 2D airfoil calculations (DSGN), lifting line calibration (CAL) and numerical simulation (RANS) for pitch angles $\Theta_p = 0^\circ, 1^\circ, 2^\circ$.

Figure 6.20 shows lift and drag polars based on the blade forces of the three-dimensional RANS simulation and derived by the inverse BEM method described in Section 6.4.1. These are compared to the airfoil characteristic used in the design process (DSGN) and the one obtained in the lifting line calibration (CAL). In the design process and the lifting line calibration no radial dependency of the airfoil characteristics is considered (i) for simplicity and (ii) in case of the lifting line calibration due to the low observability and collinearity of the radial blade elements. However, from the characteristics of the inverse BEM method based on the RANS simulation, the radial dependency of the lift and drag characteristics due to rotational and three-dimensional effects can easily be seen: (i) Lift values are reduced for all AoA α along the complete span of the blade which is even more significant at the blade tip due to presence of the strong blade tip vortices there; (ii)

Drag values for low AoA are similar in the middle of the blade span whereas they are increased for high AoA and at the outer sections of the blade.

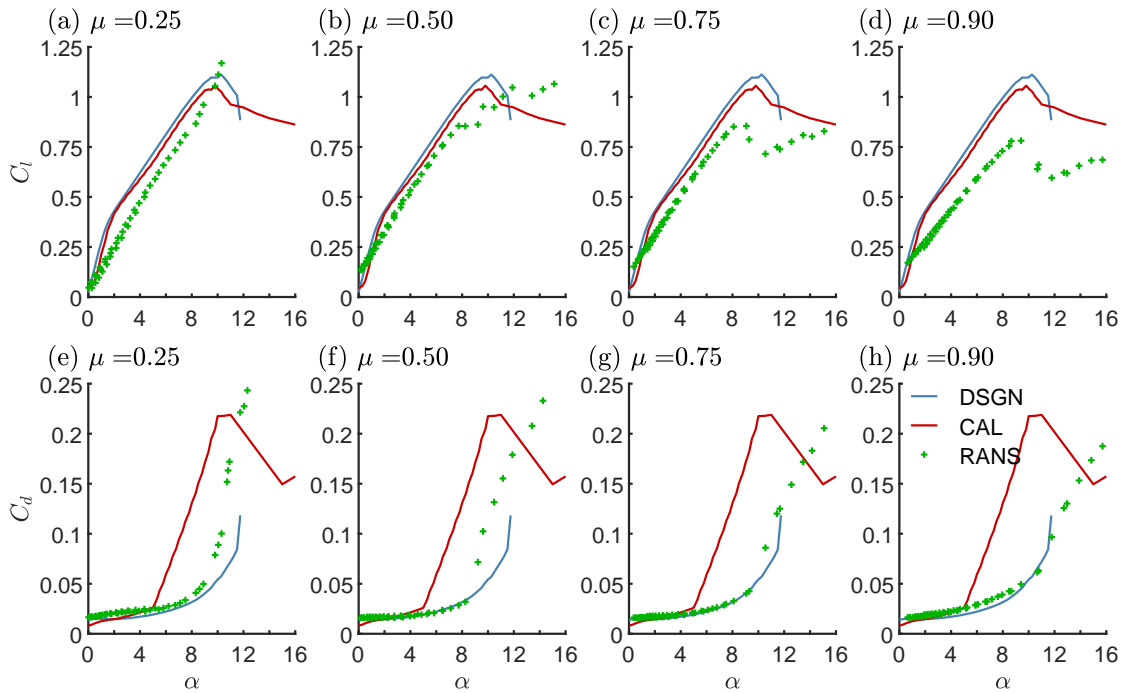


Figure 6.20: Comparison of blade polars obtained from 2D airfoil calculations (DSGN), lifting line calibration (CAL) and numerical simulation (RANS): (a)-(d) lift C_l and (e)-(h) drag C_d coefficients as function of AoA α at selected blade sections $\mu = 0.25, 0.5, 0.75, 0.9$.

According to the BEM Theory, see Section 2.2.3, the contribution of lift and drag to thrust δT and torque δQ produced by a blade element of the length δr can be described as given in Eq.(2.35). From that it becomes clear that the generation of thrust is mainly dominated by the lift coefficient. Hence it is consistent that similar lift characteristics result in similar thrust coefficients as it is the case for the design and the calibrated airfoil characteristic. The generally lower lift coefficient and its radial dependency predicted by the inverse BEM method is the main reason for the very good agreement with the measurement results.

The argumentation for the connection of power coefficient and airfoil characteristic is more complex as the generation of torque is not solely dominated by the lift but also the drag coefficient. Therefore it is helpful to distinguish between the ranges of low and high tip speed ratios. However, as this is only a qualitative analysis to show the consistency of the results, a border between these ranges can not be set sharp. For low tip speed ratios the angle of relative wind and hence also the AoA α is high along the complete blade span. In this regime the drag coefficients computed by the inverse BEM method are higher than predicted by the two-dimensional method. Together with the lower lift coefficient, according to Eq.(2.35) and as observed in figure 6.19(d)-(f) this results in a reduced power coefficient for low tip speed ratios ($\lambda \lesssim 5$). The same holds for the calibrated airfoil characteristic, which due to the high drag for AoAs $\alpha > 5^\circ$ results in an even lower power coefficient for low tip speed ratios close to the measured values. For high tip speed ratios, the angle of relative wind and the AoA α become small. With that the contribution of lift to the generation of torque reduces. Given the similar drag coefficients in all characteristics, in this regime a convergence of the power coefficients is to be

expected and can also be observed in figure 6.19(d)-(f) for high tip speed ratios ($\lambda \gtrsim 5$).

The thrust of the rotor determines the velocity deficit in the wake of the wind turbine and the airfoil characteristics obtained with the inverse BEM method based on the RANS simulation predict the thrust with high accuracy. Therefore, these characteristics are used as input data for the actuator line method, improving the accuracy of the velocity fields predicted by the LES simulation to be presented in Chapter 7.

6.5 Summary

This chapter provided the numerical methods specifically implemented in the flow solver applied for the simulation of the model wind turbine immersed in turbulent boundary layer flows over rough surfaces.

For this purpose an established wall shear stress model was implemented. Studies found in literature observed that for turbulent flows over smooth walls the subgrid modelling errors affecting the wall model decrease when, for the evaluation of the shear stress, grid points other than the first adjacent to the wall are chosen. Inspired by these results, the implemented wall model for rough surfaces was adapted for the evaluation of the shear stress on arbitrary grid points. It was shown that for grid points with increasing distance the wall shear stress asymptotically increases and converges, such that the non-dimensional velocity profile u^+ in the boundary layer becomes more accurate while non-dimensional Reynolds shear stresses $\overline{u_i' u_i'}^+$ are only altered in the lowest part of the boundary layer.

A sensitivity study regarding the grid resolution showed that the required wall normal resolution for the wake modelling is sufficient to obtain grid convergence. However, it was revealed that results are more sensitive to aspect ratios of the cells in the horizontal plane. Due to limited resources for this study, it could not be clarified for which aspect ratios grid convergence is achieved. Nevertheless, it is important to notice that a grid refinement within the computational domain inevitably results in transitional effects, leading to subtle changes in the boundary layer properties. Such a transition is observed in the LES study presented in the next chapter where the computational domain is not entirely resolved by cubic cells due to the high computational costs connected with it.

For large roughness lengths in the order of the wall normal grid resolution it was observed that the current implementation of the standard wall model predicts negative mean axial velocities in the grid cells close to the wall. Therefore, a new wall model was derived in which the domain is virtually lifted above ground and the no-slip wall condition at the lower domain boundary is replaced with a zero-divergence boundary condition which is controlled by a PI-Controller such that a certain (positive) mean axial velocity is achieved in the first grid cell adjacent to the wall. It was shown that for low surface roughness both wall models result in similar predictions regarding the non-dimensional axial velocity and Reynolds stresses. For large surface roughness the lifted wall model resulted in the intended mean axial velocity for the first grid cell and approximated the logarithmic law well in the outer region of the boundary layer. However, with increasing roughness length the wall model resulted in excessive Reynolds stresses close to the wall $z/\delta < 0.03$, whereby the effect on the outer layer was shown to be small. Since both wall models make use of different definitions of the wall shear stress, predicted Reynolds stresses were observed to differ, especially for larger values of the roughness length. Moreover, it was shown that the considered boundary layer configurations are in the fully rough regime, where self similarity of the Reynolds stresses is typically not expected. A qualitative comparison with measurement results over smooth and rough surface shows that the Reynolds stresses in axial direction $\overline{u'u'}$ are generally well predicted in the outer layer, whereas the computed Reynolds stresses in vertical direction $\overline{w'w'}$ exhibit a significant mismatch.

To model the rotor flow of the wind turbine, the actuator line method was implemented in the flow solver. In preliminary tests with uniform and laminar background flow, small

numerical oscillations in the wake were observed which were reflected and amplified at the domain boundaries, causing the simulation to become unstable. To stabilise the simulation in this flow configuration, a high-order filtering approach was implemented which successfully damped the numerical oscillations. To validate the implementation the wake of the NREL-5MW reference wind turbine was computed and results were compared with reference data found in literature. The comparison showed that the rotor loads predicted were in excellent agreement with the reference data. For the mean axial velocity only small differences could be observed in the region close to the rotor axis. Due to the absence of background turbulence in the test case and since the ALM does not resolve small scale vortices shedding from the blade, the helical blade tip vortices maintained stable over a long downstream distance and far wake conditions were not reached within the computational domain. In this flow situation, the onset of the break down of the blade tip vortices is therefore considered to be susceptible to numerical disturbances. Differences in the turbulent kinetic energy distributions found in the wake with respect to the reference data, were hence considered to stem from small disturbances, such as the outlet boundary condition or the damped numerical oscillations mentioned above.

In order to improve the accuracy of the modelled rotor flow for the model wind turbine an inverse lifting line approach was used to determine lift and drag characteristics including three-dimensional and rotational effects from results of a steady state Reynolds Averaged Navier-Stokes simulation of the rotor geometry. A comparison of the thrust coefficient predicted by the RANS simulation with data from the wind tunnel measurements presented in Section 4.6 shows a very good agreement for all considered tip speed ratios, whereas the power coefficients predicted exhibit a noticeable deviation. From aerodynamic considerations it is therefore concluded that the lift coefficient and its variation in the spanwise direction is predicted with good accuracy while the drag coefficient might be too low. Since the identified blade polars result in substantially better predictions of the rotor performance than available two-dimensional airfoil polars, these are used as input data for the actuator line method in the LES study presented in the next chapter.

LES of a Model Wind Turbine in Turbulent Boundary Layer Flows

In this chapter results of large eddy simulations of the model wind turbine immersed in three turbulent boundary layers of significantly different vertical shear and turbulence intensity (aerodynamic roughness) are presented. In addition the flow field is computed for the turbine operating in yawed conditions. As introductory part, in Section 7.1 details on the numerical setup are given. For the generation of the turbulent boundary layers precursor simulations of the undisturbed flow were carried out and are analysed in Section 7.2. In the subsequent Section 7.3 in order to analyse the grid sensitivity and to validate the simulations, results computed on two grids of different resolution are compared to measurement data. The simulated wakes are analysed in more detail according to the influence of ground roughness on the un-yawed wind turbine in Section 7.4 and on the yawed wind turbine in Section 7.5. Here special emphasis is put on the analysis of flow details which are not accessible by the wind tunnel measurements.

7.1 Numerical Setup

In Figure 7.1 a draft of the computational domain, which is used for all simulations, is shown. The domain height is chosen to be equal to the boundary layer height of $L_z = \delta = 10R = 2250\text{ mm}$, the width $L_y = 4\delta$ and the length $L_x = 21.6\delta$. To reduce the computational costs the domain is divided at half height in a lower and an upper part. In the lower part the grid resolution in vertical direction is constant everywhere with a grid spacing of $\Delta z = R/N$ where N is the number of grid points per rotor radius. In the upper part, however, the grid is gradually coarsened in vertical direction by the geometrical series $\Delta z_i = 1.04\Delta z_{i-1}$. In axial direction the computational domain can be sub-divided into four regions. The 1st region is the so-called *recycling region* in which the undisturbed boundary layer profile is generated. Therefore, at a distance of 12δ away from the inlet, a recycling plane is defined at which the flow quantities are measured to be then fed in again at the inlet. The recycling procedure is described in more detail below.

To reduce the high computational costs, the recycling region is resolved by a coarser grid resolution in the axial and lateral direction as the *wake region* where the wind turbine and its wake are located. As mentioned in Section 6.2.2.3, due to the change of grid resolution within the computational domain, transient effects in the development of the boundary layers are to be expected. However, due to the high computational costs required by a homogeneous resolution of the whole computational domain, the *recycling region* is resolved by cells with aspect ratios of $\Delta xz = \Delta x/\Delta z = 8$ and $\Delta yx = \Delta y/\Delta x = 0.5$. Due to the different grid resolutions, a *refinement region* is necessary to connect the *recycling region* with the *wake region*. Therefore, the grid is first gradually refined in the axial direction with a grid spacing of $\Delta x_i = 0.97\Delta x_{i-1}$ starting from a resolution of $\Delta x = 8R/N$ in the recycling region down to a resolution of $\Delta x = R/N$. This is then followed by a step-wise refinement of the lateral resolution from $\Delta y = 4R/N$ to $\Delta y = 2R/N$.

The 3rd region is the so-called *wake region* with a total length of $53R$. Note that the term *wake region* is also used subsequently when results for the empty domain without wind turbine and no wake are discussed. It is subdivided in a middle part with a width of $8R$ and cubic cells of $\Delta x = \Delta y = \Delta z = R/N$ and two neighbouring lateral parts where the grid is gradually coarsened. Within the middle part the wind turbine is located $8R$ downstream of the beginning of this region, which leaves another $45R$ equidistant region within which the wake development is captured. The wake region is then followed by the so-called *coarsening region*. Its purpose is to locate the outlet boundary further away from the equidistant wake region and therefore the grid is here gradually coarsened towards the outlet. Thus, in total, for a grid resolution of $N = 27$ grid points per rotor radius, the domain consists of 91.9 million grid cells which are distributed over 1344 blocks.

Due to the variety of turbulent flows various methods have been developed and tuned for the generation of turbulent inflow data. Here only a brief overview on methods applicable for fully-developed half-channel flow is given and subsequently the selected method is introduced. For a more detailed review on the generation of turbulent inflow data see e.g. [140, 37].

Library-based methods depend on an outside-source to generate instantaneous turbulent inflow planes. The source can either be a precursor simulation, which is run before the main simulation and therefore necessitates storage of the generated inflow data, or it can be run simultaneously as concurrent simulation, providing the sampled inflow data via a communication channel to the main simulation. For wind energy application these

simply be used as inflow condition, and by introducing a constant pressure gradient via body forces a fully-developed boundary layer flow would evolve. However, due to the blockage by the turbine the flow even far upstream of it is affected. Therefore it needs to be ensured that the recycled inflow data do not change over time. For this reason, time averages $\bar{u}_{i,rec}(y, z)$ and $\overline{u_{i,rec}^2}(y, z)$ of the recycled flow field are computed. The flow field is then rescaled such that for a statistically converged solution the mean flow at the inlet equals a prescribed mean flow $\bar{u}_{i,in}(y, z) = \bar{u}_{i,soll}(z)$. For the present study the prescribed mean flow was obtained from simulations with periodic boundary conditions as presented in Section 6.2. It should be noted that since in these simulations only the massflux is controlled, the obtained mean flow needs to be scaled to meet the required axial mean velocity at hub height. The rescaling procedure is then given by

$$u_{i,in}(y, z) = \bar{u}_{i,soll}(z) + \sqrt{\frac{\overline{u_{i,soll}^2}(z)}{\overline{u_{i,rec}^2}(y, z)}} \cdot (u_{i,rec}(y, z) - \bar{u}_{i,rec}(y, z)) \quad (7.1)$$

By applying this procedure, a constant instantaneous mass flux is not ensured. Therefore the velocity in axial direction $u_{in}(y, z)$ is rescaled once more by

$$u_{in}(y, z) = u_{in}(y, z) - \frac{\int (u_{in}(y, z) - u_{soll}(z)) dA}{\int dA} \quad (7.2)$$

to ensure a constant massflow. During preliminary tests it was found that a classical Neumann boundary condition for the velocity field at the outlet (e.g. $\partial u_i / \partial x = 0$) introduced non-physical behaviour which in some cases resulted in an unstable simulation. For that reason the convective boundary condition

$$\frac{\partial u_i}{\partial t} + \bar{u}_{soll}(z) \frac{\partial u_i}{\partial x} = 0 \quad (7.3)$$

is set at the outlet. Thereby the convective velocity $\bar{u}_{soll}(z)$ is the same as prescribed at the inlet to ensure an overall mass conservation.

As bottom boundary condition the surface stress wall model described in Section 6.2.1 is specified. For the top boundary a free-slip condition is prescribed with the consequence that a weak axial mean pressure gradient is imposed in the computational domain. The lateral boundary conditions are chosen to be periodic.

The effect of the wind turbine onto the flow is modelled by 36 uniformly distributed actuator points per blade. The regularisation parameter of the actuator line method is chosen to be $\epsilon = 3\Delta x$. Due to the good agreement with the rotor performance measured in the wind tunnel, blade polars with a pitch angle of $\Theta_p = 1^\circ$ identified in the study described in Section 6.4 were chosen as input throughout all simulations.

For this project, three boundary layers of different aerodynamic roughness were simulated. Boundary layers with intermediate and high roughness are designed to meet experimental boundary layer SBL and RBL regarding velocity shear and turbulence level. The boundary layers with intermediate and high roughness length were determined by variation of the boundary layer height and roughness length till configurations were found which match the turbulent kinetic energy at the rotor center. Thereby an optimal boundary layer height of $H = 2.25\text{m}$ was found, at which the roughness lengths $z_0 = 0.5\text{mm}$ and $z_0 = 4\text{mm}$ meet best the experimental boundary layer configurations SBL and RBL. For comparison purposes a third configuration with a roughness length

of $z_0 = 0.05\text{mm}$ was simulated. To be able to study the influence of ambient turbulence on the wake trajectory of a wind turbine in yawed conditions, different yaw angles were simulated for each boundary layer configuration. Table 7.1 gives an overview over all simulated configurations.

Table 7.1: Overview on simulated boundary layer configurations and yaw conditions.

BL	stage	N	$z_0[\text{mm}]$	$\gamma[\text{deg}]$	T_{rec}
sF014	initABL	27	0.05	-	60 s
	recALM	27		0	1100 rev
	recALM	27		15	1100 rev
	recALM	27		30	1100 rev
sF016	initABL	18	0.5	-	60 s
	recALM	18		0	1800 rev
sF016	initABL	27	0.5	-	60 s
	recALM	27		0	1800 rev
	recALM	27		15	1800 rev
	recALM	27		30	1800 rev
	recALM	27		-30	1800 rev
sF032	initABL	27	4.0	-	60 s
	recALM	27		0	2100 rev
	recALM	27		15	2100 rev
	recALM	27		30	2100 rev

The simulations were performed in three consecutive stages. The 1st stage is named *initABL* within which the boundary layer flow in the empty domain is generated. Herein the flow field is initialised with a power law distribution plus some random fluctuations. After simulating a timespan of $T = 60\text{s}$, which is equivalent to 25 flow through of the *recycling region*, the flow is considered to be fully developed and the flow field is recorded over the timespan T_{rec} . In the 2nd stage, named *initALM* the actuator line method is activated and the simulation is run for $T = 8.07\text{s}$, which is equivalent to 400 rotor revolutions at design tip speed ratio, in order to obtain a fully developed wake over the whole *wake region*. Subsequently the flow field is recorded for a timespan of T_{rec} during the 3rd stage, named *recALM*. The data recorded within the stages *initABL* and *recALM* consists of (i) the time averaged velocity \bar{u}_i and all components of the Reynolds stress tensor $\overline{u'_i u'_j}$ within the complete computational domain; (ii) all terms of the momentum equations and transport equations of the normal Reynolds stresses $\overline{u'_i u'_j}$ with $i = j$, and the turbulent kinetic energy on the planes $z = z_{hub}$, $y = 0$ and $(x - x_r)/R = 0, 1, 2, 4, 6, 8, 12, 16, 20, 24, 28, 32$; (iii) time series on selected points in the vertical and lateral (just *recALM*) direction of the aforementioned x-planes; (iv) time series and average values for each actuator point of magnitude V_{rel} and angle ϕ of the relative wind, the angle of attack α as well as axial and azimuthal induction factor a and a' . To get an idea of the flow field Figure 7.2 shows the isosurfaces of the instantaneous vorticity magnitude in the wake of the model wind turbine wind turbine immersed in the sF014 boundary layer configuration aligned with the wind.

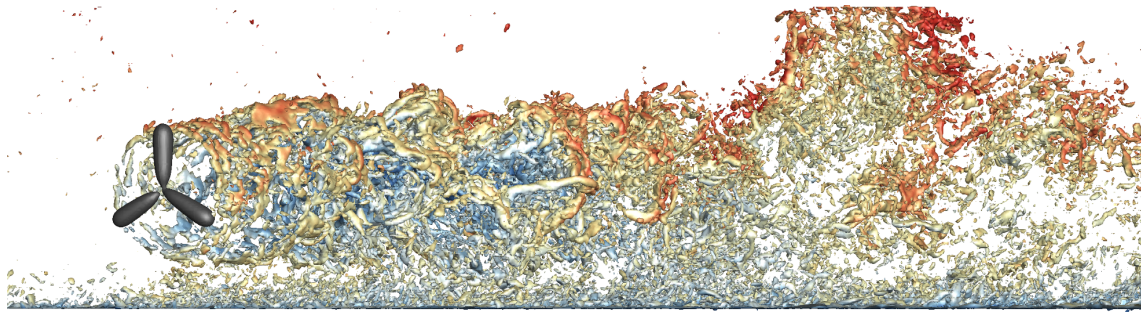


Figure 7.2: Isosurfaces of the vorticity magnitude $\omega = 150$ rad/s colored by the velocity magnitude in the wake of the model wind turbine immersed in the sF014 boundary layer configuration. Grey isosurfaces indicate the streamwise body forces $f_x = 1250$ N/m³ introduced by the actuator line method.

7.2 Flow Evolution in the Empty Domain

In order to analyse the axial development of the turbulent boundary layers, Figure 7.3 shows (a) the mean axial velocity $\bar{u}(x, z_h)$ and (b) the turbulent kinetic energy $K(x, z_h)$, both measured at hub height z_h , along the empty domain without the turbine. Both quantities are normalised with their respective value at the rotor center. From the results obtained with a grid resolution of $N = 27$ points per radii (27ppR) it is clearly visible that both quantities vary in axial direction. This behaviour can be explained by the different grid resolutions used within the *recycling region* and *wake region*, which causes the boundary layer to reorganize at the beginning of the *wake region* as the flow adapts to the changes in the grid resolution. This issue is discussed in more detail in the following. The change of the axial velocity at hub height $\bar{u}(x, z_h)$ is $< 5\%$ within the whole computational domain. However more important, within the wake region of interest, which is about $0 < (x - x_r)/R < 24$, the axial velocity at hub height just changes within less than 1% for all three boundary layers. From Figure 7.3(a) it can also be noticed that the variation of the axial velocity within the wake region increases with increasing roughness length. Even though the variation of the axial velocity might have a rather minor influence, the turbulent kinetic energy at hub height $K(x, z_h)$ changes more significantly along the computational domain. At the inlet a transient is triggered by the recycling technique which however converges within the *recycling region*. Afterwards however, the grid refinement causes a more significant reorganization of the boundary layer which does not converge to a constant value within the *wake region*. Similar to the change of the axial velocity, the axial change of the turbulent kinetic energy at hub height also becomes more significant with increasing roughness length. For the boundary layer configuration sF032 the axial change is $\approx 15\%$ within $0 < (x - x_r)/R < 24$, whereas for the configurations sF014 and sF016 it is less than 5% in the same interval.

By comparing the results of the sF016 configuration obtained with the grid resolution of $N = 18$ and $N = 27$ points per radii, an influence of the grid resolution on the axial development becomes noticeable. For the axial velocity $\bar{u}(x, z_h)$ the coarser grid resolution might seem more favourable as the axial velocity changes less within the wake region of interest. However, the turbulent kinetic energy $K(x, z_h)$ changes less in case of the higher grid resolution ($\approx 10\%$ with respect to $N = 18$)

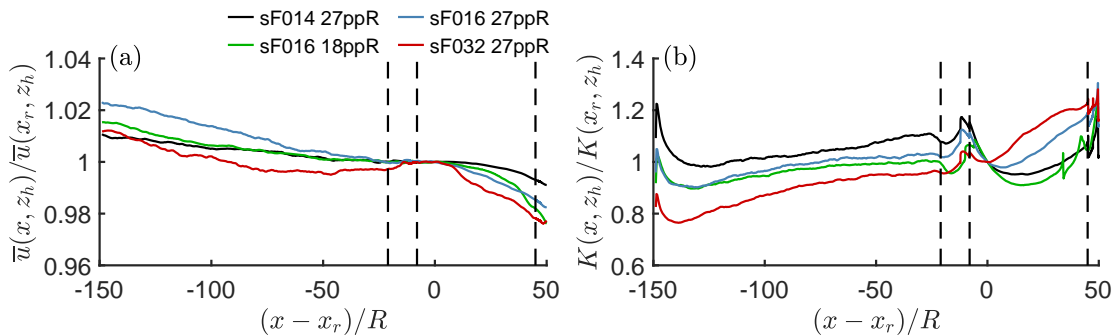


Figure 7.3: (a) mean axial velocity $\bar{u}(x, z_h)$ and (b) turbulent kinetic energy $K(x, z_h)$ as function of the axial distance to the rotor, both normalised to their respective values $\bar{u}(x_r, z_h)$, $K(x_r, z_h)$ at the rotor center along the entire domain without turbine. The *dashed* vertical lines indicate the borders between the regions and the *legend* denotes flow condition and grid resolution

In order to discuss the effect of the grid refinement between the *recycling region* and *wake region* on the vertical profiles, Figure 7.4 shows these for all three simulated boundary layers at selected axial positions within the *wake region* ($-4 < (x - x_r)/R < 20$) for the mean axial velocity \bar{u} , the normal Reynolds stress components in axial direction $\overline{u'u'}$, the Reynolds shear stress $\overline{u'w'}$ and the turbulent kinetic energy K , all normalised with the mean axial velocity at hub height $\bar{u}(z_h)$. For comparison measurement data of the SBL and RBL configurations are shown as well together with their numerical counterpart.

From the figures 7.4 (a), (e), (i) it becomes clear that the velocity profiles $\bar{u}(z)$ just vary indiscernible within the *wake region*. On the other hand, the normalised profiles of the Reynolds stresses are significantly affected by the grid refinement. Thereby it is interesting to notice that the change of the normal Reynolds stress component in axial direction $\overline{u'u'}$ increases with increasing roughness length, see 7.4 (b), (f), (j) (note the different x-scales). Not shown here, the same holds for the normal Reynolds stress component in the lateral direction $\overline{v'v'}$ but not for the component in the vertical direction $\overline{w'w'}$. Therefore, roughness length dependent changes in the turbulent kinetic energy K in Figure 7.4 (d), (h), (l) are predominately caused by the normal Reynolds stress component in axial direction $\overline{u'u'}$, since it is the main contributor to the turbulent kinetic energy.

The influence of the grid resolution on the boundary layer flow can be observed by comparing the profiles of the Reynolds stresses $\overline{u'u'}$ for the sF016 configuration, obtained with the coarse resolution of $N = 18$ and the reference resolution of $N = 27$ grid points per rotor radii as shown in Figure 7.4 (f). It is clearly visible that the results obtained with $N = 18$ grid points vary more significantly in the axial direction. The development of the Reynolds stresses in axial direction within the *wake region* and its dependency on the grid resolution is considered to be a result of under resolving the inertial subrange of the turbulent scales in the *recycling region* and will be discussed in more detail further below.

Despite the variation of the Reynolds stresses, the comparison with the measurement data shows a good agreement of the numerical sF016 and experimental SBL configuration regarding the vertical profiles of the mean axial velocity, the normal Reynolds stress component in the axial direction $\overline{u'u'}$ and the turbulent kinetic energy K , see Figure 7.4 (e), (f) and (h). At high roughness length, the measured boundary layer deviates more from the numerical results which shows the comparison of the numerical sF032 configuration and the experimental RBL configuration, see Figure 7.4 (i)-(l). In this case only the vertical profiles of the mean axial velocity are in good agreement, whereas the profiles of the Reynolds stress components are not. Their magnitude at hub height are somehow comparable as the numerical sF032 configuration is designed to meet the turbulent kinetic energy of the experiment in this region.

The difficulty of matching numerical and experimental results of boundary layers at high roughness length is less an insufficiency of the numerical method than rather a limitation of the experimental approach for the boundary layer generation (Counihan Method). In case of the boundary layer wind tunnel at TUM, this approach is optimised for the generation of boundary layers with a roughness length in the order of the SBL configuration. By applying a more dense distribution of roughness elements to increase the roughness length, the Reynolds stresses predominantly increase in the lower part of the wind tunnel. With that a good approximation is obtained for the lowest part of a boundary layer over very rough surface. However, seen over its complete height the obtained boundary layer does not represent an equilibrium solution. Hence, to obtain perfectly matching boundary layers in the simulation and in the experiment it would be necessary to resolve the whole experimental process of the boundary layer generation within the simulation.

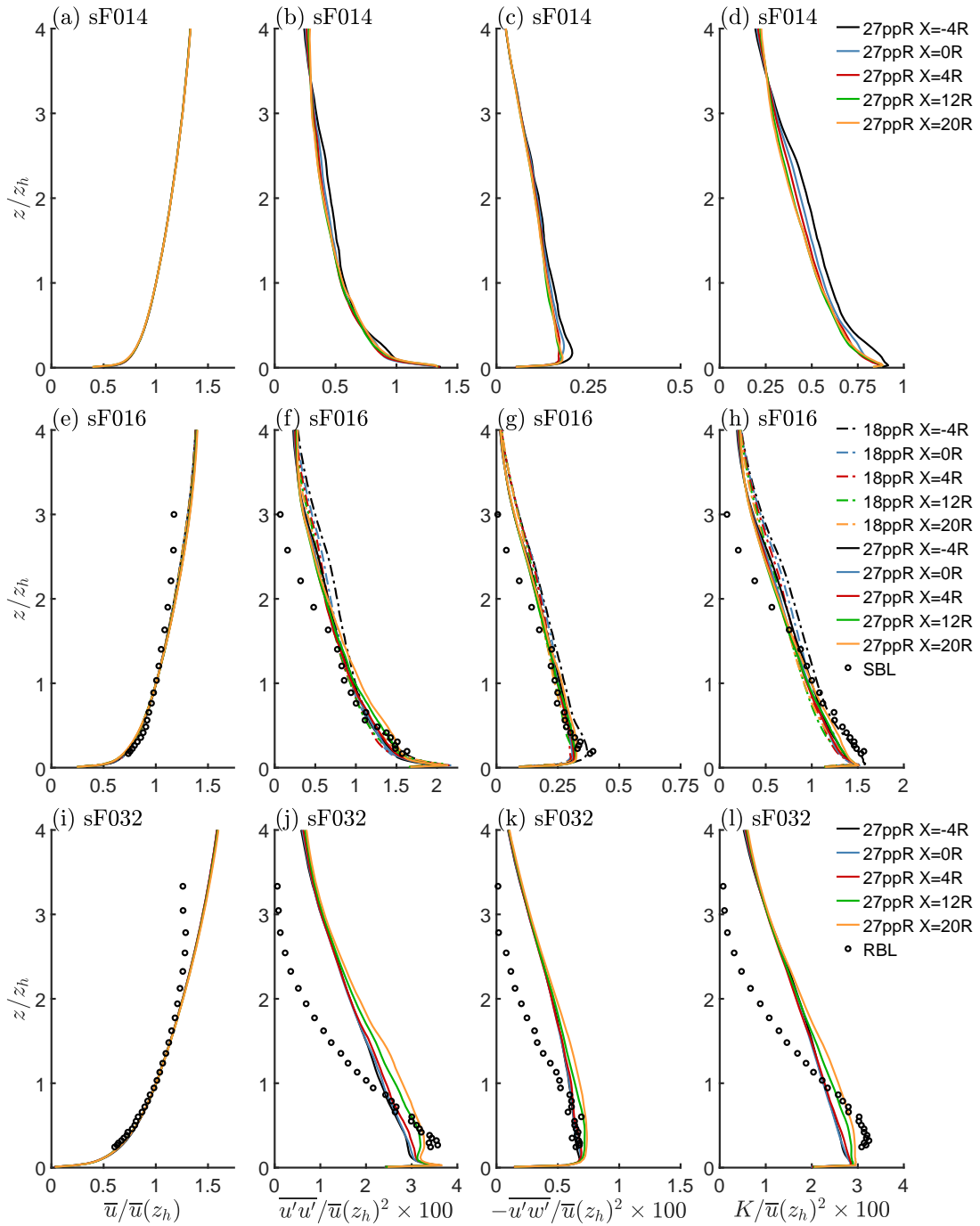


Figure 7.4: Vertical profiles of the simulated boundary layer configurations at selected locations in the *wake region* of the empty domain (a), (e), (i) mean axial velocity \bar{u} ; (b), (f), (j) Reynolds stress component $\overline{u'u'}$; (c), (g), (k) Reynolds shear stress $\overline{u'w'}$; (d), (h), (l) turbulent kinetic energy K ; all normalised with axial mean velocity at hub height.

Figure 7.5 shows the normalised energy spectral density of the three velocity components as function of the wave length k , normalised with the hub height z_h . Thereby, wave lengths are computed from frequencies based on Taylor's well known hypothesis of frozen turbulence $k = 2\pi f / \bar{u}(z_h)$. Results are shown for the grid resolutions of $N = 18$ and $N = 27$ in (d)-(f) recorded at the location of the rotor center and in (a)-(c) 8 boundary

layer heights upstream of it at the same height. Therefore the first location is within the *wake region* and the later within the *recycling region*. Spectra measured within the SBL configuration at the location of the rotor are shown as well for comparison. At the rotor center the energy production range (energy containing scales) and inertial subrange are well resolved for both grid resolutions and are in good agreement with measurement data. The slope of the power spectra for the vertical velocity component differs slightly between measurement and simulation, see Figure 7.5 (f).

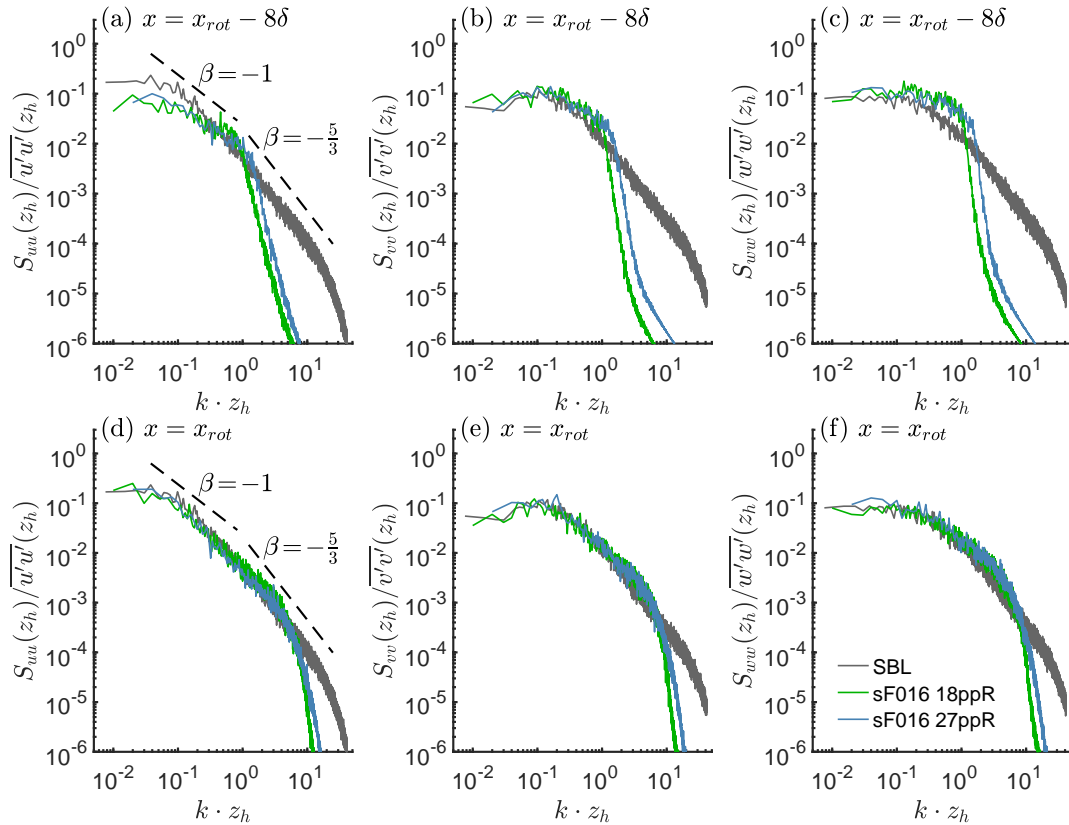


Figure 7.5: Normalised energy spectral density of the three different wind components at the rotor center $S_{u_i u_j}(z_h)/\overline{u_i' u_j'}(z_h)$ with $i = j$, within simulated boundary layers and experimental SBL configuration: (a), (d) u-component; (b), (e) v-component and (c), (f) w-component. Legend denotes flow conditions, dashed lines denote the slope of the Kolmogorov cascade.

Upstream of the rotor center within the *recycling region* at $x - x_r = -8\delta$, see Figure 7.5 (a)-(c), a clear cut-off is observable at $k \cdot z_h \approx 10^0$ within the spectra of all three velocity components. This is considered to be a result of the coarse grid resolution within the *recycling region*, due to which the inertial subrange is not sufficiently resolved. As a consequence the composition of turbulent scales over the spectral range is not well predicted. For the grid resolution of $N = 27$ the prediction is improved but the energy cascade is still not captured correctly. Hence, when transported into the well resolved *wake region* the turbulent scales start to reorganise and cause the axial development of the Reynolds stress components as shown in Figure 7.4. As the energy cascade within the *recycling region* is better resolved for $N = 27$ as for $N = 18$, the reorganisation of turbulent scales in this case is reduced within the wake region, see Figure 7.4 (f)-(h).

7.3 Comparison with Measurements & Grid Study

As discussed in Section 7.2, a refinement of the grid resolution between *recycling region* and *wake region* causes a transition of the boundary layer flow which covers a large axial range of the *wake region*. However, these somewhat axial variations within the boundary layer flow might be small compared to the development of the wake and hence a minor issue for most of the analysis. To quantify the relevance of the boundary layer variation on the wake development and to verify the simulation, in this section results of the simulated wake immersed within the sF016 boundary layer configuration are compared to experimental wake measurements within the SBL configuration. As explained above, for large surface roughness numerical and experimental boundary layer configurations do not match over height, which results in significant differences in the wake development. Therefore a detailed comparison of wakes immersed within the numerical sF032 boundary layer and the experimental RBL configuration is left out. However, for the sake of completeness, wake characteristics of these configurations are compared in Section 7.4. As the observed variation of the boundary layer flow within the *wake region* exhibits a dependency on the grid resolution, the comparison is carried out with results obtained on a resolution of $N = 18$ and $N = 27$ grid points per rotor radius (ppR).

Before the resulting flow fields are discussed and compared to the measurement data, the predicted rotor performance is presented. Therefore, Figure 7.6 shows the power and thrust coefficient as function of the yaw angle for the simulations of the sF016 boundary layer configuration with grid resolutions of $N = 18$ and $N = 27$ ppR and compares it to the coefficients measured within the experimental SBL configuration. For the sake of completeness, the resulting coefficients for simulations within the sF014 and sF032 boundary layer configurations with a grid resolution of $N = 27$ ppR are shown as well. As it can directly be seen for a given yaw angle all numerical configurations result in similar coefficients which are in very good agreement with the experimental results. The small differences in between the boundary layer configurations of different roughness length is to be expected as the same holds for the experimental results, see Figure 4.12 in Section 4.6. For the simulations of the sF016 boundary layer configurations differences are noticeable in the results obtained for different grid resolutions, especially for large yaw angles. However, even for this operational conditions the grid sensitivity with regards to the rotor performance is low, as the power and thrust coefficients just differ

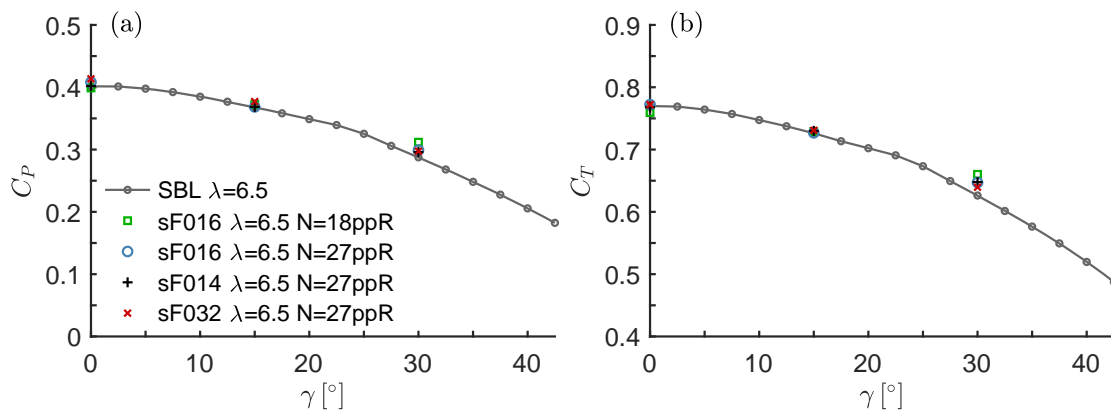


Figure 7.6: Comparison of measurements and numerical results for (a) power C_P and (b) thrust coefficient C_T as function of yaw angle γ . Legend gives flow conditions.

by 4% and 2%, respectively. Therefore, for the following discussion the body forces introduced into the flow field by the ALM are considered to be independent of the grid resolution. It should also be noticed that, thanks to the calibration of the tabulated airfoil data presented in Section 6.4.3, the error of the rotor performance predicted by the simulations with grid resolutions of $N = 27$ ppR is $< 4\%$ for the power coefficient and $< 3\%$ for the thrust coefficients.

Figure 7.7 shows the spatial distribution of the normalised mean axial velocity component $\bar{u}/\bar{u}_{bl}(z_h)$ in (a) the mid-vertical and (b) the mid-horizontal plane. Most salient in the comparison of the numerical results is that there are only small differences in the velocity distribution for both grid resolutions. The most significant difference can be observed in the near wake at $x/R = 2$ close to the rotor center. Nevertheless, both simulations almost perfectly capture the velocity distribution at this axial location. The only visible deviation between the simulation and the experiment below the rotor disk is considered to result from the interaction of the tower with the flow which is not modelled in the simulation. In the downstream direction the simulated wakes develop differently from the measurement results and the velocity distributions depart from each other. This is especially noticeable in the mid-vertical plane and is considered to result from the different mean wind shear in the simulation and the experiment. In the mid-horizontal plane, however, the wake deficit develops very similar in all cases, only an almost constant offset in the wake center is noticeable.

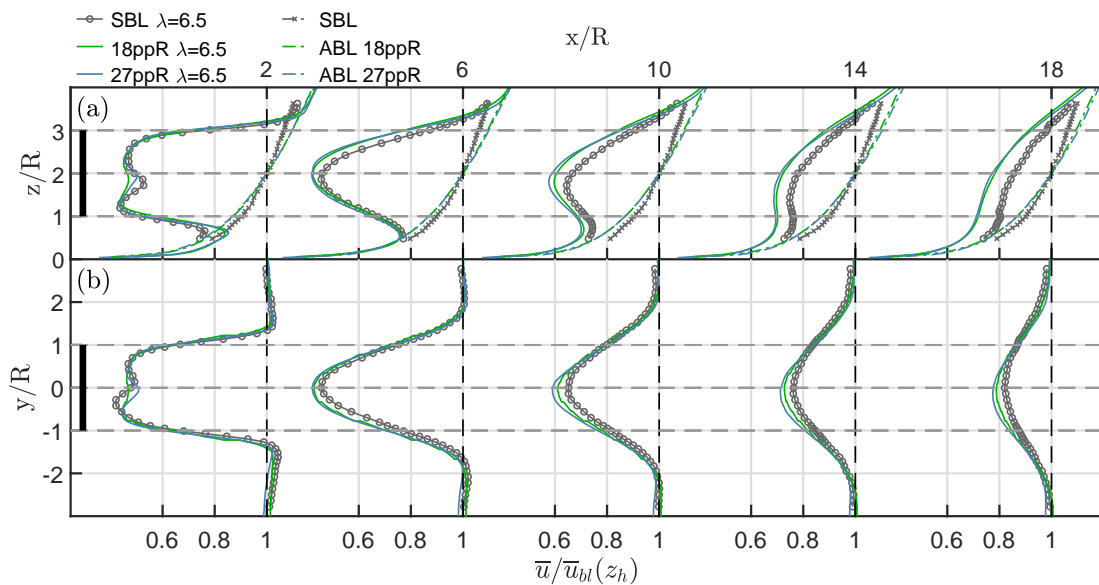


Figure 7.7: Profiles of the normalised mean axial velocity component $\bar{u}/\bar{u}_{bl}(z_h)$ in the (a) mid-vertical and (b) mid-horizontal plane at axial positions $x/R = 2, 6, 10, 14, 18$. Symbols denote measurements, whereas lines correspond to LES results. The legend denotes the flow condition and grid resolution.

Figure 7.8 shows the spatial distribution of the shear stress (a) $\overline{u'w'}$ in the mid-vertical and (b) $\overline{u'v'}$ the mid-horizontal plane, both normalised with respect to the axial velocity at hub height of the undisturbed boundary layer $\bar{u}_{bl}^2(z_h)$. In general the shear stress is well predicted by the simulations. The most significant deviations can be observed (i) for the near wake in the proximity of the rotor edges, where sharp peaks in the distribution of the shear stress are less pronounced by the simulation due to the smeared body forces

introduced by the actuator line method and (ii) above the top tip in the far wake region which is considered to result from the mean wind shear which is increased in the simulation compared to the measurement. As the radial gradient of the shear stress is the driving force for the development of the velocity deficit in the far wake, this is consistent with observations in the distribution of the axial velocity seen in Figure 7.7(a).

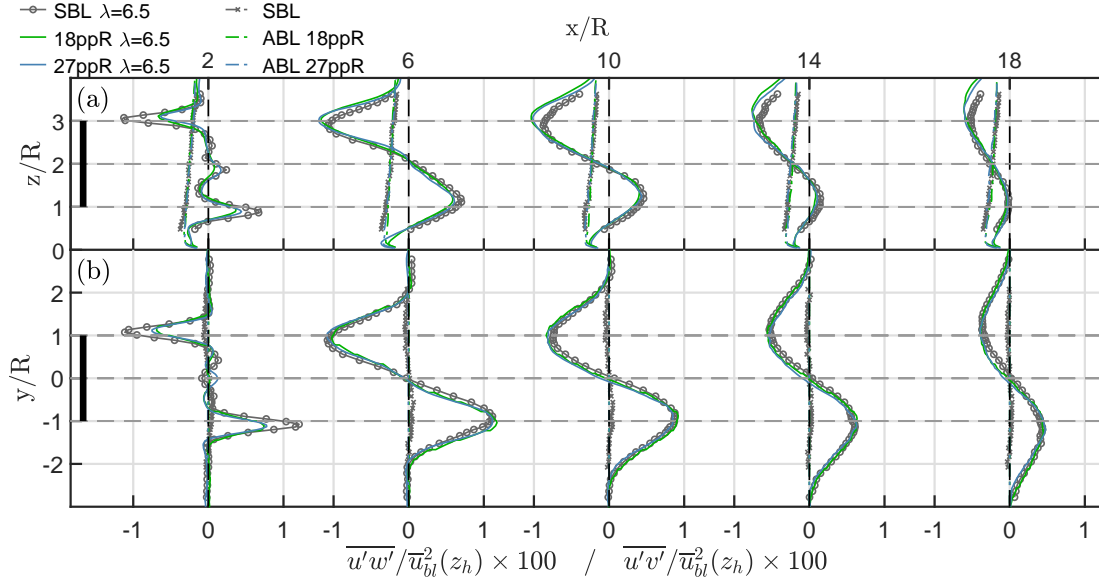


Figure 7.8: Profiles of the normalised shear stress (a) $\overline{u'w'}/\overline{u_{bl}^2}(z_h)$ in the mid-vertical and (b) $\overline{u'v'}/\overline{u_{bl}^2}(z_h)$ the mid-horizontal plane at axial positions $x/R = 2, 6, 10, 14, 18$. Symbols denote measurements, whereas lines correspond to LES results. The legend denotes the flow condition and grid resolution.

The comparison of measured and simulated normal Reynolds stresses exhibits a similar trend as for the Reynolds shear stresses. For the sake of brevity this is discussed on the basis of the normalised turbulent kinetic energy $K/\overline{u_{bl}^2}(z_h)$ shown in Figure 7.9 for (a) the mid-vertical and (b) the mid-horizontal plane. It should be noticed that only resolved contributions to the turbulent kinetic energy from the LES are shown here. As already observed above for the Reynolds shear stresses, sharp peaks in the proximity of the rotor are not well resolved by the simulation due to the application of smeared body forces. More significant, however, is the almost constant mismatch between experiment and simulation visible in the mid-vertical plane, see 7.9(a). This is considered to result from the non-matching boundary layer profiles in measurement and simulation, see Figure 7.4 (f)-(h). The good agreement of the simulation and the experiment in the mid-horizontal plane shown in 7.9(b) is consistent with this statement as the simulated boundary layer is designed to meet the turbulent kinetic energy at hub height. The deviations, observable at the wake centreline, are likely to result from the effect of the nacelle on the flow which is not considered in the simulation.

The chosen grid resolution has only a minor effect on the turbulent kinetic energy, similar as observed for the Reynolds shear stress in Figure 7.8. The observable differences in the turbulent kinetic energy between both grid resolutions are less considered to result from an improved capturing of the wake development by the higher resolution than rather from the adaptation of the boundary layer to grid changes. As discussed in Section 7.2 due to the grid refinement between the *recycling region* and the *wake region* the boundary layer flow exhibits a reorganisation of the turbulent scales which causes a variation in

the profiles of the Reynolds stresses. This reorganisation is grid dependent and is significantly less distinctive in case of the higher grid resolution of $N = 27$ grid points per radius, see Figure 7.4(h), and causes the observable differences in the wake. As these differences are small and the wake development is captured well within both simulations, the effect of the boundary layer adaptation is rather negligible, at least at the higher grid resolution of $N = 27$. Since the reorganisation of the boundary layer has been observed to depend on the roughness length, see Section 7.2, this statement holds for the sF014 and sF016 boundary layer configurations. However, for the sF032 configuration the reorganisation is more significant and its effect is taken into account in the further analysis.

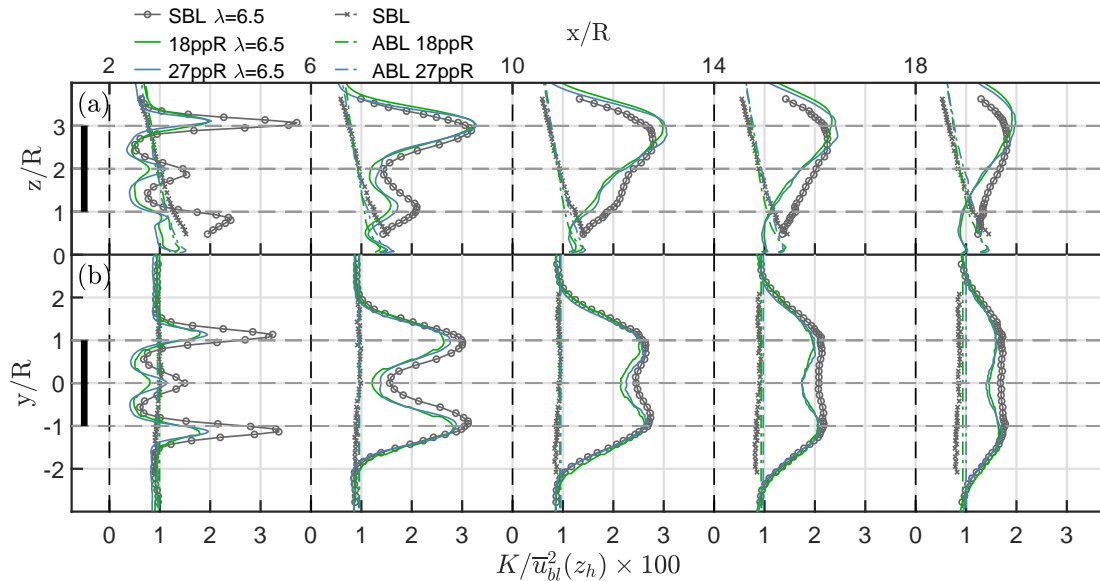


Figure 7.9: Profiles of the normalised turbulent kinetic energy $K/\bar{u}_{bl}(z_h)^2$ in the (a) mid-vertical and (b) mid-horizontal plane at axial positions $x/R = 2, 6, 10, 14, 18$. Symbols denote measurements, whereas lines correspond to LES results. The legend denotes the flow condition and grid resolution.

To conclude the discussion on the effect of the boundary layer reorganisation caused by the grid refinement upstream of the *wake region* and its dependency on the grid resolution Figure 7.10 shows some key wake characteristics obtained from numerical and experimental data: (a) the wake center velocity deficit Δu_C , (b) and (c) the lateral and vertical wake width σ_y and σ_z and (d) the wake center position in the vertical direction z_C . As already mentioned before, the centreline velocity deficit is very similar in both simulations but exhibits an almost constant offset regarding the experimental data. This might result from the neglected effect of the nacelle which is not modelled in the simulation. The predicted lateral wake growth is in almost perfect agreement with the measurement results in case of the simulation with a grid resolution of $N = 27$ grid points per radius. However, the vertical wake width is predicted to be substantially larger than measured in the experiment. This is considered to result from the mean wind shear which is increased in the simulation in comparison to the measurement. As already discussed in Section 5.2.2 a descent of the vertical wake centre position towards the ground can be caused by a loss of flow momentum in the wake. Hence, despite the (initial) offset between measurement and simulation, the similar axial rate of vertical displacement of the wake center indicates that the loss of flow momentum is well predicted by the simulation. This issue will be discussed in more detail in the next section.

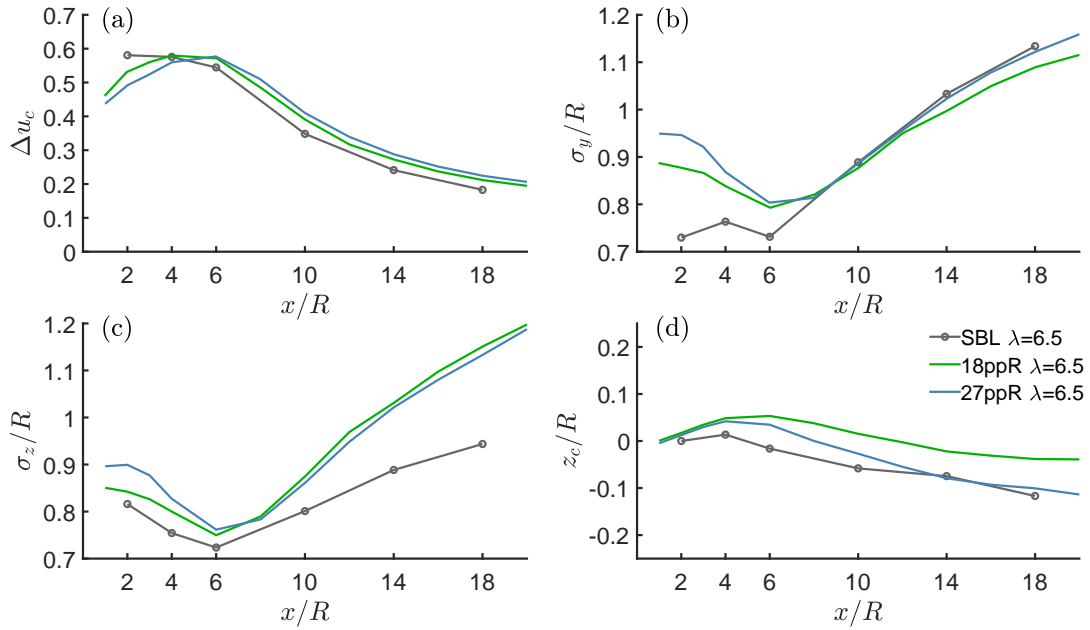


Figure 7.10: Wake characteristics of the un-yawed model wind turbine operating at $\lambda = \lambda_{dsgn}$ immersed in sF016 boundary layer configuration: (a) centreline velocity deficit, (b) lateral and (c) vertical wake half width, (d) vertical centreline position. The *legend* indicates the grid resolution in points per Radius (ppR).

7.4 Influence of the Ground Roughness on an Un-yawed Wind Turbine

As already discussed theoretically in Section 2.3.1 and observed in the measurement results presented in Section 5.2.2, the decomposition of a wind turbine wake into a boundary layer flow and an axisymmetric wake might be inaccurate within a highly sheared boundary layer. Data from Large Eddy Simulations allows to discuss this issue in more detail as all terms of the momentum equations can be computed separately at each point in space. Therefore in this section first an overview of obtained simulation results for the unyawed model wind turbine in varying ground roughness is given. Subsequently the effect of ground roughness on the accuracy of the superposition approach is discussed by analysing the momentum deficit in the wake as well as transport terms which bias its axisymmetric character. The discussion is then finalised with an approximation of the error in the determined wake characteristics by assuming an axisymmetric wake.

7.4.1 Wake Characteristics

Figure 7.11 and 7.12 show the normalised mean axial velocity $\bar{u}/\bar{u}_{bl}(z_h)$ within the mid-vertical and mid-horizontal plane in the wake of the model wind turbine immersed in (a) the sF014, (b) the sF016, and (c) the sF032 boundary layer configuration. As shown above the wind turbine rotor produces similar thrust coefficients which result in similar velocity deficits in the near wake for all three boundary layers, as can be observed in the figures. This is consistent with the results of the wind tunnel measurement presented in Section 4.6. However, with increasing background turbulence in the different boundary layer configurations the momentum exchange between the wake and the outer flow is

enhanced and the wake recovers faster.

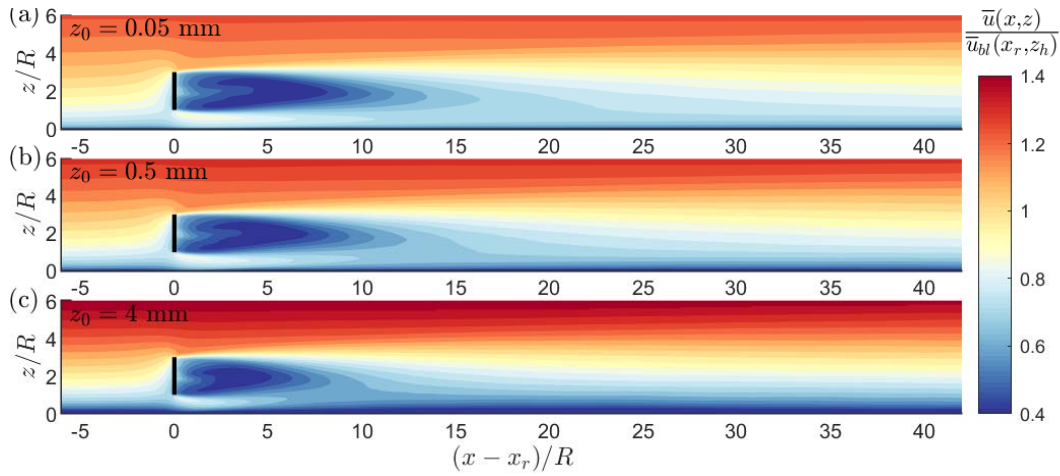


Figure 7.11: Normalised mean axial velocity $\bar{u}/\bar{u}_{bl}(z_h)$ within the mid-vertical plane in the wake of the model wind turbine immersed in (a) the sF014, (b) the sF016 and (c) the sF032 boundary layer configuration.

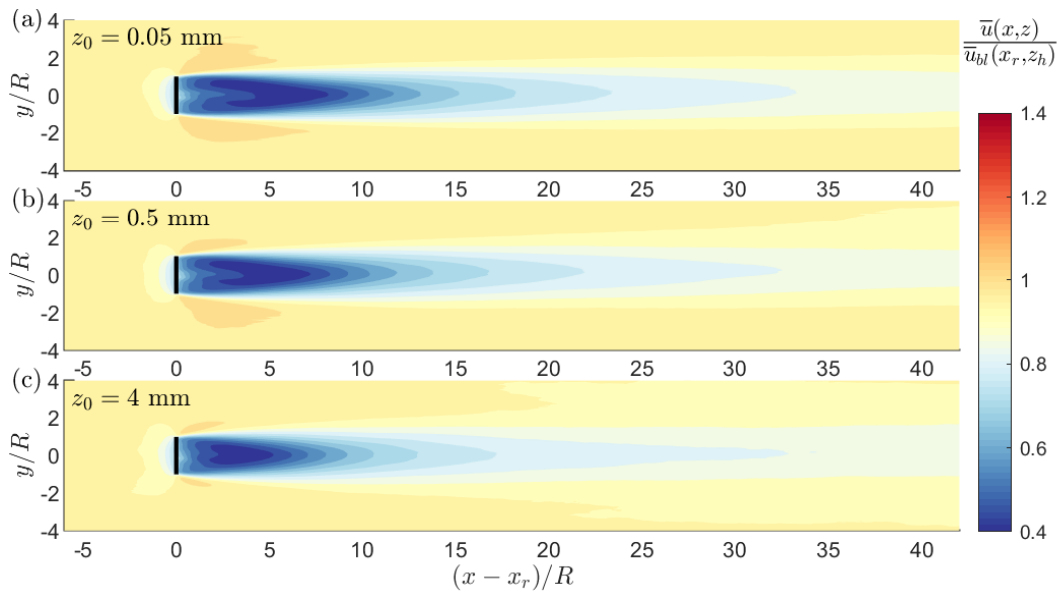


Figure 7.12: Normalised mean axial velocity $\bar{u}/\bar{u}_{bl}(z_h)$ within the mid-horizontal plane in the wake of the model wind turbine immersed in (a) the sF014, (b) the sF016 and (c) the sF032 boundary layer configuration.

Figure 7.13 and 7.14 show the normalised turbulent kinetic energy $K/\bar{u}_{bl}^2(z_h)$ within the mid-vertical and mid-horizontal plane in the wake of the model wind turbine immersed in (a) the sF014, (b) the sF016 and (c) the sF032 boundary layer configuration. Due to the strong shear at the boundary between the wake and the outer flow a high amount of turbulent kinetic energy is produced which results in significant peak values at the top tip level in the mid-vertical plane, shown in Figure 7.13, and at the side-tip positions in the mid-horizontal plane, shown in Figure 7.14. Thereby the magnitude of the maximum turbulent kinetic energy clearly rises with increasing level of background turbulence. Due to these turbulent fluctuations more energetic flow is transported from the outer region into

the wake causing the wake to recover within shorter distance. Directly behind the rotor it can additionally be observed that for all simulated configurations the level of turbulent kinetic energy is suppressed below the level of the approaching undisturbed boundary layer. This suppression becomes more significant with increasing background turbulence and in case of the sF032 configuration persists below hub height up to a distance of about $x/R \approx 22$. This has also been observed in the wind tunnel measurement presented in Section 5.2.1 and 5.2.2.

Figure 7.15 shows some key wake characteristics obtained from the numerical data: (a) the wake center velocity deficit $\Delta u_C = \max(\Delta u)$, (b) and (c) the lateral and vertical wake width σ_y and σ_z , calculated by eq.(2.56), and (d) the wake center position in the vertical direction z_C , determined by the momentum deficit center given in eq.(2.56). For comparison purposes, wake characteristics from the wind tunnel measurements presented in Section 5.2.2 are shown additionally. The faster recovery of the wake with increasing background turbulence, and hence ground roughness, can well be observed in the centreline velocity deficit shown in Figure 7.15(a). Based on the assumption of a constant momentum deficit in the wake, e.g. constant momentum thickness see eq.(2.57), and that the wake can be approximated as axisymmetric represented by a Gaussian distribution the centreline velocity deficit is directly linked to the wake width. In other words a faster wake recovery has to result also in a faster wake growth as it is clearly the case in the presented results shown in Figure 7.15(b) and (c). As already observed in the wind tunnel measurements presented in Section 5.2.2 within boundary layers with moderate mean wind shear the wake growth in lateral and vertical direction is approximately linear. Within the sF032 boundary layer configuration, however, the growth rate decreases for axial distances $x/R > 12$.

As already discussed above, the wake development within the numerical sF016 configuration and the experimental SBL configuration is in good agreement. The comparison of the numerical sF032 configuration and the experimental RBL configuration, however, shows a larger mismatch regarding the lateral and vertical wake growth. This is considered to result from differences in the boundary layer profiles, which increase with surface roughness. Nevertheless, even for high roughness length, experiment and simulation ex-

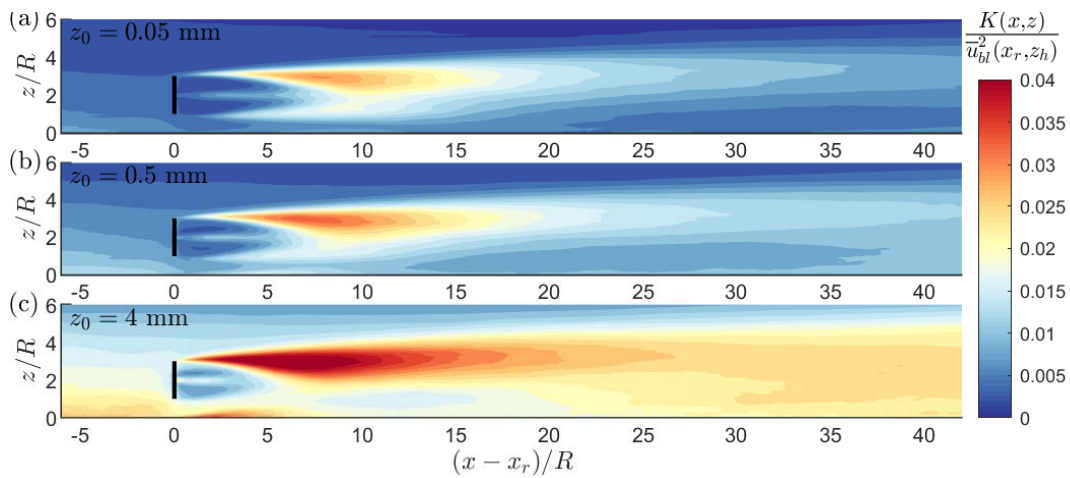


Figure 7.13: Normalised turbulent kinetic energy $K/\bar{u}_{bl}^2(z_h)$ within the mid-vertical plane in the wake of the model wind turbine immersed in (a) the sF014, (b) the sF016 and (c) the sF032 boundary layer configuration.

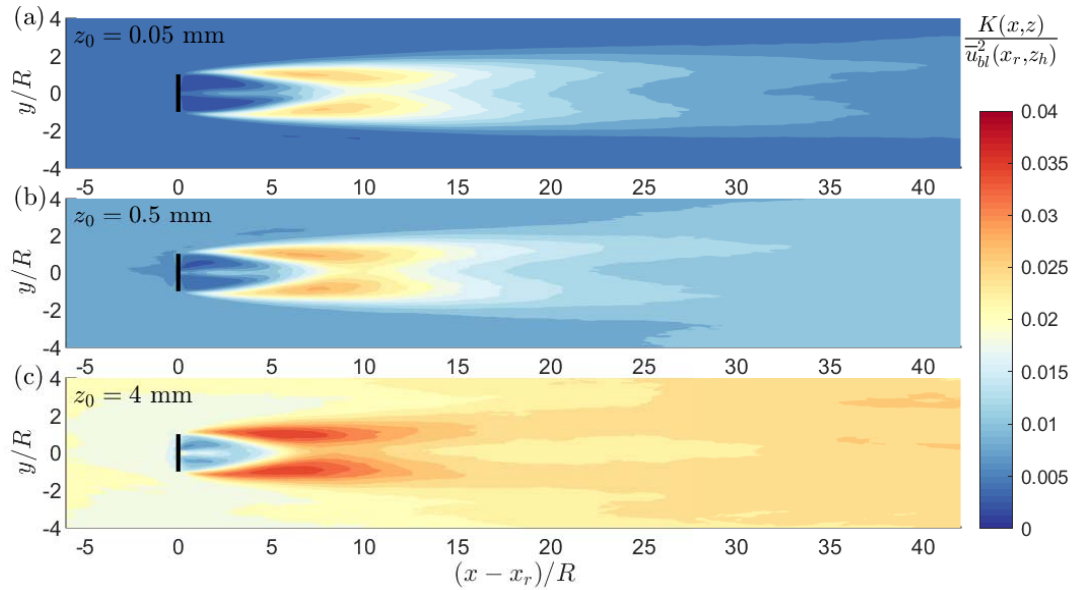


Figure 7.14: Normalised turbulent kinetic energy $K/\bar{u}_{bl}^2(z_h)$ within the mid-horizontal plane in the wake of the model wind turbine immersed in (a) the sF014, (b) the sF016 and (c) the sF032 boundary layer configuration.

hibit an analogous behaviour regarding the vertical displacement of the wake centreline towards the ground, see Figure 7.15(d). In Section 5.2.2 it is hypothesized that the wake centreline is biased by an additional momentum deficit close to the ground due to the mean wind shear which causes the wake to become asymmetric with respect to z . As all terms of the momentum equation can be extracted from the LES data, this effect is discussed in more detail in the following section.

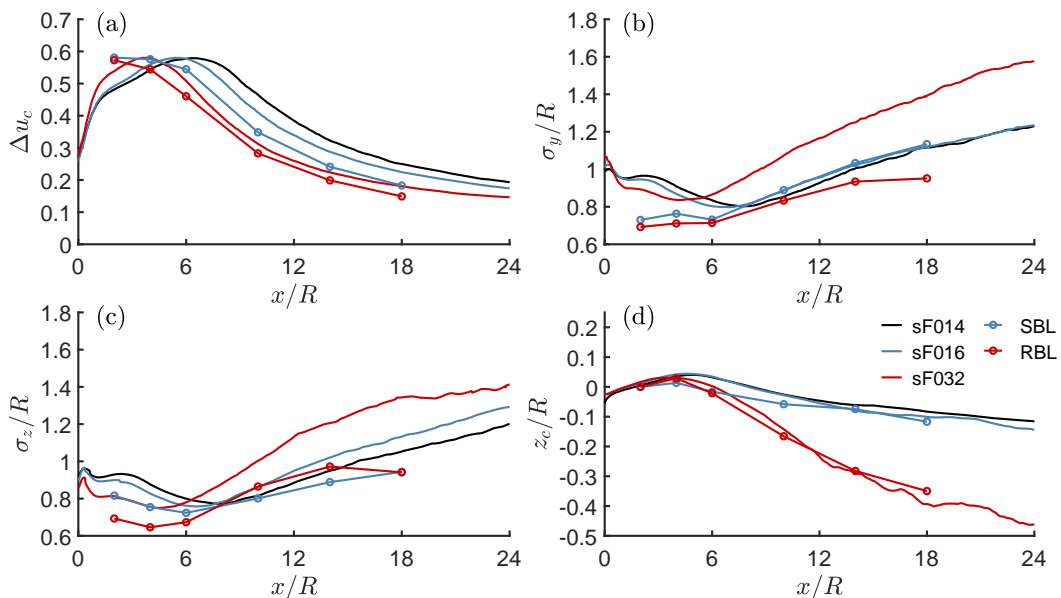


Figure 7.15: Wake characteristics of the un-yawed model wind turbine operating at $\lambda = \lambda_{dsgn}$ immersed in different boundary layer configurations: (a) centreline velocity deficit Δu_c , (b) lateral σ_y and (c) vertical half width σ_z , and (d) vertical centreline position z_c . The legend indicates the flow condition.

For that reason Figure 7.16 shows the momentum deficit in the mid-vertical plane of the simulated wakes immersed in the three different boundary layer configurations. Within the sF014 boundary layer configuration with the lowest roughness length the wake remains almost symmetric with respect to z even in the very far wake region. With increasing roughness length it can be observed that a momentum deficit forms close to the ground due to which the momentum deficit becomes asymmetric regarding the rotor axis. As the calculation of the vertical position of the wake centreline, see eq.(2.56), is based on the location of the momentum deficit centre, it is biased towards the ground.

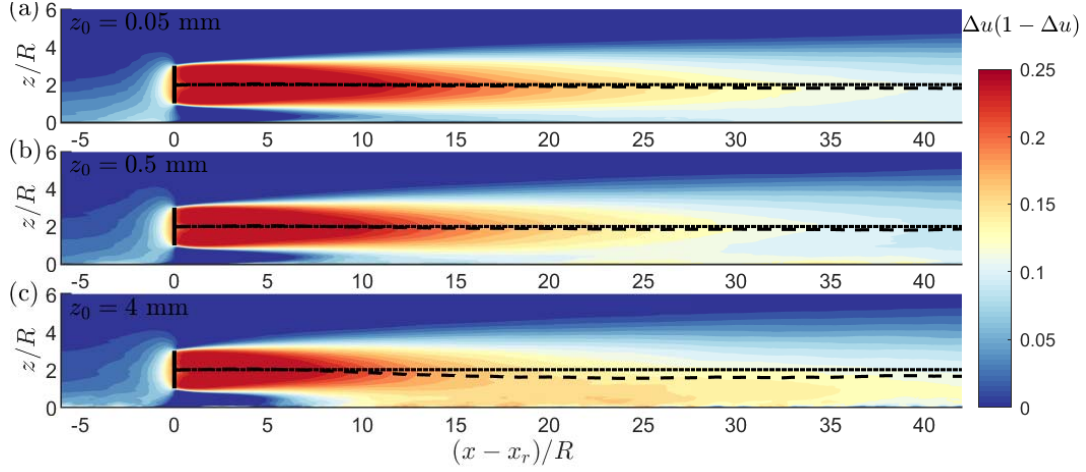


Figure 7.16: Momentum deficit $\Delta u(1 - \Delta u)$ within the mid-vertical plane in the wake of the model wind turbine immersed in (a) the sF014, (b) the sF016 and (c) the sF032 boundary layer configuration. The *dotted* line indicates the rotor axis and the *dashed* line indicates the wake center.

7.4.2 Momentum Budget

As mentioned in the foregoing section, for high roughness length the wake develops asymmetrically which results in an additional momentum deficit below hub height. A similar behaviour was observed in the wind tunnel measurements with the model wind turbine immersed in a boundary layer of high roughness length, see Section 5.2.2. It was argued that the high vertical mean shear close to the ground causes a loss of flow momentum, which in turn increases the momentum deficit. Since the momentum budget in the wake can not be analysed on the basis of the measurement data, this argument could not be proven. However, the LES data provides all terms of the momentum balance, derived in Section 2.3.1, necessary to analyse the development of the asymmetric distribution of the momentum deficit in the wake, which in the following will be discussed. For the sake of a better understanding of the discussion, the streamwise momentum deficit in the wake Θ_x^2 and its change rate $\frac{d}{dx}\Theta_x^2$, as defined in Eq.(2.54) is restated here and given as

$$\Theta_x^2 = \int_{-\infty}^{\infty} \int_0^{\infty} \theta \, dz \, dy = \int_{-\infty}^{\infty} \int_0^{\infty} \frac{\bar{u}_w(\bar{u}_{bl} - \bar{u}_w)}{\bar{u}_{bl}^2} \, dz \, dy = \int_{-\infty}^{\infty} \int_0^{\infty} \Delta u(1 - \Delta u) \, dz \, dy, \quad (7.4)$$

$$\begin{aligned} \frac{d}{dx}\Theta_x^2 &= \frac{d}{dx} \int_{-\infty}^{\infty} \int_0^{\infty} \theta \, dz \, dy \\ &= \frac{d}{dx} \int_{-\infty}^{\infty} \int_0^{\infty} \frac{\bar{u}'u'_w}{\bar{u}_{bl}^2} \, dz \, dy + \int_{-\infty}^{\infty} \int_0^{\infty} \frac{1}{\bar{u}_{bl}^2} \left[\frac{1}{\rho} \frac{\partial \bar{p}_w}{\partial x} + \frac{\partial \bar{u}'w'_w}{\partial z} - \frac{\partial \bar{u}_w \bar{w}_w}{\partial z} + \bar{w}_w \frac{\partial \bar{u}_{bl}}{\partial z} \right] \, dz \, dy. \end{aligned} \quad (7.5)$$

In the derivation of the momentum balance, far wake conditions were assumed and the axial pressure gradient was considered to be small. In the discussion here, however, the momentum balance from upstream to far downstream of the turbine will be analysed and therefore the pressure gradient needs to be included.

As starting point of this discussion, Figure 7.17 compares the change rate of the local momentum deficit in axial direction $\partial\theta/\partial x = \partial\Delta u(1 - \Delta u)/\partial x$ at two heights below and above the rotor disk, $z = 0.5R$ and $z = 3.5R$, which are equidistant to the rotor axis. At both heights the change rate of the local momentum deficit experiences a strong negative gradient at the axial position of the rotor caused by the pressure jump across the rotor disk. In the near wake region the gradient becomes positive and asymptotically decreases towards zero in the far wake. For the sF014 boundary layer configuration the change rate of the local momentum deficit below and above the rotor disk develops quite similar in the axial direction. As the roughness length increases, however, within the near wake $x/R < 6$ the axial development close to the ground deviates significantly from its counterpart above the rotor disk, whereas the latter shows only a slight dependency on the roughness length. These results support the assumption that within a boundary layer with moderate mean wind shear, e.g. low roughness length, the wake can be approximated by the superposition of an undisturbed boundary layer and an axisymmetric wake.

However, it is still to determine which of the terms contributing to the streamwise momentum deficit change rate cause the asymmetry of the wake. Therefore, Figure 7.18 shows for all simulated boundary layer configurations at the heights of $z = 0.5R$ and $z = 3.5R$ all terms which can cause asymmetry in the far wake, i.e. all terms on the right hand side of eq.(7.5) before the integration. Since the axial gradient of the normal Reynolds stress $\partial u' u' w / \partial x$, even if symmetric, can cause a loss of flow momentum, it is shown as well. From this figure it becomes clear that the aforementioned asymmetry in the change rate of the local momentum deficit can only be caused (i) by the vertical gradient of the Reynolds shear stress $\bar{u}_{bl}^{-2}(z) \partial \bar{u}' w' / \partial z$, which in the near wake region ($x/R < 6$) is much larger below the rotor disk as above, and (ii) by the vertical gradient of the axial velocity in the undisturbed boundary layer $\bar{w}_w \partial \bar{u}_{bl} / \partial z$, which in the wake exhibits an almost constant contribution. Moreover it is interesting to notice that even within the sF032 boundary layer configuration, where the high ambient turbulence causes a faster wake development, the axial gradient of the normal Reynolds stress component $\bar{u}_{bl}^{-2}(z) \partial \bar{u}' w' / \partial x$ is still small in magnitude compared to the other terms.

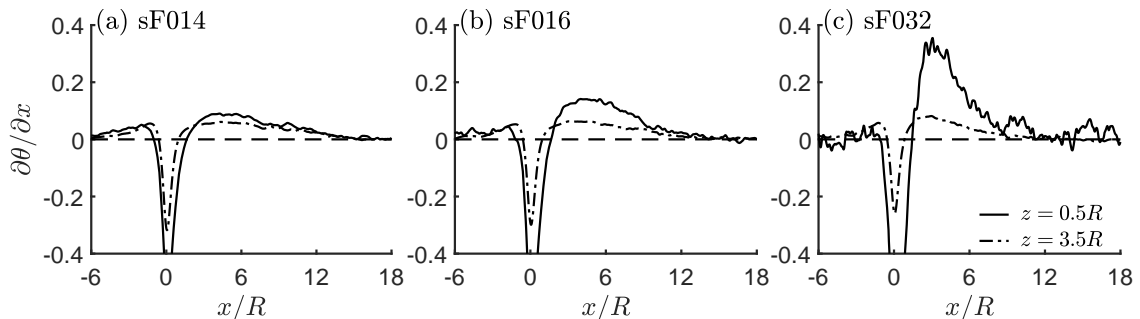


Figure 7.17: Axial change rate of the local momentum deficit $\partial\theta/\partial x = \partial(\Delta u(1 - \Delta u))/\partial x$ as function of x , evaluated in the mid-vertical plane at $z = 0.5R$ and $3.5R$ in the wake of the model wind turbine immersed in (a) the sF014, (b) the sF016 and (c) the sF032 boundary layer configuration.

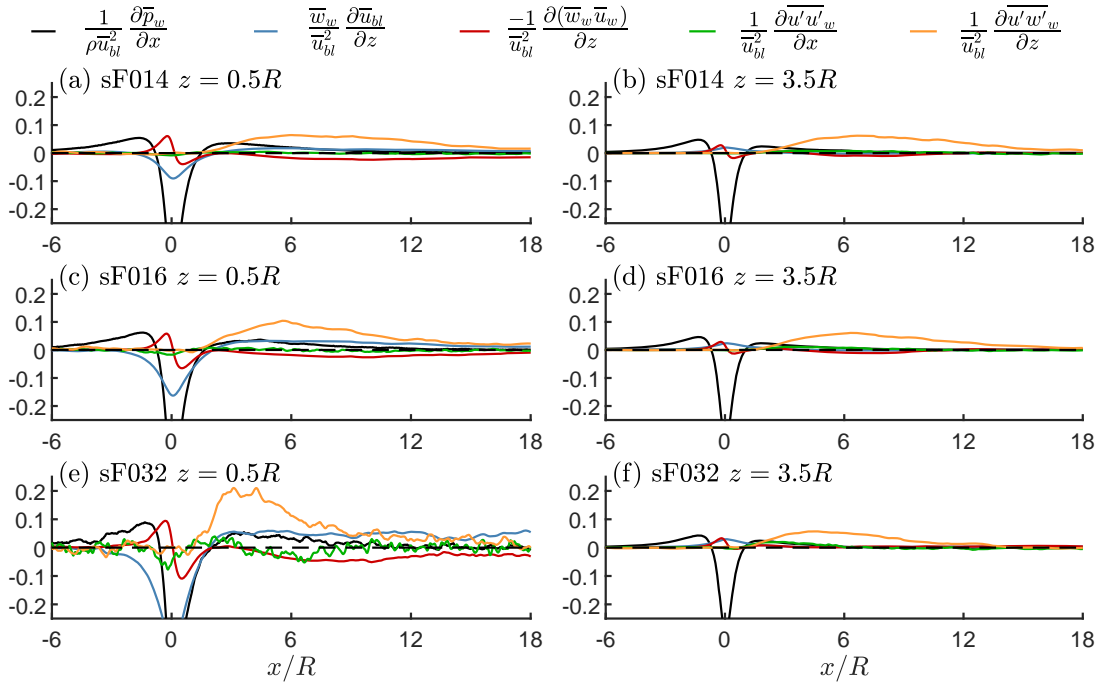


Figure 7.18: Break down of the axial change rate of the momentum deficit

$\partial\theta/\partial x = \partial(\Delta u(1-\Delta u))/\partial x$ as function of x in the wake of the model wind turbine immersed in (a),(b) the sF014, (c),(d) the sF016 and (e),(f) the sF032 boundary layer configuration evaluated in the mid-vertical plane at $z = 0.5R$ and $3.5R$ respectively.

Having discussed the local contribution of various terms to the local change rate of the momentum deficit $\partial\theta/\partial x$, it is now to analyse its effect on the streamwise momentum deficit Θ_x^2 and its change rate. Figure 7.19 (a) shows the streamwise momentum deficit Θ_x^2 and (b) its axial change rate $d\Theta_x^2/dx$ as defined in eq.(7.4) and eq.(7.5). Thereby the range $-4R < y < 4R$ is considered for integration in lateral direction and $0 < z < \delta$ for the integration in vertical direction. As with increasing roughness length the vertical asymmetry in the change rate of the local momentum deficit $\partial\theta/\partial x$ increases for downstream distances $x/R < 8$, its cross sectional integral, the change rate of the streamwise momentum deficit $d\Theta_x^2/dx$, increases as well, as shown in Figure 7.19 (b). Further downstream $d\Theta_x^2/dx$ becomes independent of the roughness length and decreases asymptotically to zero. Due to this, the streamwise momentum deficit in the wake Θ_x^2 , increases with increasing roughness length for distances $x/R < 12$ but reaches a constant level further downstream, see Figure 7.19(a). Therefore, the asymmetric distribution of the streamwise momentum deficit can not be caused by a continuous loss of flow momentum, which the constant level of $\bar{w}_w \partial \bar{u}_{bl} / \partial z$ in the far wake, as observed above, would suggest. It is rather caused within a distance of $x/R < 8$ and then advected downstream.

Similar to the discussion above regarding the local contributions of different momentum terms, Figure 7.20 shows all terms which are considered to contribute to the change rate of the streamwise momentum deficit $d\Theta_x^2/dx$, i.e. all terms on the right hand side of eq.(7.5). For low vertical shear, as it is the case in the sF014 boundary layer configuration, the change rate of the momentum thickness is mainly driven by the pressure gradient in the near wake. With increasing roughness length, and hence mean vertical shear, the terms $\bar{u}_{bl}^{-2} \bar{w}_w \partial \bar{u}_{bl} / \partial z$ and $\bar{u}_{bl}^{-2} \partial u' w'_w / \partial z$ become asymmetric, as shown above in Figure 7.18, due to which their cross sectional integrals have a considerable contribution to the

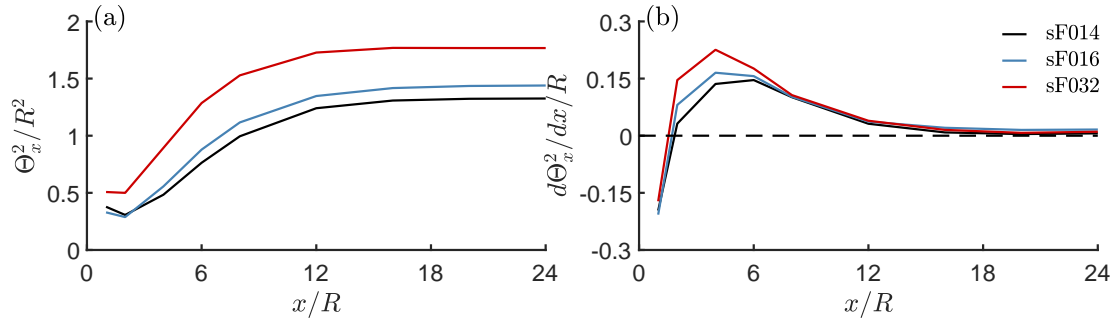


Figure 7.19: (a) Momentum thickness Θ_x^2 and (b) its axial change rate $d\Theta_x^2/dx$ as function of x within the wake of the model wind turbine operating at $\lambda = \lambda_{dsgn}$ immersed in different boundary layer configurations. The *legend* indicates the flow condition.

change rate of the streamwise momentum deficit. This is especially the case within the range of $x/R < 8$ where the change rate of the streamwise momentum deficit increases with the roughness length.

Therefore, it can be concluded that within highly sheared boundary layers an additional momentum deficit is caused in the near wake due to the vertical asymmetry of the momentum terms $\overline{u_{bl}^{-2} w_w \partial \overline{u_{bl}} / \partial z}$ and $\overline{u_{bl}^{-2} \partial u' w'_w / \partial z}$ and which is then advected into the far wake region. In Section 5.3.3 a suppression of Reynolds stresses in the wake below the ambient level, present in the experimental RBL configuration, is discussed and analysed in detail. It is shown, that within highly sheared boundary layers the turbulence production within the lower part of the wake $z < z_h$ can be significantly reduced. Therefore, an initial suppression of turbulence can be present over large axial distances, since the turbulence level in the wake, to a large extent, has to rise by the entrainment of the surrounding flow. Such a suppression of turbulence is also present in the wake immersed in the sF032 boundary layer configuration as can be observed in Figure 7.14(c). As already mentioned, the momentum exchange between the wake and the surrounding flow, e.g. the wake recovery, is significantly influenced by the turbulence level. Hence, due to the suppression of turbulence the additional momentum deficit formed in the near wake can persist over large axial distances into the far wake, as it can be observed in Figure 7.16(c). Moreover, the slower wake recovery below hub height compared to the recovery above the hub eventually results in the bias of the wake centre towards the ground, see Figure 7.15(d).

The presented results have shown that within a highly sheared boundary layer the momentum deficit and hence also the velocity deficit in the wake becomes asymmetric over the height. If this asymmetry is too excessive, the wake characteristics, which are based on the assumption of a Gaussian distribution, cannot longer accurately describe the wake, like it is the case for the wake width. To quantify the effect of the asymmetry on the calculation of the wake width in Figure 7.21(a) the wake width has been 'modelled' by calculating it on the basis of the centreline velocity deficit Δu_C and the momentum thickness Θ_x^2 derived from the LES data by applying eq.(2.57). As the centreline is considered to be biased, for the purpose of this comparison the velocity deficit is evaluated at the height of the rotor axis instead. The same 'modelling' is applied for the centreline velocity deficit on the basis of the measured wake width σ and the streamwise momentum deficit Θ_x^2 and is shown in Figure 7.21(b).

It can easily be seen that for the wakes immersed in the sF014 and sF016 boundary layer configurations the modelled values approach the values computed from the LES data

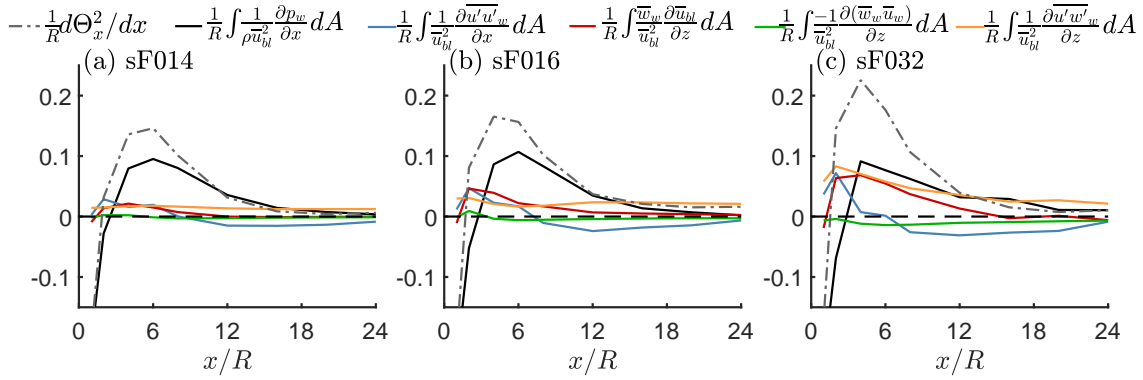


Figure 7.20: Breakdown of contributions to the axial change rate $d\Theta_x^2/dx$ as function of x in the wake of the model wind turbine immersed in (a) the sF014, (b) the sF016 and (c) the sF032 boundary layer configuration

asymptotically in the far wake region. The mismatch in the near wake results since the velocity deficit can not be approximated by a Gaussian distribution in this region. For the wake immersed in the sF032 boundary layer configuration, computed and modelled values first converge in the beginning of the far wake region $x/R \approx 6$ but begin to diverge for $x/R > 12$. This coincides well with the location where a momentum/velocity deficit close to the ground forms due to which the wake becomes asymmetric, see Figure 7.16(c). Due to this asymmetry modelled and computed values at a distance of $x/R = 24$ deviated by about 5% and 10% for the wake width and the velocity deficit respectively.

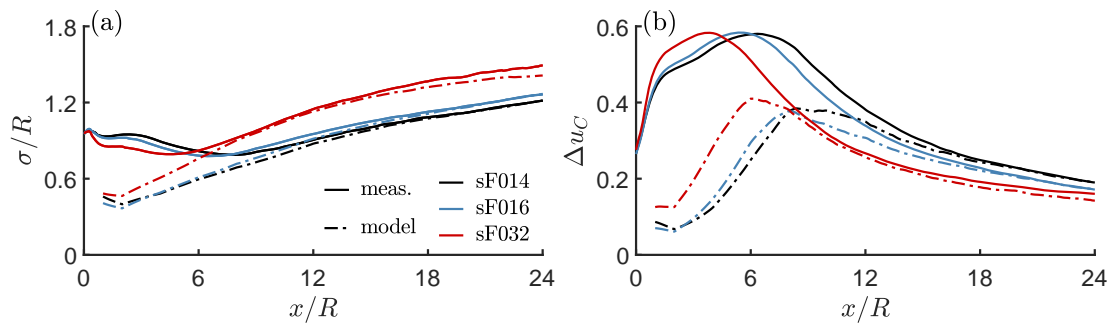


Figure 7.21: Comparison of computed and modelled (a) wake width σ and (b) centreline velocity deficit Δu_C in the wake of the model wind turbine immersed in three different boundary layers. The legend denotes the flow condition.

7.5 Influence of the Ground Roughness on a Yawed Turbine

In this section first the flow field in yawed conditions is discussed for the wind turbine immersed in the sF016 boundary layer configurations. Thereby it is shown that besides the intended lateral deflection also a vertical deflection occurs. Subsequently, the influence of ground roughness on the deflection in both directions is analysed and discussed. Furthermore, similar to the previous section, the momentum budget in the lateral direction is analysed regarding its conservation. Since with increasing ground roughness the loss of lateral momentum in downstream direction increases, the contribution of each momentum term is analysed and effects causing the momentum loss are identified.

7.5.1 Wake Characteristics

Figure 7.22 shows the normalised mean axial velocity $\bar{u}/\bar{u}_{bl}(z_h)$ for yaw angles of (a) $\gamma = 0^\circ$, (b) $\gamma = 15^\circ$, (c) $\gamma = 30^\circ$ and (d) $\gamma = -30^\circ$ in the horizontal plane at hub height for the wind turbine immersed in the sF016 boundary layer configuration. The yaw angle is thereby the angle between the rotor disk and y-axis with its sign defined according to the positive direction of rotation around the z-axis. As mentioned above the total thrust force exerted by the turbine reduces as the yaw angle increases, see Figure 7.6. With that also the velocity deficit in the wake reduces, as it can clearly be seen in Figure 7.22 by the color coding. Moreover, the thrust vector of the turbine, which is oriented normal to the rotor disk and directed upstream of the flow, has now a lateral component due to the yawing of the turbine. In the same manner as the axial force induces a velocity in the upstream direction, the lateral component induces a velocity in the direction towards which the turbine is yawed and causes the wake to deflect. With downstream distance, as the axial velocity recovers, so does the lateral component and the rate of deflection decreases resulting in the curved wake trajectory shown in Figure 7.22 as black dashed lines.

Figure 7.23 shows the normalised turbulent kinetic energy $K/\bar{u}_{bl}^2(z_h)$ for yaw angles of (a) $\gamma = 0^\circ$, (b) $\gamma = 15^\circ$, (c) $\gamma = 30^\circ$ and (d) $\gamma = -30^\circ$ in the horizontal plane at hub height for the wind turbine immersed in the sF016 boundary layer configuration. As turbulent kinetic energy is mainly produced by the strong shear at the border between the core of the wake and the outer flow, it is deflected in the same manner as the velocity deficit. Thereby it maintains an almost symmetric distribution regarding the wake centreline to downstream distances of $x/R \approx 20$. However, for large yaw angles of $|\gamma| = 30^\circ$ subsequently the distribution becomes asymmetric. In Figure 7.22(c) and (d) it can clearly be seen that on the rotor axis faced side the level of turbulent kinetic energy stays higher over a larger distance. The origin of this effect can be explained by a vertical movement of the wake which occurs in addition to the lateral deflection. This will be discussed in more detail below.

To analyse the wake trajectory in the vertical direction as well, Figure 7.24 shows contours of the velocity deficit in the yz -plane at four selected axial locations within the wake of the wind turbine immersed in the sF016 boundary layer configuration for all simulated yaw angles. Additional to each contour, the in-plane velocity components are shown as vectors. The wake centre position for each downwind location is indicated as white dot and the projected frontal area of the rotor disk is represented by an ellipse drawn as solid black line. With increasing yaw angle the lateral component of the thrust force exerted by the turbine causes a counter rotating pair of vortices, one at the height of the top and

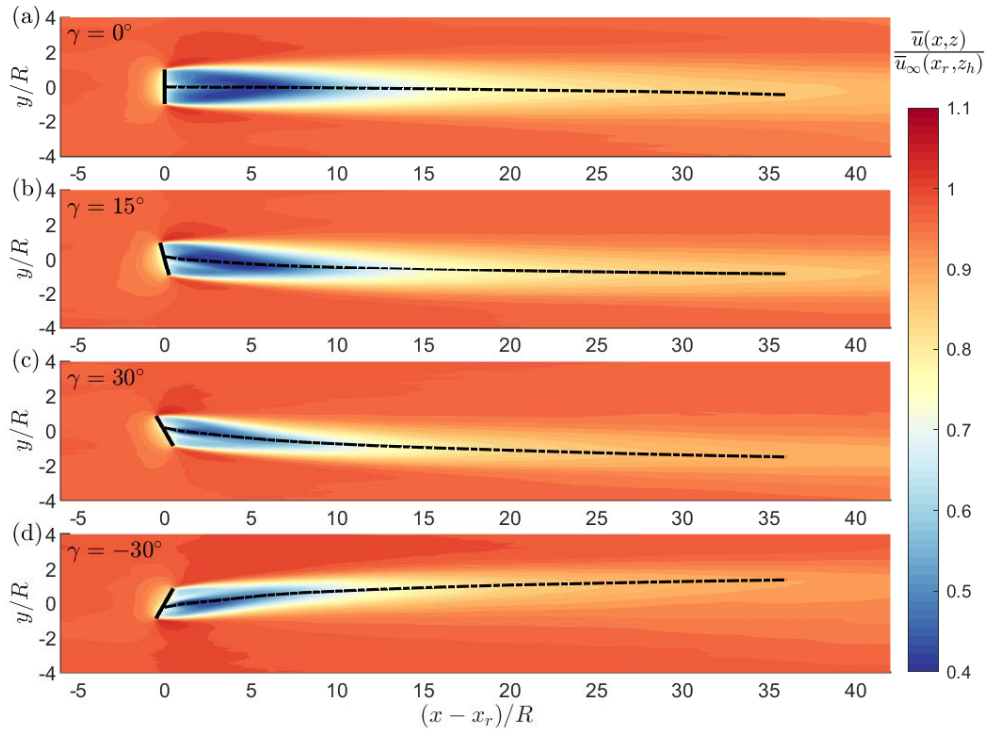


Figure 7.22: Normalised mean axial velocity $\bar{u}/\bar{u}_{bl}(z_h)$ within the mid-horizontal plane in the wake of the model wind turbine immersed in the sF016 boundary layer configurations for yaw angles of (a) $\gamma = 0^\circ$, (b) $\gamma = 15^\circ$, (c) $\gamma = 30^\circ$ and (d) $\gamma = -30^\circ$.

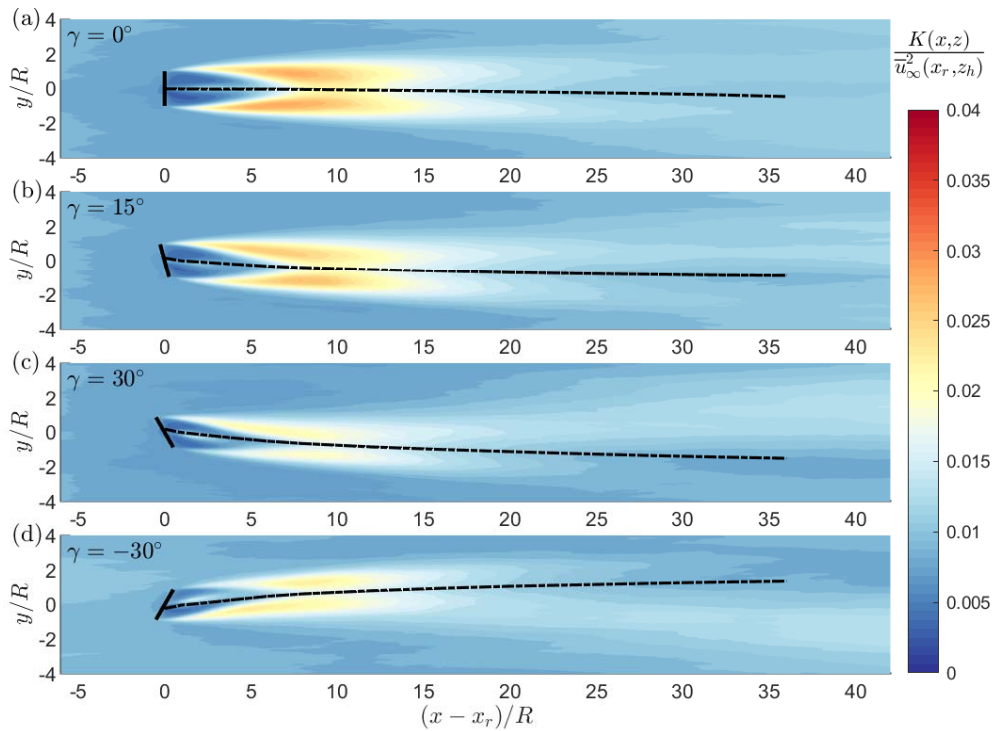


Figure 7.23: Normalised turbulent kinetic energy $K/\bar{u}_{bl}^2(z_h)$ within the mid-horizontal plane in the wake of the model wind turbine immersed in the sF016 for yaw angles of (a) $\gamma = 0^\circ$, (b) $\gamma = 15^\circ$, (c) $\gamma = 30^\circ$ and (d) $\gamma = -30^\circ$.

one at the bottom tip of the rotor disk. Due to the effect of the vortex pair the wake is not only deflected sideways but is also deformed and exhibits a 'kidney' like shape as it can be observed for $\gamma = \pm 30^\circ$ at $x/R = 8$.

Howland *et al.* [65] observed a similar kidney-shaped cross-section for the wake of a yawed porous disk in uniform flow. On the basis of potential theory and wind tunnel measurements, Bastankhah *et al.* [12] analysed the effect of a counter rotating vortex pair on a wake with and without rotation. It was shown that for a wind turbine wake (with the typical clock-wise direction of rotation) the wake exhibits a downward and upward movement for positive and negative yaw angle, respectively. For the numerical results presented here, however, only an upward motion can be observed in both cases with $\gamma = \pm 30^\circ$. This also holds for the boundary layer configurations sF014 and sF032, as can be seen in Figure 7.26(a) where the vertical centreline position z_C as function of the axial distance is shown for all simulations. Nevertheless, it can still be observed that for negative yaw angle the vertical displacement is larger than for a positive yaw angle. The main reason for this behaviour other than predicted by potential theory is the interaction of the counter rotating vortex pair with the ground. As can be seen in Figure 7.24 for distances $x/R = 16$ and 24 the intensity of the lower vortex diminishes and with that also its downward induction on the in-plane velocity components. Therefore, the upper vortex becomes more dominant and pushes the wake upwards.

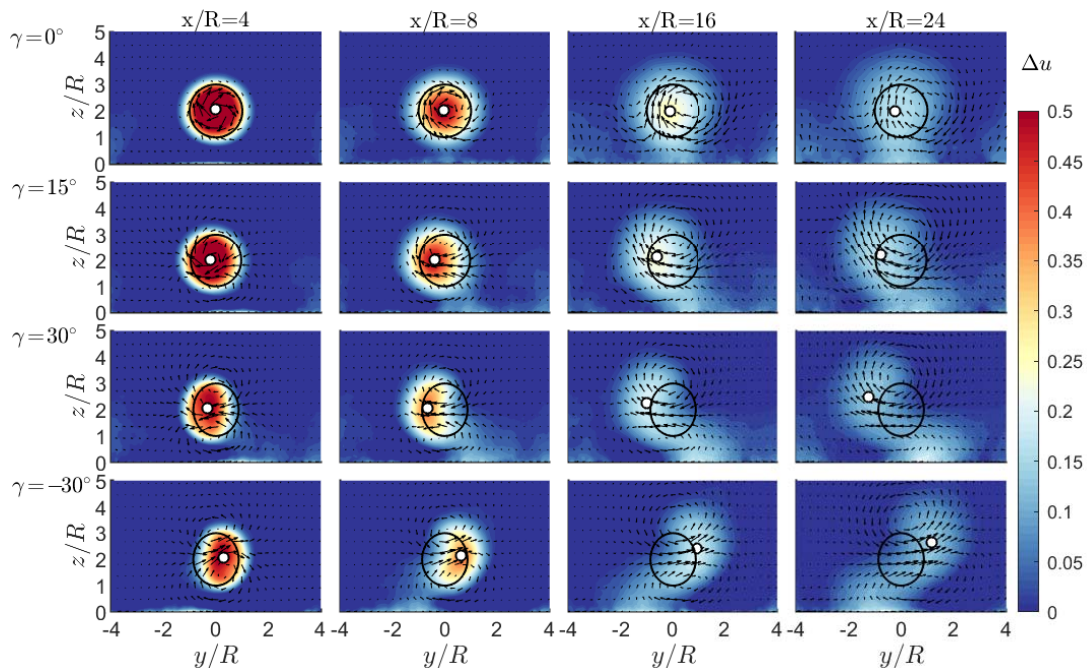


Figure 7.24: Contours of the velocity deficit Δu in yz -planes at different downstream locations and yaw angles γ within the sF016 boundary layer configuration. Black circles indicate the projected frontal area of the wind turbine and white dots represent the wake centre position at each downwind location. The vector field represents the in-plane velocity components.

It should be noted that the definition of the vertical coordinate of the wake center z_C might not be totally accurate, especially within highly sheared boundary layers, as it does not exclude the effect of the biased wake displacement due to the loss of flow momentum. From the present data the vertical displacement can not be decomposed into a biased part

and a shifted part. Therefore, in the following the vertical wake centre position $z_C(x)$ is defined to only be computed by eq.(2.56) in yawed condition, whereas in unyawed conditions it is set equal to the hub height $z_C(\gamma = 0^\circ, x) = z_h$.

The lateral deflection as well as the interaction of the vortex pair with the ground is significantly dependent on the aerodynamic surface roughness. Figure 7.25 shows contours of the velocity deficit in the yz -plane of the wake immersed in the sF014 and sF032 boundary layer configuration for a yaw angle of $\gamma = 30^\circ$. As in comparison to the sF016 configuration the level of the ambient turbulence is lower/higher in these configurations the wake gains/loses potential to penetrate the lateral undisturbed flow, resulting in higher/lower lateral deflection of wake centreline. Furthermore, the ground interaction of the vortex pair is decreased/increased which results in a lower/higher additional upward movement of the wake. It is also important to notice, that with increasing surface roughness the 'kidney' like shape of the wake is skewed in the region below hub height and exhibits a rather diagonal shape. Due to that, in case of the sF032 configuration, even at large yaw angles a significant velocity deficit can be observed around the rotor axis.

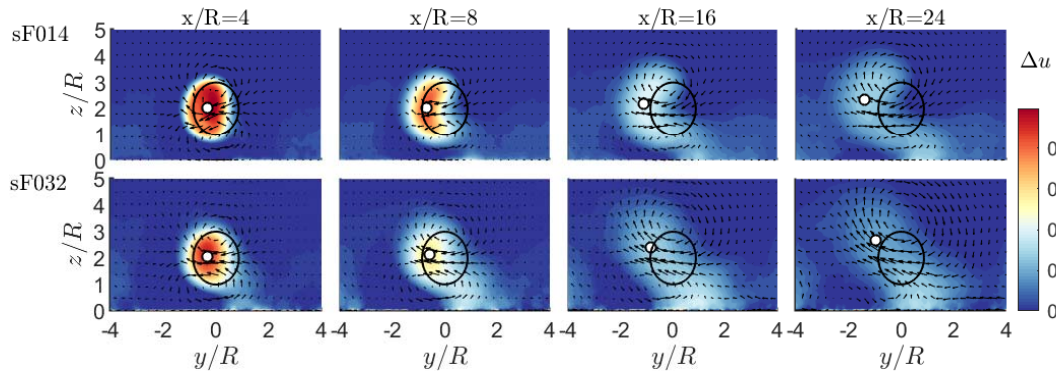


Figure 7.25: Contours of the velocity deficit Δu in yz -planes at different downstream locations within the sF014 and sF032 boundary layer configuration for a yaw angle of $\gamma = 30^\circ$. Black circles indicate the projected frontal area of the wind turbine and white dots represent the wake centre position at each downwind location. The vector field represents the in-plane velocity components.

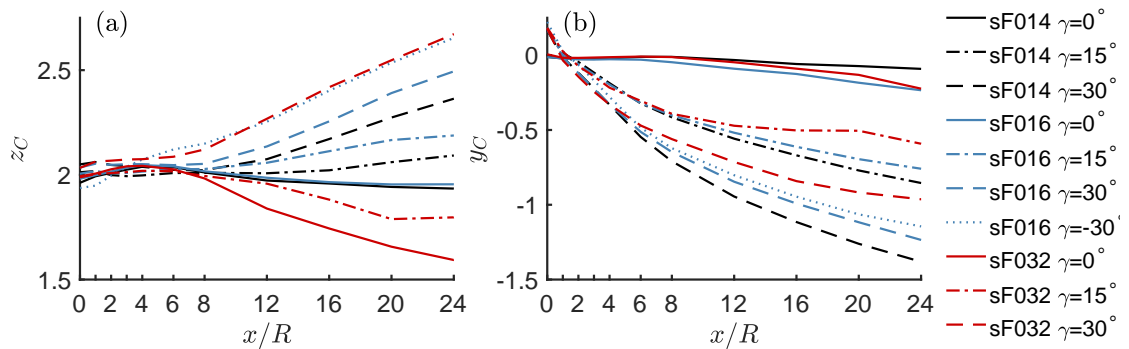


Figure 7.26: (a) vertical and (b) lateral wake centre position as function of the axial position for different yaw angles and different boundary layer configurations. For $\gamma = -30^\circ$ the lateral deflection is mirrored.

Similarly, the distribution of the turbulent kinetic energy is skewed as well (for large yaw angle) as shown in Figure 7.27. With increasing roughness and downstream distance, the distribution in the wake loses its elliptical shape while at hub height on the opposing

side of the deflection a region of increased turbulent kinetic energy maintains. This region causes the asymmetric distribution in the mid-horizontal plane shown above in Figure 7.23.

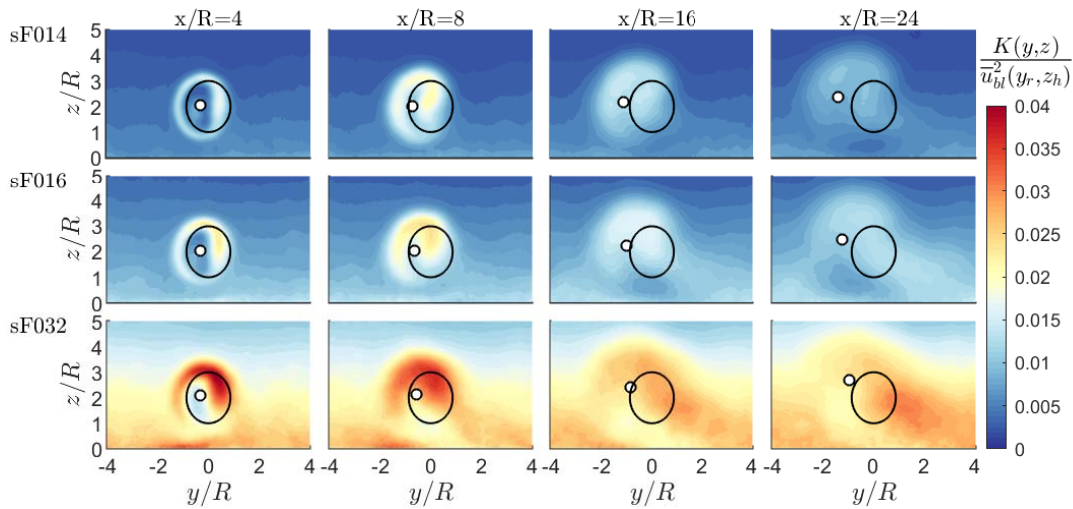


Figure 7.27: Contours of the normalised turbulent kinetic energy $K/\bar{u}_{bl}^2(x_r, z_h)$ in yz -planes at different downstream locations within the sF014 and sF032 boundary layer configuration for a yaw angle of $\gamma = 30^\circ$. Black circles indicate the projected frontal area of the wind turbine and white dots represent the wake centre position at each downwind location.

As the vertical movement and the skewing of the wake is not known a priori, an accurate determination of the wake centreline requires data with sufficient resolution in the yz -plane of the wake. In numerical studies, as presented here, this is typically not an issue. In wind tunnel studies, as presented in Chapter 5, however, it can be technically not feasible or too time consuming to obtain this resolution. Using only data within the horizontal plane at hub height is an appropriate surrogate, nevertheless it can become inaccurate within a highly sheared boundary layer. This is demonstrated in Figure 7.28 where the lateral wake centre position is shown as function of the axial distance for the wind turbine operating at a yaw angle of $\gamma = 30^\circ$ within all three simulated boundary layer configurations. Thereby the lateral position of the wake centre line is determined on the basis of various yz -planes in downstream direction and on the basis of the horizontal xy -plane at hub height shown as dashed and dotted lines, respectively. It can clearly be seen that with increasing surface roughness the deflection of the wake centreline derived from the flow field in the horizontal plane at hub height is underestimated.

Figure 7.29 shows (a) the centreline velocity deficit $\Delta u_C = \max(\Delta u)$, (b) the lateral wake width σ_y and (c) the vertical wake width σ_z as function of the axial distance x/R . Due to the additional vertical deflection of the wake in yawed conditions, as discussed above, all values are derived the yz -plane at the corresponding axial location. As already discussed in Section 5.2.3, due to the reduced frontal area in yawed conditions the forces acting normal to the rotor disk are reduced, which results in a reduction of the thrust coefficient, see Figure 7.6, and subsequently in a reduction of the maximum velocity deficit and the initial lateral wake width, see figure 7.29(a) and (b), respectively. In the near wake region, the vertical wake width is altered, this however is not further discussed in detail as eq.(2.56) used to calculate the lateral and vertical wake width σ_y and σ_z is only valid for the far wake region. At the onset to this region, at $x/R \approx 6 - 8$ the vertical wake width

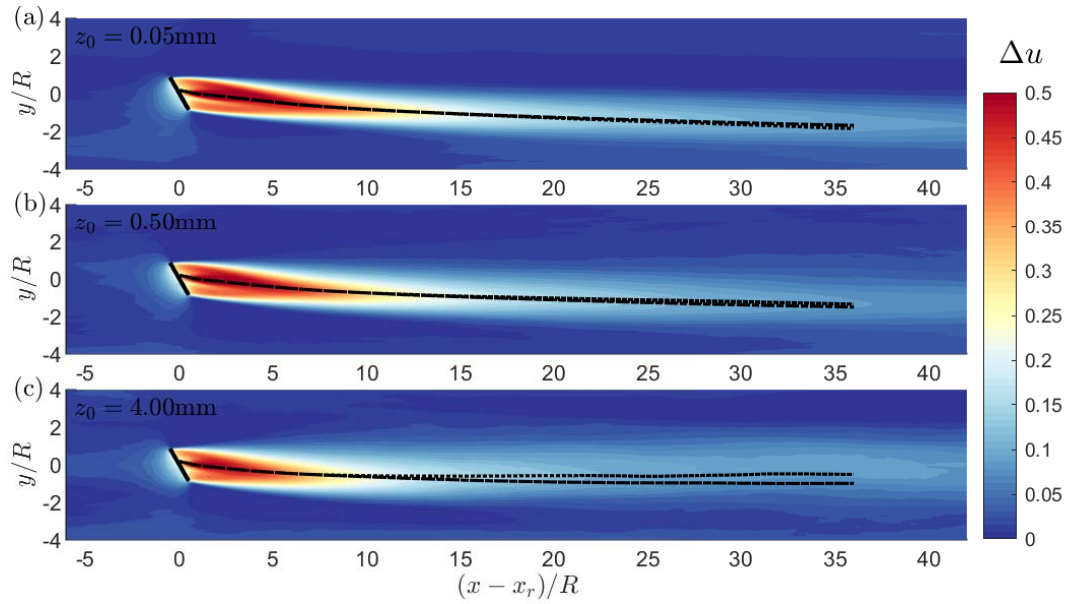


Figure 7.28: Velocity deficit Δu within the mid-horizontal plane in the wake of the model wind turbine for a yaw angle of $\gamma = 30^\circ$ immersed in the (a) sF014, (b) sF016 and (c) sF032 boundary layer configuration. Wake centre position derived from results in the mid-horizontal plane is indicated by a dotted line and from planes with $x = \text{const.}$ by a dashed line.

is not significantly affected by the yawing and in downstream direction the wake grows similarly for a given boundary layer.

The latter also holds for the lateral growth rate. Only in case of the sF032 boundary layer

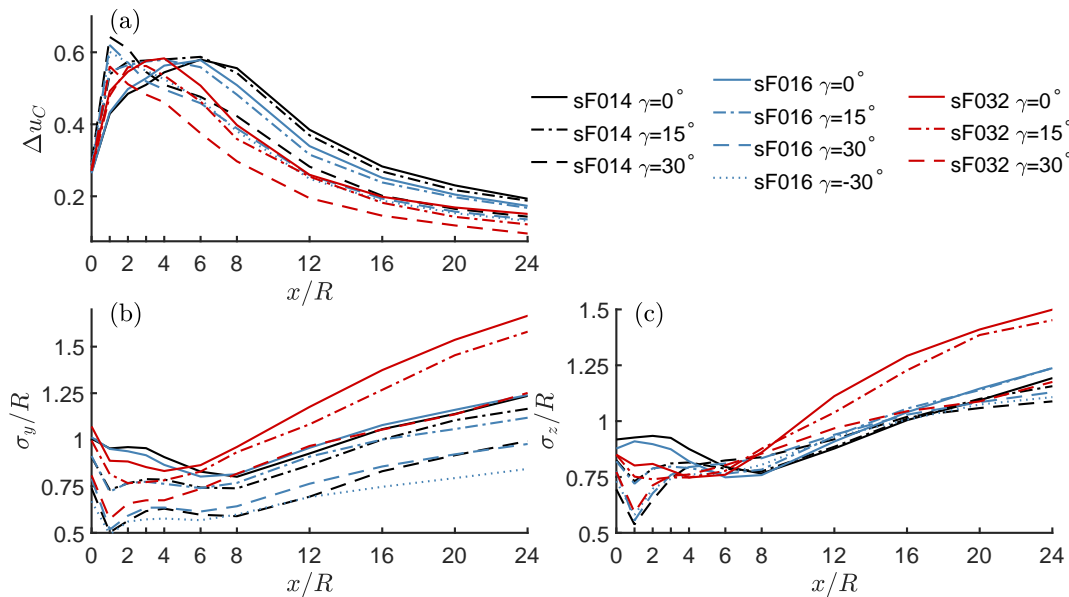


Figure 7.29: Wake characteristics of the yawed model wind turbine operating at $\lambda = \lambda_{dsgn}$ immersed in different boundary layer configurations: (a) centreline velocity deficit Δu_C , (b) lateral σ_y and (c) vertical half width σ_z . The legend indicates the flow condition and yaw angle.

configuration with the wind turbine operating at $\gamma = 30^\circ$, the growth rate in the lateral and vertical direction is significantly reduced. However, this result is questionable as in this case the wake is largely skewed, see Figure 7.25, and might no longer be represented by a Gaussian distribution as assumed to calculate the lateral and vertical wake width. Nevertheless, from these results it can be concluded that for modelling purposes the vertical wake width can be assumed to be nearly independent from the yaw angle. This was not possible to confirm in the wind tunnel experiment presented in Section 5.2.3, since there the flow field was only recorded in the mid-vertical and -horizontal plane from which the vertical wake width can not be computed in yawed conditions.

7.5.2 Momentum Budget

In order to model the wake deflection of the wake in yawed conditions, a common approach is to assume the conservation of lateral momentum in the wake, see e.g. [72, 12]. Given that, the wake deflection then becomes mainly a function of the initial wake deflection and the wake width, due to which wakes with large growth rates not only recover faster but also are less deflected. However, it is worth to analyse for which downstream distances this assumption is valid and how much it is influenced by the ground roughness.

As starting point the lateral momentum and its axial change rate, as defined in eq. (2.59) are analysed. For the sake of a better understanding of the discussion, the lateral momentum in the wake Θ_y^2 and its change rate $\frac{d}{dx}\Theta_y^2$ is restated here and given as

$$\Theta_y^2 = \int_{-\infty}^{\infty} \int_0^{\infty} \frac{\bar{u}\bar{v}}{\bar{u}_{bl}^2} dz dy, \quad (7.6)$$

$$\begin{aligned} \frac{d}{dx}\Theta_y^2 &= \frac{d}{dx} \int_{-\infty}^{\infty} \int_0^{\infty} \frac{\bar{u}\bar{v}}{\bar{u}_{bl}^2} dz dy \\ &= - \int_{-\infty}^{\infty} \int_0^{\infty} \frac{1}{\bar{u}_{bl}^2} \left(\frac{1}{\rho} \frac{\partial \bar{p}}{\partial y} + \frac{\partial \bar{v}\bar{v}}{\partial y} + \frac{\partial \bar{v}\bar{w}}{\partial z} + \frac{\partial \bar{u}'v'}{\partial x} + \frac{\partial \bar{v}'v'}{\partial y} + \frac{\partial \bar{w}'v'}{\partial z} \right) dz dy. \end{aligned} \quad (7.7)$$

Figures 7.30(a)–(c) show the lateral momentum and its axial change rate as function of the axial distance from the wind turbine x/R within all boundary layer configurations for yaw angles of $\gamma = 0^\circ, 15^\circ$ and 30° , respectively. As for the analysis of the streamwise momentum budget above, the range $-4R < y < 4R$ is considered for integration in lateral direction and $0 < z < \delta$ for the integration in vertical direction. In the un-yawed case the integral value of the lateral momentum is close to zero indicating that the distribution of the lateral velocity \bar{v} is symmetric regarding the mid-vertical plane. With increasing yaw angle the lateral momentum increases in magnitude (values are negative due to deflection in -y direction). Thereby, for a given yaw angle the initial integral value of the lateral momentum is independent of the boundary layer configuration. This is consistent with the similar wake trajectories found in the near wake region, see Figure 7.26(b). In downstream direction the lateral momentum decreases asymptotically in magnitude, whereby the change rate decreases slower with increasing roughness length, see Figures 7.30(d)–(f). For the sF014 and sF016 boundary layer configurations the change rate becomes nearly zero for $x/R > 12$ and the integral value of the lateral momentum approaches an almost constant value. Only in case of the sF032 boundary layer configuration and large yaw angles of $\gamma = 30^\circ$ the integral value of the lateral momentum significantly decreases in downstream direction.

To analyse the reason for this behaviour, Figures 7.31(a)–(f) show all terms which potentially contribute to the change rate of the lateral momentum $d\Theta_y^2/dx$ as function of the

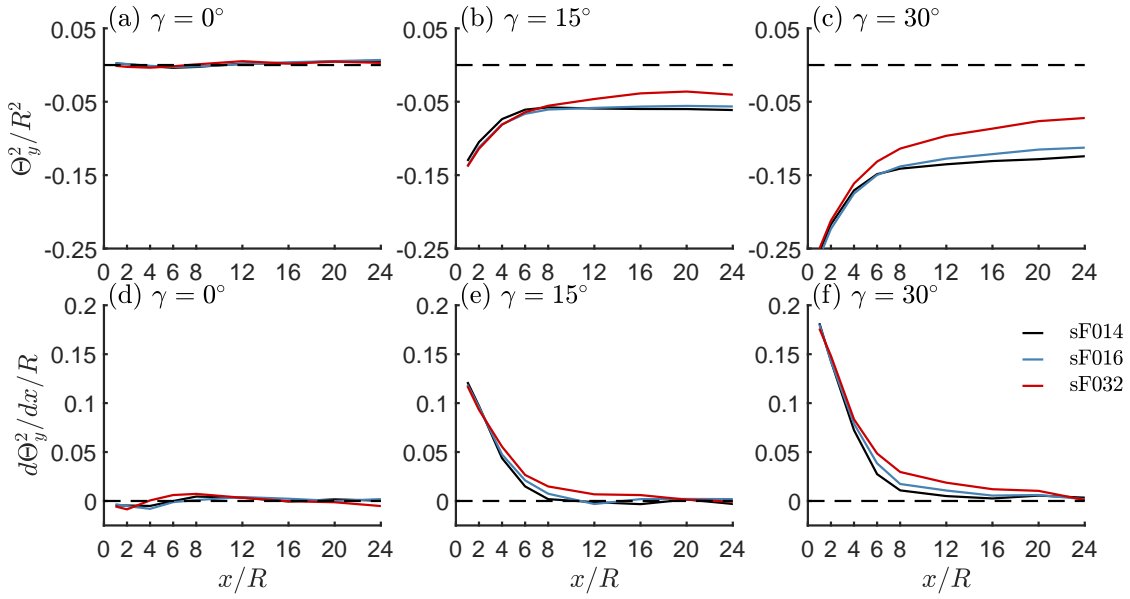


Figure 7.30: (a)–(c) Lateral momentum Θ_y^2 and (d)–(f) its axial change rate $d\Theta_y^2/dx$ as function of x/R within the wake of the model wind turbine operating at $\lambda = \lambda_{dsgn}$ immersed in different boundary layer configurations for yaw angles of $\gamma = 0^\circ$, 15° , and 30° . The legend indicates the flow condition.

axial distance from the wind turbine x/R within all boundary layer configurations for yaw angles of $\gamma = 0^\circ$ in (a)–(c) and $\gamma = 30^\circ$ in (d)–(f). In Section 2.3.1 it is discussed that in the lateral momentum balance all integrals of gradients in y - and z -direction equate to zero since the corresponding primitives at the integration boundaries are equal (e.g. $\bar{p}(y = -\infty) = \bar{p}(y = \infty)$, hence $\int_{-\infty}^{\infty} \partial \bar{p} / \partial y dy = 0$). As it can easily be seen, this is only approximately the case for the un-yawed cases within the sF014 and sF016 boundary layer. In all other cases the non-zero integral values of gradients in y -direction are a result of the limited lateral dimension of the computational domain and the asymmetric wake development in these cases. This becomes especially prominent for yawed conditions in the near wake for the integral value of the pressure gradient.

However, it can also be observed that only within the sF032 boundary layer configuration the cross sectional integral of $\partial \overline{u'v'} / \partial x$ results in values which can not be neglected, especially in the far wake. To show that this term causes the decrease of lateral momentum, the change rate of the lateral momentum is analysed by combining all integrals of gradients in x -direction in $\frac{d}{dx} \Theta_{y,x}^2$ and gradients in y - and z -direction in $\frac{d}{dx} \Theta_{y,y/z}^2$. Therefore, the change rate of the lateral momentum can be given as

$$\frac{d}{dx} \Theta_y^2 = \frac{d}{dx} \Theta_{y,x}^2 + \frac{d}{dx} \Theta_{y,y/z}^2 \quad (7.8)$$

with

$$\begin{aligned} \frac{d}{dx} \Theta_{y,x}^2 &= - \int_{-\infty}^{\infty} \int_0^{\infty} \frac{1}{\bar{u}_{bl}^2} \frac{\partial \overline{u'v'}}{\partial x} dz dy, \\ \frac{d}{dx} \Theta_{y,y/z}^2 &= - \int_{-\infty}^{\infty} \int_0^{\infty} \frac{1}{\bar{u}_{bl}^2} \left(\frac{1}{\rho} \frac{\partial \bar{p}}{\partial y} + \frac{\partial \bar{v}\bar{v}}{\partial y} + \frac{\partial \bar{v}\bar{w}}{\partial z} + \frac{\partial \overline{v'v'}}{\partial y} + \frac{\partial \overline{w'v'}}{\partial z} \right) dz dy. \end{aligned} \quad (7.9)$$

In Figure 7.32 (a)–(f) the change rate of the lateral momentum in this notation is shown as function of the axial distance from the wind turbine x/R within all boundary layer

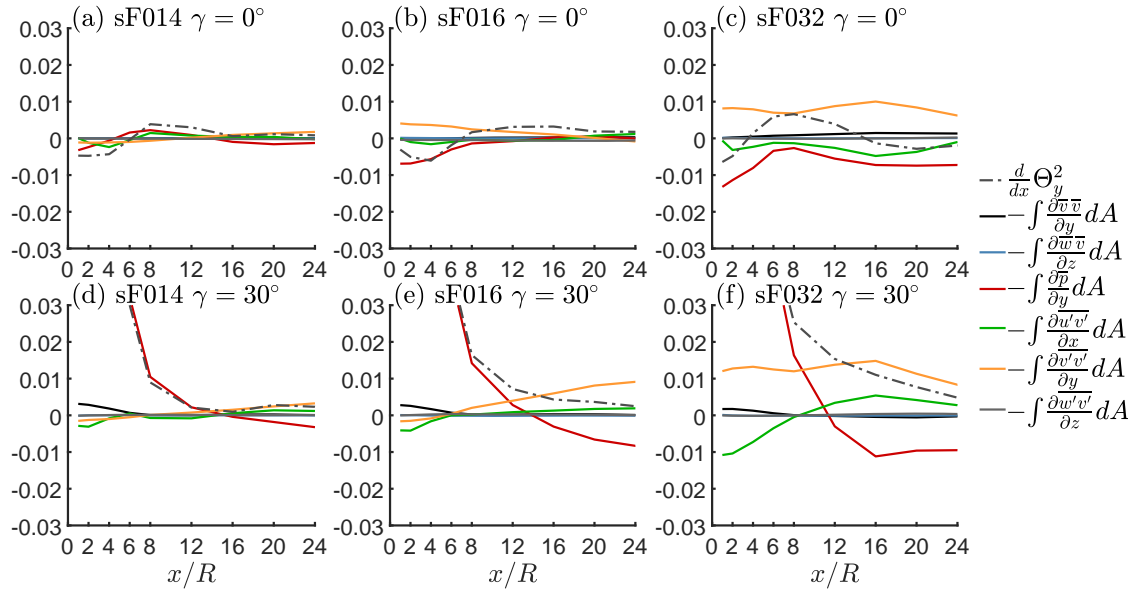


Figure 7.31: Break down of the axial change rate of the lateral momentum $d\Theta_y^2/dx$ into all contributing terms in the wake of the model wind turbine immersed in (a)/(d) the sF014, (b)/(e) the sF016 and (c)/(f) the sF032 boundary layer configuration for yaw angles $\gamma = 0^\circ$ and 30° .

configurations for yaw angles of $\gamma = 0^\circ$ in (a)–(c) and $\gamma = 30^\circ$ in (d)–(f). For yawed conditions it can be observed that $\frac{d}{dx}\Theta_{y,y/z}^2$ decays nearly to zero in the far wake, which supports the statement that non-zero values of it are only a numerical phenomena. However, more important, in this representation it becomes clear that only $\frac{d}{dx}\Theta_{y,x}^2$, and hence $\int \partial u'v'/\partial x dA$, causes the non-zero change rate of the lateral momentum in the far wake.

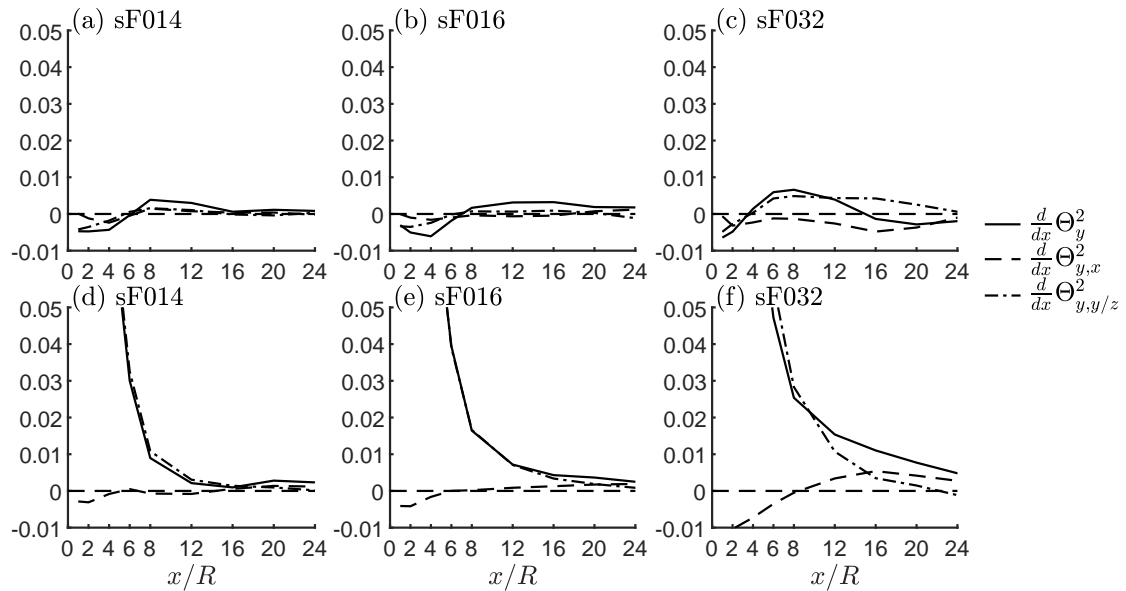


Figure 7.32: Break down of the axial change rate of the lateral momentum $d\Theta_y^2/dx$ into $\frac{d}{dx}\Theta_{y,x}^2$ and $\frac{d}{dx}\Theta_{y,y/z}^2$ in the wake of the model wind turbine immersed in (a)/(d) the sF014, (b)/(e) the sF016 and (c)/(f) the sF032 boundary layer configuration for yaw angles $\gamma = 0^\circ$ and 30° .

In an axisymmetric wake the shear stress distribution and its axial gradient would be skew symmetric in lateral direction regarding the centreline and would hence equate to zero when integrated in this direction. Since in the far wake the shear stress and the velocity deficit in the wake are directly connected, a non-zero value of $\int \overline{\partial u'v'}/\partial x dy$ indicates a skewing of the wake, which in turns reduces the lateral momentum and hence the wake deflection. As discussed above in Section 7.5.1 for yawed conditions a skewing of the wake is clearly present and increases with ground roughness. Figure 7.33 shows the lateral integrals of $\overline{\partial u'v'}/\partial x$ as function of the height at the downstream location of $x/R = 16$. The non-zero values of $\int \overline{\partial u'v'}/\partial x dy$, which also increase with ground roughness, confirm this observation. Furthermore, it can be observed that the main contribution to the change rate of the lateral momentum can be found below hub height. Therefore, the reduction of lateral momentum is considered to be connected with a skewing of the wake caused by the ground interaction of the counter rotating vortex pair mentioned above.

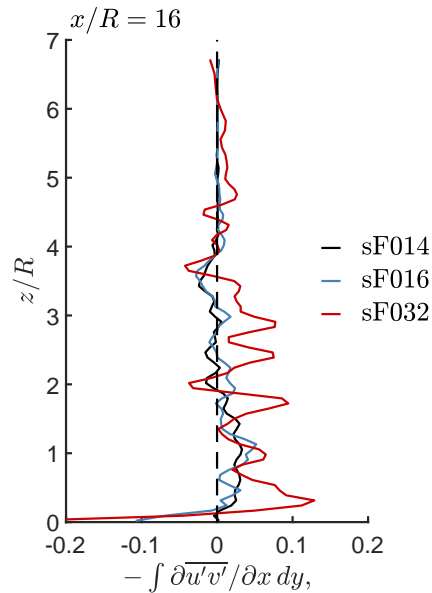


Figure 7.33: Lateral integral of $\overline{\partial u'v'}/\partial x$ as function of height at the downstream distance of $x/R = 16$ for a yaw angle of $\gamma = 30^\circ$. The *legend* indicates the flow condition.

7.6 Summary

In the current chapter results of large eddy simulations of the model wind turbine immersed in three turbulent boundary layers with low, moderate and high ground roughness, named sF014, sF016, and sF032, were presented. Thereby, the ground roughness of the sF016 configuration is chosen such to meet the flow characteristics of the experimental smooth boundary layer (SBL) configuration at hub height. Similar to the wind tunnel measurements presented in Chapter 5, the flow field was simulated for the turbine operating at design tip speed ratio $\lambda_{dsgn} = 6.5$ and yaw angles of $\gamma = 0^\circ$, $\gamma = 15^\circ$ and 30° . All cases were computed with a grid resolution of $N = 27$ cubic cells per rotor radii in the so called *wake region*. Upstream of the turbine a so called *recycling region* is defined with coarser grid resolution which serves to generate the flow of an undisturbed boundary layer. For a grid convergence analysis, additionally one simulation was carried out using a coarser grid resolution of $N = 18$ with the wind turbine aligned to the incoming flow and immersed in the sF016 boundary layer configuration. All simulations were carried out in three consecutive stages, a simulation of the empty domain to obtain a statistically developed boundary layer flow, a transient stage in which the wind turbine wake develops, and a recording stage in which the flow field is recorded for at least 1000 rotor revolutions.

Analysis of the empty domain simulation revealed that due to the grid refinement between the recycling region and the wake region the boundary layer flow reorganises, which becomes more significant with increasing roughness length. Within the wake region the reorganisation primarily affects profiles of the Reynolds stresses, whereas no changes of the mean velocity profile were observed. Spectral analysis of the flow recorded within the recycling region and the wake region showed that the reorganisation occurs since the inertial subrange of the flow is not sufficiently resolved within the recycling region. However, a comparison with data of the undisturbed boundary layer flow measured in the wind tunnel indicates that the power spectra in the wake region is well predicted by the simulation.

To validate the simulation results, the thrust and power coefficients predicted by the simulations were compared with data from the wind tunnel measurements. It was found that in all simulations the rotor performance is predicted with an error $< 3\%$ for the thrust coefficient and $< 4\%$ for the power coefficient. For validation of the predicted flow field, data from hot wire measurements in the wake of the model wind turbine immersed in the SBL configuration were compared to the predicted flow field in the sF016 boundary layer. Due to the application of the blade polars identified in Section 6.4, in the near wake the computed velocity deficit is in excellent agreement with the experimental results. However, in the mid-vertical plane the simulated wake is found to develop differently from the wind tunnel experiment, which is considered to result from differences in the boundary layer profiles. Nevertheless, in the mid-horizontal plane the predicted velocity deficit, the Reynolds shear stress and the turbulent kinetic energy exhibit only slight deviations from the measurement results. A comparison of the wake key characteristics for the numerical sF032 configuration and the experimental RBL configuration, shows even a larger mismatch regarding the lateral and vertical wake growth. This is considered to result from differences in the boundary layer profiles, which increase with surface roughness. Results would potentially be in even better agreement if (i) a boundary layer configuration would be found in which the mean wind shear is closer to the experimental value and if (ii) the effect of tower and nacelle would be modelled in the

simulation.

A comparison of the data obtained on grids with different resolutions of $N = 18$ and $N = 27$ grid points per rotor radii showed only slight deviations in the prediction of the flow quantities. Reorganisation effects triggered by the grid refinement within the computational domain were shown to have no significant effect on the wake development. The wake and its development are therefore considered to be well resolved by both grid resolutions. Moreover, it has been shown that the reorganisation of the boundary layer triggered by the grid refinement upstream of the wake region has only a minor effect on the wake development under the condition of (i) the grid resolution is sufficient and (ii) ground roughness is moderate or low, for high ground roughness the reorganisation might affect the results.

The wake of the wind turbine aligned with the incoming boundary layer flow was found to recover faster with increasing roughness length, since the higher level of background turbulence enhances the momentum exchange between the wake and the outer flow. Similar to the findings based on the wind tunnel measurements, presented in Chapter 5, within the sF014 and sF016 boundary layers with low and moderate surface roughness the wake width was shown to grow approximately linear. However, in the sF032 boundary layer the wake initially grows faster, but with decreasing growth rate in downstream direction. Moreover, within this boundary layer a significant vertical displacement of the wake centreline towards the ground was observed. It was shown that this stems from an asymmetric development of the momentum deficit in the wake, due to which the calculation of the wake centreline position is biased towards the ground. Furthermore, with increasing roughness an extended region of suppressed turbulent kinetic energy was observed as in the experiment.

To analyse the asymmetric development in more detail the momentum budget in the wake of the un-yawed turbine was analysed. A comparison of the change rate of the momentum deficit above and below hub height revealed an asymmetric development in the axial direction for increasing roughness length. For moderate shear the asymmetry is low, which supports the assumption that within a boundary layer with moderate mean wind shear, e.g. low roughness length, the wake can be approximated by the superposition of an undisturbed boundary layer and an axisymmetric wake. For high shear, e.g. high roughness length, the analysis of the local and cross-sectional momentum budget revealed that the asymmetric momentum deficit is caused in the near wake due to the vertical asymmetry of the vertical gradient of the Reynolds shear stress $\overline{u_{bl}^{-2}}(z)\partial\overline{u'w'_w}/\partial z$ and the vertical gradient of the axial velocity in the undisturbed boundary layer $\partial\overline{u_{bl}}/\partial z$ and which is then advected into the far wake region. It was concluded that the suppressed turbulent kinetic energy and the resulting reduced momentum exchange between the wake and the surrounding flow enable the additional momentum deficit below hub height to persist over large axial distances.

Definitions used in this work to characterise the wake, such as the centreline velocity deficit and the wake width, are based on the assumption of an axisymmetric wake. Due to the observed asymmetric development of the wake these values are suspected of being afflicted with error. An error estimation showed that for the boundary layer configurations sF014 and sF016, with low and moderate mean wind shear, the error is neglectable, whereas for the sF032 configuration with high mean wind shear the error is about 5% for the wake width and 10% for the centreline velocity deficit.

For intentional misalignments of the wind turbine with the incoming flow a counter rotating pair of vortices was observed, forming at the lower and upper edge of the rotor

disk, which is consistent with recent observations reported in literature. Due to the interaction of the lower vortex with the ground its intensity diminishes. As a result a vertical deflection of the wake in the upward direction occurs. It was shown that this deflection depends on the roughness length of the boundary layer and the yawing direction. However, the deflection does not change its direction with $\gamma > 0$ or $\gamma < 0$ as derived from potential flow theory in [12]. The numerical results confirm the dependency of the lateral deflection on the surface roughness as observed in the measurement results presented in Chapter 5. Moreover, it was observed that ground interaction and vertical deflection lead to a skewing of the wake. As a result, using solely profiles of the velocity deficit measured in the mid-horizontal plane to estimate the wake center position, as realized for the wind tunnel measurements, might over pronounce the effect of ground roughness on the wake deflection. In conclusion, intentional yaw misalignment as control strategy to improve the overall power production in wind farms can benefit from the additional upward motion of the wake. Its potential, however, is strongly influenced by the surface roughness. Furthermore, the numerical results confirm the observation that the lateral wake growth rate as well as the vertical wake width are nearly independent of the yaw angle.

In order to probe the assumption of the conservation of lateral momentum, as applied in current analytical wake models, the lateral momentum budget in the wake of the wind turbine with intentional yaw misalignment was analysed. In the near wake region a decay of the lateral momentum was observed which is mainly caused by the lateral pressure gradient. This, however, is considered to be a numerical deficiency, occurring due to the limited lateral dimension of the computational domain. Nevertheless, in the far wake region $x/R \geq 12$ and for large surface roughness the change rate of the lateral momentum persists at a non-negligible level over a wide axial range in the far wake where the pressure gradient is negligible. A break down of the momentum budget revealed that for this configuration the cross sectional integral of the axial gradient of the Reynolds shear stress does not cancel out. Further analysis of its local contribution shows that this effect is mainly present below hub height, where the ground interaction of the counter rotating vortex pair causes a skewing of the wake, and which in turn affects the change rate of the lateral momentum.

To the author's knowledge this is the first study which analyses the momentum budget in the wake of a wind turbine immersed in boundary layers of different surface roughness and yaw angles. It was shown that within highly sheared turbulent boundary layers effects occur which alter the streamwise and lateral momentum budget. Taking this effect into consideration might help to improve analytical wake predictions in rough terrain.

Assessment of Self Similarity & Analytical Wake Modelling

In this chapter the self similarity of first and second order flow statistics in the wake and the axial scaling of these is assessed. Therefore, use is made of the idea that the far wake of a wind turbine in steady operation, immersed in a neutrally-stratified turbulent boundary layer, can approximately be described by the superposition of the undisturbed approaching flow and an 'added' axisymmetric wake, as derived in Chapter 2. The analysis of the self similarity and the underlying axial scaling laws of the velocity deficit and the added Reynolds stresses is used to derive a set of consistent exponents for the axial evolution of these quantities. Based on these findings an analytical model to predict turbulence properties in the far wake region is developed.

First in Section 8.1, regarding the evolution of axisymmetric turbulent wakes immersed in low turbulence uniform background flow, the theory of equilibrium and non-equilibrium dissipation and the resulting scaling laws are summarized and then adapted for the description of wakes immersed in turbulent boundary layers. Subsequently, in section 8.2 data from the wind tunnel measurements presented in Chapter 5 and the large eddy simulations presented in Chapter 7 is then assessed regarding the self similarity of flow quantities in the wake and their axial scaling. Then a simple analytical model to predict the diagonal components $\overline{u'_i u'_i}$ of the Reynolds stress tensor and its anisotropy in the wake is proposed and tested against the experimental and numerical data in section 8.3. Finally a summary is given in section 8.4. Major parts of this chapter are based on the author's article [137].

8.1 Theory of Self Similarity

8.1.1 Wake Width and Velocity Deficit Scaling

The self similarity of axisymmetric turbulent wakes has been extensively studied in experimental and numerical investigations for more than half a century (see [74] for a historical review). In general, it describes the normalised velocity deficit in the wake Δu , as defined in Eq.(8.14), as a product of the centreline velocity deficit $\Delta u_C(x)$ and a shape function $f(\eta)$, where η is the radial coordinate r normalized by the wake width σ

$$\Delta u(x, r) = \Delta u_C(x) f(\eta). \quad (8.1)$$

George [50] showed in his equilibrium similarity analysis that, for the streamwise evolution of the velocity deficit and the wake width within an axisymmetric wake, two scalings are possible, namely a low- and a high-Reynolds number scaling. The low-Reynolds number scaling is not further considered in this work since it is not valid in fully developed turbulent shear flows [107]. The classical equilibrium high-Reynolds number scaling is obtained by neglecting the viscous term in the mean momentum equation and assuming that the turbulence dissipation rate is $\epsilon = C_\epsilon K^{3/2}/\sigma$, where K is the turbulent kinetic energy, σ the width of the axisymmetric wake and C_ϵ a constant. This leads to the *equilibrium* high-Reynolds number scaling for the centreline velocity deficit Δu_C and the wake width σ

$$\Delta u_C \propto \left(\frac{x - x_0}{\Theta} \right)^{-2/3}, \quad \sigma \propto \left(\frac{x - x_0}{\Theta} \right)^{1/3}, \quad (8.2)$$

where x_0 is a virtual origin, and Θ the momentum thickness as defined in Eq.(2.54). This scaling law is termed *equilibrium* since it is assumed that the turbulent dissipation rate instantaneously equals the rate with which large eddies feed energy into the cascade of turbulent kinetic energy (Richardson-Kolmogorov cascade). Any different scaling of the turbulence dissipation must therefore characterize an instantaneous imbalance between dissipation and the rate with which energy is fed into the cascade at the large scales [109]. In these regions it was found that C_ϵ is not a constant but $C_\epsilon \propto Re_G^m/Re_L^n$ [146], where Re_G is a global Reynolds number determined by the inlet conditions and Re_L is a local Reynolds number based on local velocity and length scale. Nedic et al. [107] argued that this non-equilibrium scaling law can be explained in terms of the similarity analysis of George [50]. For the centreline velocity deficit Δu_C and the wake width σ it yields

$$\Delta u_C \propto \left(\frac{x - x_0}{\Theta} \right)^{\frac{-2}{3-n}} \left(\frac{l}{\Theta} \right)^{\frac{-2n}{3-n}} Re_G^{\frac{2(n-m)}{3-n}}, \quad \sigma \propto \left(\frac{x - x_0}{\Theta} \right)^{\frac{1}{3-n}} \left(\frac{l}{\Theta} \right)^{\frac{n}{3-n}} Re_G^{\frac{m-n}{3-n}}, \quad (8.3)$$

where l is the size of the bluff body generating the wake. Vassilicos [148] points out that in the non-equilibrium region of turbulent axisymmetric wakes generated by fractal plates the values m and n are $m \approx n \approx 1$ (note $m = n = 0$ results in the equilibrium scaling law). Given that, the scaling law Equations (8.3) result into

$$\Delta u_C \propto \left(\frac{x - x_0}{\Theta} \right)^{-1} \left(\frac{l}{\Theta} \right)^{-1}, \quad \sigma \propto \left(\frac{x - x_0}{\Theta} \right)^{1/2} \left(\frac{l}{\Theta} \right)^{1/2}. \quad (8.4)$$

It will be termed *square-root wake growth scaling* throughout this chapter. This scaling should not be confused with the equilibrium low-Reynolds number scaling of George [50],

for which $\epsilon \propto \nu K/\sigma^2$.

It is important to notice that the theory of non-equilibrium dissipation also allows wakes to scale with exponents other than $m \approx n \approx 1$. In fact Dairay et al. [35] points out that the theory could also be generalised for exponents $n \neq m$. Especially in sheared background flows which are neither uniform nor almost laminar, dissipation rates might differ from the *equilibrium scaling* or the *square-root wake growth scaling* and unequal exponents n and m are conceivable. However, the exponent m does not influence the axial scaling of the centreline velocity deficit Δu_C nor the wake width σ in Equation 8.4 and will therefore not be further considered in this work.

Wind turbine wakes immersed in turbulent boundary layers are often reported to grow linearly, see e.g., [1, 12]. Hence, along with the commonly assumed constant momentum thickness $\Theta = \text{const.}$ (conservation of the streamwise momentum deficit) in the far wake, it might be possible that this observed linear wake growth region can be described as a non-equilibrium wake region for which the scaling would be $n \approx 2$. Therefore this case is also considered in the following discussion which will be referred to as *linear wake growth scaling law* and which reads as

$$\Delta u_C \propto \left(\frac{x - x_0}{\Theta} \right)^{-2} \left(\frac{l}{\Theta} \right)^{-4}, \quad \sigma \propto \left(\frac{x - x_0}{\Theta} \right)^1 \left(\frac{l}{\Theta} \right)^2. \quad (8.5)$$

To determine the underlying scaling law, a power law Ansatz is fitted to the measurement data

$$\Delta u_C = A (x - x_{0u})^{-n_u} \quad (8.6)$$

$$\sigma_i = B (x - x_{0\sigma})^{n_\sigma}, \quad (8.7)$$

where $A, B, x_{0u}, x_{0\sigma}$ are case dependent constants, $n_u = 2/(3 - n)$ and $n_\sigma = 1/(3 - n)$ the corresponding exponents of the considered scaling laws and $i = y, z$.

8.1.2 Streamwise Evolution of Reynolds Stresses

George's theory [50] not only predicts the self similarity of the velocity deficit $\Delta u(x, r)$ but also of the 'radial' Reynolds shear stress $\overline{u'u'_r}(x, r)$ and of the turbulent kinetic energy $K(x, r)$ for an axisymmetric wake. Similar to the velocity deficit it describes the profiles of the Reynolds shear stress and the turbulent kinetic energy as a product of its maximum values $\overline{u'u'_r}_M$ and K_M and corresponding shape functions g and h as

$$\overline{u'u'_r} = \overline{u'u'_r}_M g(\eta), \quad K = K_M h(\eta). \quad (8.8)$$

Thereby the factors K_M and $\overline{u'u'_r}_M$ scale in the *equilibrium* case as

$$\overline{u'u'_r}_M \propto U_\infty^2 \Delta u_C d\sigma/dx, \quad K_M \propto U_\infty^2 \Delta u_C^2, \quad (8.9)$$

where U_∞ is the magnitude of the uniform background flow. On the contrary, Dairay et al. [35] showed that in the *non-equilibrium* region behind a fractal plate both K_M and $\overline{u'u'_r}_M$ follow the same scaling law

$$\overline{u'u'_r}_M \propto K_M \propto U_\infty^2 \Delta u_C d\sigma/dx. \quad (8.10)$$

Inserting the three proposed scaling laws for the velocity deficit and the wake width

Equations (8.2), (8.4) and (8.5) in the corresponding Reynolds stress scaling law Equations (8.9) and (8.10), returns in each case a different x-dependency for K_M and $\overline{u'u'_r}_M$. This is an important finding as it opens another possibility to determine which kind of scaling is present in the wake if measurements or simulation results of sufficient accuracy are available for these quantities. Nevertheless, in the measured cases changes in the wake width growth are subtle and deriving its axial gradient $d\sigma/dx$ from the few measurement stations which lie within the far wake region is rather inaccurate. As discussed in section 7.4.2 the streamwise momentum deficit in the far wake region is conserved. Therefore, a constant momentum thickness can be assumed, for which Equation (2.57) gives $\sigma \propto \sqrt{\Delta u_C}$ (with $\sigma_z \approx \sigma_y = \sigma$). This relation is used to get rid of the necessity to determine $d\sigma/dx$ from the flow field by simply substituting the wake width by the function of the centreline velocity deficit. Given that, we arrive at

$$\frac{K_M}{U_\infty^2} \propto \Delta u_C \frac{d\sigma}{dx} \propto \Delta u_C \frac{d}{dx} \left(\Delta u_C^{-1/2} \right) \propto \Delta u_C^{-1/2} \frac{d\Delta u_C}{dx}. \quad (8.11)$$

It is important to mention that Dairay et al. [35] argue that non-equilibrium flows in which $n \neq 1$ should only be possible if the anisotropy of the Reynolds stresses remains constant along a surface $\eta = 1$. That means that the ratios of the diagonal components of the Reynolds stress tensor $\overline{u'_i u'_i}$ are constant at the location of the maximum Reynolds shear stresses $\overline{u'u'_r}$. Although in their work a detailed discussion on the necessity of this assumption is left for future studies, this argument is considered in the analysis of the measurement results presented here.

As the presented wind turbine wakes are immersed in turbulent boundary layers with a considerable level of background turbulence and vertical shear stress, the classical definitions used for analysing the self similarity and the scaling of wakes within low turbulence and uniform background flows is not applicable. However, following the idea of the superposition of a boundary layer flow and a wake, it is reasonable to consider the so-called added quantities of the Reynolds shear stress and the turbulent kinetic energy as defined below. Due to the mentioned argument of constant anisotropy, also the diagonal components of the added Reynolds stress tensor are taken into account. Since the velocity deficit of a wake imposed in a boundary layer at a certain height z scales with the axial velocity of the undisturbed background flow $\overline{u}_{bl}(z)$, it is expected that all components of the Reynolds stress tensor and its added equivalents scale with the square of it. With that the non-dimensional added components of the Reynolds stress tensor $\Delta \overline{u'_i u'_j}$ and the non-dimensional added turbulent kinetic energy ΔK can be defined as

$$\Delta \overline{u'_i u'_j} = \frac{\overline{u'_i u'_j}_w(x, y, z)}{\overline{u}_{bl}^2(z)} = \frac{\overline{u'_i u'_j}(x, y, z) - \overline{u'_i u'_j}_{bl}(z)}{\overline{u}_{bl}^2(z)}, \quad \Delta K = \frac{K(x, y, z) - K_{bl}(z)}{\overline{u}_{bl}^2(z)}, \quad (8.12)$$

with its maximum values $\Delta \overline{u'_i u'_j}_M = \max(\Delta \overline{u'_i u'_j})$ and $\Delta K_M = \max(\Delta K)$. Together with the corresponding exponents of the considered scaling law the x-dependencies of the added Reynolds shear stress and turbulent kinetic energy can be expressed for

$$\begin{aligned} \text{the equilibrium scaling as} & \quad \Delta \overline{u'u'_r}_M, \Delta K_M \propto \Delta u_C^2, \\ \text{for the square-root wake growth scaling as} & \quad \Delta \overline{u'u'_r}_M, \Delta K_M \propto \Delta u_C^{3/2}, \\ \text{and for the linear wake growth scaling as} & \quad \Delta \overline{u'u'_r}_M, \Delta K_M \propto \Delta u_C. \end{aligned} \quad (8.13)$$

These distinct differences of the exponent in the dependency on the centreline velocity

deficit identified in Equation (8.13) allows us to distinguish between the different scaling laws without having to determine the x -dependency of the wake width or the centreline velocity deficit.

8.2 Assessment of Self Similarity in Wind Turbine Wakes

In the spectral analysis presented in section 5.3.4 it was shown that downstream of the far wake onset $x/R \geq 6$ a representation can be found in which power spectra for a particular operational state and flow condition appear to be nearly self similar for a given height. Therefore, the purpose of this section is to show, based on the concept of an added wake (see section 2.3.1 for explanation), that self similarity in the far wake region of the model wind turbine can not only be found for the velocity deficit but also for the components of the added Reynolds stress. Furthermore, the underlying scaling law of the velocity deficit, the wake width, the Reynolds shear stress and the turbulent kinetic energy is analysed. For the sake of a better comprehension, this analysis is first carried out in Section 8.2.1 for results obtained from the wind tunnel measurements presented in Chapter 5, and in Section 8.2.2 for results obtained from the large eddy simulations presented in Chapter 7. Thereby the aim of the latter analysis is to confirm findings from the wind tunnel experiment and to evaluate the computational method.

8.2.1 Self Similarity in the Wind Tunnel Measurement Results

Before analysing the velocity deficit in the wake regarding self similarity, the definition of the normalised velocity deficit used in this work is discussed. For the sake of a better understanding the definition Eq.(8.14) is restated here and given as

$$\Delta u(x, y, z) = \frac{\bar{u}_w(x, y, z)}{\bar{u}_{bl}(z)} = \frac{\bar{u}_{bl}(z) - \bar{u}(x, y, z)}{\bar{u}_{bl}(z)}. \quad (8.14)$$

The choice of normalisation is an important point since in the literature the velocity deficit is typically normalised by the velocity of the incoming wind at hub height $\bar{u}_{bl}(z_h)$ (see e.g. [1, 28, 29, 158, 160]), rather than using the local velocity $\bar{u}_{bl}(z)$. In Chapter 2 it was shown that within the actuator disc theory a wake immersed in a turbulent boundary layer can only be axisymmetric when normalised by the local velocity of the boundary layer. Due to this argument, also the added Reynolds stresses have to be normalised in the same way, as defined in Eq.(8.12).

In Figure 8.1 the velocity deficit in the wake immersed in the SBL and RBL is shown in self similar form (a),(c) when normalised by the local velocity $\bar{u}_{bl}(z)$ and (b),(d) when normalised by the velocity at hub height $\bar{u}_{bl}(z_h)$. To obtain the self similar representation the profiles are normalised by the x -dependent maximum velocity deficit at the respective downstream position $\Delta u_M(x) = \max(\Delta u(x))$, and the lateral and vertical coordinate are shown in the non-dimensional form $\eta_y = (y - y_C)/\sigma_y$ and $\eta_z = (z - z_h)/\sigma_z$. As discussed in Section 5.2.2, it is presumed that the vertical displacement of the centreline position observed in Figure 5.13(d) is rather biased by an additional momentum deficit below hub height than a real shift of the wake center. Therefore, in the analysis here the vertical direction the wake center is set equal to the hub height for all axial positions. For both definitions of the normalised velocity deficit self similarity can be observed for heights $\eta_z > 0$.

In case of the RBL the normalized profiles are incomplete for heights $\eta_z < 0$ and do no longer collapse onto a single curve. This behaviour is considered to stem from the high mean velocity shear, which in this case is dominant enough to disturb the axial symmetry of the wake as well as the wake growth, see Section 5.2.2. As a result, the concept of decomposition of the flow in a boundary layer and a wake does no longer seem to be

appropriate in this region.

Within the SBL, in the near wake region $x/R = 2$ the velocity deficit appears to be almost axisymmetric when normalised by the local velocity $\bar{u}_{bl}(z)$, whereas it appears to be slightly skewed when normalised by the velocity at hub height $\bar{u}_{bl}(z_h)$, compare Figure 8.1(a) and (b), which supports the theoretical discussion mentioned above. In the far wake region the results for the different normalisations deviate only significantly within the RBL for heights $\eta_z < 0$ where the concept of flow decomposition is in question.

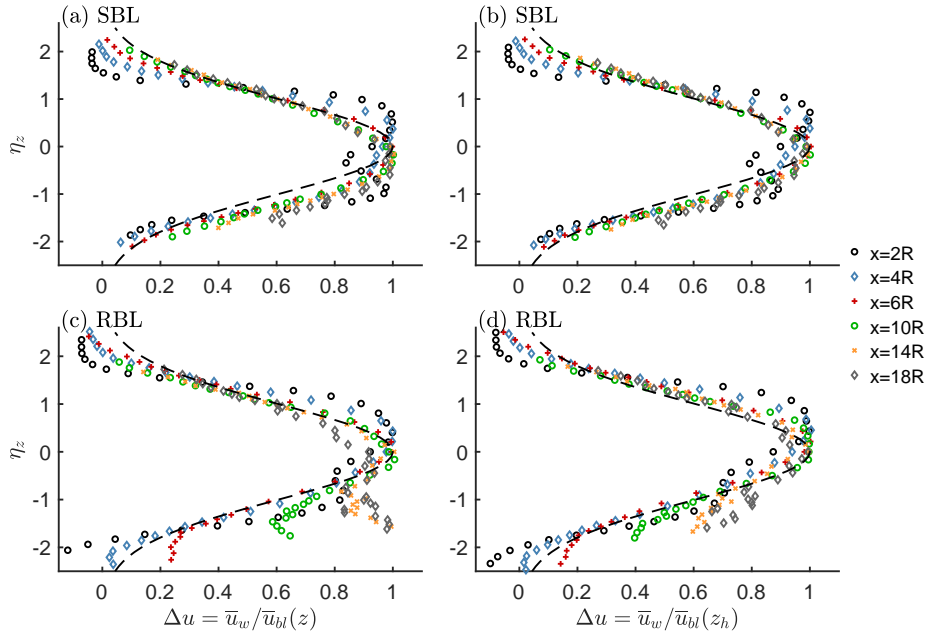


Figure 8.1: Vertical profiles of the normalised velocity deficit $\Delta u/\Delta u_M$ versus η_z in the wake of the model wind turbine immersed in the SBL/RBL using the definition (a)/(c) $\Delta u = \bar{u}_w/\bar{u}_{bl}(z)$ and (b)/(d) $\Delta u = \bar{u}_w/\bar{u}_{bl}(z_h)$, where $\bar{u}_w = \bar{u}_{bl}(z) - \bar{u}$. The black dashed line denotes a Gaussian shape function $e^{-0.5\eta_z^2}$. The legend indicates the downstream position.

However, the velocity distribution in the far wake in the vertical direction is mainly associated with the distribution of the Reynolds shear stress $\overline{u'w'}$ and subtle differences in the velocity distribution appear more pronounced. Therefore, Figure 8.2 shows the added Reynolds shear stress $\Delta\overline{u'w'}$ in self similar form (a),(c) when normalised by the local velocity $\bar{u}_{bl}(z)$ and (b),(d) when normalised by the velocity at hub height $\bar{u}_{bl}(z_h)$. As already observed for the velocity deficit, the vertical mean wind shear also prevents the vertical profiles of the added Reynolds shear stress to collapse in the region below the hub. Therefore, the profiles are normalised by the maximum value of the added shear stress which occurs above the hub height $\Delta\overline{u'u'_r}_M = \max(|\Delta\overline{u'u'_r}|(z > z_{hub}))$ as only here self similarity can be expected. In the region above the hub and for downstream distances $x/R \geq 10$, the profiles nearly collapse to the same distribution as observed in the horizontal plane, independent from the choice of normalisation. Below the hub height the profiles, however, differ significantly, especially in the case of the RBL.

For the discussion on the choice of normalisation it is interesting to notice that within the SBL for heights $\eta_z < 0$ the profiles approximately converge towards the self similar shape function when normalised by the local velocity $\bar{u}_{bl}(z)$, whereas the profiles reach lower values when normalised by the velocity at hub height $\bar{u}_{bl}(z_h)$. Even though the profiles

are skewed within the RBL, a similar trend can be observed.

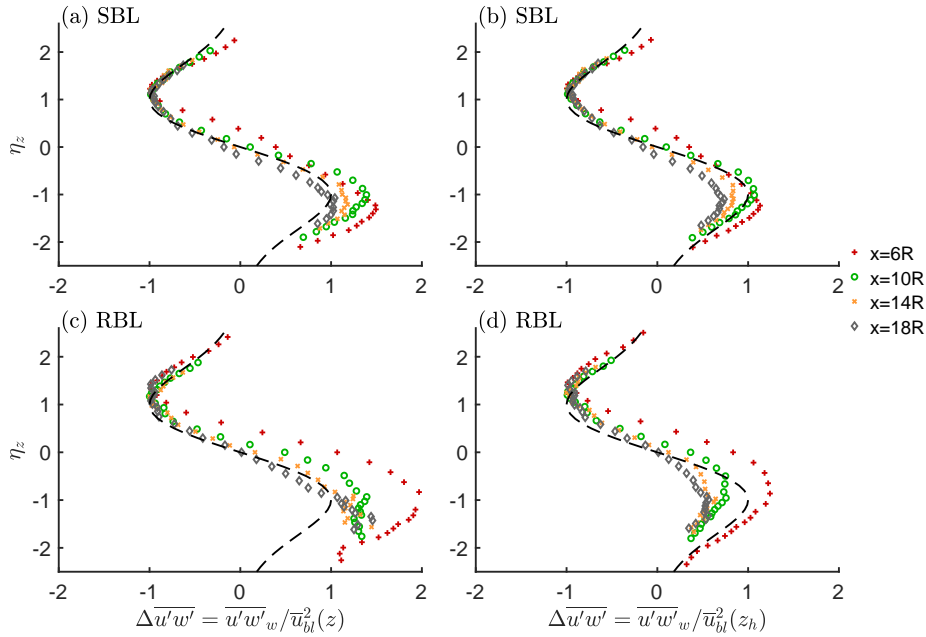


Figure 8.2: Vertical profiles of the added Reynolds shear stress $\Delta \overline{u'w'}$ versus η_z in the wake of the model wind turbine immersed in the SBL/RBL using the definition (a)/(c) $\Delta \overline{u'w'} = \overline{u'w'_w} / \overline{u_{bl}^2}(z)$ and (b)/(d) $\Delta \overline{u'w'} = \overline{u'w'_w} / \overline{u_{bl}^2}(z_h)$, where $\overline{u'w'_w} = \overline{u'w'_{bl}}(z) - \overline{u'w'}$. The black dashed line denotes the shape function $-\eta_z e^{-0.5(\eta_z^2-1)}$. The legend indicates the downstream position.

For the self similar representation of the velocity deficit and the added Reynolds stresses the centreline velocity deficit and the wake width need to be computed, which are also affected by the choice of normalisation. The same holds for the centreline position, even though the vertical centerline was assumed to be at hub height for all downstream positions. Therefore, Figure 8.3 shows (a) the centreline velocity deficit $\Delta u_C(x)$, (b) the vertical wake width $\sigma_z(x)$, and (c) the vertical centreline position $z_C(x)$ as function of the axial position of the wake immersed in the SBL and RBL for both types of normalisation. It can be observed that for the centreline velocity deficit and the vertical wake width the choice of normalisation appears to cause an almost constant offset in the values, which increases with surface roughness. For the vertical centreline position, see Figure 8.3(c), a similar trend can be observed, however, with an increasing offset with downstream distance. Even more interesting is that within the RBL the vertical centreline position in the near wake $x/R \leq 6$ exhibits an offset of about 10% of the rotor radius above the hub height when the velocity deficit is normalised with the velocity at hub height $\overline{u_{bl}}(z_h)$. The centreline position is calculated on the basis of the momentum deficit, see Eq.(2.56). Due to the vertical wind shear the velocity deficit is larger above the hub height than below, and therefore the momentum deficit centre is, physically speaking, above the hub. However, when the velocity deficit is normalised with the local velocity of the incoming boundary layer $\overline{u_{bl}}(z)$, the vertical wind shear is considered in the calculation and more weight is given to the momentum deficit below the hub. As a result, even within the highly sheared RBL configuration, the vertical centreline position in the near wake is close to the hub height as it is characteristic for an axisymmetric wake.

In conclusion, the above mentioned results support the view that the in vertical direc-

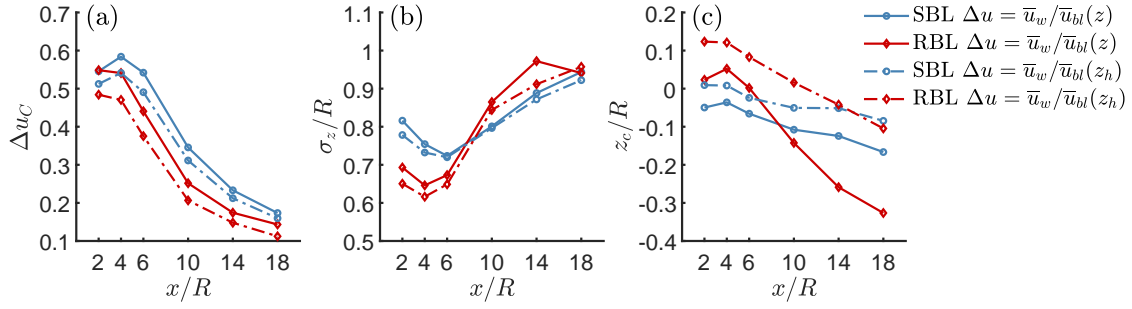


Figure 8.3: Wake characteristics of the model wind turbine immersed in the SBL and RBL using different definitions of the normalised velocity deficit: (a) centreline velocity deficit Δu_C , (b) vertical wake width σ_z , and (c) vertical centreline position z_c . The *legend* indicates the boundary layer configuration and applied definition.

tion asymmetric velocity deficit of wakes immersed in turbulent boundary layers can be transformed into an approximately axisymmetric representation when normalised by the local velocity of the boundary layer. Therefore, this type of normalisation should be preferred for the self similarity analysis of wind turbine wakes.

Having discussed the degree of self similarity for vertical profiles of the velocity deficit and the added Reynolds shear stress in the wake, the following discussion will concentrate on the self similarity within the mid-horizontal plane. The analysis will be carried out for both boundary layer configurations as well as for yawed conditions. As starting point of this discussion, profiles of the velocity deficit in the mid-horizontal plane are shown in Figure 8.4 in self similar representation, (a)–(c) for the SBL and (d)–(f) for the RBL.

For a sufficient axial distance from the rotor, all lateral profiles nearly collapse to a Gaussian like distribution (shown as *black dashed line*) and therefore become self similar. Within

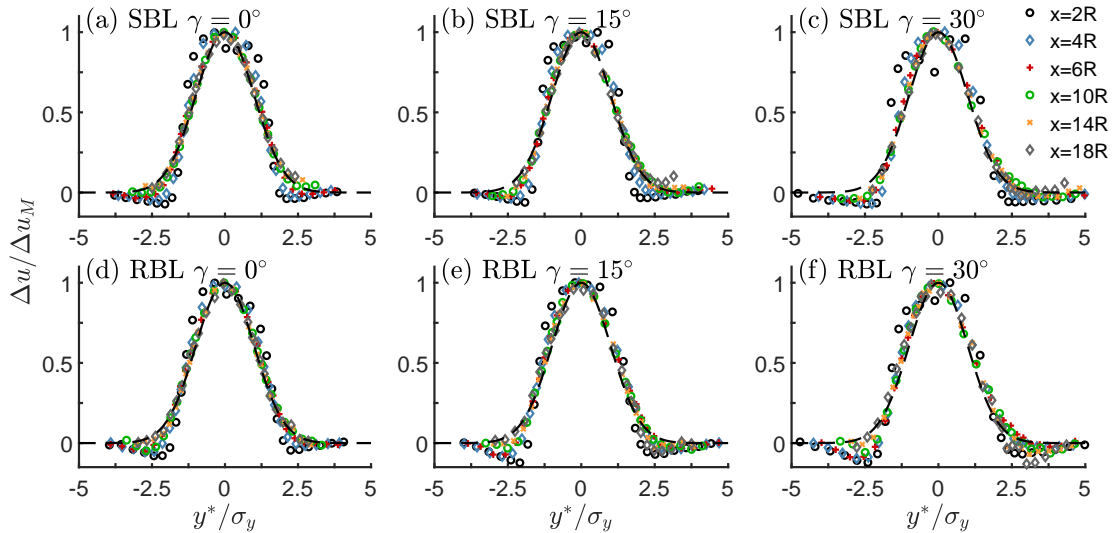


Figure 8.4: Lateral profiles of the normalised velocity deficit $\Delta u / \Delta u_M$ versus η_y in the wake of the model wind turbine immersed in the SBL with (a) $\gamma = 0^\circ$, (b) $\gamma = 15^\circ$, (c) $\gamma = 30^\circ$ and in the RBL with (d) $\gamma = 0^\circ$, (e) $\gamma = 15^\circ$, (f) $\gamma = 30^\circ$. The *black dashed line* denotes a Gaussian distribution $e^{-0.5\eta_y^2}$. The *legend* indicates the downstream position.

both boundary layers this state is reached within a distance of $x/R = 6$ which in the following is considered to be the onset of the far wake.

In both boundary layers the profiles become slightly skewed with increasing yaw angle. Anyway, for the lateral profiles the degree of self similarity can be considered as high across all measured yaw angles and boundary layer conditions.

Having shown the self similarity of the axial mean velocity component in the wake of the model wind turbine for various yaw angles and boundary layer conditions, one is tempted to determine the underlying scaling law for the centreline velocity deficit Δu_C and the vertical and lateral half width σ_z and σ_y by fitting Equations (8.6) and (8.7) to the measurement data. However, Obligado et al. [109] showed that optimal coefficients A , B and virtual origins x_{0u} , $x_{0\sigma}$ can be found that give a reasonable fit to the measurement data within a certain range of values for the exponents n_u , n_σ . They therefore concluded that it is impossible to discriminate between equilibrium and non-equilibrium scaling by only fitting the centreline velocity deficit and wake width data. To probe this statement, a simple linear regression regarding the scaling laws discussed in Section 8.1.1 is performed which results in a similar finding. As the wake growth is significantly different within the near wake $x/R < 6$, and in case of the RBL configuration also for $x/R \geq 14$, these data points are not used in the fitting procedure. Figure 8.5 shows the resulting fits in a linear representation, where in (a)–(c) the lateral wake widths and (d)–(f) the centreline velocity deficits are shown. In this representation the resulting fits to different scaling laws are almost indistinguishable by eye, just the fit to the equilibrium scaling law of the velocity deficit in Figure (d) does not cope with the measurements. Thus, in order to arrive at a distinct conclusion on the appropriate scaling law, it is highly desirable to get an independent assessment by analysing the evolution of the added Reynolds shear stress and the added turbulent kinetic energy.

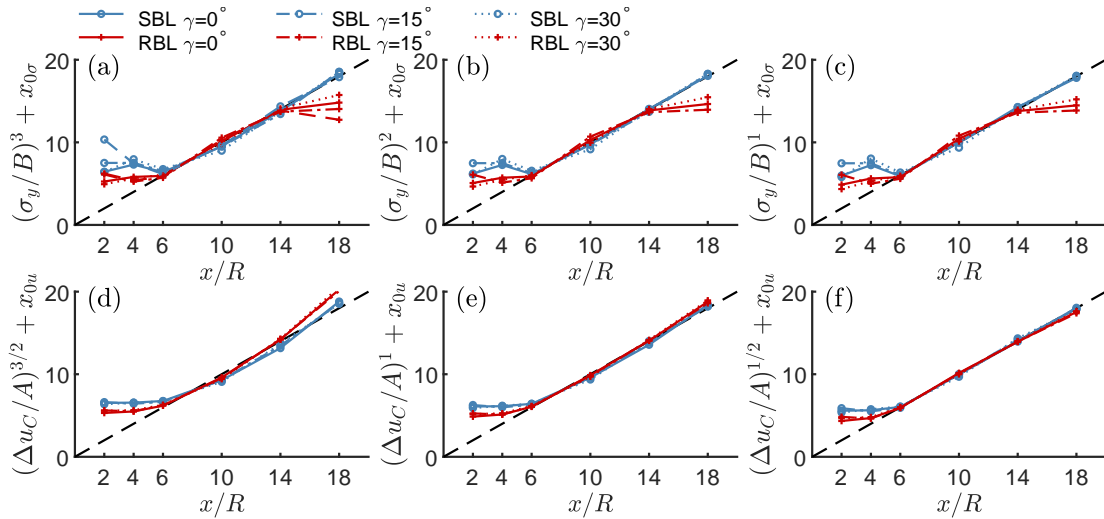


Figure 8.5: Normalised lateral wake width σ_y and normalised centreline velocity deficit Δu_C as function of x/R for (a)/(d) the equilibrium scaling $\Delta u_C^{3/2}$, $\sigma_y^3 \propto x$; for (b)/(e) the square-root wake growth scaling Δu_C , $\sigma_y^2 \propto x$; for (c)/(f) the linear wake growth scaling $\Delta u_C^{1/2}$, $\sigma_y \propto x$. Fits include the range $6 \leq x/R \leq 18$ for SBL and $6 \leq x/R \leq 14$ for RBL. The legend indicates the flow conditions.

As the equilibrium and non-equilibrium scaling laws only predict the self similarity of the Reynolds shear stress and the turbulent kinetic energy, and not of their added equivalent,

the self similarity of these quantities has first to be established. This can be tested by normalising the profiles by the x -dependent profile's maximum as done above for the velocity deficit. For the added Reynolds shear stress in the vertical direction this was shown in Figure 8.2 and discussed above with the result that for heights below the hub no self similarity can be observed. For the added Reynolds shear stress in lateral direction $\overline{\Delta u'v'}$ profiles in self similar representation are shown in Figure 8.6(a)–(c) for the SBL and Figure 8.6(d)–(f) for the RBL. The streamwise evolution of the respective maximum values $\overline{\Delta u'v'}_M(x) = \max(|\overline{\Delta u'v'}(x)|)$ is shown in Figure 8.9(a). It can be seen that all profiles nearly collapse to a single curve, even at high yaw angles. Only in case of the RBL with the wind turbine operating at a yaw angle of $\gamma = 30^\circ$ more significant deviations can be observed. The self similar profiles approximately follow a distribution of $-\eta e^{-0.5(\eta^2-1)}$ shown in the Figures as black dashed line.

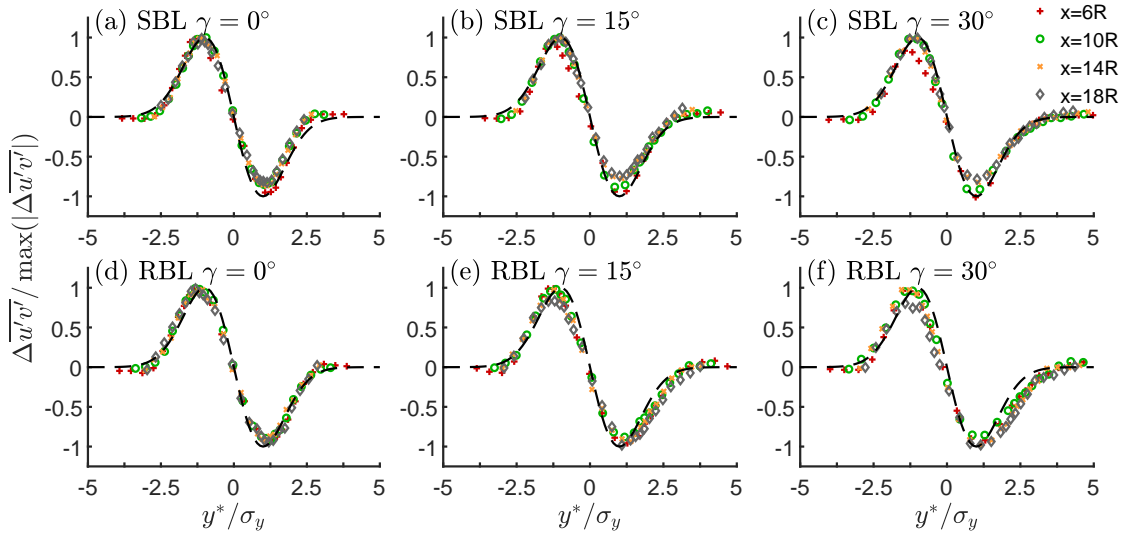


Figure 8.6: Lateral profiles of the normalised added Reynolds shear stress $\overline{\Delta u'v'} / \overline{\Delta u'v'}_M$ versus η_y in the wake of the model wind turbine immersed in the SBL with (a) $\gamma = 0^\circ$, (b) $\gamma = 15^\circ$, (c) $\gamma = 30^\circ$ and in the RBL with (d) $\gamma = 0^\circ$, (e) $\gamma = 15^\circ$, (f) $\gamma = 30^\circ$. The black dashed line denotes the shape function $-\eta_z e^{-0.5(\eta_z^2-1)}$. The legend indicates the downstream position.

Figure 8.7 shows the vertical and horizontal profiles of the added turbulent kinetic energy in self similar form. The respective maximum values ΔK_M , used for normalising the profiles, are given in Figure 8.9(e). For the vertical profiles of the added turbulent kinetic energy, shown in Figure 8.7(a),(e), self similarity can just be observed in the region above the hub and for downstream distances $x/R \geq 10$. In the horizontal plane, however, other than in the case of the added shear stress, the degree of self similarity differs significantly between both boundary layers, as can be seen in Figure 8.7(b)–(d) for the SBL and in Figure 8.7(f)–(h) for the RBL. In case of the SBL, the profiles become self similar for downstream distances $x/R \geq 10$ whereby they also become slightly skewed with increasing yaw angle. For the cases within the RBL, however, the profiles just exhibit a low degree of self similarity, especially for yawed conditions. In these cases, the side of the profiles toward which the wake is deflected ($\eta_y < 0$) does not collapse onto a single curve whereas the opposite side does. It is important to note that neither the equilibrium nor the non-equilibrium theory explicitly predicts the self similarity of the diagonal components of the added Reynolds stress tensor. However, motivated by the observed self similarity of the added turbulent kinetic energy in case of the SBL flow, these quantities

are also shown in self similar form for this flow condition in Figure 8.8. It can be observed that all three quantities exhibit a similar degree of self similarity as the added turbulent kinetic energy does. Additionally, the Gaussian distributions, shown as *black dashed lines*, are obtained by a least square curve fit to the added Reynolds stresses measured in the horizontal plane for a yaw angle of $\gamma = 0^\circ$. With that it becomes clear that with increasing yaw angle the profiles of the added Reynolds stresses $\overline{u'u'}$ and $\overline{w'w'}$ become asymmetric regarding the wake centreline while the component in the lateral direction $\overline{v'v'}$ stays almost symmetric. Despite the increasing asymmetry all profiles maintain their degree of self similarity.

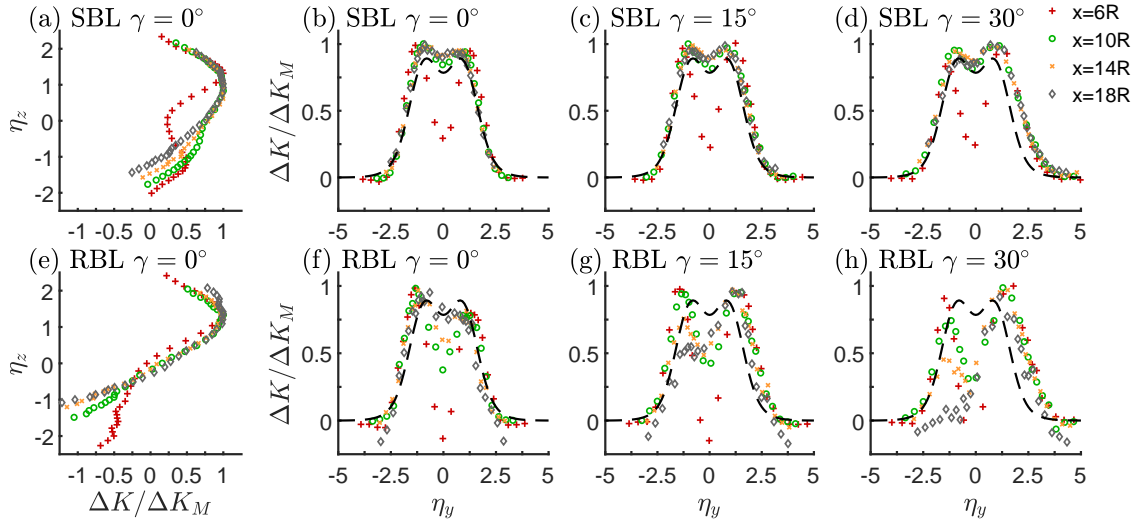


Figure 8.7: Vertical and lateral profiles of the normalised added turbulent kinetic energy $\Delta K/\Delta K_M$ versus η_z and η_y in the wake of the model wind turbine immersed in the SBL with (a)/(b) $\gamma = 0^\circ$, (c) $\gamma = 15^\circ$, (d) $\gamma = 30^\circ$ and in the RBL with (e)/(f) $\gamma = 0^\circ$, (g) $\gamma = 15^\circ$, (h) $\gamma = 30^\circ$. *Black dashed line* denotes the self similar shape function. The *legend* indicates the downstream position.

Having confirmed the existence of self similarity for the added components $\Delta\overline{u'u'_r}$ and $\Delta\overline{u'_i u'_i}$ of the Reynolds stress tensor and the added turbulent kinetic energy ΔK , the x -dependency of the underlying scaling of these quantities can now be analysed in detail. Therefore, Figure 8.9(b)–(d) assesses the validity of the three scalings stated in Equation (8.13) for the added Reynolds shear stress and Figure 8.9(f)–(h) for the added turbulent kinetic energy. Whereas in (b)/(f) the equilibrium scaling law is used, in (c)/(g) the square-root wake growth scaling law and in (d)/(h) the linear wake growth scaling law is applied. For the sake of clarity, the ratios are additionally normalised by their respective value at $x/R = 6$, as this location is considered as the onset of the far wake. In this representation it becomes clear that neither the equilibrium nor the square-root wake growth scaling law reproduces the x -dependence of the added Reynolds shear stress and the added turbulent kinetic energy in the wake of the model wind turbine correctly. However, the linear wake growth scaling normalises both quantities to an approximately constant value which suggests a scaling of $\Delta\overline{u'u'_r}_M, \Delta K_M \propto \Delta u_C \propto x^{-2}$. An important consequence from these findings is that only a member of the non-equilibrium scaling laws, namely the linear wake growth scaling, can form a base for a *consistent scaling of all fundamental* wind turbine wake parameters, including the velocity deficit, wake width, and maxima for all components of the Reynolds stress tensor. This finding is one of the main results of the present study and might be helpful in assessing the predictive

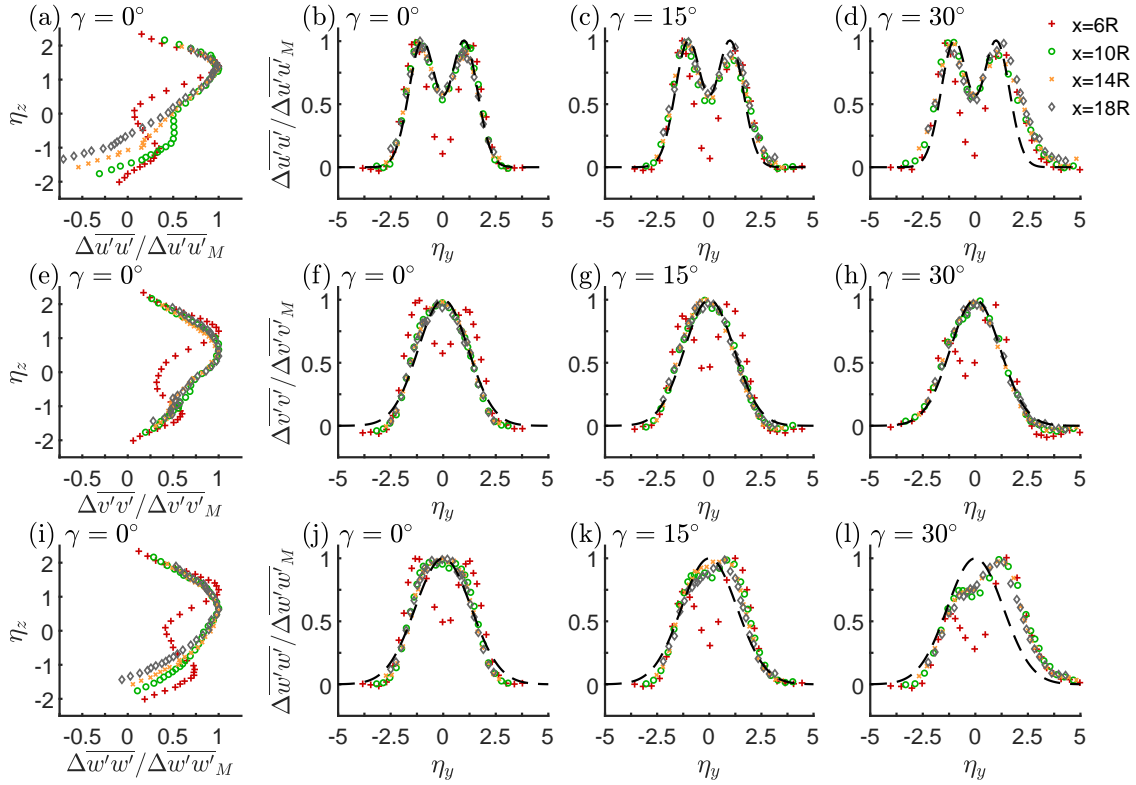


Figure 8.8: Vertical and lateral profiles of the normalised diagonal components of the added Reynolds stress tensor $\Delta u'_i u'_i / \Delta u'_i u'_{iM}$ versus η_z and η_y in the wake of the model wind turbine immersed in the SBL. Black dashed line denotes the distributions (b)–(d) $f_1 = e^{-1.25(\eta_y^2-1)} + e^{-1.25(\eta_y^2+1)}$, (f)–(h) $f_2 = e^{-0.35\eta_y^2}$ and (j)–(l) $f_3 = e^{-0.28\eta_y^2}$. The legend indicates the downstream position.

capability of wake models as done in [136].

Due to the high degree of self similarity observed also for the added Reynolds stresses $\Delta u'_i u'_i$, naturally the question arises how these quantities scale in the axial direction. As mentioned in Section 8.1.2, Dairay et al. [35] argue that non-equilibrium flows in which $n \neq 1$ should only be possible under the assumption of a constant anisotropy on the surface $\eta = 1$. For that reason the ratio $(\Delta u'_i u'_i / \Delta K)(\eta = 1)$ is shown in Figure 8.10(a)–(c) along the line $\eta_z = 1$ and in (e)–(g) along the line $\eta_y = 1$. On the line $\eta_z = 1$ the ratio $(\Delta u'_i u'_i / \Delta K)(\eta_z = 1)$ is almost equal for both boundary layers and converges clearly to constant values as it is postulated by Dairay. However, on the line $\eta_y = 1$ the ratio differs for both boundary layers. Nevertheless, for the SBL the ratio also clearly converges towards values which just vary by about 5% from the values at $\eta_z = 1$ and are similar even at large yaw angles. Within the RBL the ratios differ by about 30% from their counterpart within the SBL. Also for yawed conditions the curves deviate more, yet without any clear trend. These deviations can be explained by the lower degree of self similarity of the added turbulent kinetic energy in case of the RBL, which for increasing yaw angles is subsequently perturbed, see Figure 8.7.

Nevertheless, the significant differences between both boundary layers for the ratio $\Delta K(\eta_y = 1) / \Delta u_C$, shown in Figure 8.10(h), are not likely to result from a deviation of the self similarity as they just exhibit a slight dependency on the yaw angle. The difference is rather assumed to result from the different level of background turbulence. This is also

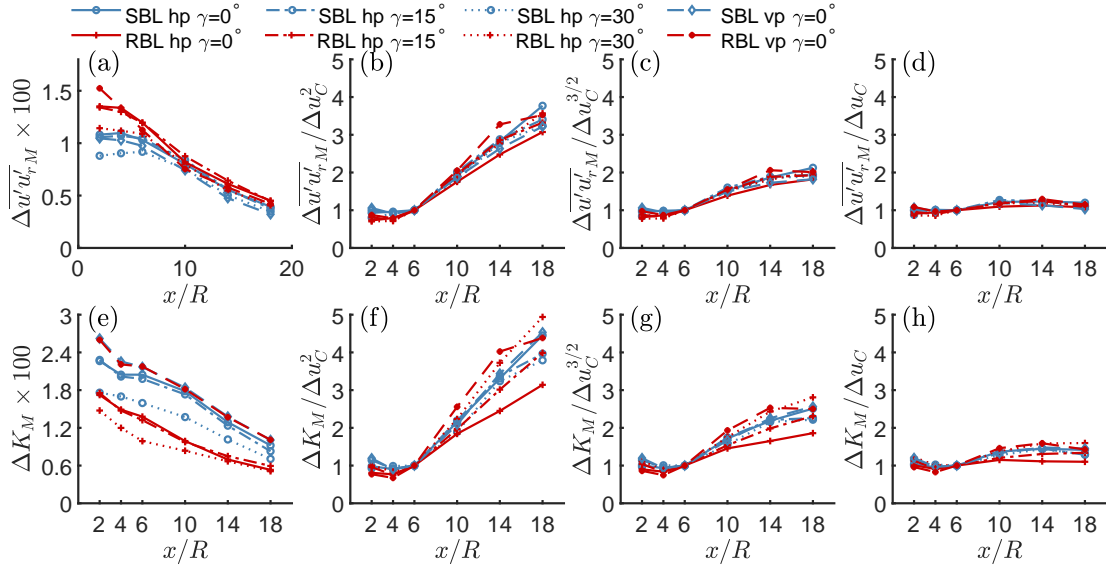


Figure 8.9: (a) Maximum added Reynolds shear stress $\Delta \overline{u'u'_r}_M$ and (e) maximum added turbulent kinetic energy ΔK_M in the wake of the model wind turbine, measured in the horizontal (hp) and vertical plane (vp), normalised using (b)/(f) equilibrium scaling $\Delta u_C^{3/2} \propto x$, (c)/(g) square-root wake growth scaling $\Delta u_C \propto x$, (d)/(h) linear wake growth scaling $\Delta u_C^{1/2} \propto x$. The legend indicates the flow and yaw conditions.

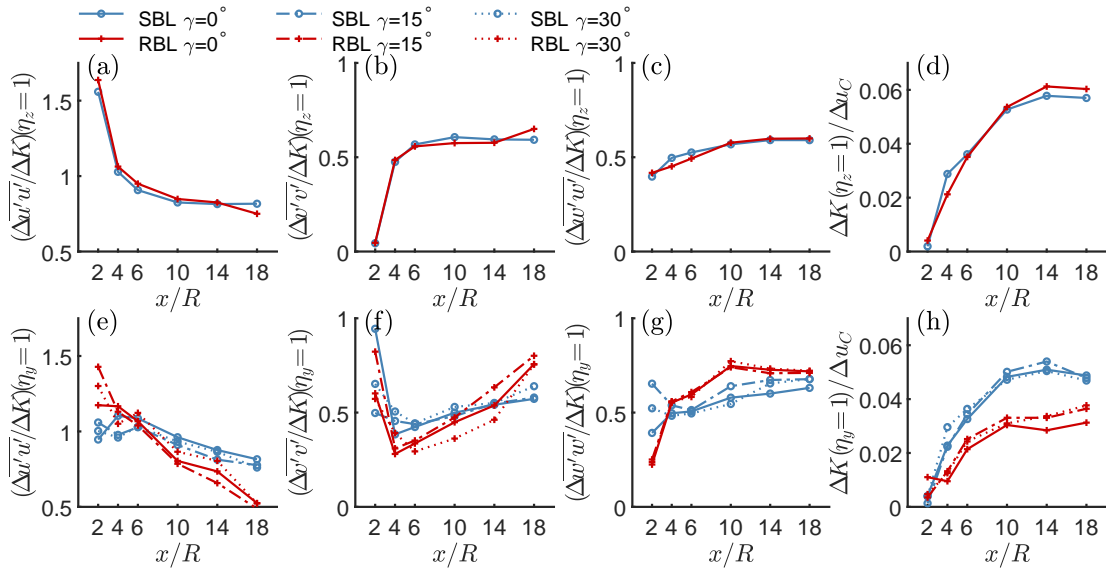


Figure 8.10: Structural parameters $(\Delta u'_i u'_i / \Delta K)(\eta = 1)$ and $\Delta K(\eta = 1) / \Delta u_C$ in the wake of the model wind turbine for (a)–(d) $\eta_z = 1$ and (e)–(h) $\eta_y = 1$. The legend gives flow and yaw conditions.

consistent with the almost similar ratios $\Delta K(\eta_z = 1) / \Delta u_C$, shown in Figure (d), since the difference in background turbulence at this height vanishes.

In the introduction of this work, see Section 1.2, the variety of scaling exponents found in literature for the added turbulence intensity I_+ was addressed. By fitting measurement data and numerical results scalings from $I_+ \propto x^{-0.32}$ to $I_+ \propto x^{-1}$ have been reported, see e.g. [34, 115, 48]. Also dependencies on the surface roughness have been observed but

with contradictory trends [28, 5]. The quite different exponents in these empirical formulas illustrate the difficulty in obtaining a distinct set of optimal parameters in a curve fit with multiple unknowns. As it was shown that the *linear wake growth scaling* correctly predicts a scaling of $\Delta K_M \propto \Delta u_C \propto x^{-2}$, the observation of (i) self similarity of the diagonal components of the added Reynolds stress tensor and (ii) an approximately constant anisotropy consequently suggests a physically motivated scaling of $I_+ = \sqrt{\Delta \overline{u'v'}} \propto x^{-1}$.

8.2.2 Self Similarity in the Large Eddy Simulation Results

The starting point of this analysis is Figure 8.11 which shows profiles in self similar representation of (a)-(c) the velocity deficit Δu , (d)-(f) the added Reynolds shear stress $\Delta \overline{u'v'}$, and (g)-(i) the added turbulent kinetic energy ΔK in the mid-vertical plane of the unyawed model wind turbine immersed in the boundary layer configurations sF014, sF016 and sF032, respectively. All profiles are normalised by their respective maximum value above hub height, hence $\Delta \phi_M = \max(|\Delta \phi(z > z_h)|)$. As it is presumed that for unyawed conditions the vertical displacement of the wake is biased by an additional momentum deficit, the wake center is set equal to the hub height z_h for all axial positions, as it was done in the analysis of the wind tunnel measurements in Section 8.2. Therefore, for unyawed conditions the vertical coordinate in non-dimensional form is defined as $\eta_z = (z - z_h)/\sigma_z$. As can be seen, all flow quantities only exhibit a significant degree of self similarity in the region above hub height for all boundary layer configurations. Below hub height, only in case of the sF014 boundary layer configuration a considerable degree of self similarity can be observed for the velocity deficit and the Reynolds shear stress. With increasing roughness length any self similarity in this region is rapidly lost. A similar behaviour is observed in the analysis of the experimental results presented in the section above, which confirms the statement that the concept of decomposition of the flow in a boundary layer and a wake is not accurate in the lower region of the wake.

As the degree of self similarity in the vertical plane is low even for unyawed conditions, results in this plane for the yawed cases are not further considered. Therefore, the following discussion focuses on profiles obtained in the horizontal plane for all considered boundary layer configurations and yaw angles. As before the self similar representation of the velocity deficit Δu , the added Reynolds shear stress $\Delta \overline{u'v'}$ and the added turbulent kinetic energy ΔK are analysed. As discussed in Section 7.5 the vertical displacement needs to be taken into consideration in yawed conditions. Hence, in the following discussion the lateral profiles of the yawed wake are evaluated in the horizontal plane of the wake center at the height $z = z_C(x)$, whereas in unyawed conditions these are evaluated at hub height $z = z_h$ (even though a bias of the centreline can be present).

In Figure 8.12 lateral profiles of the velocity deficit in self similar representation are shown. For a sufficient axial distance from the rotor all lateral profiles of the velocity deficit nearly collapse to a Gaussian shape (shown as *black dashed line*) and therefore become self similar. This holds for all yaw angles and boundary layer configurations. For the sF016 and the sF032 configuration the self similar state is reached within a distance of $x/R = 6$, which is similar to the findings in the experimental results. Due to the lower background turbulence in the sF014 configuration the self similar state in this case is reached further downstream at a distance of $x/R = 8$.

Figure 8.13 shows the lateral profiles of the added Reynolds shear stress $\Delta \overline{u'v'}$. As the velocity deficit the added Reynolds shear stress exhibits a high degree of self similarity for a sufficient axial distance from the rotor. However, it can be noticed that the state of self

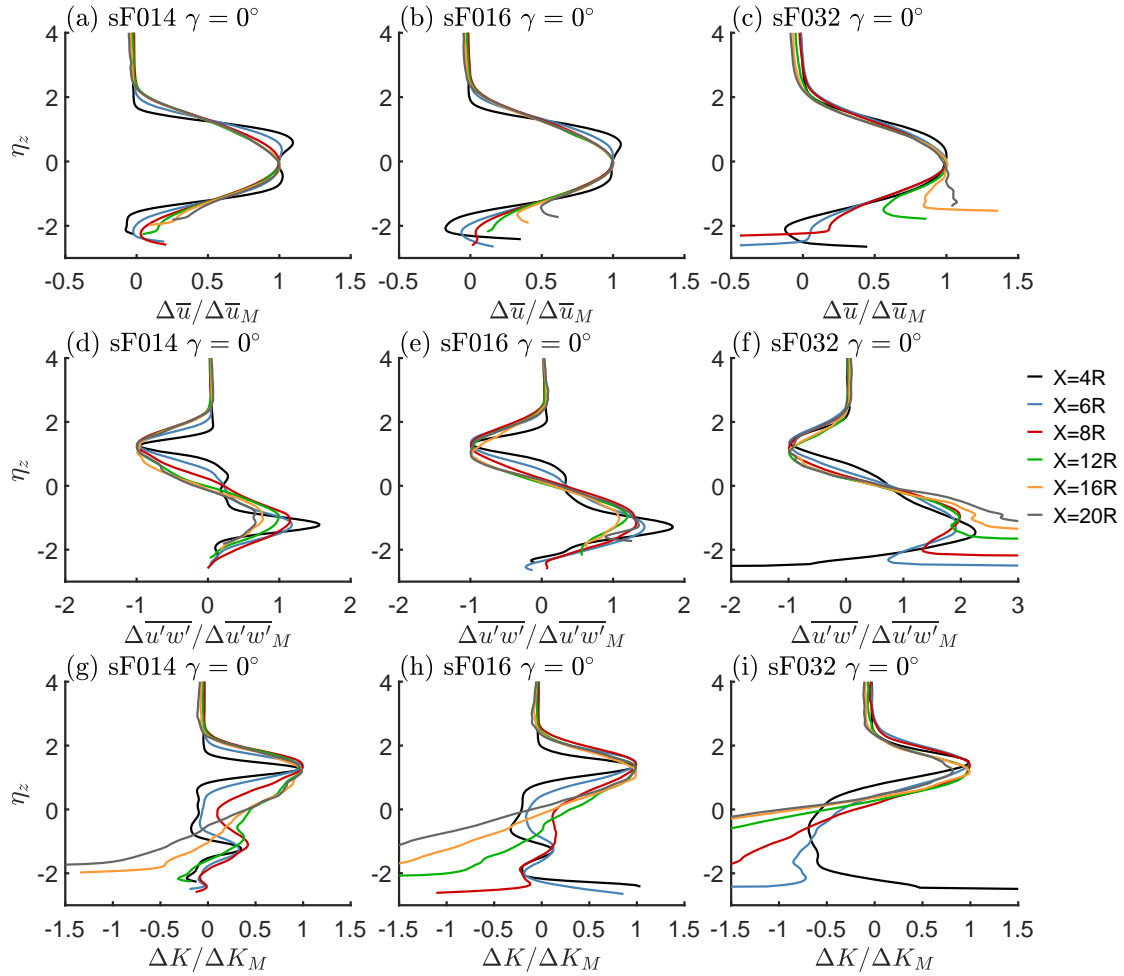


Figure 8.11: Vertical profiles of (a)-(c) the velocity deficit $\Delta u/\Delta u_M$, (d)-(f) the added Reynolds shear stress $\Delta u'w'/\Delta u'w'_M$ and (g)-(i) the added turbulent kinetic energy $\Delta K/\Delta K_M$ as function of η_y in the wake for the configurations sF014, sF016 and sF032, respectively. The legend indicates the downstream position.

similarity is reached about $2R$ further downstream for the added Reynolds shear stress than it is the case for the velocity deficit. As observed in the experimental results, the self similar distribution can approximately be described by the form function $-\eta e^{-0.5(\eta_y^2-1)}$.

Figure 8.14 shows that the lateral profiles of the added turbulent kinetic energy ΔK exhibit self similar behaviour as well, whereby the profiles become slightly skewed with increasing yaw angle and the degree of self similarity decreases with increasing roughness length. Especially in case of the sF032 configuration self similarity is significantly disturbed. This confirms the experimental findings, discussed in Section 8.2.1, and the theoretical discussion about the validity of the concept of decomposition of the flow in a boundary layer and a wake, see Section 2.3.1. Therefore, the sF032 configuration is not further considered in the following discussion on the axial scaling and the anisotropy of turbulence in the wake. For the sF014 and sF016 configurations the state of self similarity is reached at similar distance or slightly further downstream as in case of the added Reynolds shear stress, shown in Figure 8.13. A comparison with the experimental results within the SBL configuration at a downstream distance of $x/R = 18$ shows that the self similar shape function of the added turbulent kinetic energy is well predicted by

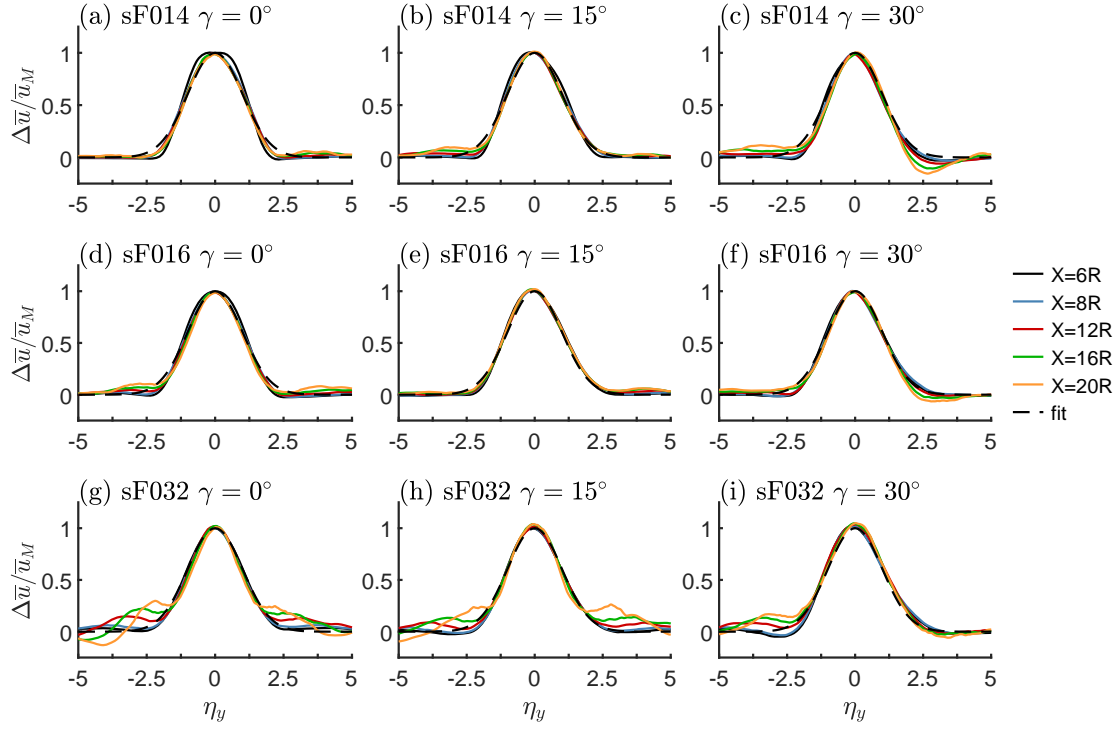


Figure 8.12: Lateral profiles of the velocity deficit $\Delta\bar{u}/\Delta u_M$ as function of η_y in the wake for the configurations sF014 (a)-(c), sF016 (d)-(f) and sF032 (g)-(i) for $\gamma = 0^\circ, 15^\circ, 30^\circ$. The black dashed line denotes the Gaussian form function $\exp[-0.5\eta_y^2]$. The legend indicates the downstream position.

the simulation, even for large yaw angles. Only in the inner part of the wake the LES underestimates the added turbulent kinetic energy.

In Section 8.2.1 the self similarity of the diagonal components of the added Reynolds stress tensor $\Delta\bar{u}'_i u'_i$ is shown and discussed for the experimental results. Since the LES results presented here closely follows the experimental setup, similar results can be expected. However, pointing out the differences in the experimental and numerical results is helpful to evaluate the computational method. For this reason the diagonal components of the added Reynolds stress tensor $\Delta\bar{u}'_i u'_i$ in case of the sF014 configuration are shown in self similar form in Figure 8.15. As in this boundary layer configuration the highest degree of self similarity is observed, these results serve best for a comparison with the experimental results. For this reason results within the SBL configuration at a downstream distance of $x/R = 18$ are shown additionally.

First of all, the results are quite similar regarding their distribution in the self similar form. For large yaw angles experimental and numerical results even exhibit a similar asymmetry for the components $\Delta\bar{u}'u'$ and $\Delta\bar{w}'w'$, whereas the component $\Delta\bar{v}'v'$ maintains almost symmetric. Nevertheless, some differences can still be observed. The shape function f_3 which best describes the self similar distribution of the component $\Delta\bar{w}'w'$ in unyawed conditions is different for the experimental and numerical results. In the LES results presented here the distribution develops slowly from an approximate double into a single Gaussian function, resulting in a wide plateau in the proximity of the centre line which is still well approximated by a double Gaussian function even at a distance of $x/R = 20$ (not shown here, this also holds for the results in the sF016 configuration).

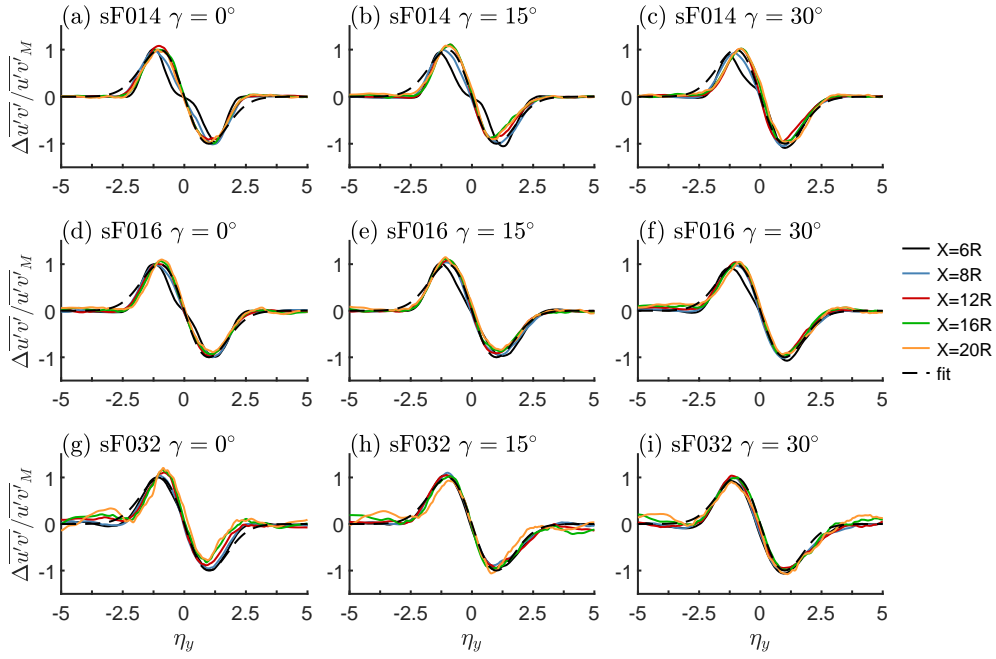


Figure 8.13: Lateral profiles of the added Reynolds shear stress $\overline{\Delta u'v'}/\overline{\Delta u'v'_M}$ as function of η_y in the wake for the configurations sF014 (a)-(c), sF016 (d)-(f) and sF032 (g)-(i) for $\gamma = 0^\circ, 15^\circ, 30^\circ$. The black dashed line denotes the form function $-\eta \exp[-\frac{1}{2}(\eta_y^2 - 1)]$. The legend indicates the downstream position.

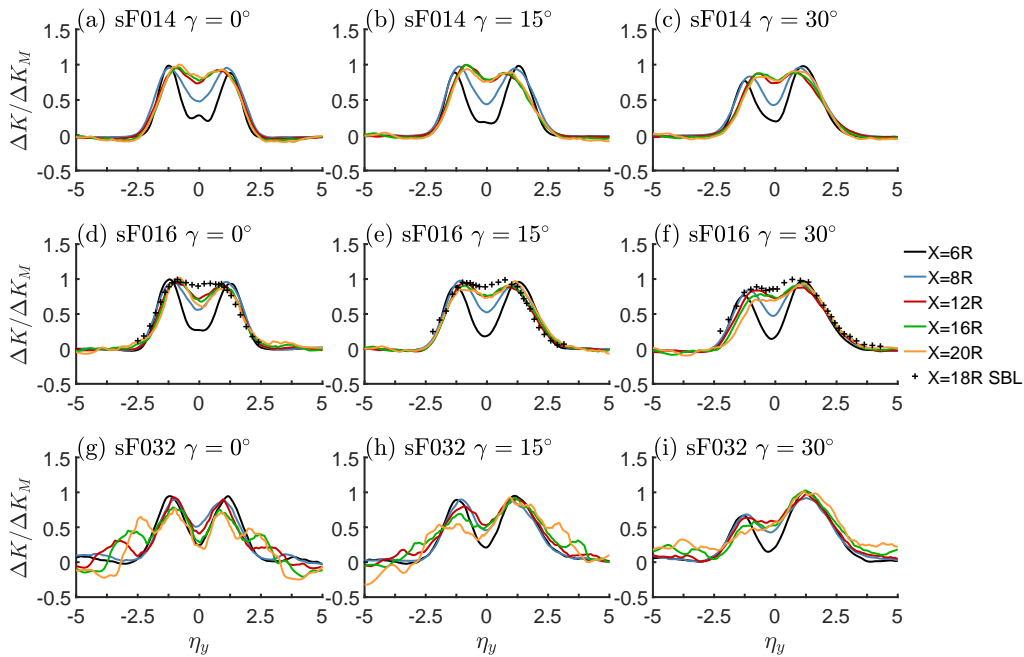


Figure 8.14: Lateral profiles of the added turbulent kinetic energy $\Delta K/\Delta K_M$ as function of η_y in the wake for the configurations sF014 (a)-(c), sF016 (d)-(f) and sF032 (g)-(i) for $\gamma = 0^\circ, 15^\circ, 30^\circ$. The legend indicates the downstream position.

In the experimental results however this distribution rapidly undergoes a transition from an approximate double to a single Gaussian function which is completed shortly after the

onset of the far wake region $x/R > 10$, see Figure 8.8(j). Reason for this difference could be the absence of vortices shedding from the nacelle or from the blades in the simulation, of which the first is not modelled and the latter is not captured by the ALM.

However, it is interesting to notice that in yawed conditions the asymmetric distribution of the component $\Delta \overline{w'w'}$ observed in the experiment is well captured by the simulation, see Figure 8.15(i). It could be hypothesised that in yawed conditions, the effect of the rotor dominates the distribution of $\Delta \overline{w'w'}$. Assuming that the contribution of the single unyawed rotor is approximately a symmetric double Gaussian distribution even in the far wake, it is reasonable to conclude that this distribution is skewed for large yaw angles, resulting in an asymmetric double Gaussian distribution with peaks of different magnitude.

In Table 8.1 parameters $\alpha_{i,S/D}$ resulting from a least square fit to the self similarity shape functions of the added Reynolds stresses $\Delta \overline{u'_i u'_i} / \Delta \overline{u'_i u'_i}_M$ in the wake are shown for the boundary layer configurations sF014 and sF016. Thereby the subscripts S and D denote the corresponding shape function of a single and a double Gaussian distribution. For comparison the curve fit parameters which best describe the self similarity shape functions in the wake of the experimental configuration SBL are $\alpha_{1,D} = 1.25$, $\alpha_{2,S} = 0.35$, $\alpha_{3,S} = 0.28$.

Now the most important aspect of the similarity analysis of the wake evolution is addressed: Similar to the analysis of the experimental results the numerically obtained axial distri-

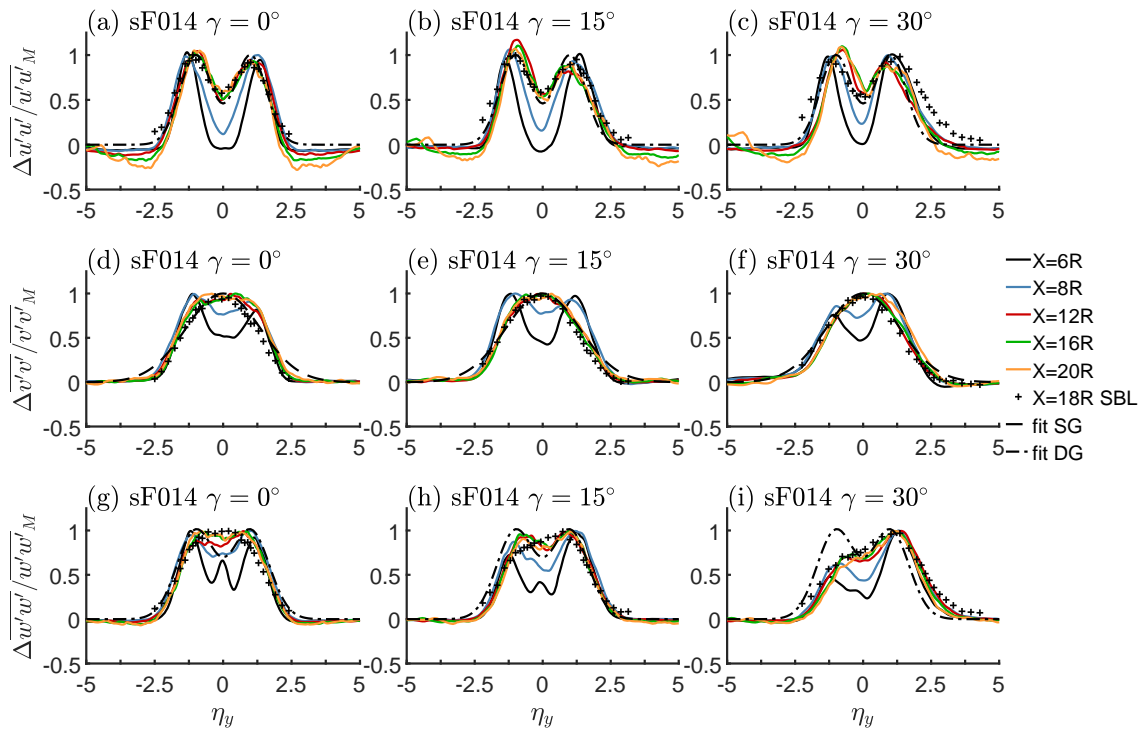


Figure 8.15: Lateral profiles of the added Reynolds stresses $\Delta \overline{u'_i u'_i} / \Delta \overline{u'_i u'_i}_M$ as function of η_y in the wake for the configurations sF014 for $\gamma = 0^\circ, 15^\circ, 30^\circ$, respectively. Dashed line denotes the distributions $f_{i,S} = e^{-\alpha_{i,S} \eta_y^2}$, dashed dotted line denotes $f_{i,D} = e^{-\alpha_{i,D}(\eta_y^2+1)} + e^{-\alpha_{i,D}(\eta_y^2-1)}$, parameters $\alpha_{i,S/D}$ are given in Table 8.1. The legend indicates the downstream position.

Table 8.1: Curve fit parameters to the self similarity shape functions of the added Reynolds stresses $\Delta \overline{u'_i u'_i} / \Delta \overline{u'_i u'_i}_M$ in two boundary layer configurations. The subscripts S and D denote the corresponding shape function of a single and a double Gaussian distribution.

γ	0°	15°	30°	γ	0°	15°	30°
$\alpha_{1,D}$	1.47	1.41	1.31	$\alpha_{1,D}$	1.86	1.38	1.27
$\alpha_{2,S}$	0.27	0.30	0.31	$\alpha_{2,S}$	0.26	0.23	0.27
$\alpha_{3,D}$	1.05	1.10	1.21	$\alpha_{3,D}$	1.03	0.96	1.21
$\alpha_{3,S}$	0.30	0.29	0.27	$\alpha_{3,S}$	0.29	0.23	0.25

(a) sF014

(b) sF016

butions of the maximum added Reynolds stress $\Delta \overline{u'_i u'_j}_M$ and turbulent kinetic energy ΔK_M are analysed regarding the underlying scaling law. Therefore, Figure 8.16 shows these distributions normalised by (a)/(d) the *equilibrium scaling*, (b)/(e) the *square-root wake growth scaling* law, and (c)/(f) the *linear wake growth scaling* law. For comparison, wind tunnel measurements of the unyawed wind turbine immersed in the SBL boundary layer configuration are included. When normalised by the correct scaling law, the distributions of $\Delta \overline{u'_i u'_j}_M$ and ΔK_M should maintain a roughly constant value. As in the experiment this behaviour can be observed in Figure 8.16(c) for the maximum added Reynolds shear stress $\Delta \overline{u'_i u'_j}_M$ normalised by the linear wake growth scaling law. Nevertheless, as the linear wake growth scaling is a member of the non-equilibrium scaling law, it requires the added turbulent kinetic energy to scale in the same way to meet the law (this holds also for equilibrium scaling law). This requirement, other than in the experiment, is not fulfilled by the numerical results as can be observed in Figure 8.16(f).

To quantify the scaling a least square fit of the simulation data to the functions $\Delta \overline{u'_i u'_j}_M = A \Delta u_C^{n_1}$ and $\Delta K_M = B \Delta u_C^{n_2}$ for the axial positions $x/R \geq 12$ results in the exponents n_1, n_2 given in Table 8.3 for the two boundary layer configurations sF014 and sF016. As the non-equilibrium dissipation theory provides a link between the axial scaling of the Reynolds shear stress and the turbulent kinetic energy, exponents n_σ of the wake growth scaling $\sigma \propto x^{n_\sigma}$ can also be determined from these results. Therefore, exponents $n_{1,2}$ close to 1 indicate that the corresponding scaling law is the *linear wake growth scaling* (with $n_\sigma = 1$), whereas exponents $n_{1,2}$ close to 1.5 indicate that the corresponding scaling law is the *square-root wake growth scaling* (with $n_\sigma = 0.5$), and exponents $n_{1,2}$ close to 2.0 indicate a scaling according to the *equilibrium scaling* law (with $n_\sigma = 0.33$). The table shows that the scaling exponents n_1 determined on the basis of the added Reynolds shear stresses are close to 1 for unyawed conditions and increase with the yaw angle up to values of about 1.5. For the scaling exponent n_2 determined on the basis of the added turbulent kinetic energy no dependency on the yaw angle can be observed, however, the values significantly differ between the two boundary layers of different surface roughness. About the reasons for this behaviour it can only be speculated at this point. One possible reason of which can be thought of is that the reorganisation of the boundary layer within the *wake region*, caused by the coarse resolution in the *recycling region* as discussed in Section 7.2, does influence the development of the added Reynolds stresses $\Delta \overline{u'_i u'_i}$. Since the lateral Reynolds shear stress in the boundary layer $\overline{u'v'}_{bl} = 0$, the added Reynolds shear stress in the wake $\Delta \overline{u'_i u'_j}_M$ might not or only slightly be affected by the axial development of the boundary layer and does therefore scale in a rather undisturbed manner, and hence

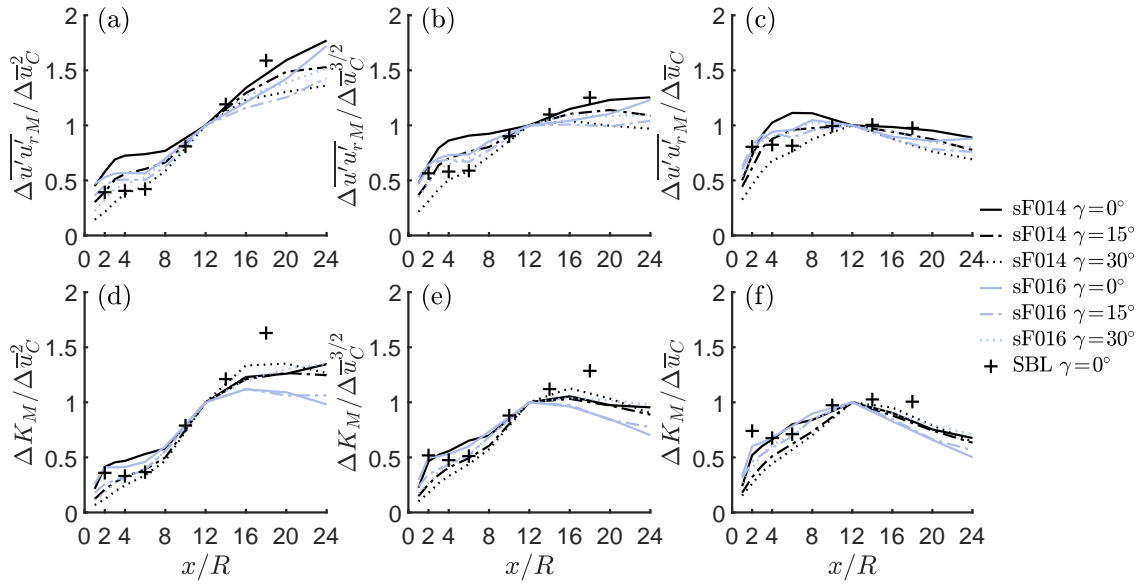


Figure 8.16: Maximum added Reynolds shear stress $\Delta \overline{u' u'_{r,M}}$ and turbulent kinetic energy ΔK_M in the wake of the model wind turbine normalised using (a)/(d) the equilibrium scaling $\Delta u_C^{3/2} \propto x$, (b)/(e) the square-root wake growth scaling $\Delta u_C \propto x$, and (c)/(f) the linear wake growth scaling $\Delta u_C^{3/2} \propto x$. Values at $x/R = 12$ are used as reference. The legend indicates the flow and yaw conditions.

appears to be independent of the surface roughness. Another possible reason is that due to the periodic recycling of the flow within the recycling region large turbulent scales are not resolved correctly and affect the development of the added Reynolds stresses [93].

Table 8.3: Curve fit parameters for the axial scaling of the added Reynolds shear stress and turbulent kinetic energy, $\Delta u' u'_{r,M} = A \Delta u_C^{n_1}$ and $\Delta K_M = B \Delta u_C^{n_2}$. Values n_σ are the resulting exponents for the wake growth $\sigma \propto x^{n_\sigma}$.

γ	n_1	n_2	$n_\sigma(n_1)$	$n_\sigma(n_2)$	γ	n_1	n_2	$n_\sigma(n_1)$	$n_\sigma(n_2)$
0°	1.1645	1.6463	0.7524	0.4362	0°	1.0955	1.9751	0.8396	0.3390
15°	1.3659	1.7191	0.5775	0.4101	15°	1.2689	1.9391	0.6503	0.3474
30°	1.5209	1.6664	0.4897	0.4287	30°	1.2901	1.5867	0.6329	0.4601

(a) sF014

(b) sF016

Despite the inconclusive results regarding the axial scaling of the added Reynolds shear stress and turbulent kinetic energy, as mentioned in Section 8.1.2, Dairay et al. [35] postulated that non-equilibrium flows in which $n \neq 1$ should only be possible under the assumption of a constant anisotropy on the surface $\eta = 1$. For that reason, analogous to Figure 8.10 for the experimental results, Figure 8.17 shows the ratios $(\Delta \overline{u'_i u'_i} / \Delta K)(\eta = 1)$ as function of the axial distance along the line (a)-(c) $\eta_z = 1$ and (d)-(f) $\eta_y = 1$. The direct comparison with the experimental results in general reveals a satisfactory agreement with the numerical data. For $\eta_z = 1$ all ratios converge towards a constant value, indicating an approximately constant anisotropy. However, along the line $\eta_y = 1$ the contribution of the Reynolds stress component $\Delta \overline{u' u'}$ to the added turbulent kinetic energy decreases steadily with downstream distance, whereas the contribution of the components $\Delta \overline{v' v'}$

and $\overline{\Delta w'w'}$ steadily increases. This is slightly different to the behaviour observed in the experimental results where the particular Reynolds stress components are considered to reach constant anisotropy in the far wake. Taking into consideration the inconclusive results regarding the axial scaling of the added turbulent kinetic energy, the observed change of the anisotropy within the numerical results could be seen as another indication that the above mentioned reorganisation of the boundary layer flow within the *wake region* does affect the evolution of the added Reynolds stresses $\Delta u'_i u'_i$ in the wake.

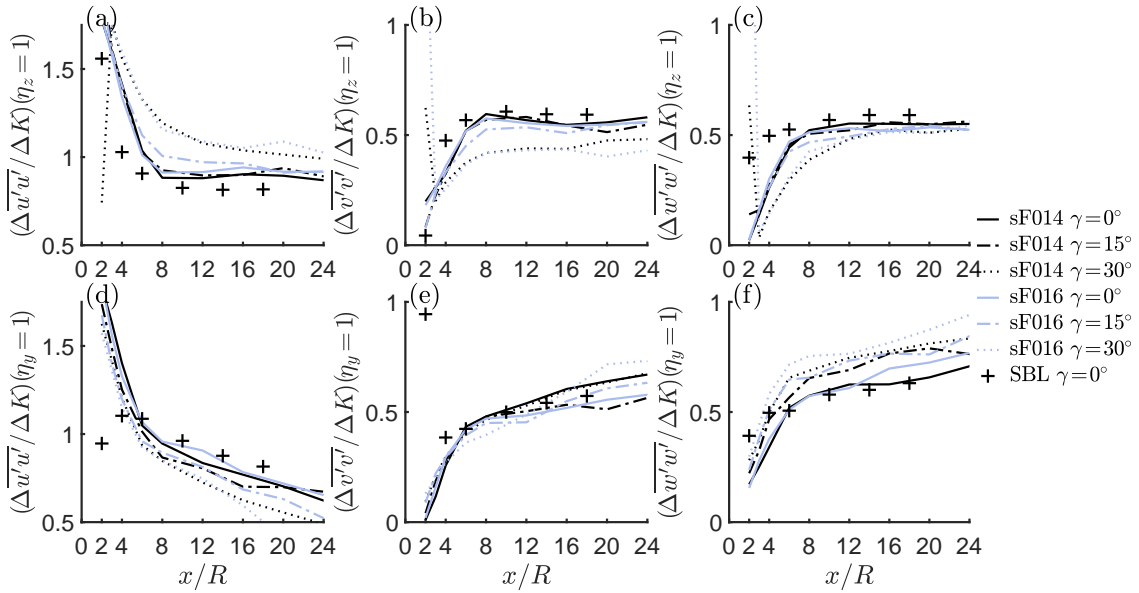


Figure 8.17: Structural parameters $(\Delta u'_i u'_i / \Delta K)(\eta = 1)$ in the wake of the model wind turbine for (a)-(c) $\eta_z = 1$ and (d)-(f) $\eta_y = 1$. The legend gives flow and yaw conditions.

8.3 An Analytical Model for Predicting Turbulence Quantities in the Far Wake

In the following findings of the self similarity analysis are used to develop a model that allows for a fast prediction of turbulence in the far wake. For the sake of a better readability, in this section, the Einstein summation notation is not used. Therefore, summation is not performed over duplicate indices and $\overline{u'_i u'_i}$ denotes the Reynolds stress corresponding to the velocity component u_i .

In Section 8.2 it was shown that the diagonal components of the Reynolds stress tensor $\overline{u'_i u'_i}$ and the turbulent kinetic energy K in the wake can be expressed in terms of the added quantities $\Delta\overline{u'_i u'_i}$ and ΔK . Therefore, it is made use of this observation and values $\overline{u'_i u'_i}$ and K predicted by the model are given as

$$\frac{\overline{u'_i u'_i}(x,y,z)}{\overline{u_{bl}^2}(z)} = \frac{\overline{u'_i u'_{ibl}}(z,I_0)}{\overline{u_{bl}^2}(z)} + \Delta\overline{u'_i u'_i}(x,y,z,C_T,\gamma,I_0), \quad \frac{K(x,y,z)}{\overline{u_{bl}^2}(z)} = \frac{K_{bl}(z,I_0)}{\overline{u_{bl}^2}(z)} + \Delta K(x,y,z,C_T,\gamma,I_0) \quad (8.15)$$

where I_0 shall indicate the dependency on the level of background turbulence, which here is not further defined. In the following use is made of the findings in Section 8.2 to meet reasonable assumptions. It was found that the components of the added Reynolds stress tensor $\Delta\overline{u'_i u'_i}$ and the added turbulent kinetic energy ΔK exhibit a high degree of self similarity in the wake. Therefore, it is assumed that these quantities can be approximated by

$$\Delta\overline{u'_i u'_i} = \Delta\overline{u'_i u'_i}(\eta=1) \cdot f_i(\eta), \quad \Delta K = \Delta K(\eta=1) \cdot h(\eta). \quad (8.16)$$

Furthermore, the results shown in Figure 8.10 suggest a constant anisotropy in the far wake region $\Delta\overline{u'_i u'_i} \propto \Delta K$, as well as the axial scaling $\Delta K_M \propto \Delta u_C$ that was identified in Figure 8.9 and which governs the streamwise evolution of the magnitude of the stresses. Hence, the constants $C_i = \Delta\overline{u'_i u'_i}(\eta=1)/\Delta K(\eta=1)$ and $C_K(I_0) = \Delta K(\eta=1)/\Delta u_C$ are defined which can readily be taken from Figure 8.10 (note the condition $0.5 \sum C_i = 1$). Inserting these into Equation (8.15) then gives

$$\frac{\overline{u'_i u'_i}}{\overline{u_{bl}^2}} = \frac{\overline{u'_i u'_{ibl}}}{\overline{u_{bl}^2}} + C_i \cdot C_K(I_0) \cdot \Delta u_C(x,C_T,\gamma) \cdot f_i(\eta), \quad \frac{K}{\overline{u_{bl}^2}} = \frac{K_{bl}}{\overline{u_{bl}^2}} + C_K(I_0) \cdot \Delta u_C(x,C_T,\gamma) \cdot h(\eta). \quad (8.17)$$

The shape functions f_i , however, have to be determined from the measurements. It is likely that these, as well as the constants C_i and C_K , might depend on the rotor design and could also vary with operational parameters as the tip speed ratio. Therefore it should be noted that, as mentioned in Chapter 4, our rotor is designed for constant bound circulation and is operated at its optimum tip speed ratio in terms of power production. The slight asymmetry of the shape functions, see Figure 8.8, in yawed conditions is here neglected. With that the shape functions can be approximated by

$$f_{i,S} = \exp[-\alpha_{i,S}\eta^2], \quad f_{i,D} = \exp[-\alpha_{i,D}(\eta-1)^2] + \exp[-\alpha_{i,D}(\eta+1)^2] \quad (8.18)$$

and are all formulated such that $f_i(|\eta| = 1) = 1$. Since $\Delta K = 0.5 \sum \Delta\overline{u'_i u'_i}$, the shape function of the turbulent kinetic energy can simply be formulated as

$$h(\eta) = 0.5 \sum C_i f_i(\eta). \quad (8.19)$$

Parameters which are derived from the mean velocity field, as Δu_C , y_C and σ_y , can be computed from any appropriate analytical wake model (base model) which predicts the velocity distribution in the wake. A comparison of two analytical wake models against the measurement data presented here can be found in [136]. However, for testing purposes these parameters are derived directly from the experimental and numerical data in order not to introduce any errors from modelling assumptions on the velocity field.

Since the curve fits to the shape functions result in slightly different coefficients for the numerical data, in the following the proposed model is tested against the measurement results and the numerical data separately. For both tests all necessary parameters are determined on the basis of the results in the horizontal plane at hub height for the unyawed turbine.

For the measurement results the shape function parameters show up as $\alpha_{1,D} = 1.25$, $\alpha_{2,S} = 0.35$, $\alpha_{3,S} = 0.28$, $C_1 = 0.8$, $C_2 = 0.6$, and $C_3 = 0.6$. The constants C_K are calculated as the average value at the last three axial measurement stations which gives $C_K(SBL) = 0.049$ and $C_K(RBL) = 0.030$. As shown in Figure 8.18, the model predictions and measurements gradually converge. For large yaw angles the neglected asymmetry of the shape functions becomes noticeable, especially in case of the RBL. However, as intentional large yaw angles are rather impractical for wake control strategies, due to the substantial decrease of the power coefficient, this might be a rather less important inaccuracy of the model.

For the LES data it was found that the shape function of the added Reynolds stress $\overline{\Delta w'w'}$ is best approximated by a double Gaussian distribution, instead of a single Gaussian distribution as observed in the measurement results. Within the unyawed wake the obtained shape function parameters are similar for the sF014 and sF016 configuration. Therefore, the shape function parameters used in this test are based on the sF014 configuration and are $\alpha_{1,D} = 1.47$, $\alpha_{2,S} = 0.27$, $\alpha_{3,D} = 1.05$. The numerical results were inconclusive regarding the axial scaling of the added Reynolds shear stress and the added turbulent kinetic energy. However, for testing purposes the *linear wake growth* scaling law is assumed to be valid and the constants C_K are calculated as the average value of the last three axial stations used in this test ($x/R = 12, 16, 20$), which result in $C_K(sF014) = 0.038$ and $C_K(sF016) = 0.034$. Since the level of the turbulent kinetic energy in the numerical sF016 configuration is similar and in the numerical sF014 configuration even lower than in the experimental SBL configuration, the constants $C_K(sF016)$ and $C_K(sF014)$ would be expected to be similar or larger than $C_K(SBL)$. This is considered to be a result of the different axial scaling present in the wind tunnel measurements and the large eddy simulations. Similar to the procedure to obtain the constant C_K , the constants C_i are obtained by calculating the average value of the last three axial stations within both boundary layer configuration. Given that, the constants result in $C_u = 0.78$, $C_v = 0.64$, and $C_w = 0.58$, which is in good agreement with the values obtained for the experimental results.

In Figure 8.19 the modelled values of the normal Reynolds stresses and the turbulent kinetic energy are compared to the simulation results. In general the modelled values are in very good agreement with the simulation results for the considered axial stations, whereby the neglected asymmetry of the shape functions for large yaw angles becomes noticeable. However, more important, it can be observed that the assumption of a *linear wake growth* scaling, even though the numerical results for the added turbulent kinetic energy do not support this assumption, has only a minor influence on the accuracy of the model. This indicates that, given a proper choice for C_K , in the context of an engineering

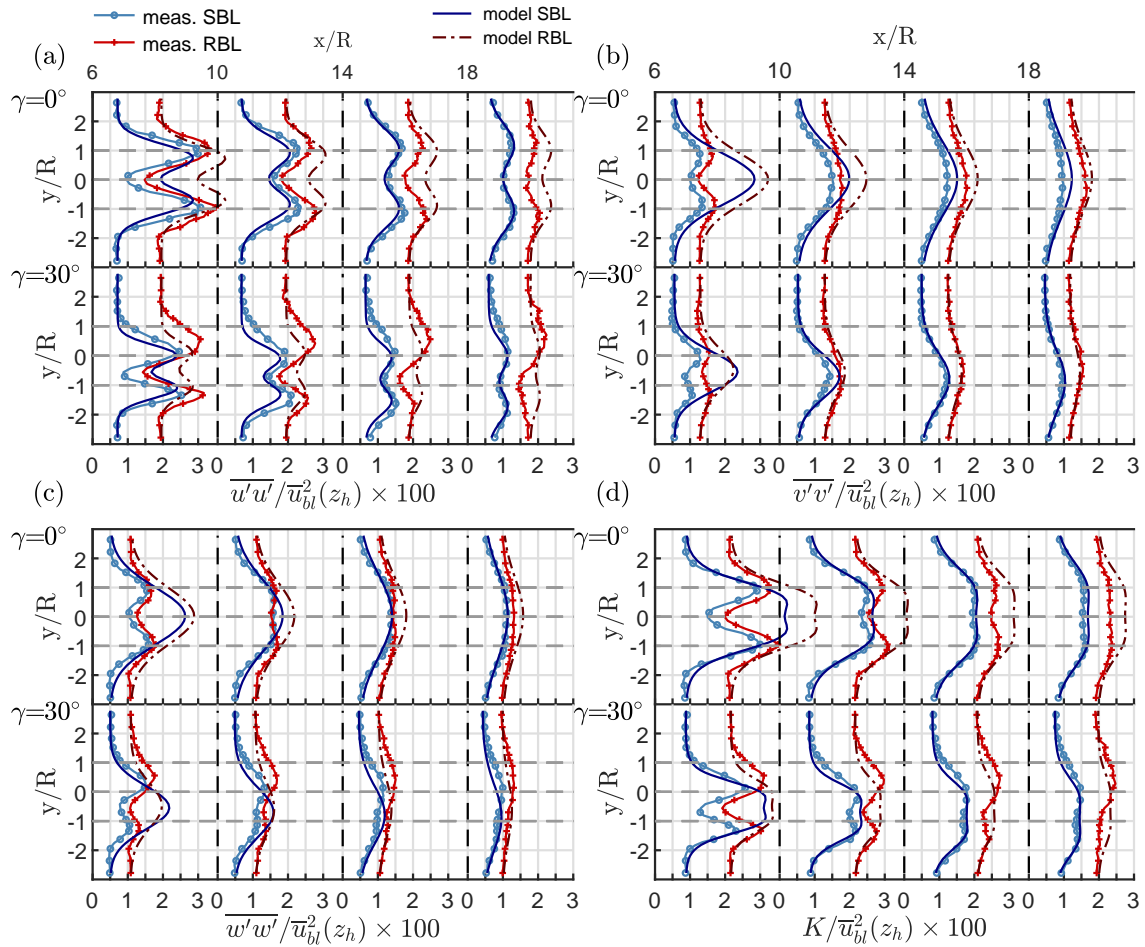


Figure 8.18: Comparison of model predictions (*lines*) and measurement results (*symbols and lines*) in the horizontal plane at hub height z_h for the Reynolds stress components (a) $\overline{u'u'}$, (b) $\overline{v'v'}$ and (c) $\overline{w'w'}$, and (d) the turbulent kinetic energy K , all normalised by $\overline{u_{bl}^2}(z_h)$. The *legend* gives flow conditions.

model the discussion on the scaling law plays a rather minor role.

Since typical turbine spacings in windfarms are in the range covered by this simple model, it might be useful within the context of real time wake control strategies when coupled to a suitable base model for Δu_C , y_C and σ_y .

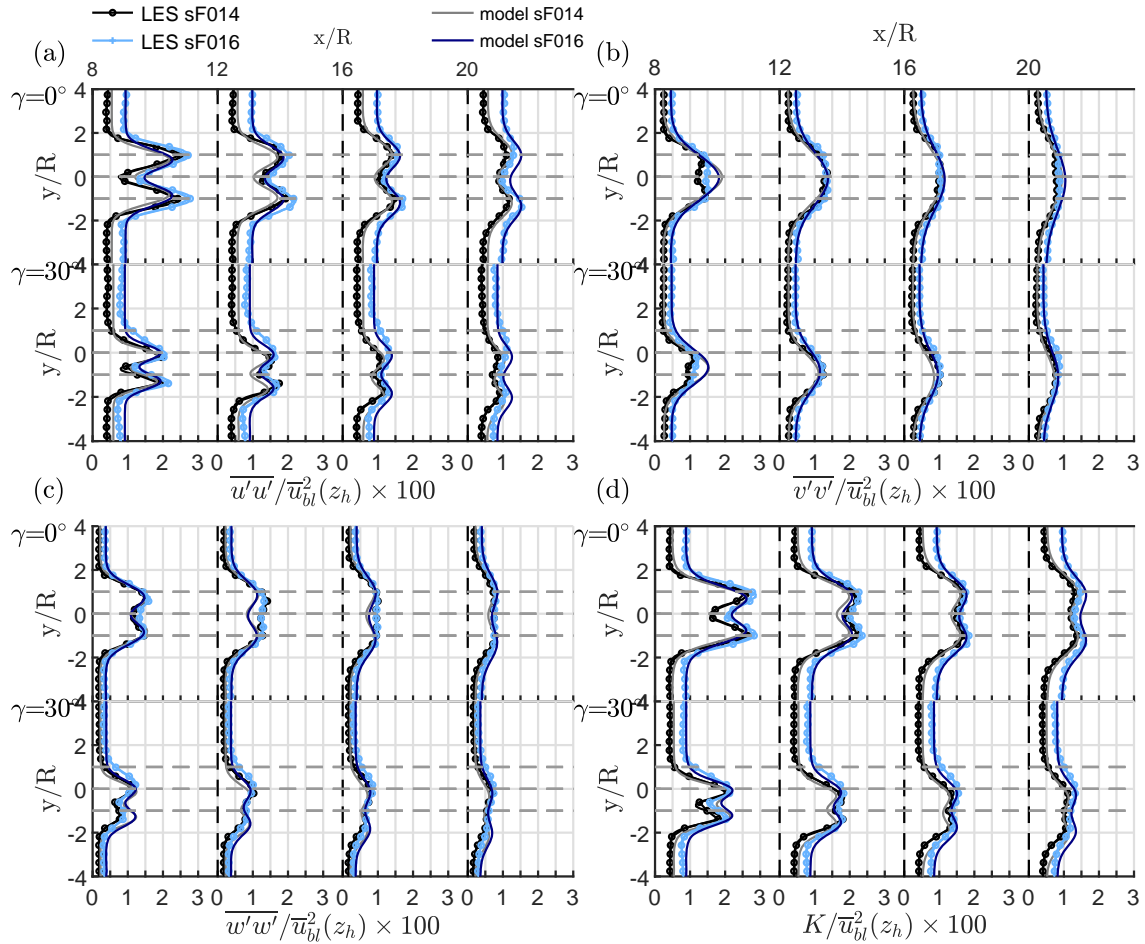


Figure 8.19: Comparison of model predictions (*lines*) and LES results (*symbols and lines*) in the horizontal plane at hub height z_h for the Reynolds stress components (a) $\overline{u'u'}$, (b) $\overline{v'v'}$ and (c) $\overline{w'w'}$, and (d) the turbulent kinetic energy K , all normalised by $\overline{u_{bl}^2}(z_h)$. The legend gives flow conditions.

8.4 Summary

In this chapter results from the wind tunnel experiment, presented in Chapter 5, and the large eddy simulations, presented in Chapter 7, of a small scale model wind turbine were analysed regarding the self similarity and the axial scaling of flow quantities within the wake. For this analysis, analytical considerations found in literature on the evolution of axisymmetric turbulent wakes in low turbulence uniform approaching flow conditions were introduced and adapted for the application in wind turbine wakes immersed in turbulent boundary conditions.

It was found that, if described in terms of an added quantity, lateral and vertical profiles of the mean axial velocity, the Reynolds shear stress and the turbulent kinetic energy become self similar in the far wake, even at high yaw angles.

Based on the high degree of self similarity, results from the wind tunnel measurements were analysed with respect to the underlying scaling law of the velocity deficit, the wake growth, the added Reynolds shear stress and the added turbulent kinetic energy. It was shown that the streamwise scaling of the velocity deficit and the wake growth cannot

be clearly identified by fitting the centreline velocity deficit and the wake width data. Analysis of the added Reynolds shear stress and the added turbulent kinetic energy revealed that the maxima of these quantities scale proportional to the centreline velocity deficit $\Delta \overline{u' u'_{r,M}}, \Delta K_M \propto \Delta u_C$. This is consistent with the non-equilibrium scaling eq.(8.10) which predicts $\overline{u' u'_{r,M}} \propto K_M$ [35] and allows a proportionality to the centreline velocity deficit Δu_C if the exponents m, n are chosen to be $m = n = 2$. In this case, the non-equilibrium scaling also predicts a linear wake growth, which is observed in the presented results for the wind turbine immersed in a boundary layer with smooth ground roughness as well as in other studies of wind turbines immersed in turbulent boundary layers.

In the rough boundary layer the wake width does not strictly follow a linear growth rate despite convincing self similarity of mean flow and Reynolds stress profiles. Since other wake parameters develop according to the non-equilibrium scaling law, it is believed that the proposed scaling concept is applicable to a wide range of ambient conditions. To the authors' knowledge, it is the first time that the non-equilibrium scaling theory is applied to the wake of a wind turbine immersed in a turbulent boundary layer.

Moreover, the anisotropy of the added Reynolds stresses is considered along the non-dimensional coordinate $\eta = 1$ and found to be approximately constant within the far wake region, whereas the contributions of the added Reynolds stresses slightly change with increasing background turbulence. The ratio $C_K = \Delta K(\eta = 1)/\Delta u_C$, however, is significantly influenced by the level of background turbulence and further research is necessary to determine its value for various flow and operational conditions. Given an approximately constant anisotropy, a self similarity of the diagonal components of the added Reynolds stress tensor and the validity of the linear wake growth scaling $\Delta K_M \propto \Delta u_C$, the findings suggest a physically motivated scaling of $I_+ = \sqrt{\Delta \overline{u' u'}} \propto x^{-1}$.

Analysis of the LES results revealed an inconclusive behaviour regarding the axial scaling of the added Reynolds shear stress and the added turbulent kinetic energy. The maxima of the added Reynolds shear stress were shown to scale approximately proportional to the centreline velocity deficit $\Delta \overline{u' u'_{r,M}} \propto \Delta u_C$, just as in the wind tunnel experiment, whereas the scaling of the added turbulent kinetic energy exhibited a dependency on the roughness length of the boundary layer configuration. Furthermore, it was shown that the anisotropy of the added Reynolds stresses along the non-dimensional coordinate $\eta = 1$ predicted by the LES is in good agreement with experimental results. However, the results indicate slightly larger changes of the anisotropy than observed within the wind tunnel measurements. Both, the inconclusive scaling of the added Reynolds shear stress and the added turbulent kinetic energy as well as the changes in the anisotropy are considered to originate from a grid refinement within the computational domain which causes a reorganisation of the boundary layer.

Based on these findings, a simple model to predict the diagonal components of the Reynolds stress tensor was proposed. It applies to steady ambient conditions and fixed operational parameters. Due to its formulation, it can be used as extension to existing analytical wake models which predict the flow field in the wake and needs only $C_K(I_0) = \Delta K(\eta = 1)/\Delta u_C$ as additional input parameter. A qualitative comparison of the model predictions with the measurement results and the numerical data in the horizontal plane of the rotor is in good agreement. Nevertheless, for a generalisation of the model, in future studies the dependencies of the parameter $C_K(I_0)$, C_i and the shape functions f_i on the ambient conditions and the operational state of the wind turbine have to be analysed in detail. Since the study is based on the analysis of a single wake, additional research effort

is necessary for extending the model to predict the evolution of turbulence within multiple interacting wakes. With such an extension, the model could be applied in real-time wind farm controllers for the optimization of power production and alleviation of fatigue loads.

Summary and Conclusions

For the first time, a systematic assessment of wind turbine wakes interacting with neutral stratified atmospheric boundary layers over homogeneous flat surfaces of different aerodynamic roughness is carried out by means of an experimental and a numerical study. The experimental study is based on measurements in a boundary layer wind tunnel with a small scale model wind turbine, which is specifically designed and verified for this project, in order to reasonably cope with relevant scaling effects. The numerical study complements the wind tunnel tests by reproducing the experimental set-up in large-eddy simulations, utilizing the Actuator Line Method for modelling the rotor flow and wall models for the generation of turbulent boundary layers over rough surfaces.

A novel aspect of this thesis is the application of non-equilibrium scaling theory for wakes to a wind turbine. Through joint assessment of the streamwise evolution of the velocity deficit and the Reynolds stresses in the wake, a consistent set of power law coefficients for the description of the axial scaling of these quantities has been derived. Based on the findings of this analysis a simple model to predict the diagonal components of the Reynolds stress tensor in the wake is proposed.

In a preparatory study the generation of two turbulent boundary layers of moderate and high aerodynamic surface roughness in a boundary layer wind tunnel is established. Other than observed in field studies, the integral turbulent length scales and the normalised energy spectral density of the tested boundary layers are similar. Even though this behaviour is a characteristic of the modelling technique in the wind tunnel, it facilitates the wake analysis as it reduces the number of effects having influence on the wake evolution.

For the purpose of this project a small scale model wind turbine for the application in a boundary layer wind tunnel is designed. The dimensions of the wind turbine are chosen such that the experiment models the interaction of a multi megawatt wind turbine with the atmospheric boundary layer at a scale of $1 : \mathcal{O}(350)$. Thereby special care is taken in the rotor design to obtain an energy conversion similar to a full scale turbine, despite the low Reynolds number range in which the rotor operates. As a result of the consequent design for operation in a low Reynolds number regime a realistic rotor performance over a wide range of tip speed ratios is shown for different flow conditions, ranging from low turbulence uniform approaching flow to highly sheared turbulent boundary layers. A

comparison with a full scale multi megawatt wind turbine with a comparable design tip speed ratio shows that the model wind turbine exhibits very similar thrust coefficients while the maximum power coefficient is about 15% lower. When compared to other small scale wind turbines for wind tunnel applications, the maximum power coefficient achieved for the model wind turbine presented here is similar or even superior.

For the experimental study, wind tunnel tests of the small scale model wind turbine immersed in low-turbulence uniform approaching flow conditions and the two turbulent boundary layers of different ground roughness are carried out. The tests include measurements with the wind turbine operating at design conditions and aligned to the incoming flow, at higher tip speed ratios, and with intentional yaw-misalignment. In all cases time series of the flow field in the wake of the wind turbine are recorded by means of a triple hot wire probe along with simultaneous sampling of the thrust and torque generated by the wind turbine.

For the numerical study in a preparatory step, the academic flow solver INCA is extended for simulations with the Actuator Line Method [132] and for the generation of neutrally stratified turbulent boundary layers over flat and homogeneous rough surfaces. The accuracy of the Actuator Line Method relies predominantly on the quality of the tabulated airfoil data. Therefore, to model correctly the rotor performance of the small scale model wind turbine, a blade polar identification, as described by Schneider *et. al* [124], is conducted. Subsequently, the rotor flow is simulated for various tip speed ratios and blade pitch angles and the numerical data obtained is then utilized in an inverse lifting line calculation. The result of the identification is a set of airfoil data, calibrated for the effect of rotation and three dimensional flow. Due to this calibration, the rotor performance measured in the wind tunnel tests is predicted by the actuator line method with an error $< 4\%$.

In the numerical study large eddy simulations of the small scale model wind turbine immersed in three turbulent boundary layers of different aerodynamic roughness are carried out. One of the boundary layers is specifically configured such that it meets the experimental set-up for a moderate surface roughness. For the generation of an undisturbed turbulent boundary layer the flow field in a section upstream of the wind turbine is continuously recycled and utilized as inlet condition for the computational domain. Similar to the wind tunnel tests, for each boundary layer configuration the interaction with the wind turbine is simulated for operation at design conditions aligned to the incoming flow and with intentional yaw-misalignment.

A comparison of wake measurements recorded at different tip speed ratios for which the rotor generates similar thrust coefficients, shows that differences in the axial mean velocity rapidly vanish and become indistinguishable for distances $x/R \geq 10$. This behaviour is similar to results of the velocity deficit in the near wake, found in literature, where a non-rotating porous disc and a small scale wind turbine model were compared [3]. Nevertheless, significant differences in the Reynolds stresses can even be noticed at a distance of $x/R = 18$. This observation is in accordance with the mutual inductance instability described in literature [90], which for high tip speed ratios causes the helical blade tip vortices to break down closer to the rotor and induces an initially faster recovery of the wake. Spectral analysis is applied and confirms the early break down of the blade tip vortices at high tip speed ratio. Regarding the design of model wind turbines for wind tunnel tests the results indicate that for accurate near and far wake predictions rotors with design tip speed ratios close to those found in full-scale are to be preferred. Furthermore, for the design process of a wind turbine it can be concluded that consid-

ering the mutual inductance instability and its dependency on the tip speed ratio in the design process of a wind turbine could help to alleviate fatigue loads seen by wind turbines situated downstream. Systematic analysis of wakes generated by rotors designed for operations at different tip speed ratios, but with similar thrust and power coefficient, could provide an in-depth understanding of the mechanism and its effect on the turbulence in the far wake.

Analysis of the wake development within low-turbulence uniform flow and turbulent boundary layers, for the numerical and experimental results, reveals a faster wake recovery for increasing surface roughness, which is considered to stem from an enhanced momentum transfer from the outer flow into the wake, caused by the higher level of ambient turbulence. In uniform flow conditions as well as turbulent boundary layer flows with low and moderate roughness the wake is observed to remain nearly symmetric. In these cases the wake is shown to expand linear with growth rates which increase with the ambient level of turbulence. For wakes immersed in very rough boundary layers it is observed that in the near wake region the interaction with the boundary layer causes an additional momentum deficit below hub height and turbulence is suppressed below the ambient level. Spectral analysis of the measured flow field reveals that in this situation the production of turbulence in the lower part of the wake is reduced over large downstream distances. As a result the momentum exchange with the outer flow is reduced, causing the additional momentum deficit and the suppressed level of turbulence to persist even far downstream. Furthermore, the wake becomes asymmetric with a non-linear wake growth which decreases with axial distance.

For wakes generated by the wind turbine operating under intentional yaw-misalignment, experimental and numerical results show that an increase of the surface roughness does not alter the lateral deflection of the near wake, whereas it decreases the lateral deflection in the far wake. The latter is considered to result from the enhanced momentum transfer caused by the ambient level of turbulence due to which the wake loses potential to penetrate the surrounding flow in the lateral direction. Furthermore, analysis of the numerical data confirms the formation of a counter rotating vortex pair at the top and bottom edge of the wake, due to which the form of the velocity deficit in the near wake appears to be shaped like a kidney. In the far wake region it is shown that with increasing surface roughness the intensity of the lower vortex diminishes in shorter downstream distance which causes a skewing of the wake. Since the ground interaction of the counter rotating vortex pair does potentially also reduce the wake deflection, more research is necessary to separate the effect of the ambient turbulence level and the ground interaction. However, the findings indicate that considering yaw misalignment as a control strategy to improve the power production in on-shore wind farms, might be less beneficial with increasing terrain roughness.

Based on the wind tunnel data, a detailed spectral analysis of the flow field is performed in order to analyse the evolution of turbulence in the wake and the effect of surface roughness on the process. For the near wake region it is shown that the wind turbine destroys the large scale vortex patterns found in the turbulent boundary layers while generating turbulence at a much smaller scale. Within the two considered boundary layers the normalised power spectra $S_{uu}/\overline{u'u'}$ and the axial Reynolds stress $\overline{u'u'}$ in the proximity of the turbine are shown to be quite similar. These results support the view of Chamorro *et. al* [31], who stated that the turbine acts as an 'active filter' which modulates the turbulent scales according to its operational state. Moreover, the results indicate that the concept of added turbulence is not applicable in the near wake region.

In the transitional region between near and far wake the normalised power spectra $S_{uu}/\overline{u'u'}$ clearly deviate within the two considered boundary layer configurations, since the ambient level of turbulence affects the helical blade tip vortices and the position of their break down. However, further downstream the normalised power spectra $S_{uu}/\overline{u'u'}$ in the wake is found to become similar and converge asymptotically towards the spectra of the undisturbed boundary layer. Since the latter is nearly self similar, differences in the normalised power spectra within the wakes are considered to result from the different wake recovery rates. Indeed, analysis of the normalised power spectra $S_{uu}/\overline{u'u'}$ evaluated at hub height for various lateral and axial positions within the wake immersed in the turbulent boundary layer over small surface roughness revealed a self similar distribution of the power spectrum.

Motivated by these findings a self similarity analysis of the axial velocity deficit and the components of the Reynolds stress tensor in the wake is carried out for the experimental and numerical data. To compare the evolution of Reynolds stresses in wakes immersed in turbulent boundary layers of different surface roughness, flow quantities are separated based on the assumption that the flow can be described by superposing a boundary layer flow and an 'added' axisymmetric wake. A theoretical discussion on this concept and its limitations is given. It is found that, if described in terms of an added quantity, lateral and vertical profiles of the mean axial velocity, the Reynolds shear stress and the turbulent kinetic energy become approximately self similar in the far wake, even for high yaw angles. Furthermore, it is revealed that the axial scaling of the added Reynolds shear stress and the added turbulent kinetic energy is consistent with the non-equilibrium scaling [35]. Moreover, it is found that the anisotropy of the added Reynolds stresses is approximately constant within the far wake.

Based on these findings, a simple model to predict the diagonal components of the Reynolds stress tensor is proposed. It applies to steady ambient conditions and fixed operational parameters. Due to its formulation, it can be used as extension to existing analytical wake models which predict the flow field in the wake. A qualitative comparison of the model predictions with the measurement results and the numerical data is in good agreement. Nevertheless, for a generalisation of the model, more research effort is necessary to reveal dependencies of model parameters on the ambient conditions and the operational state of the wind turbine. The derived concept for the superposition of wake and boundary layer could serve as basis for developing a physics-based 'theory' for describing the interaction of multiple wakes immersed in turbulent boundary layers, so that it can be used to improve the prediction of both power losses and fatigue loads in wind farms.

Bibliography

- [1] Abkar, M.; Porté-Agel, F. Influence of atmospheric stability on wind-turbine wakes: A large-eddy simulation study. *Phys. Fluids* **2015**, *27*, 035104
- [2] Al-Abadi, A.; Kim, Y.J.; Ertunc, Ö; Delgado, A. Turbulence Impact on Wind Turbines: Experimental Investigations on a Wind Turbine Model. *J. Phys. Conf. Ser.* **2016**, *753*, 032046
- [3] Aubrun, S.; Loyer, S.; Hancock, P.E.; Hayden, P. Wind turbine wake properties: Comparison between a non-rotating simplified wind turbine model and a rotating model. *J. Wind Eng. Ind. Aerod.* **2013**, *120*, pp. 1-8.
- [4] Baggett, J.S.; Jimenez, J.; Kravchenko, A.G. Resolution requirements in large-eddy simulations of shear flows. *Annual Research Briefs* **1997**, Center for Turbulence Research, Stanford.
- [5] Barlas, E.; Buckingham, S.; van Beeck, J. Roughness Effects on Wind-Turbine Wake Dynamics in a Boundary-Layer Wind Tunnel. *Boundary-Layer Meteorol.* **2016**, *158*, pp. 27-42.
- [6] Barlow, J.B.; Rae, W.H.; Pope, A.; Low-speed Wind Tunnel Testing, 3rd Edition. *John Wiley & Sons* **1999**; 978-0-471-5577-46.
- [7] Bartl, J.; Pierella, F.; Sætran, L. Wake measurements behind an array of two model wind turbines. *Energy Procedia* **2012**, *24*; pp. 305-312.
- [8] Bartl, J.; Mühle, F.; Schottler, J.; Sætran, L.; Peinke, J.; Adaramola, M.; Hölling, M. Wind tunnel experiments on wind turbine wakes in yaw: effects of inflow turbulence and shear. *Wind Energy Science* **2018**, *3*; pp. 329-343.
- [9] Bartl, J.; Mühle, F.; Sætran, L.; Wind tunnel study on power output and yaw moments for two yaw-controlled model wind turbines. *Wind Energy Science* **2018**, *3*; pp. 489-502.
- [10] Bastankhah, M.; Porté-Agel, F. A new analytical model for wind-turbine wakes *Renewable Energy* **2014**, *70*, pp. 116-123.
- [11] Bastankhah, M.; Porté-Agel, F. A wind-tunnel investigation of wind-turbine wakes in yawed conditions *Journal of Physics: Conference Series* **2015**, *625*, 012014.
- [12] Bastankhah, M.; Porté-Agel, F. Experimental and theoretical study of wind turbine wakes in yawed conditions. *J. Fluid Mech.* **2016**, *806*, pp. 506-541.
- [13] Bastankhah, M.; Porté-Agel, F. A New Miniature Wind Turbine for Wind Tunnel Experiments. Part I: Design and Performance. *Energies* **2017**, *10*, 908.
- [14] Bastankhah, M.; Porté-Agel, F. Wind tunnel study of the wind turbine interaction with a boundary-layer flow: upwind region, turbine performance, and wake re-

- gion. *Phys. Fluids* **2017**, 29, 065105.
- [15] Betz, A. Das Maximum der theoretisch möglichen Ausnützung des Windes durch Windmotoren. *Zeitschrift für das gesamte Turbinenwesen* **1920**, 26, pp. 307-309.
- [16] Bou-Zeid, E.; Meneveau, C.; Parlange, M.B. A scale-dependent Lagrangian dynamic model for large-eddy simulation of complex turbulent flows. *Phys. Fluids* **2005**, 17, 025105.
- [17] Bons, M.; Döring, M.; Klessmann G.; Knapp, J.; Tiedemann S. Analyse der kurz- und mittelfristigen Verfügbarkeit von Flächen für die Windenergienutzung an Land *Umweltbundesamt* **2019**.
- [18] Bossanyi, E.A. Individual Blade Pitch Control for Load Reduction. *Wind Energy* **2003**, 6, pp. 119-128.
- [19] Bottasso, C.L.; Campagnolo, F.; Petrović, V. Wind tunnel testing of scaled wind turbine models: Beyond aerodynamics. *J. Wind Eng. Ind. Aerod.* **2014**, 127, pp. 11-28.
- [20] Bottema, M. Roughness parameters over regular rough surfaces: Experimental requirements and model validation. *J. Wind Eng.* **1996**, 64, pp. 249-265.
- [21] Breitsamter, C. Turbulente Strömungsstrukturen an Flugzeugkonfigurationen mit Vorderkantenwirbeln. PhD Thesis, Technical University of Munich, Germany, **1997**.
- [22] Burton, T.; Jenkins, N.; Sharpe, D.; Bossanyi, E. Wind Energy Handbook. *John Wiley & Sons* **2011**, Chichester, UK; 978-0-470-69975-1.
- [23] Cabot, W.; Moin, P. Approximate wall boundary conditions in the large-eddy simulation of high Reynolds number flow. *Flow, Turbulence and Combustion* **1999**, 63, pp. 269-291.
- [24] Bottasso, C.L.; Cacciola S.; Iriarte, X. Calibration of wind turbine lifting line models from rotor loads. *J. Wind Eng. Ind. Aerodyn.* **2014**, 124, pp. 29-45.
- [25] Carmichael, B. Low Reynolds Number Airfoil Survey Volume 1. *NASA CR*, **1981** 165803.
- [26] Carmody, T. Establishment of the wake behind a disk. *J. Basic Eng.* **1964**, 86, 869.
- [27] Castro, I.P. Rough-wall boundary layers: mean flow universality. *J. Fluid Mech.* **2007**, 585, pp. 469-485.
- [28] Chamorro, L.P.; Porté-Agel, F. A Wind-Tunnel Investigation of Wind-Turbine Wakes: Boundary-Layer Turbulence Effects. *Boundary-Layer Meteorol.* **2009**, 132, pp. 129-149.
- [29] Chamorro, L.P.; Porté-Agel, Effects of Thermal Stability and Incoming Boundary-Layer Flow Characteristics on Wind-Turbine Wakes: A Wind-Tunnel Study. *Boundary-Layer Meteorol.* **2010**, 136, pp. 515-533.
- [30] Chamorro, L.P.; Arndt R.E.A.; Sotiropoulos F. Reynolds number dependence of turbulence statistics in the wake of wind turbines. *Wind Energ.* **2012**, 15, pp. 733-742.
- [31] Chamorro, L.P.; Guala, M.; Arndt R.E.A.; Sotiropoulos F. On the evolution of turbulent scales in the wake of a wind turbine model. *Journal of Turbulence* **2012**, 13, N27.

- [32] Counihan, J. An improved method of simulating an atmospheric boundary layer in a wind tunnel. *Atmos. Environ.* **1969**, *3*, 197-214.
- [33] Counihan, J. Adiabatic atmospheric boundary layers: A review and analysis of data from the period 1880-1972. *Atmos. Environ.* **1975**, *9*, pp. 871-905.
- [34] Crespo, A; Hernández, J. Turbulence characteristics in wind-turbine wakes. *J. Wind Eng. Ind. Aerod.* **1996**, *61*, pp. 71-85.
- [35] Dairay, T.; Obligado, M.; Vassilicos, J.C. Non-equilibrium scaling laws in axisymmetric turbulent wakes. *J. Fluid Mech.* **2015**, *781*, pp.166-195.
- [36] De Stadler, M.B.; Rapaka, N.R.; Sarkar, S. Large eddy simulation of the near to intermediate wake of a heated sphere at $Re = 10000$. *Intl J. Heat Transfer Fluid Flow* **2014**, *49*, pp. 2-10.
- [37] Dhamankar, N.S.; Blaisdell, G.A. An Overview of Turbulent Inflow Boundary Conditions for Large Eddy Simulations, *22nd AIAA Computational Fluid Dynamics Conference*, **2015**, AIAA 2015-3213.
- [38] Deutsches Institut für Normung e. V. DIN EN 1991-1-4:2010-12, Eurocode 1: Einwirkungen auf Tragwerke - Teil 1-4: Allgemeine Einwirkungen, Windlasten. *Beuth Verlag GmbH* **2011**, Berlin, Germany.
- [39] Drela, M. Viscous-Inviscid Analysis of Transonic and Low Reynolds Number Airfoils. *AIAA Journal* **1987**, *25*, pp. 1347-1355.
- [40] Emeis, S. Wind Energy Meteorology. *Springer* **2013**, Berlin, Germany; 978-3-642-30522-1.
- [41] Engineering Sciences Data Unit. Characteristics of atmospheric turbulence near the ground. *ESDU International plc* **2011**; 978-0-85679-526-7.
- [42] España, G.; Aubrun, S.; Loyer, S.; Devinant, P. Spatial study of the wake meandering using modelled wind turbines in a wind tunnel. *Wind Energy* **2011**, *14*, pp. 923-937.
- [43] Fang, C.; Sill, B.L. Aerodynamic roughness length: correlation with roughness elements *8th Int. Conf. Wind Eng.*
- [44] Fleck, A. Optimierung der experimentellen Simulation atmosphärischer Grenzschichten im Grenzschichtwindkanal der TUM. Bachelor Thesis, Technical University of Munich, Germany, **2015**.
- [45] Fleming, P.A.; Gebraad, P.M.O.; Lee, S. Evaluating techniques for redirecting turbine wakes using SOWFA. *Renewable Energy* **2014**, *70*, pp. 211-218.
- [46] Fleming, P.A.; Gebraad, P.M.O.; Lee, S. Simulation comparison of wake mitigation control strategies for a two-turbine case. *Wind Energy* **2015**, *18*, pp. 2135-2143.
- [47] Flores, O.; Jiménez, J. Effect of wall-boundary disturbances on turbulent channel flows. *J. Fluid Mech.* **2006**, *566*, pp. 357-376.
- [48] Frandsen, A. Turbulence and turbulence generated structural loading in wind turbine clusters. PhD Thesis, Risø National Laboratory, Denmark, **2007**.
- [49] Gasch, R.; Tvele, J. Windkraftanlagen - Grundlagen, Entwurf, Planung und Betrieb. *Springer Vieweg* **2013**, Stuttgart, Germany; 978-3-322-99446-2.
- [50] George, W.K.; Arndt, R. The self-preservation of turbulent flows and its relation to initial conditions and coherent structures. *Adv. Turbulence* **1989**, pp. 39-73.

- [51] Germano, M.; Piomelli, U.; Moin, P.; Cabot, W. A dynamic subgrid-scale eddy viscosity model. *Phys. Fluids A* **1991**, *3*, pp. 1760-1765.
- [52] Ghosal, S. An analysis of numerical errors in large-eddy simulations of turbulence. *J. Comput. Phys.* **1996**, *125*, pp. 187-206.
- [53] Glauert, H. Airplane propellers. *Springer* **1935**, Berlin, Germany, pp. 169–360.
- [54] Grötzbach, G. Direct numerical and large eddy simulation of turbulent channel flows. *Encyclopedia of Fluid Mechanics, Vol.6 - Complex Flow Phenomena and Modeling* **1987**, Gulf Publ.Co., Houston, USA.
- [55] Hau, E. Windkraftanlagen - Grundlagen, Technik, Einsatz, Wirtschaftlichkeit. *Springer* **2008**, Berlin, Germany; 978-3-540-72151-2
- [56] Hancock, P.; Pascheke, F. Wind-Tunnel Simulation of the Wake of a Large Wind Turbine in a Stable Boundary Layer: Part 2, the Wake Flow. *Boundary-Layer Meteorol.* **2014**, *151*, pp. 23-37.
- [57] Hancock, P.; Zhang, S. A Wind-Tunnel Simulation of the Wake of a Large Wind Turbine in a Weakly Unstable Boundary Layer. *Boundary-Layer Meteorol.* **2015**, *156*, pp. 395-413.
- [58] Hand, M.; Simms, D.; Fingersh, L.; Jager, D.; Cotrell, J.; Schreck, S.; Larwood, S. Unsteady Aerodynamics Experiment Phase VI: Wind Tunnel Test Configurations and Available Data Campaigns. Technical Report, TP-500-29955, National Renewable Energy Laboratory, USA, **2001**.
- [59] Hansen, M.O.L. Aerodynamics of Windturbines. *Earthscan* **2008**, London, UK; 978-1-84407-438-9.
- [60] Heist, D. K.; Castro, I.P. Combined laser-doppler and cold wire anemometry for turbulent heat flux measurement. *Exp. Fluids* **1998**, *24*, pp. 375-381.
- [61] Hickel, S.; Adams, N.A.; Domaradzki, J.A. An adaptive local deconvolution method for implicit LES. *Journal of Computational Physics* **2006**, *213*, pp.413-436.
- [62] Hickel, S.; Adams, N.A. Efficient Implementation of Nonlinear Deconvolution Methods for Implicit Large-Eddy Simulation. In: *High Performance Computing in Science and Engineering'06* **2007**. Springer, Berlin, Heidelberg
- [63] Hickel, S.; Adams, N.A. On implicit subgrid-scale modeling in wall-bounded flows. *Phys. Fluids* **2007**, *19*, 105106.
- [64] Hickel, S.; Adams, N.A.; Mansour, N. N. Implicit subgrid-scale modeling for large-eddy simulation of passive-scalar mixing. *Phys. Fluids* **2007**, *19*, 095102.
- [65] Howland, M.F.; Bossuyt, J.A.; Martinez-Tossas, L.; Meyers, J.; Meneveau, C. Wake structure in actuator disk models of wind turbines in yaw under uniform inflow conditions. *J. Renew. Sustain. Energy* **2016**, *8*, 043301.
- [66] Iyengar, A.K.S.; Farell, C. Experimental issues in atmospheric boundary layer simulations: roughness length and integral length scale determination. *Journal of Wind Engineering and Industrial Aerodynamics* **2001**, *89*, pp. 1059–1080.
- [67] Jensen, N.O. A note on wind generator interaction. Technical Report, Risø-M 2411, Risø National Laboratory, Roskilde, Denmark, **1983**.
- [68] Jia, Y.; Sill, B.L.; Reinhold, T.A. Effects of surface roughness element spacing on boundary-layer velocity profile parameters. *Journal of Wind Engineering and Indus-*

- trial Aerodynamics* **1998** 73, pp. 215–230.
- [69] Jiménez, J. Turbulent Flows over Rough Walls. *Annu. Rev. Fluid Mech.* **2004** 36, pp. 173-196.
- [70] Jiménez, Á.; Crespo, A.; Migoya, E.; Garcia, J. Advances in large-eddy simulation of a wind turbine wake. *J. of Phys.: Conf. Ser.* **2007** 75, 012041.
- [71] Jiménez, Á.; Crespo, A.; Migoya, E.; Garcia, J. Large-eddy simulation of spectral coherence in a wind turbine wake. *Enviro. Res. Lett.* **2008** 3, 015004.
- [72] Jiménez, Á.; Crespo, A.; Migoya, E. Application of a LES technique to characterize the wake deflection of a wind turbine in yaw. *Wind Energy* **2010** 13, pp. 559-572.
- [73] Jin, Y.; Chamorro, L. Effects of Freestream Turbulence in a Model Wind Turbine Wake. *Energies* **2016**, 9, 830.
- [74] Johansson, P.B.; George, W. K. Equilibrium similarity, effects of initial conditions and local Reynolds number on the axisymmetric wake. *Phys. Fluids* **2003**, 15, pp. 603-617.
- [75] Jonkman, J.M.; Buhl, M.L. FAST User's Guide v3.01. *National Renewable Energy Laboratory, USA, 2005*, NREL/EL-500-29798.
- [76] Jonkman, J.M.; Butterfield, S.; Musial, W.; Scott, G. Definition of a 5-MW Reference Wind Turbine for Offshore System Development. *National Renewable Energy Laboratory, USA, 2009*, NREL/TP-500-38060.
- [77] Joukowsky, N. Windmill of the NEJ type. *Transactions of the Central Institute for Aero-Hydrodynamics of Moscow* **1920**
- [78] Katic, I.; Højstrup, J.; Jensen, N. A simple model for cluster efficiency. *EWEA Conference* **1986**, pp. 407-410.
- [79] Knudsen, T.; Bak, T.; Svenstrup, M. Survey of wind farm control—power and fatigue optimization. *Wind Energy* **2015**, 18, pp. 1333-1351.
- [80] Kozmar, H. Utjecaj mjerila na strukturu modeliranog atmosferskog graničnog sloja. PhD Thesis, Sveučilište u Zagrebu, Fakultet strojarstva i brodogradnje, Croatia, **2005**.
- [81] Kunkel, J.G.; Marusic, I. Study of the near-wall-turbulent region of the high-Reynolds-number boundary layer using an atmospheric flow. *J. Fluid Mech.* **2006**, 548, pp. 375-402.
- [82] Komusanac, I.; Fraile, D.; Brindley G. Wind energy in Europe in 2018 *WindEurope Business Intelligence* **2019**
- [83] Kost, C.; Shammugam, S.; Jülch V.; Nguyen H.-T.; Schlegl T. Levelized Cost of Electricity Renewable Energy Technologies *Fraunhofer Institute for Solar Energy Systems ISE* **2018**
- [84] Krogstad, P.; Adaramola, M. Performance and near wake measurements of a model horizontal axis wind turbine. *Wind Energy* **2012**, 15, pp. 743-756.
- [85] Larsen, G.C. A simple wake calculation procedure. DTU, Denmark, **1988**, 15, Risø-M 2760.
- [86] Larsen, G.C.; Madsen, H.A.; Thomsen, K.; Larsen, T.J. Wake meandering: a pragmatic approach. *Wind Energy* **2008**, 11, pp. 377–395.
- [87] Larsson, J.; Kawai, S. Wall-modeling in large eddy simulation: length scales, grid

- resolution and accuracy. *Annual Research Briefs* **2010**, Center for Turbulence Research, Stanford.
- [88] Leonard, A. Energy cascade in large eddy simulations of turbulent fluid flows. *Adv. Geophys.* **1974**, *18A*, pp. 237-248.
- [89] Lettau, H. Note on Aerodynamic Roughness-Parameter Estimation on the Basis of Roughness-Element Description. *Journal of Applied Meteorology* **1969**, *8*, pp. 828-832.
- [90] Lignarolo, L.E.M.; Ragni, D.; Krishnaswami, C.; Chen, Q.; Simão Ferreira, C.J.; van Bussel, G.J.W. Experimental analysis of the wake of a horizontal-axis wind-turbine model. *Renewable Energy* **2014**, *70*, pp. 31-46.
- [91] Lignarolo, L.E.M.; Ragni, D.; Scarano, F.; Simão Ferreira C.J.; van Bussel, G.J.W. Tip-vortex instability and turbulent mixing in wind-turbine wakes. *J. Fluid Mech.* **2015**, *781*, pp. 467-493.
- [92] Lissaman, P.B.S. Low-Reynolds-Number Airfoils. *Annu. Rev. Fluid Mech.* **1983**, *15*, pp. 223-239.
- [93] Lozano-Durán, A.; Jiménez, J. Effect of the computational domain on direct simulations of turbulent channels up to $Re_\tau = 4200$. *Physics of Fluids* **2014**, *26*, 011702.
- [94] MacDonald, R. W.; Griffiths, R. F.; Hall, D. J. An improved method for the estimation of surface roughness of obstacle arrays. *Atmospheric Environment* **1998**, *32*, pp. 1857-1864.
- [95] Mann, J. The spatial structure of neutral atmospheric surface-layer turbulence. *J. Fluid Mech.* **1994**, *273*, pp. 141-168.
- [96] Manwell, J. F.; McGowan, J. G.; Rogers, A. L. Wind Energy Explained - Theory, design and application. *John Wiley & Sons* **2009**, Chichester, UK; 978-0-470-01500-1.
- [97] Mason, P.J.; Callen, N.S. On the magnitude of the subgrid-scale eddy coefficient in large-eddy simulations of turbulent channel flow. *J. Fluid Mech.* **1986**, *162*, pp. 439-462.
- [98] Mason, P.J.; Thomson, D.J. Large-eddy simulations of the neutral-static-stability planetary boundary layer. *Q. J. R. Meteorol. Soc.* **1987**, *113*, pp. 413-443.
- [99] Mazellier, N.; Vassilicos, J.C. Turbulence without Richardson-Kolmogorov cascade. *Phys. Fluids* **2010**, *22*, 075101
- [100] McMasters, J. H.; Henderson, M. L. Low speed single element airfoil synthesis. *Tech. Soaring* **1980**, *6*, pp. 1-21.
- [101] Medici, D.; Alfredsson, P. Measurement on a wind turbine wake: 3D effects and bluff body vortex shedding. *Wind Energy* **2006**, *9*, pp. 219-236.
- [102] Mikkelsen, R. Actuator Disc Methods Applied to Wind Turbines. PhD Thesis, Technical University of Denmark, Denmark, **2003**.
- [103] Muller, Y.A.; Aubrun, S.; Masson, C. Determination of real-time predictors of the wind turbine wake meandering. *Exp Fluids* **2015**, *56*, 53.
- [104] Muetze, K. 3D Polar Identification of a Model Wind Turbine Rotor based on RANS Simulation. Term Paper, Technical University of Munich, Germany, **2017**.
- [105] Nagata, K.; Sakai, Y.; Inaba, T.; Suzuki, H.; Terashima, O.; Suzuki, H. Turbulence structure and turbulence kinetic energy transport in multiscale/fractal-generated turbulence. *Phys. Fluids* **2013**, *25*, 065102.

-
- [106] Nanos, E.M.; Kheirallah, N.; Campagnolo, F.; Bottasso, C.L. Design of a multipurpose scaled wind turbine model. *J. Phys.: Conf. Ser.* **2018**, *1037*, 052016.
- [107] Nedic, J.; Vassilicos, J.C.; Ganapathisubramani, B. Axisymmetric turbulent wakes with new non-equilibrium similarity scalings. *Phys. Rev. Lett.* **2013**, *111*, 144503.
- [108] Nicoud, F.; Baggett, J.S.; Moin, P.; Cabot, W. Large eddy simulation wall-modeling based on suboptimal control theory and linear stochastic estimation. *Phys. Fluids* **2001**, *13*, pp. 2968-2984.
- [109] Obligado, M.; Dairay, T.; Vassilicos, J.C. Nonequilibrium scalings of turbulent wakes. *Phys. Rev. Fluids* **2016**, *1*, 044409.
- [110] Odemark, Y.; Fransson, J.H.M. The stability and development of tip and root vortices behind a model wind turbine. *Exp. Fluids* **2013**, *54*, 1591.
- [111] Petersen, R. L. A wind tunnel evaluation of methods for estimating surface roughness length at industrial facilities. *Atmospheric Environment* **1997**, *31*, pp.45-57.
- [112] Pope, S.B. *Turbulent Flows*. Cambridge University Press **2000**
- [113] Porté-Agel, F.; Meneveau, C.; Parlange, M.B. A scale-dependent dynamic model for large-eddy simulation: application to a neutral atmospheric boundary layer. *J. Fluid Mech.* **2000**, *415*, pp. 261-284.
- [114] Porté-Agel, F.; Bastankhah, M.; Shamsoddin, S. Wind-Turbine and Wind-Farm Flows: A Review. *Boundary-Layer Meteorology* **2020**, *174*, pp. 1-59.
- [115] Quarton, D.C. Wake turbulence characterisation. *Final report from Garrad Hassan and partners to the energy technology support unit of the Department of Energy of the UK*; Contract No. ETSUWN 5096, **1989**.
- [116] Raupach, M.R. Drag and drag partition on rough surfaces. *Bound.-Layer Meteorol.* **1992** *7*, pp.211-216.
- [117] Remmler, S.; Hickel, S. Direct and large eddy simulation of stratified turbulence. *Int. J. Heat Fluid Flow* **2012** *35*, pp.13-24.
- [118] Saito, N.; Pullin, D.I.; Inoue, M. Large eddy simulation of smooth-wall, transitional and fully rough-wall channel flow. *Phys. Fluids* **2012**, *24*, 075103.
- [119] Salbert, B. Windkanalmodell einer generischen Windenergieanlage. Bachelor Thesis, Technical University of Munich, Germany, **2014**.
- [120] Salbert, B. Measurements and simulations of model wind turbine rotor loads for calibration of blade airfoil polars. Term Paper, Technical University of Munich, Germany, **2015**.
- [121] Sarlak, H.; Meneveau, C.; Sørensen, J.N. Role of subgrid-scale modeling in large eddy simulation of wind turbine wake interactions. *Renewable Energy* **2015**, *77*, pp. 386-399.
- [122] Sarmast, S.; Dadfar, R.; Mikkelsen, R.F.; Schlatter, P.; Ivanell, S.; Sørensen, J.N.; Henningson, D.S. Mutual inductance instability of the tip vortices behind a wind turbine. *J. Fluid Mech.* **2014**, *755*, pp. 705-731.
- [123] Schlichting, H.; Gersten, K. *Boundary-Layer Theory*. Springer **2016**, Berlin, Germany; 978-3-662-52919-5.
- [124] Schneider, M.S.; Nitzsche, J.; Hennings, H. Accurate load prediction by BEM with airfoil data from 3D RANS simulations. *Journal of Physics: Conference Series* **2016**,

- 753, 082016.
- [125] Schumann, U. Subgrid Scale Model for Finite Difference Simulation of Turbulent Flows in Plane Channels and Annuli. *Journal of Computational Physics* **1975**, *18*, pp.376-404.
- [126] Selig, M.; Donovan, J.; Frase, D. Airfoils at low speeds. H.A. Stokely, Virginia Beach USA, 1989.
- [127] Selig, M.; Guglielmo, J. J.; Broeren, A. P.; Giguère, P. Summary of Low-Speed Airfoil Data - Volume 1. *SoarTech* **1995**, Virginia Beach, USA.
- [128] Seoud, R.E.; Vassilicos, J.C. Dissipation and decay of fractal-generated turbulence. *Phys. Fluids* **2007**, *19*, 105108.
- [129] Smagorinsky, J. General circulation experiments with the primitive equations, Part 1: the basic experiment. *Mon. Weath. Rev.* **1963**, *91*, pp. 99-164.
- [130] Snel, H; Schepers, J.G; Montgomerie, B. The MEXICO project: The database and first results of data processing and interpretation. *Journal of Physics: Conference Series* **2007**, *75*, 012014.
- [131] Sørensen, J.N.; Myken, A. Unsteady actuator disc model for horizontal axis wind turbines. *Journal of Wind Engineering & Industrial Aerodynamics* **1992**, *39*, pp. 139-149.
- [132] Sørensen, J.N.; Shen, W.Z. Numerical modelling of Wind Turbine Wakes. *Journal of Fluids Engineering* **2002**, *124*, pp. 393-399.
- [133] Sørensen, J.N.; Mikkelsen R.F.; Henningson D.S.; Ivanell S.; Sarmast S.; Andersen S.J. Simulation of wind turbine wakes using the actuator line technique. *Philos Trans R Soc* **2015**, *373*, 20140.
- [134] Sørensen, J.N. General Momentum Theory for Horizontal Axis Wind Turbines. *Springer* **2016**, New York, USA; 978-3-319-22114-4.
- [135] Stein, V.P.; Kaltenbach, H.J. Wind-tunnel modelling of the tip-speed ratio influence on the wake evolution. *J. Phys.: Conf. Ser.* **2016**, *753*, 032061.
- [136] Stein, V.P.; Kaltenbach, H.J. Influence of ground roughness on the wake of a yawed wind turbine - a comparison of wind-tunnel measurements and model predictions. *J. Phys.: Conf. Ser.* **2018**, *1037*, 072005.
- [137] Stein, V.P.; Kaltenbach, H.J. Non-Equilibrium Scaling Applied to the Wake Evolution of a Model Scale Wind Turbine. *Energies* **2019**, *12*, 2763.
- [138] Stevens, R.J.A.M.; Graham, J.; Meneveau, C. A concurrent precursor inflow method for Large Eddy Simulations and applications to finite length wind farms. *Renewable Energy* **2014**, *68*, pp. 46-50.
- [139] Stull, R.B. An Introduction to boundary layer meteorology. *Springer* **1988**, Dordrecht, Netherlands; 978-94-009-3027-8.
- [140] Tabor, G.R.; Baba-Ahmadi, M.H. Inlet conditions for large eddy simulation: A review. *Computers & Fluids* **2010**, *39*, pp. 553-567.
- [141] Martinez Tossas, L.A.; Leonardi, S. Wind Turbine Modeling for Computational Fluid Dynamics. *NREL Report* **2013**, NREL, Golden, NREL/SR-5000-55054.
- [142] Townsend, A.A.; The Structure of Turbulent Shear Flow, 2nd ed. *Cambridge University Press* **1976**.
- [143] Troldborg, N.; Sørensen, N.N.; Mikkelsen, R.F. Numerical Simulations of Wakes of

- Wind Turbines Operating in Sheared and Turbulent Inflow. In *EWEC 2009 Proceedings online*, EWEC.
- [144] Troldborg, N.; Zahle, F.; Réthoré, P.E.; Sørensen, N.N. Comparison of wind turbine wake properties in non-sheared inflow predicted by different computational fluid dynamics rotor models. *Energies* **2014**, DOI: 10.1002/we.1757.
- [145] Uberoi, M.S.; Freymuth, P. Turbulent Energy Balance and Spectra of the Axisymmetric Wake. *Phys. Fluids* **1970**, *13*, pp. 2205-2210.
- [146] Valente, P.C.; Vassilicos, J.C. Universal Dissipation Scaling for Nonequilibrium Turbulence. *Phys. Rev. Lett.* **2012**, *108*, 214503.
- [147] Vasilyev, O.V.; Lund, T.S.; Moin, P. A General Class of Commutative Filters for LES in Complex Geometries *J. Comput. Phys.* **1998**, *146*, pp. 82-104.
- [148] Vassilicos, J.C. Dissipation in Turbulent Flows. *Annu. Rev. Fluid Mech.* **2015**, *47*, pp. 95-114.
- [149] Vassilicos, J.C. From Tennekes and Lumley to Townsend and to George: A Slow March to Freedom. In *Whither Turbulence and Big Data in the 21st Century?*; Pollard A., Castillo L., Danaïla L., Glauser M., Eds.; Springer, Switzerland, Cham, 2017. pp. 3-11.
- [150] Vermeer, L.J.; Sørensen, J.N.; Crespo, A. Wind turbine wake aerodynamics. *Progress in Aerospace Sciences* **2003**, *39*, pp. 467-510
- [151] Vollmer, L.; Steinfeld, G. Estimating the wake deflection downstream of a wind turbine in different atmospheric stabilities: an LES study. *Wind Energ. Sci.* **2016**, *1*, pp. 129-141
- [152] Wang, S.; Zhou, Y.; Mahbub Alam, M.; Yang, H. Turbulent intensity and Reynolds number effects on an airfoil at low Reynolds numbers. *Phys. Fluids* **2014**, *26*, 115107
- [153] Watkins, S.; Ravi, S.; Loxton, B. The Effect of Turbulence on the Aerodynamics of Low Reynolds Number Wings. *Engineering Letters* **2009**, *18*, pp. 279-284
- [154] Welch, P.D. The Use of the Fast Fourier Transform for the Estimation of Power Spectra: A Method Based on Time Averaging Over Short, Modified Periodograms. *IEEE Transactions on Audio and Electroacoustics* **1967**, *15*, pp. 70-73
- [155] Windenergie in Nutzwäldern. *Bundesverband WindEnergie e.V.* **2019**
- [156] Wu, Y.; Porté-Agel, F. Large-eddy simulation of wind-turbine wakes: Evaluation of turbine parametrisations. *Boundary-Layer Meteorology* **2011**, *138*, pp. 345-366.
- [157] Wu, Y.; Porté-Agel, F. Atmospheric Turbulence Effects on Wind-Turbine Wakes: An LES Study. *Energies* **2012**, *5*, pp. 5340-5362.
- [158] Xie, S.; Archer, C. Self-similarity and turbulence characteristics of wind turbine wakes via large-eddy simulation. *Wind Energy* **2015**, *18*, pp. 1815-1838
- [159] Zhang, W.; Markfort, C.D.; Porté-Agel, F. Near-wake flow structure downwind of a wind turbine in a turbulent boundary layer. *Exp. Fluids* **2011**, *52*, pp. 1219-1235.
- [160] Zhang, W.; Markfort, C.D.; Porté-Agel, F. Wind-Turbine Wakes in a Convective Boundary Layer: A Wind-Tunnel Study. *Boundary-Layer Meteorol.* **2013**, *146*, pp. 161-179.
- [161] Zwerger, C.; Hickel, S.; Breitsamter, C.; Adams, N.A. Wall modeled large-eddy simulation of the VFE-2 delta wing. *AIAA paper* **2015**, 2015-2572.

Appendix

A.1 Calibration of the Generator

To measure the torque generated by the rotor of a model wind turbine, a torque meter can be integrated in the nacelle. However, for small scale model wind turbines torque meters which meet the size of the nacelle are typically not available. Therefore, for the model wind turbine designed in this project the generated torque is estimated from the electric current of the generator. The method is accurate if (i) friction losses of the shaft bearings are known and (ii) the motor torque constant k_M , necessary to convert electric current to torque, is calibrated for the individual generator. Even for generators of high quality as used in this project, the manufacturer does only provide estimates on the friction losses and gives the motor torque constant with an error of $k_M \pm 3\%$. Furthermore, to protect the motor from excessive axial forces acting on the rotor, additional bearings in the present wind turbine model are installed. These bearings are preloaded which causes additional friction losses.

Therefore, the generator ECMAX40 of the model wind turbine including the additional bearings was calibrated using the torque meter rig developed by Bastankhah & Porté-Agel. A detailed description of the setup can be found in [13]. In the course of the calibration campaign a generator DCX22L for another model wind turbine was calibrated as well. For documentary purposes, the results of this calibration are included as well.

The calibration procedure is as follows: A load machine is driven by the constant electric current I_{LM} . The generator is connected to the load machine and is controlled for constant rotational speed N . To maintain the rotational speed the generator needs to decelerate or accelerate by generating or consuming the electrical current I_G . A rotary torque sensor installed between the load machine and the generator measures the generated torque at the shaft Q_{SH} . A sketch of the torque meter rig is shown in Figure A.1. Given that the motor torque constant is known, the frictional losses Q_F can then be calculated by

$$Q_F = Q_{SH} - k_M I_G. \quad (\text{A.1})$$

For the two generators Figure A.2 shows the measured friction losses obtained for various electric currents of the load machine. For the calculation the motor torque constant

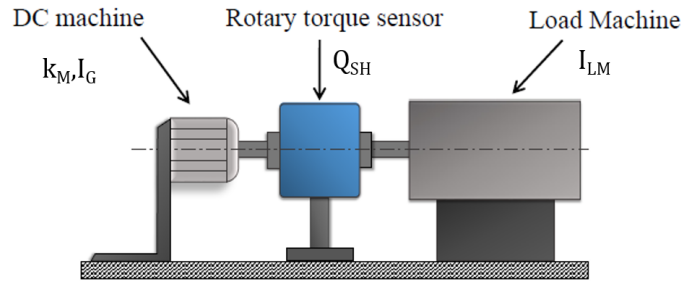


Figure A.1: Sketch of the torque meter rig; Based on [13]

$k_{M,dat}$ provided by the manufacturer is used. Due to its size and the additional preloaded bearings the friction losses for the generator ECMAX40 are more than an order larger than for the generator DCX22L. It is interesting to notice that the computed friction losses for the generator DCX22L spread relatively wide and become even negative. It is assumed that due to the low friction in the generator DCX22L the calibration is quite sensitive to uncertainties in the motor torque constant $k_{M,dat}$.

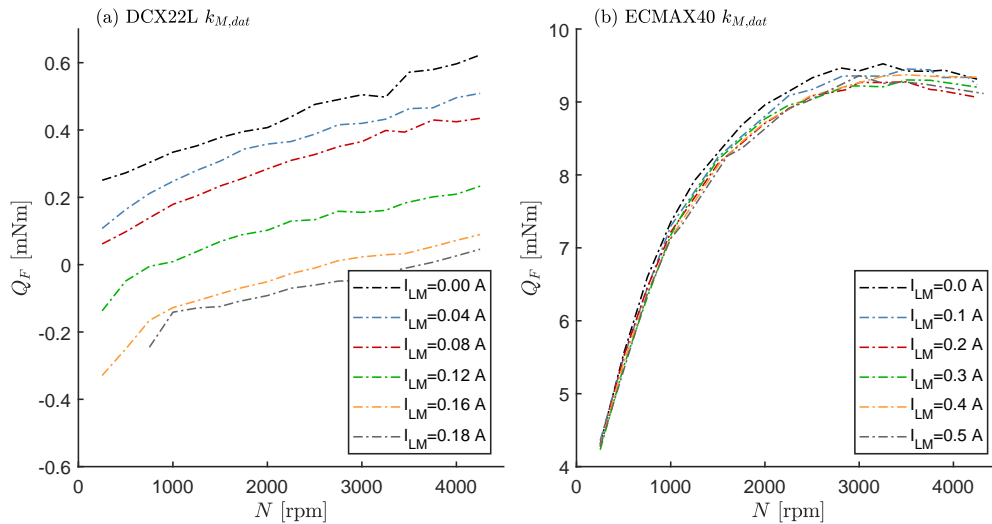


Figure A.2: Friction losses Q_F for various electric currents I_{LM} of the load machine for the generator (a) DCX22L and (b) ECMAX40. For the calculation of Q_F , motor constants provided by the manufacturer $k_{M,dat}$ are applied.

For this reason the motor torque constant k_M is calibrated such that the standard deviation of the friction losses σ_{Q_F} over all measured loads becomes minimal. The standard deviation of the friction losses σ_{Q_F} as function of the motor torque constant k_M is shown in Figure A.3. It can be seen that a change of the motor constant of about 3.5% reduces the standard deviation σ_{Q_F} for the generator DCX22L significantly from a value of 0.2 mNm/A to 0.026 mNm/A. For the generator ECMAX40 the standard deviation σ_{Q_F} can also be reduced from a value of 0.09 mNm/A to 0.06 mNm/A by changing the motor constant by about 2.5%. Since this generator has a higher capacity of generating torque the improvement, however, has a rather insignificant effect.

Figure A.4 shows the measured friction losses obtained for various electric currents of the load machine for the calibrated motor torque constant $k_{M,opt}$ for the generators (a) DCX22L and (b) ECMAX40. For the generator DCX22L the benefit of the calibration

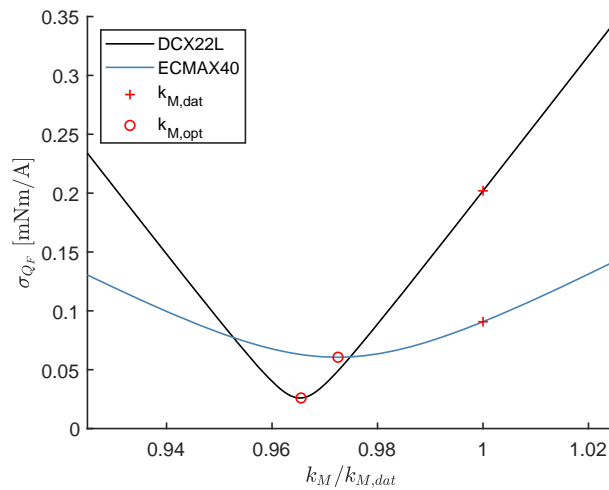


Figure A.3: Standard deviation of the friction losses σ_{Q_F} as function of the motor constant k_M

can clearly be seen. The friction losses do not spread and do not become negative. As indicated above, for the generator ECMAX40 the calibration has only little effect, as the standard deviation of the measured friction losses σ_{Q_F} for this generator is already low when the motor constant provided by the manufacturer $k_{M,dat}$ is applied. Manufacturer-provided data of the generators and the calibrated motor constants are given in Table A.1.

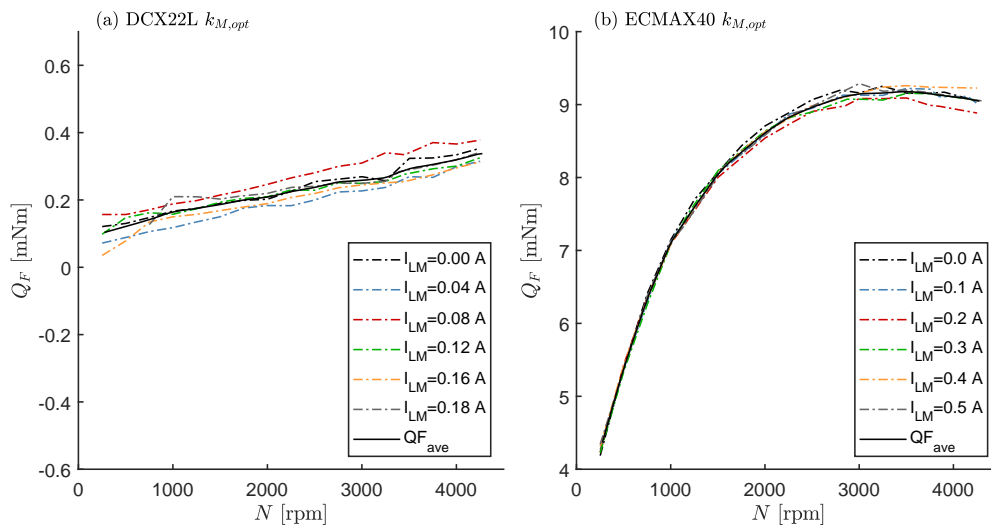


Figure A.4: Friction losses Q_F for various electric currents I_{LM} of the load machine for the generator (a) DCX22L and (b) ECMAX40. For the calculation of Q_F , calibrated motor constants $k_{M,opt}$ are applied.

Table A.1: Manufacturer-provided data of the generators and the calibrated motor torque constants.

		DCX22L	ECMAX40
Outer diameter (mm)		22	40
Nominal voltage (V)	V_N	18	48
Nominal speed (rpm)	Ω_N	10,800	3,770
Nominal torque (mNm)	Q_N	32.2	203
Nominal current (A)	I_N	2.26	2.19
No load speed (rpm)	Ω_n	11,800	4,720
No load current (mA)	I_n	54.6	104
Nominal torque constant (mNm/A)	$k_{M,dat}$	14.6	96.1
Calibrated torque constant (mNm/A)	$k_{M,opt}$	14.10	93.46

A.2 Rotational Matrices

All rotational matrices used in the coordinate transformations of the Actuator Line Method described in section 6.3.1 are given here. The coordinate transformations described by the rotational matrices ${}_I\mathbf{R}_r$ and ${}_b\mathbf{R}_I$ can be derived from the elementary coordinate transformations ${}_I\mathbf{R}_{II}$, ${}_{II}\mathbf{R}_r$, and ${}_r\mathbf{R}_b$. These can be written as

$${}_I\mathbf{R}_r = {}_I\mathbf{R}_{II} {}_{II}\mathbf{R}_r \quad (\text{A.2})$$

$${}_b\mathbf{R}_I = {}_I\mathbf{R}_b^{-1} = [{}_I\mathbf{R}_r {}_r\mathbf{R}_b]^{-1} \quad (\text{A.3})$$

All elementary coordinate transformations are given by the rotational matrices

$${}_I\mathbf{R}_{II} = \begin{bmatrix} \cos(\gamma) & -\sin(\gamma) & 0 \\ \sin(\gamma) & \cos(\gamma) & 0 \\ 0 & 0 & 1 \end{bmatrix} \quad {}_{II}\mathbf{R}_r = \begin{bmatrix} \cos(\Psi(t)) & -\sin(\Psi(t)) & 0 \\ \sin(\Psi(t)) & \cos(\Psi(t)) & 0 \\ 0 & 0 & 1 \end{bmatrix}$$

$${}_r\mathbf{R}_b = \begin{bmatrix} \cos(\Psi_{0,i}) & -\sin(\Psi_{0,i}) & 0 \\ \sin(\Psi_{0,i}) & \cos(\Psi_{0,i}) & 0 \\ 0 & 0 & 1 \end{bmatrix} \quad {}_b\mathbf{R}_a = \begin{bmatrix} 1 & 0 & 0 \\ 0 & -\cos(\phi) & \sin(\phi) \\ 0 & \sin(\phi) & \cos(\phi) \end{bmatrix}$$

were γ is the yaw angle, $\Psi(t)$ the angular angle, $\Psi_{0,i} = 2\pi(i - 1)/N_b$ the angular phase shift of the blade i , and ϕ the angle of the relative wind at the considered control point.

A.3 Measurement Positions

In the following all positions at which hot-wire measurements were recorded for the wind tunnel tests presented in Chapter 5 are given. Axial coordinates of measurement stations in downstream direction are listed in Table A.2. For measurements in the mid-horizontal plane, lateral coordinates for each axial measurement station can be found in Table A.3. For measurements in the mid-vertical plane, vertical coordinates for each axial measurement station can be found in Table A.4.

Table A.2: List of measurement positions in the wind tunnel, axial coordinates. Origin of the coordinate system is the rotor center.

Number	1	2	3	4	5	6
X/R	2	4	6	10	14	18
$X[\text{mm}]$	450	900	1350	2250	3150	4050

Table A.3: List of measurement positions in the wind tunnel, lateral coordinates. Origin of coordinate system is the rotor center.

Number	Y/R	Y[mm]	Number	Y/R	Y[mm]
1	-2.78	-625.23	28	0.14	31.50
2	-2.64	-593.73	29	0.28	63.00
3	-2.50	-562.23	30	0.42	94.50
4	-2.36	-530.73	31	0.56	126.00
5	-2.22	-499.23	32	0.70	157.50
6	-2.08	-467.73	33	0.81	181.51
7	-1.95	-438.45	34	0.89	199.80
8	-1.83	-411.83	35	0.95	213.75
9	-1.72	-387.63	36	1.01	227.70
10	-1.63	-365.63	37	1.07	241.64
11	-1.52	-342.24	38	1.14	255.59
12	-1.43	-321.16	39	1.20	269.53
13	-1.34	-302.14	40	1.27	284.99
14	-1.27	-284.99	41	1.34	302.14
15	-1.20	-269.53	42	1.43	321.16
16	-1.14	-255.59	43	1.52	342.24
17	-1.07	-241.64	44	1.63	365.63
18	-1.01	-227.70	45	1.72	387.63
19	-0.95	-213.75	46	1.83	411.83
20	-0.89	-199.80	47	1.95	438.44
21	-0.81	-181.51	48	2.08	467.73
22	-0.70	-157.50	49	2.22	499.23
23	-0.56	-126.00	50	2.36	530.73
24	-0.42	-94.50	51	2.50	562.23
25	-0.28	-63.00	52	2.64	593.73
26	-0.14	-31.50	53	2.78	625.23
27	0.00	0.00			

Table A.4: List of measurement positions in the wind tunnel, vertical coordinates. Origin of coordinate system is the rotor center.

Number	Z/R	Z[mm]	Number	Z/R	Z[mm]
1	-1.52	-342.24	18	0.14	31.50
2	-1.43	-321.16	19	0.28	63.00
3	-1.34	-302.14	20	0.42	94.50
4	-1.27	-284.99	21	0.56	126.00
5	-1.20	-269.53	22	0.70	157.50
6	-1.14	-255.59	23	0.81	181.51
7	-1.07	-241.64	24	0.89	199.80
8	-1.01	-227.70	25	0.95	213.75
9	-0.95	-213.75	26	1.01	227.70
10	-0.89	-199.80	27	1.07	241.64
11	-0.81	-181.51	28	1.14	255.59
12	-0.70	-157.50	29	1.20	269.53
13	-0.56	-126.00	30	1.27	284.99
14	-0.42	-94.50	31	1.34	302.14
15	-0.28	-63.00	32	1.43	321.16
16	-0.14	-31.50	33	1.52	342.24
17	0.00	0.00	34	1.63	365.63